Photo-Induced Effects in Cuprate Systems

Dissertation
zur
Erlangung der naturwissenschaftlichen Doktorwürde
(Dr. sc. nat.)

vorgelegt der

Mathematisch-naturwissenschaftlichen Fakultät

der

Universität Zürich

von

Andrea Evelyn Stilp

aus

Deutschland

Promotionskomitee

Prof. Dr. Elvezio Morenzoni (Vorsitz)
Dr. Andreas Suter (Leitung der Dissertation)
Prof. Dr. Hugo Keller
Prof. Dr. Christian Bernhard

Zürich, 2014

“Life isn’t about waiting for the storm
to pass - it’s about learning
to dance in the rain!”

Vivian Greene

Abstract

Superconductivity is a fascinating phenomenon, which is until today in the focus of fundamental research. Especially, the discovery of the cuprate high temperature superconductors greatly promoted the field. The electrical properties of these brittle ceramics depend a lot on the number of free charge carriers in the CuO_2 planes. In general, the isolating parent compounds become superconducting by chemical doping, which modifies the structural properties of the cuprate system at the same time. In order to obtain a better understanding of the microscopic mechanism yielding superconductivity, it is of interest to incorporate charge carriers in the CuO_2 planes without introducing additional disorder.

Disorder present within the cuprate systems does not only effect superconductivity, but also the antiferromagnetic ground state in the lightly doped case. In the present study the differences in the magnetic properties between $La_{2-x}Sr_xCuO_4$ (LSCO) thin films and single crystals were investigated, since strong differences in the critical temperature T_c were observed before. We show that thin-film samples exhibit a lower Néel temperature and that the freezing of the mobile holes is strongly suppressed to much lower temperatures. In the doping range $0.02 \leq x \leq 0.06$ the transition temperature to the so called cluster spin glass phase is by contrast increased compared to bulk values. No changes are observed in the temperature and doping dependence of the staggered magnetization. We identify misfit dislocations, appearing when the LSCO film relaxes during growth, as the main reason of these differences between thin films and single crystals. Oxygen off-stoichiometry, strain caused by the lattice mismatch between the sample and the substrate, and higher-order corrections of the magnetic coupling constants are improbable origins.

In $YBa_2Cu_3O_{6+x}$ (YBCO) the ordering of the Cu-O chains, which are only present in a few cuprate systems, strongly influences the electronic properties. In general, YBCO thin films exhibit lower critical temperatures compared to single crystals. The incorporation of gold nanoparticles reduces the difference. The resulting thin-film systems have in addition a higher critical current density. Utilizing low energy muon spin rotation (LE-μSR) we studied the microscopic changes due to the Au nanoparticles in detail. As observed from magnetic screening profiles, YBCO thin films with Au nanoparticles screen the applied magnetic field stronger compared to pristine YBCO thin films. They exhibit a higher superfluid density, whereas the value of the superconducting band gap remains unchanged. While the increased critical current density may be explained by a stronger pinning of the vortices, the increase in the critical temperature may be related to a lowered defect density,

probably due to a condensation of defects at the Au nanoparticles.

To introduce additional charge carriers without increasing the disorder we use photo-induced electron-hole pairs. In La_2CuO_4 photo-illumination leads to an enhanced conductivity. The induced photoconductivity strongly depends on the oxygen content and is difficult to reproduce. By doping Sr into the system the photoconductivity is increased at low temperatures and becomes reproducible. The general temperature dependence changes remarkably with Sr doping. Above 100 K the recombination rate of the electron-hole pairs is strongly increased. Thus, the induced photoconductivity is of the same order independent of the Sr content. We were not able to resolve a lowering of the staggered magnetization by LE-μSR, since the recombination times appeared to be too short. Only a small fraction of the created charge carriers persists longer than 1 s. The photo-induced effects in LSCO are transient.

In contrast to LSCO, illumination causes a persistent increase in conductivity in YBCO for $T < 270\,\mathrm{K}$. LE-μSR measurements of the illuminated state revealed an increased superfluid density close to the vacuum interface on a length scale comparable to the light penetration depth, in agreement with previously observed increases in T_c. In addition, we identified an anisotropic change within the in-plane magnetic penetration depths λ_a and λ_b. A lowering of the penetration depth is only induced by illumination when the shielding currents flow along the Cu-O chains. This implies that the Cu-O chains significantly contribute to the screening of the external magnetic field. A possible explanation of the photo-persistent findings is a non-trivial modification of the local band structure, e.g. due to a hybridization of the CuO_2 planes and the Cu-O chains.

The presented study shows the tremendous impact of nano-scale disorder on the superconducting properties of cuprates.

Zusammenfassung

Supraleitung ist ein faszinierendes Phänomen, das bis heute im Fokus der experimentellen Grundlagenforschung steht. Dazu hat vor allem die Entdeckung der Kupfer basierten Hochtemperatursupraleiter beigetragen. Die elektrischen Eigenschaften dieser brüchigen Keramiken hängen stark von der Anzahl der freien Ladungsträger in den CuO_2-Ebenen ab. Im Allgemeinen werden die isolierenden Ausgangssysteme durch Austauschen chemischer Elemente supraleitend. Dieser Prozess verändert jedoch gleichzeitig die Struktur. Um den Ursprung der Supraleitung besser zu verstehen ist es von Interesse zusätzliche Ladungsträger möglichst störungsfrei in die CuO_2-Ebenen einzubringen.

Es hat sich gezeigt, dass die auftretenden Unordnungsphenomäne der Kupratsysteme nicht nur äusserst relevant in Bezug auf die Supraleitung sind, sondern auch den antiferromagnetischen Zustand der leicht dotierten Kuprate beeinflussen. So wurden in dieser Arbeit zunächst die Unterschiede der magnetischen Eigenschaften zwischen $La_{2-x}Sr_xCuO_4$ (LSCO) Dünnschichtsystemen und Einkristallen untersucht, da deutliche Abweichungen hinsichtlich der kritischen Temperaturen T_c bereits bekannt waren. Dabei zeigte sich, dass die Néel Temperatur T_N in dünnen Filmen deutlich niedriger ist und das Ausfrieren der mobilen Ladungsträger zu tiefen Temperaturen hin unterdrückt wird. Bei einer Dotierung von $0.02 \leq x \leq 0.06$ hingegen ist die Übergangstemperatur zu der sogenannten Cluster-Spin-Glas-Phase erhöht. Die Temperatur- und Dotierungsabhängigkeit der Untergittermagnetisierung bleiben andererseits unverändert. Dies legt nahe, dass die Fehlversetzungen, die auftreten wenn die LSCO Struktur von den Substratgitterparametern zu ihren intrinsischen Gitterkonstanten wechselt, hauptverantwortlich sind für die Unterschiede zwischen dünnen Filmen und Einkristallen. Auf der anderen Seite können eine erhöhte Sauerstoffstöchiometrie, Spannungseffekte von Seiten des Substrates sowie der Einfluss von magnetischen Kopplungsgrössen höherer Ordnung als Ursache der Unterschiede eher ausgeschlossen werden.

In $YBa_2Cu_3O_{6+x}$ (YBCO) ist die Ordnung der Sauerstoffketten, die nur in wenigen Kupraten vorkommen, von enormer Bedeutung für die elektrischen Eigenschaften. Es hat sich gezeigt, dass dünne YBCO Filme im Allgemeinen geringere kritische Temperaturen aufweisen als Einkristalle bei gleicher Sauerstoffdotierung. Das Einbringen von Goldnanopartikeln wirkt diesem entgegen. Die golddotierten Dünnschichtsysteme weisen zudem eine höhere kritische Stromdichte auf. Mit Hilfe der Myon-Spin-Rotations-Technik bei niedrigen Myonimplantationsenenergien (LE-μSR) haben wir im Rahmen dieser Studie die daraus

resultierenden Veränderungen der mikroskopischen Eigenschaften näher untersucht. Aus magnetischen Eindringprofilen zeigt sich, dass die mit Goldnanopartikeln dotierten YBCO Filme das angelegte Magnetfeld stärker verdrängen als die reinen YBCO Filme. Damit weisen sie eine höhere suprafluide Ladungsträgerdichte auf. Der Wert der supraleitenden Bandlücke bleibt hingegen unverändert. Während die erhöhte kritische Stromdichte mit dem stärkeren Verankern der Flussschläuche erklärt wird, führen wir die Erhöhung der kritischen Temperatur auf die Reduktion der Defektdichte zurück, die möglicherweise durch eine Defektkonzentration an den Goldnanopartikel erzielt wird.

Um in die untersuchten Systeme möglichst störungsfrei zusätzlichen Ladungsträger einzubringen, nutzen wir photoinduzierte Elektron-Loch-Paare. In La_2CuO_4 ergibt sich dadurch eine Erhöhung der Leitfähigkeit, die jedoch stark vom Sauerstoffgehalt der Probe abhängt und nur schwer zu reproduzieren ist. Mittels Dotierung von Sr wird der Effekt vor allem bei tiefen Temperaturen verstärkt und kann reproduzierbar gemessen werden. Die Temperaturabhängigkeit ändert sich dabei stark. Oberhalb von 100 K rekombinieren die Elektron-Loch-Paare schneller, sodass die photoinduzierte Leitfähigkeit vergleichbar gross ist in allen untersuchten LSCO Proben. Eine Erniedrigung der Untergittermagnetisierung konnte mittels LE-μSR nicht beobachtet werden, was zeigt das die Rekombinationszeiten sehr kurz sein müssen. Nur ein Bruchteil der induzierten Ladungsträger hat eine Lebensdauer länger als 1 s. Die photoinduzierten Effekte in LSCO sind somit transient.

In YBCO hingegen kann durch Beleuchtung mit sichtbarem Licht die Leitfähigkeit permanent erhöht werden, solange $T < 270\,\mathrm{K}$. LE-μSR Messungen zeigen nach intensiver Beleuchtung eine Erhöhung der suprafluiden Ladungsträgerdichte nahe der Oberfläche auf der Längenskala der Lichteindringtiefe des Materials. Dies ist im Einklang mit der zuvor beobachteten Erhöhung der kritischen Temperatur durch Beleuchtung. Zudem konnten wir zeigen, dass sich die photoinduzierten Ladungsträger anisotrop auf die magnetischen Eintringtiefen λ_a und λ_b auswirken. Eine Erniedrigung der Eindringtiefe wird nur gemessen, wenn die Abschirmströme entlang der Cu-O Ketten fliessen. Dies legt nahe, dass die Ketten zur Abschirmung des Magnetfeldes beitragen. Eine nicht triviale Modifikation der lokalen Bandstruktur, z.B. durch Hybridisierung der CuO_2 Ebenen mit den Cu-O Ketten, wäre eine mögliche Erklärung für die beobachteten photoinduzierten Effekte.

Es hat sich im Rahmen dieser Studien gezeigt, das die mikroskopische Ordnung der Kuprate einen wesentlichen Einfluss auf die supraleitenden Eigenschaften hat.

Contents

1 Introduction

Superconductivity is already known for more than 100 years [1]. In 1986 Bednorz and Müller discovered with $La_{2-x}Ba_xCuO_4$ a new class of superconductors referred to as cuprates [2]. These oxide materials exhibit a much higher transition temperature T_c compared to classical superconductors like elemental metals as niobium or mercury. Until today, the highest $T_c \approx 133\,K$ at ambient pressure was found in $HgBa_2Ca_2Cu_3O_{8+\delta}$ [3], which is far above the boiling temperature of liquid nitrogen (77 K). The possibility of practical use and the idea to find a room temperature superconductor triggered intensive research on this field.

Cuprate systems have a layered structure in common, containing CuO_2 planes separated by different kinds of interlayers. The coupling between the CuO_2 layers is weak resulting in a quasi-two dimensional behavior and highly anisotropic properties. While the BCS theory of Bardeen, Cooper and Schrieffer [4, 5] explains the microscopic properties of classical superconductors by assuming a weak electron-phonon coupling, the underlying pairing mechanism in cuprates is still under heavy debate. Very different types of pairing mechanisms have been proposed. They can be divided into two main lines. One assumes pure electronic correlations as the driving force for the pairing, e.g. magnetic spin excitations theories [6] , the "resonant valence bond" idea [7], or a relation to a quantum-phase transition [8, 9]. The other approach stresses very strong electron-phonon couplings [10]. A prominent example of the later is the formation of polarons and bipolarons [11, 12]. Due to these open issues, cuprates are still in the focus of current research.

One opportunity to get new insights on the microscopic properties of cuprate high temperature superconductors, and hence to their coupling mechanisms, is the systematic manipulation of the charge carrier density. By adding charge carriers to the parent compound cuprate systems are tuned from charge transfer insulators to metals and even to superconductors. Chemical substitution is the common route to introduce charge carriers, but typically it is leading to structural disorder, which is strongly influencing the fundamental properties of the systems. Hydrostatic pressure also may strengthen the superconducting state [13, 14], but still changes the crystallographic lattice constants [15] and introduces therefore additional disorder. Applying electrical fields is another tool to directly manipulate the charge carrier density. Here, electrical contacts are required and heating effects have to be taken into account, to mention only two disadvantages. To increase the charge carrier density without changing the composition and keeping the amount of disorder as little as possible we used instead photo illumination.

The creation of charge carriers due to photo-doping is widely known in amorphous semiconductors. Multilayered systems, like hydrogenated amorphous silicon (a-Si:H) [16] or crystalline GaAs doping superlattices [17], exhibit persistent photoconductivity after illumination with visible light. Exposure to light creates electron-hole pairs being separated by the p-n junction fields. The spatial separation and the potential barriers inhibit recombination and extend their lifetime. Photo-induced charge carriers were also studied in the normal state of cuprate systems [18]. The recombination time depends strongly on the chosen system. The changes in the charge carrier density could be transient as observed in La_2CuO_4 [19], thermally decaying on time scales of hours to days like in $Bi_2Sr_2Ca_{1-x}Y_xCu_2O_{8+\delta}$ [18] and $Tl_2Ba_2Cu_{6+x}$ [20], or even persistent like in $YBa_2Cu_3O_{6+x}$ [21] and $GdBa_2Cu_3O_{6+x}$ [22].

The impact of photo-induced charge carriers on the superconducting properties are disparate. In conventional superconductors illumination can destroy superconductivity, as it was observed in Pb films [23]. Light pulses can break the superconducting carriers and hence create quasiparticles in the superconducting state, if the photon energy exceeds the binding energy of the Cooper pairs. An excess of quasiparticles results in a smaller energy gap. So in BCS-like superconductors photo-doping weakens the superconducting ground state, as it was also observed in $Tl_2Ba_2Cu_{6+x}$ by a reduction of the critical temperature T_c [20]. Surprisingly, T_c could be increased by visible light illumination in $YBa_2Cu_3O_{6+x}$ and $GdBa_2Cu_3O_{6+x}$ [22].

Until today illumination studies on cuprates have been restricted to the investigation of the structural and electrical properties as well as to the onset of superconductivity. To give new insight on these effects we studied on one side the influence of light on the microscopic magnetic properties of $La_{2-x}Sr_xCuO_4$. The intention is to clarify whether photo-doping has an influence on the antiferromagnetic coupling at the low-doped side of the phase diagram. On the other side we focused on the investigation of the microscopic superconducting properties, like the superfluid density, in $YBa_2Cu_3O_{6+x}$ to get a microscopic understanding of the photo-induced changes at the underdoped side of the phase diagram.

In order to obtain a conclusive picture from the photo-induced effects we studied in addition the role of disorder on the magnetic state of $La_{2-x}Sr_xCuO_4$, by comparing thin-films with bulk samples, and on the superconducting state in $YBa_2Cu_3O_{6+x}$ by adding gold nanoparticles to thin films.

To investigate microscopic magnetic as well as superconducting properties in $La_{2-x}Sr_xCuO_4$

and $YBa_2Cu_3O_{6+x}$ low-energy muon spin rotation was utilized. Using 100% polarized positively charged muons, moderated to energies in the keV range, allows to study internal magnetic fields and field distributions on a nanometer length scale.

In the following we will first introduce the class of cuprates in more detail (Chapter 2). In Chapter 3 the new light source and the in-situ resistance setup, which are the basic requirement for the realization of the photo-induced studies, are introduced. The details about the muon spin rotation technique are presented in Chapter 4. In Chapter 5 the $La_{2-x}Sr_xCuO_4$ compound is introduced. After stating the differences between thin-film and bulk $La_{2-x}Sr_xCuO_4$, the consequences of visible light illumination are discussed. New insights on the photo-persistent effects in $YBa_2Cu_3O_{6+x}$ are presented in Chapter 6, after introducing its properties and the influence of Au as a specific feature. Finally, a summary of the results and ideas about prospective studies are given in Chapter 7.

2 The Class of Cuprates

The cuprate family is the first discovered class of superconductors with $T_\mathrm{c} \gtrsim 30\,\mathrm{K}$. They are often referred as "high-temperature superconductors", because some of them have even $T_\mathrm{c} > 77\,\mathrm{K}$, above the boiling point of nitrogen, which makes them potentially relevant for technical applications. In general these materials are brittle ceramics with strongly anisotropic properties due to their layered perovskite-like structure. The compounds consist of square lattices formed by copper atoms which are bonded to each other through oxygen atoms within the crystallographic ab-plane [24]. A varying number of those conducting $\mathrm{CuO_2}$ planes are separated by insulating interlayers, acting as charge-reservoirs, as depicted in Fig. 2.1. Thus, copper-oxide systems are generally described with the stoichiometric formula $(\mathrm{Ln}_{1-x}\mathrm{M}_x)_{n+1}\,\mathrm{Cu}_n\mathrm{O}_{3n+1-m}$, where Ln is a trivalent rare-earth ion or yttrium, M is an alkaline ion like Ba, Sr, or Ca, n is the number of $\mathrm{CuO_2}$ planes within the unit cell, and m is a multiplicity of the copper coordination characterizing the number of oxygen vacancies [24]. The configuration of $\mathrm{CuO_2}$ planes within the three-state model, believed to be responsible for the superconductivity of cuprate compounds, is presented in Fig. 2.1b. The $d_{x^2-y^2}$ orbitals of the copper ions and the p_x and p_y orbital of the oxygen respectively are relevant for superconductivity within this approach [25].

The parent compounds of cuprate systems $\mathrm{Ln}_{n+1}\mathrm{Cu}_n\mathrm{O}_{3n+1-m}$, as for example $\mathrm{La_2CuO_4}$, are charge transfer insulators with long-range antiferromagnetic (AF) ordering between the copper electronic magnetic moments localized at the copper sites within the $\mathrm{CuO_2}$ planes [26]. The Néel temperature is of the order of $300 - 500\,\mathrm{K}$ and can be strongly suppressed by doping holes in the $\mathrm{CuO_2}$ planes. By doping the parent compounds, e.g. with Ba or Sr, the number of mobile charge carriers is increased, turning the systems into so-called "bad-metals" [27]. The electronic properties strongly differ from the Fermi-liquid theory in this so-called underdoped region of the phase diagram. A similar behavior appears in some of the compounds by varying the oxygen content. Since the added charge carriers could be either electrons (n-doping) or holes (p-doping) two classes of cuprates are distinguished as depicted in the generic phase diagram in Fig. 2.2.

The hole-doped compounds, like e.g. $\mathrm{La}_{2-x}\mathrm{Sr}_x\mathrm{CuO_4}$ and $\mathrm{YBa_2Cu_3O}_{6+x}$, exhibit diverse structural phase diagrams, where p gives the number of holes per $\mathrm{CuO_2}$ plane in the unit cell. The parent compounds have an orthorhombic or tetragonal structure, in contrast to the electron-doped cuprates. Already low hole concentrations ($p \lesssim 0.02$) strongly reduce the Néel temperature T_N, leading to superconductivity at higher doping levels ($p \gtrsim 0.05$).

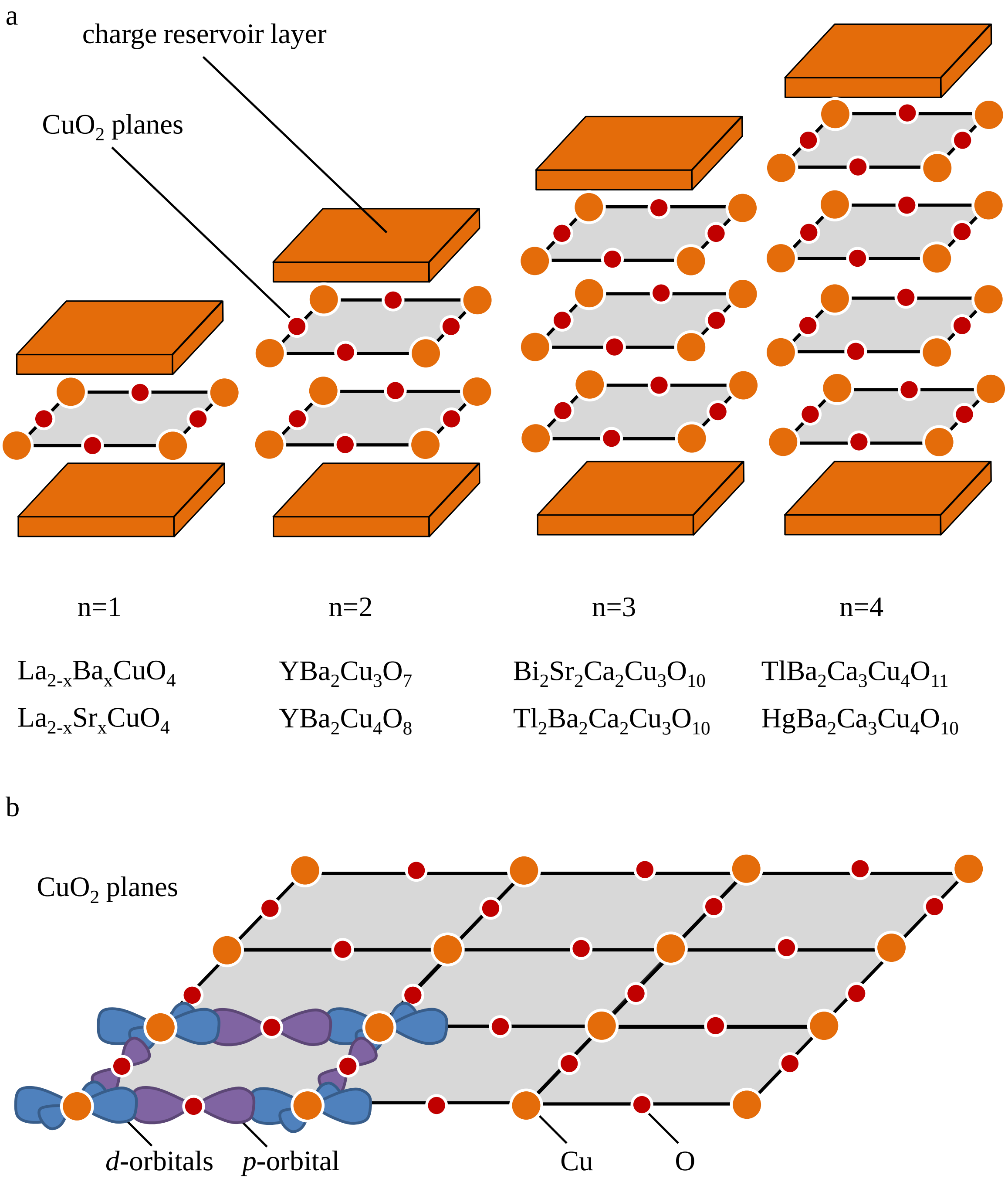

Figure 2.1: Schematic sketch of different cuprate structures (a): n layers of CuO_2 planes (gray) embedded by charge reservoir layers (orange). Some examples of cuprate systems for the respective number of CuO_2 planes n are listed. A CuO_2 layer with the copper d-orbitals (blue) and the oxygen p-orbitals (purple) are presented in b [25].

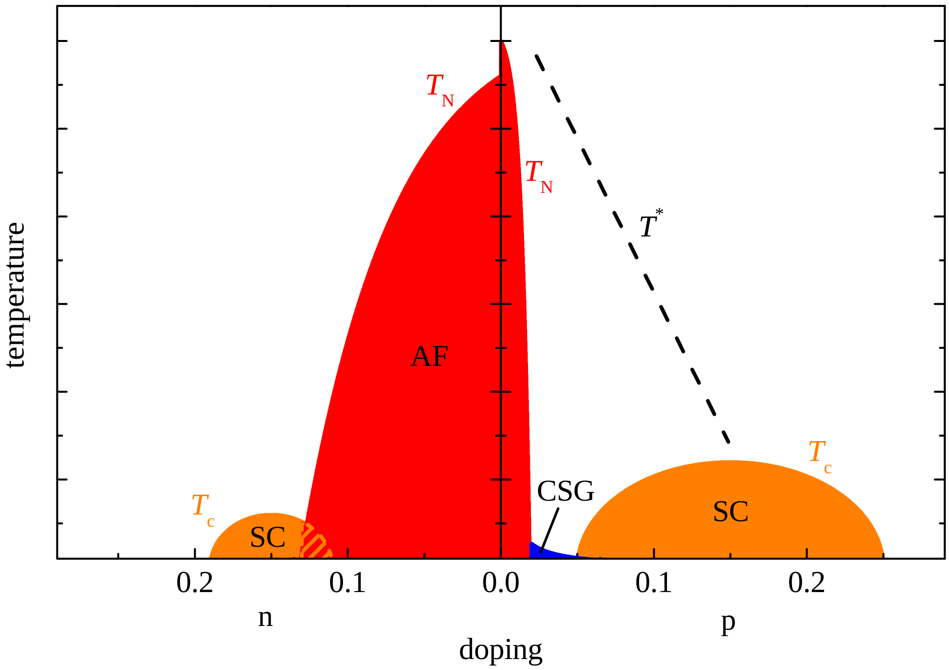

Figure 2.2: Generic phase diagram of cuprates [28, 29] for electron doping per planar Cu atom (n) and hole doping per planar Cu atom (p): AF - antiferromagnetic ordering with the corresponding Néel temperature T_{N}, CSG - cluster spin glass phase, SC - superconducting state with the corresponding critical temperature T_{c}, pseudogap crossover temperature T^*.

The dependence of the critical temperature T_{c} on oxygen concentration or doped ions can be described with a parabolic function [30], which appears to be generic for the cuprates:

$$T_{\mathrm{c}}(p) = T_{\mathrm{c,max}}(1 - 82.6 \cdot (p - 0.16)^2),$$

where the doping p is the number of holes per copper atom in the $\mathrm{CuO_2}$ planes. T_{c} is also strongly affected by disorder, like e.g. impurities or cation nonstoichiometry. Between the AF and the superconducting regions a less correlated short-range magnetic order is present, called the cluster spin glass (CSG) state. It may be interpreted as a stripe order due to microsegregation of doped holes, where hole-poor AF ordered regions are separated by non-magnetic hole-rich domain walls [31]. In the normal state of hole doped cuprates a so-called pseudogap phase is present in the excitation spectrum. First evidences of the pseudogap were obtained by nuclear magnetic resonance (NMR) studies [29], confirmed by inelastic neutron scattering measurements [32], both sensitive to the density of states in the spin channel. Angle-resolved photoemission spectroscopy (ARPES) [33] and scanning tunneling microscopy (STM) [34], sensitive to the density of states in the charge channel, showed an energy gap in the single-particle excitation spectrum. A change of the curvature of the normal state in-plane resistivity is observed at T^* [35]. The pseudogap crossover temperature T^* is generally correlated with the suppression of the static and dynamic spin susceptibility [36, 37]. The origin of this phenomenon is still under debate. On one side the pseudogap phase is assumed to be related to the superconducting state. Local pairing correlations may already exist above T_c, but the superconducting domains exist only on a nanometer scale due to phase fluctuations [27]. On the other side this phase is interpreted as an ordering of charge, spin or orbital current degrees of freedom [38], which could be static or fluctuating. At very high doping levels ($p \gtrsim 0.27$) superconductivity is suppressed and the systems turn metallic.

To obtain electron-doped cuprates, like e.g. $\mathrm{Nd}_{2-x}\mathrm{Ce}_x\mathrm{CuO}_4$ or $\mathrm{LaPr}_{1-x}\mathrm{Ce}_x\mathrm{CuO}_4$, the parent compounds has to exhibit the metastable tetragonal $\mathrm{Nd}_2\mathrm{CuO}_4$ structure, known as T'-structure [29]. On the electron-doped side of the phase diagram the AF long-range order is more robust, the superconducting doping region is narrower and T_c is lower, resulting in an asymmetric phase diagram (see Fig. 2.2). However, this picture has recently been challenged [39]. The electron-doped compounds show also signatures of a pseudogap effect, but the character differs compared to the hole-doped systems [29]. The observed pseudogap appears to be related to the antiferromagnetic ground state instead to superconductivity. A high-energy gap, on the energy scale of the magnetic coupling strength, can be directly observed in the optical conductivity, whereas a spin pseudogap or stripes are absent in the electron-doped cuprates [29].

The superconducting properties of cuprates differ not only in T_c compared to classical superconductors, but also on the two important length scales: the magnetic penetration depth λ and the correlation length ξ. All superconductors expel an external magnetic field H from their interior, regardless of the magnetic field history, as long as H is smaller than the first critical field H_c1 (smaller than the critical field H_c for conventional superconductors respectively). This behavior is known as the Meissner-Ochsenfeld effect [40]. The length scale of this magnetic screening is given by the London penetration depth λ_L, deduced from phenomenological theory of F. and H. London [41, 42]:

$$\lambda_\mathrm{L} = \sqrt{\frac{m^*}{\mu_0 n_\mathrm{s} e^2}}, \tag{2.1}$$

with the effective mass m^* and the superfluid density n_s. This London penetration depth λ_L

is an ideal theoretical limit for $T = 0\,\mathrm{K}$, which is always lower compared to the experimental obtained magnetic penetration depth $\lambda(T)$ extrapolated to zero temperature [43]. While the magnetic penetration depth is usually a few $10\,\mathrm{nm}$ in superconducting metals, it is usually larger than $100\,\mathrm{nm}$ in cuprates, leading also to much lower n_s. According to the Ginzburg-Landau theory [44] the correlation length ξ of the superconducting pairs:

$$\xi = \sqrt{\frac{\hbar^2}{2m^*\alpha}}, \tag{2.2}$$

with the phenomenological parameter α and the Planck constant $h = \hbar/2\pi$, is the second relevant length scale. With about $1-2\,\mathrm{nm}$ in the ab-plane, the correlation length is much smaller in cuprate systems compared to conventional superconductors [45]. Therefore, the Ginzburg-Landau-Parameter

$$\kappa = \frac{\lambda}{\xi} \tag{2.3}$$

is larger than 100, meaning that the cuprates are strong type II superconductors ($\kappa > 1/\sqrt{2}$) [44]. In addition to the Meissner state, the so called vortex state appears in type II systems for $H_\mathrm{c1} < H < H_\mathrm{c2}$, where H_c2 is the second critical field generally extremely large in the cuprates. In this state magnetic flux lines enter the superconductor in multiples of the magnetic flux quantum $\Phi_0 = h/(2e)$, forming the so-called vortex lattice [46].
Also the symmetry of the order parameters differ from conventional superconductors. Within the ab-plane, instead of an isotropic s-wave order parameter a $d_{x^2-y^2}$ gap symmetry is present [47]. The d-wave pairing could be observed by measuring the temperature dependence of the average magnetic penetration depth λ_{ab} [48, 49], showing a linear behavior at lower temperatures [47]

$$\lambda_{ab}(T) = \lambda_{ab}(0\mathrm{K}) \cdot \left[1 + \ln(2) \cdot k_\mathrm{B}T/\Delta_0\right], \tag{2.4}$$

where Δ_0 is the value of the superconducting gap at zero temperature. Some muon spin rotation measurements show a deviation from this low-temperature behavior [50, 51]. This was referred to a contribution of a s-wave symmetry [52], as observed e.g. also by neutron scattering [53]. Also from nuclear quadrupole resonance studies a marginal s-wave contribution can not be excluded [54]. The weak coupling BCS theory, assuming adiabatic electron-phonon coupling, can hardly be applied to cuprates since it is based on an isotropic symmetry assuming a Fermi-liquid, which is only present at the strong overdoped side of the phase diagram. Thus, the coupling mechanism has still to be resolved in the cuprates.

3 Experimental Setups

In order to investigate photo-induced effects in cuprate superconductors it is important to perform resistivity measurements as well as low-energy μSR (LEM) measurements under illumination in-situ. By resistivity studies the amount of induced charge carriers and a possible change in the critical temperature is determined, while LEM measurements are sensitive to changes of the magnetic state and the superfluid density. For resistivity measurements the standard Physical Property Measurement System (PPMS) from *Quantum Design* offers very limited space and insufficient cooling power to include a light source (sample chamber diameter is only 2.6 cm) [55], whereas a light setup, which does not disturb the measurement conditions, is fundamental for μSR studies. Therefore a new resistance setup and a new light system were developed and built.

3.1 In-situ resistance setup

Resistance measurements performed with a PPMS are a standard characterization method. The sample is glued on a small puck and the contacts are usually bonded with aluminum or gold wires on it. The puck with a limited diameter of only a few centimeters is placed inside the cryostat. So only a single light emitting diode (LED) can be placed inside this measuring unit. Three problems arise from these restrictions. First the maximal light intensity is very limited. Second the LED has to work at very low temperatures since it is in the helium flow. Finally the heat dissipation from the LED influences the temperature of the sample. Therefore, a new resistance setup was developed for a cold finger cryostat. In our setup, the cold finger cryostat is mounted in an ultra high vacuum (UHV) chamber and the light source is placed easily close-by behind an optical viewport. There are no space restrictions outside the UHV chamber and the light source is thermally decoupled from the resistance setup. Any type of light source can be used.

For LEM measurements customized UHV cold finger "Konti" cryostats from *CryoVac* [56] are in operation. To built a resistance setup on a cold finger cryostat four additional cables are required. For this, the so-called "Konti 1" cryostat is appropriate. On top of the cold finger of this cryostat a sapphire crystal is mounted followed by a silver coated aluminum plate referred to as sample plate from here on. The sample plate sticks on top of the sapphire crystal with the help of an indium foil. So the thermal contact between the cold finger and the sample plate is optimized and at the same time they are electrically

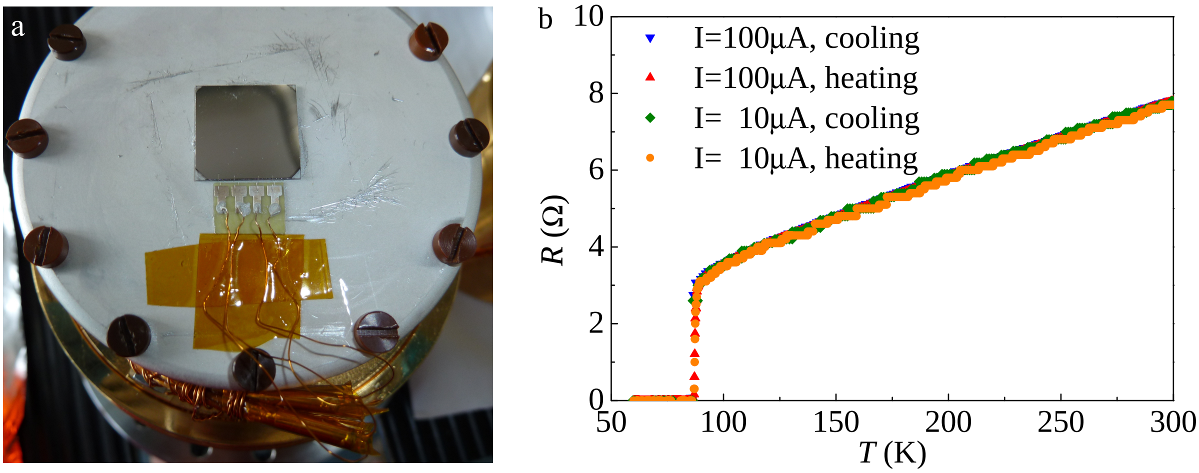

Figure 3.1: Photograph of the final resistance measurement unit (a) and the resistance R versus temperature T for a YBCO thin-film sample covered with Au (b) during cooling and heating for different currents I, as stated in the figure. The measurements were performed while keeping the current I constant.

isolated. After testing several setups on top of the sample plate we were able to conclude, that the sample has to be glued with silver paint directly on the sample plate to reach best thermal contact. As soon as a thin material (e.g. copper/carbon tape, aluminum foil) is placed between the sample and the sample plate the temperature of the sample does not correspond to the calibration anymore or it even loses thermal contact. To reduce the contact resistance, electrical contacts are made by wire bonding, using the parameters listed in Tab. 3.1. Finally, a setup is needed which connects the bonding wires with the available high voltage connector. The high voltage cables lead from the bottom of the cold finger to the outside part of the cryostat and can be connected to measuring devices. On the top of the high voltage connectors plug-in ferrules with soldered copper wires were snapped on. To apply electrical contact between the bonding wires and the copper wires

Table 3.1: The stated parameters where used to bond on AuFe, Nb and LSCO thin films with the TPT wire bonder HB06 of the HB10 series [57]. Bonding was not possible for YBCO thin films, the contacts were fixed with silver paint. The bonding parameters strongly depend on the machine used.

Parameter	Gold pad side	Sample side
Ultrasonic power	190 mW	210 mW
Time	100 ms	150 ms
Force	30 cN	45 cN
Search	200	200

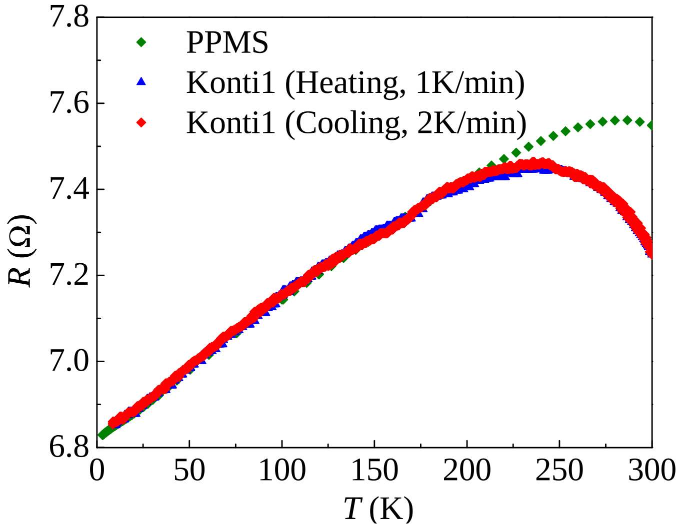

Figure 3.2: Resistance R versus temperature T for the spin glass AuFe. The measurements obtained with the cold finger cryostat "Konti 1" were performed keeping the electrical current constant. The data obtained with the PPMS are normalized to the data obtained with "Konti 1" at 10 K. The rate of the temperature change was varied as labeled in the figure. In the case of the PPMS the rate changed with temperature.

a piece of gold patterned electrical isolating carrier material, like the one used for printed circuit boards, was glued next to the sample as shown in Fig. 3.1a. The ends of the copper wires are fixed with silver paint on one side of the patterned gold pad. Bonding was done with 33 μm thick aluminum wires from the other side of gold pad to the sample. As measurement devices, *Keithley* Series 2400 and 2612A Source Meters [58] in 4-wire mode were used. With this setup it was possible to measure the resistance reproducibly as it was shown with an $YBa_2Cu_3O_{6+x}$ (YBCO) sample covered with a Au layer, as depicted in Fig. 3.1b. During the measurement the electrical current was fixed to 100 μA and to 10 μA, respectively. In both cases the temperature dependence agrees. The sample shows a superconducting transition at 87 K as obtained before in the PPMS.

Further test measurements were performed on a AuFe spin glass sample with 3 % Fe (see Fig. 3.2). Below 200 K the values obtained with the PPMS agree with the data measured with the new setup. The PPMS data are normalized to the value of the cold finger cryostat measurements at 10 K. At higher temperatures the PPMS data are well above the Konti 1 ones. The difference may result from the fast change in temperature during the PPMS measurement, so that the actual temperature differs from the measured one. This leads to the observed shift of the maxima in resistance to higher temperatures. The present results and further tests confirmed the reliability of the new resistance measurement unit.

3.2 In-situ illumination setup

Investigations of changes in novel materials by photo induced charge carriers are of great interest. Charge carriers introduced in-situ by illumination open the possibility to investigate modifications of material properties without changing the chemical composition or the lattice parameters directly. The first light setup used for LEM consists of 33 low-cost LEDs which are mounted on a ring soldered in series. The ring is mounted within the radiation shield a few centimeter up stream from the sample in UHV (see Fig. 3.3). The following LEDs are used:

- **Green:** Kingbright L-7113VGC-Z, InGaN LED, λ_{peak}=525 nm, I(max)=30 mA, $2\theta_{1/2}$=20°
- **Blue:** Kingbright L-7113QBC-D, GaN LED, λ_{peak}=470 nm, I(max)=30 mA, $2\theta_{1/2}$=20°
- **White:** Avago HLMP-CW36-UX00, InGaN LED, λ_{peak1}=460 nm, λ_{peak2}=560 nm, I(max)=30 mA, $2\theta_{1/2}$=20°

With these LEDs an intensity of about 10 mW/cm^2 is reached with an applied current of I=30 mA. The ring creates a large inhomogeneous light spot on the sample as depicted in Fig. 3.3a. The LED-ring setup is cheap and the light source is mounted close to the sample. It also does not directly disturb the μSR measurements. But when the LEDs are switched on heat is introduced into the UHV system. This is a disadvantage, because frozen water from the LED surface, housing, and surrounding is evaporated. This leads

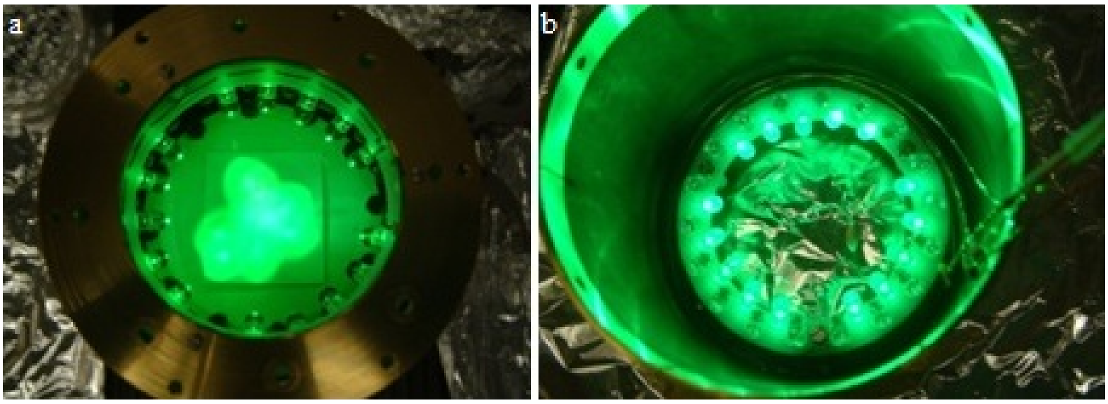

Figure 3.3: LED ring setup of 33 green commercial LEDs in operation (a) and from the bottom (b).

to the formation of a thick ice layer on top of the sample below 180 K, which may be up to 100 nm thick. In addition, the UHV conditions become unstable when the radiation shield heats up. Another disadvantage of the LED-ring setup is that broken LEDs cannot be repaired without breaking the UHV. A change of a single broken LED takes several hours, so it is very time-consuming and therefore risky to use for LEM measurements. Furthermore, to observe pronounced photo induced effects, higher intensities are required, but the current to run the LEDs could not be increased arbitrarily. LEDs with a higher I_{max} are in general not practical, since the heating increases with current. Thus, a different solution was required.

To guarantee stable UHV conditions and to fix problems with the light source easily in short times without breaking the UHV, the new setup was placed outside the LEM UHV chamber. Heating effects and the evaporation of water are prevented. In this case the light has to pass the optical viewport of the UHV chamber and the carbon foil of the trigger detector, necessary for the LEM measurements (see Section 4.3), along the beamline. The distance between the light source and the sample is therefore increased to 2.2 m.

The initial intensity of the new light source has to be high enough, so that the remaining intensity at the sample is considerably larger than $10\,\mathrm{mW/cm^2}$. On the other hand, the intensity should be low enough to not disturb the LEM measurements and to prevent a damage of the carbon foil, which is part of the trigger detector (see Section 4.3). These conditions are fulfilled by the high power LED head “Bluepoint LED 400” from *Hönle* [59]. The LED head consists of four high intensity LEDs with λ_{peak}=400(10) nm, corresponding to $E_\gamma = 3.1\,\mathrm{eV}$. The Bluepoint LED has an output intensity of $3.4\,\mathrm{W/cm^2}$ at 80% operation intensity, as determined with the UV power meter from *Hönle* [60]. The maximum intensity (100%) is not used for longer operation, because the lifetime of the LEDs ($> 10'000\,\mathrm{h}$) and therefore the total intensity is suppressed dramatically. A filter and a lens, included in the LED head, are used to reach the maximum intensity in the focus point, which is 1.5 cm away from the housing of the head. To extend the focal point distance to 2.2 m an optical bench with the following plano convex lenses is mounted in front of the LED head:

- Lens 1: PCX $f = 12\,\mathrm{mm}$, 12 mm diameter, *Edmund Optics* 45083
- Lens 2: PCX $f = 305\,\mathrm{mm}$, 89 mm diameter, *Edmund Optics* 94127

The optimal distance between LED head and Lens 1 is 17 mm. A distance of 345 mm is arranged between Lens 1 and Lens 2. A schematic sketch of the setup is shown in Fig. 3.4c.

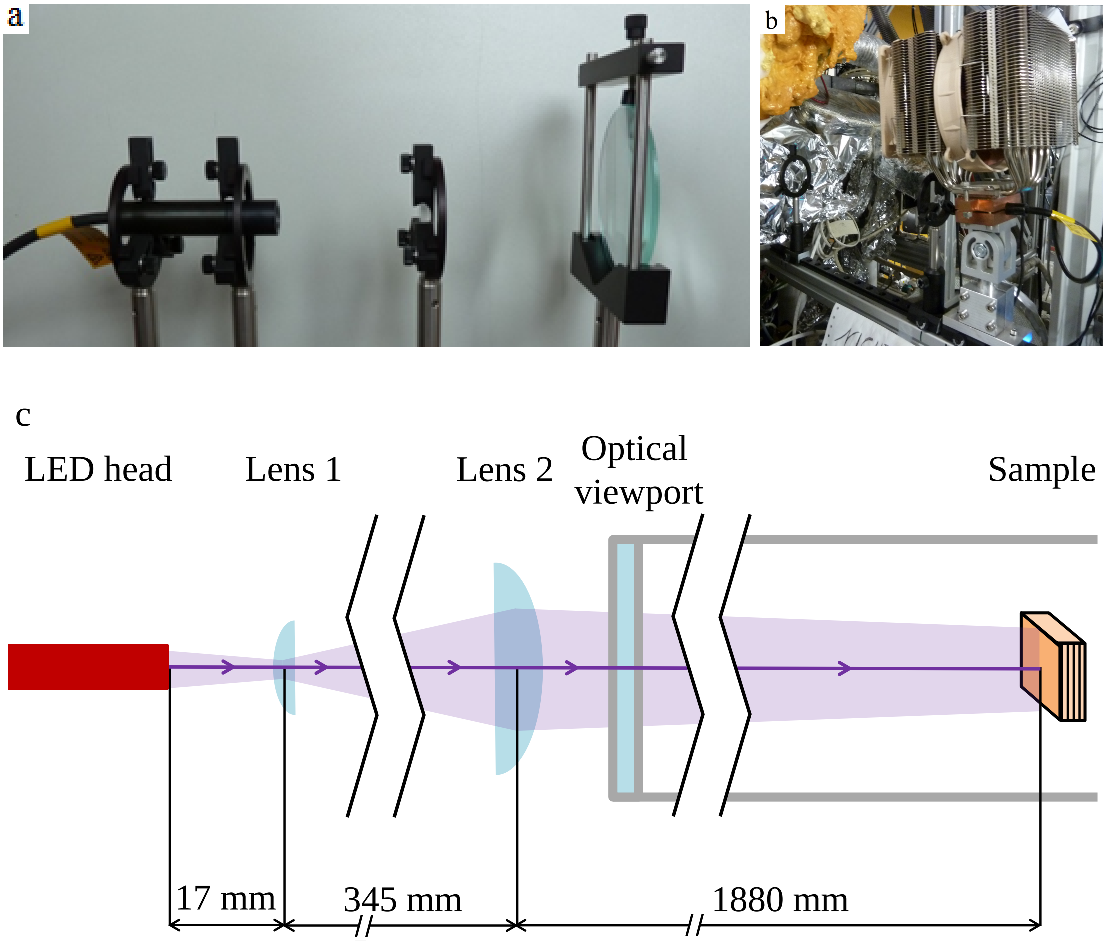

Figure 3.4: Photographs (a & b) and schematic sketch (c) of the Bluepoint LED setup.

The common operation time of the Bluepoint LED is in the range of $1 - 100$ seconds. For our purposes an operation time of several hours is required. In general the LED head overheats if it is operated for longer times. So a heat-exchange system, consisting of a copper block and a cooling unit for central processing units from *Noctua* (Model NH-D14) [61], was added to stabilize the temperature. The advantage of the Bluepoint LED setup is the possibility to run, repair and adjust it from outside the UHV chamber. The intensity can be tuned easily. To adjust the light spot one has to mount a view port instead of the cryostat, so this is usually done during accelerator service time. If the pattern of the 4 LEDS is sharp the light spot has a diameter of about 5 cm.

To determine the intensity reached on the sample of the Bluepoint LED some tests were performed in air with two intensity measurement devices: a broadband photo diode from

Table 3.2: Determined voltage and intensity values for the Bluepoint LED ($\lambda_{\mathrm{peak}} = 400(10)\,\mathrm{nm}$) obtained with the FDS100 photo diode and the LI-185B photo meter at the end of the LED housing (I_{Head}), behind the first lens (I_{L1}), and at the position of the sample (I_{final}). The second line for each device lists the calculated values using the calibration stated in the text. The value I_{dark} reflects the contribution of the ambient light present during the measurement.

Device		I_{dark}	I_{Head}	I_{L1}	I_{final}
Photodiode	measured	$0.3\,\mathrm{mV}$	$0.5\,\mathrm{V}$	$0.5\,\mathrm{V}$	$0.014\,\mathrm{V}$
	calibrated	$2.4\,\mathrm{mW/cm^2}$	$4.04\,\mathrm{W/cm^2}$	$4.04\,\mathrm{W/cm^2}$	$113\,\mathrm{mW/cm^2}$
Photometer	measured	$1.6\,\mathrm{W/m^2}$	$300\,\mathrm{W/m^2}$	$100\,\mathrm{W/m^2}$	$10\,\mathrm{W/m^2}$
	calibrated	$20\,\mathrm{mW/cm^2}$	$4.04\,\mathrm{W/cm^2}$	$1.3\,\mathrm{W/cm^2}$	$130\,\mathrm{mW/cm^2}$

Thorlabs [62] and a photo meter from *LI-COR* [63]. Since these devices are not calibrated to the Bluepoint LED we used the value, which was determined with the calibrated LED UV meter, as reference. The output intensity measured at the front end of the LED head was obtained to be $3.4\,\mathrm{W/cm^2}$ at 80% of the maximum power. During illumination an output power of 95% is selected. Using the measurement of the ambient light as error level an intensity of $115(10)\,\mathrm{mW/cm^2}$ is present at the sample position (see Table 3.2). Behind Lens 1 the determined intensities vary by a factor of four. This could be due to the different sizes of the sensors or due to different photon-energy sensitivities. From previous measurements the maximal intensity of the LED ring setup is known to be about $10\,\mathrm{mW/cm^2}$. Thus, we gain one order of magnitude in intensity with the new light setup. The stated intensity was measured without an optical viewport. Along the beamline the light has also to pass a carbon foil, as mentioned before. Thus, we estimated that an intensity of about $80\,\mathrm{mW/cm^2}$ is reached on the sample when mounted in the LEM beamline.

For resistivity measurements the Bluepoint LED setup can be mounted at the UHV test chamber MAX. Since the distance between light source and sample is with $0.9\,\mathrm{m}$ much smaller here a different second lens is used (*Thorlabs* LA1353 [64]: Plano-Convex Lens, $f = 200\,\mathrm{mm}$, $75\,\mathrm{mm}$ diameter). Therefore, an intensity of $210(10)\,\mathrm{mW/cm^2}$ is obtained at MAX. The following results on photo-induced effects were obtained using this Bluepoint LED setup.

Meanwhile a second Bluepoint LED head is in operation with a peak wavelength of $\lambda_{\mathrm{peak}} = 365(10)\,\mathrm{nm}$. This wavelength is in the ultra violet (UV) region, so that different optical viewports and lenses are needed:

- Viewport: Fused Silica CF viewport DN100, *Baruvac* AG MVPZ100-UVQ

- Lens 1: Plano Convex SQ Lens $d = 15.0\,\mathrm{mm}$, $f = 20\,\mathrm{mm}$, I.L.E.E. AG 014-0220
- Lens 2: Fused Silica Plano Convex Lens Uncoated $d = 50.8\,\mathrm{mm}$, $f = 300.0\,\mathrm{mm}$, *Thorlabs* LA4855

The new viewport also optimized the transmittance of the 400 nm light beam. For the test chamber MAX we use the uncoated fused silica plano convex lens LA4538 ($d = 50.8\,\mathrm{mm}$, $f = 250.0\,\mathrm{mm}$) from *Thorlabs* as Lens 2. In the future, an extension to higher wavelengths using red and green laser light is planned to reach intensities of several $100\,\mathrm{mW/cm^2}$.

4 Muon Spin Rotation (μSR)

Muon Spin Rotation (μSR) is a powerful technique to investigate magnetism, superconductivity, kinetics or diffusion processes in condensed matter. After presenting the fundamental properties of the muon the μSR technique is described. This is followed by the principle of the unique low-energy μSR, allowing depth resolved experiments. Finally, the theoretical tools for analyzing μSR spectra are discussed.

4.1 The muon

The muon μ is an unstable fundamental particle from the lepton family with spin 1/2. Its mass is with 105.7 MeV/c^2, about 200 times larger than the electron mass and $\sim 1/9$ of the proton mass. There exist positively and negatively charged muons. In condensed matter the μ^+ acts as a light proton which is repelled from atomic nuclei. So it generally stops at interstitial sites or defects within the lattice. The μ^- instead behaves like a heavy electron which is easily captured by nuclei. Thus, to investigate condensed matter typically μ^+ particles are used. To obtain a spin polarized μ^+ beam the production of positive charged pions is required. They are created from collisions between protons and nucleons (p - proton, n - neutron, π - pion):

$$\begin{aligned} p + p &\rightarrow p + n + \pi^+ \\ p + n &\rightarrow n + n + \pi^+. \end{aligned}$$

The threshold energy for single pion production from such a collision is about 280 MeV, whereas the cross-section reaches its maximum above 500 MeV. The creation of π^+ is realized at the Paul Scherrer Institute by using a 590 MeV proton beam directed to a carbon target [65]. Pions consist of two quarks and decay after a mean life time of 26 ns into a positively charged muon μ^+ and a muon neutrino ν_μ:

$$\pi^+ \rightarrow \mu^+ + \nu_\mu.$$

This weak decay violates parity, since neutrinos exhibits only negative helicity [66]. Therefore, π^+ decaying at rest create spin polarized μ^+ with an energy of 4.12 MeV. When the pions stop close to the surface, the decay muons are referred to “surface muons”. The spin of the produced μ^+ is antiparallel to its momentum. The μ^+ mean life time is 2.197 μs.

4.2 The μSR technique

The Muon Spin Rotation (μSR) technique, depicted in Fig. 4.1, uses predominantly positively charged muons as a local probe to investigate the magnetic state of condensed matter on a microscopic level [67]. To do so a spin-polarized muon beam is created with the help of accelerated protons hitting a carbon target. The positively charged muons are implanted into the sample, where they thermalize within picoseconds [68]. If a local magnetic field B_{loc} is present at the μ^+ stopping site in any non-collinear configuration, the muon spin precesses with the Larmor frequency $\omega_{\mathrm{L}} = \gamma_\mu B_{\mathrm{loc}}$, with the muon gyromag-

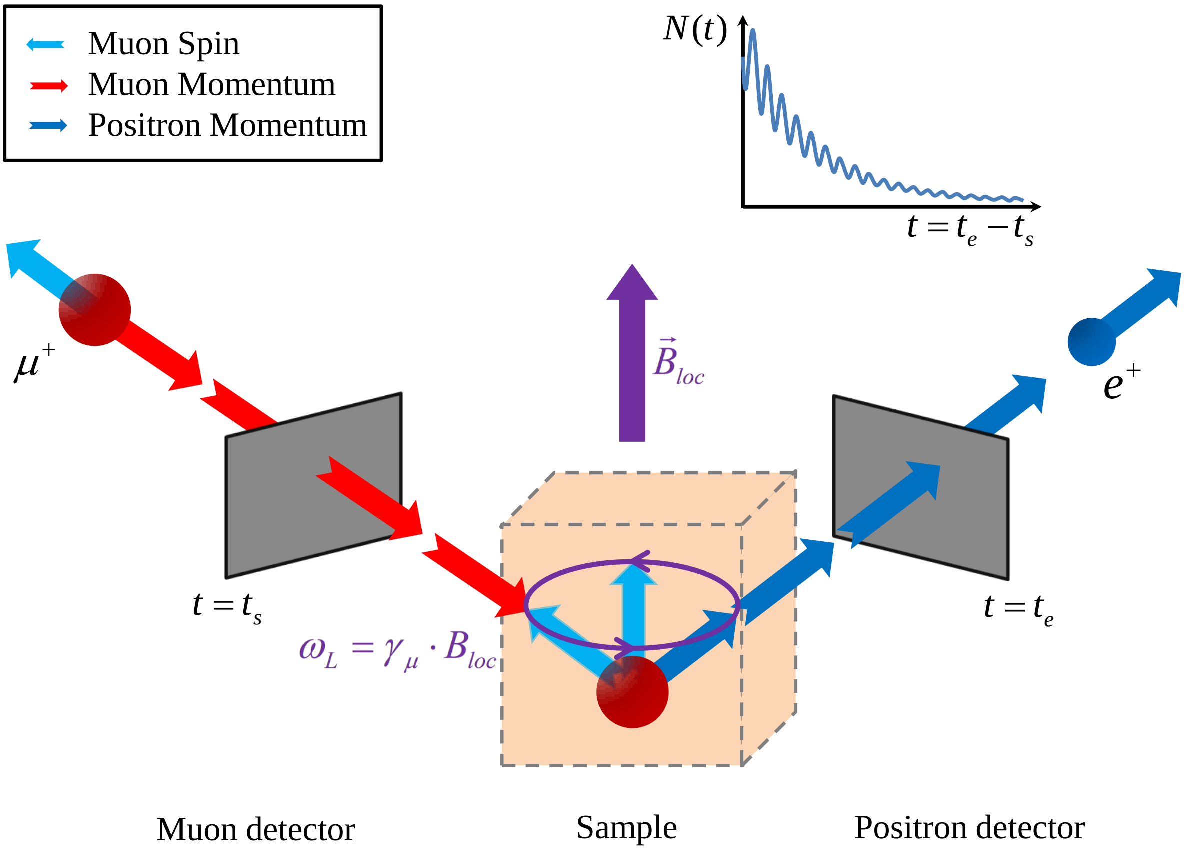

Figure 4.1: Principle of the Muon Spin Rotation technique. The muon μ^+ is detected by the muon detector at $t = t_s$. After the muon stopped in the sample (orange cube), its spin precesses around the local magnetic field B_{loc} with the Larmor frequency ω_{L}. The decay positron e^+ is detected by the positron detector at $t = t_e$. The histogram (right corner) results from the positron count rate $N(t)$ as function of the decay time $t = t_e - t_s$.

netic ratio $\gamma_\mu = 2\pi \times 135.54\,\mathrm{MHz/T}$, until the muon decays into a positron (e^+) and two neutrinos (ν_e and $\bar{\nu}_\mu$):

$$\mu^+ \rightarrow e^+ + \nu_e + \bar{\nu}_\mu.$$

The probability distribution of the positron energies is given by the Michel spectrum [66], see Fig. 4.2a. The anisotropic angular distribution of the decay positron is specified by the energy dependent asymmetry $a(E)$ and is following the relation:

$$\frac{\mathrm{d}W}{\mathrm{d}\left(\cos\theta\right)} = 1 + a\left(E\right)\cos\theta, \tag{4.1}$$

where θ is the angle between the muon spin at the time of decay and the momentum of the positron. The asymmetry $a(E) = (2E/E_{\mathrm{max}} - 1)/(3 - 2E/E_{\mathrm{max}})$ describes the degree of correlation between the positron momentum and the muon spin direction at the time of decay as depicted in the Fig. 4.2b. The muon decay is highly anisotropic, because of the parity violation. For the maximum energy of $E_{e^+,\mathrm{max}} = 52.8\,\mathrm{MeV} \approx m_\mu c^2/2$, the positron decays along the direction of the muon spin at the time of decay, which is equivalent with the maximum anisotropy and an asymmetry of $a = 1$ (see Fig. 4.3). At lower energies the probability of all other directions increases, resulting in an isotropic distribution at $E_{e^+} = 26.4\,\mathrm{MeV}$ ($a = 0$). For the lowest energies $E_{e^+} < 26.4\,\mathrm{MeV}$ the positron is mainly scattered backward so that the asymmetry becomes negative ($a < 0$). The average asymmetry over all energies weighted with the energy distribution is

$$A = \int n(E)a(E)\mathrm{d}E = \frac{1}{3}. \tag{4.2}$$

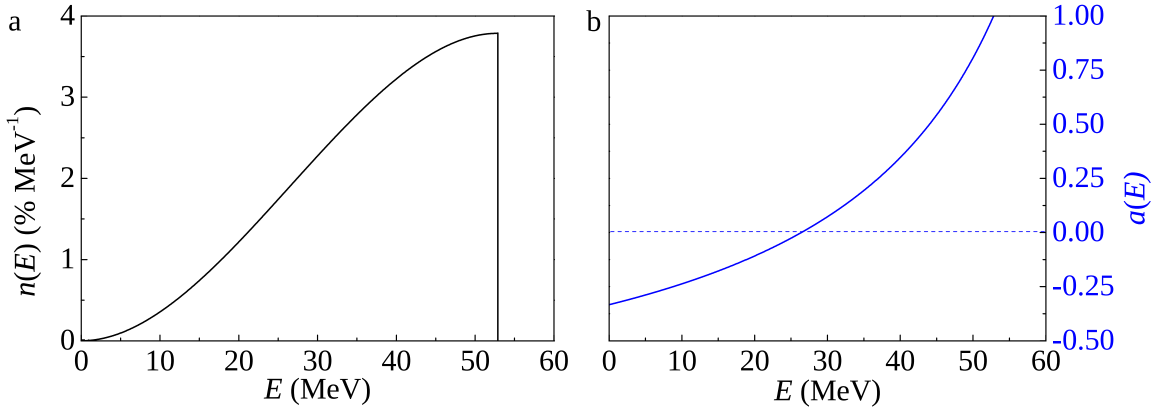

Figure 4.2: The Michel spectrum giving the energy distribution $n(E)$ of the decay positron (a). The asymmetry a versus the energy E of the decay positron (b).

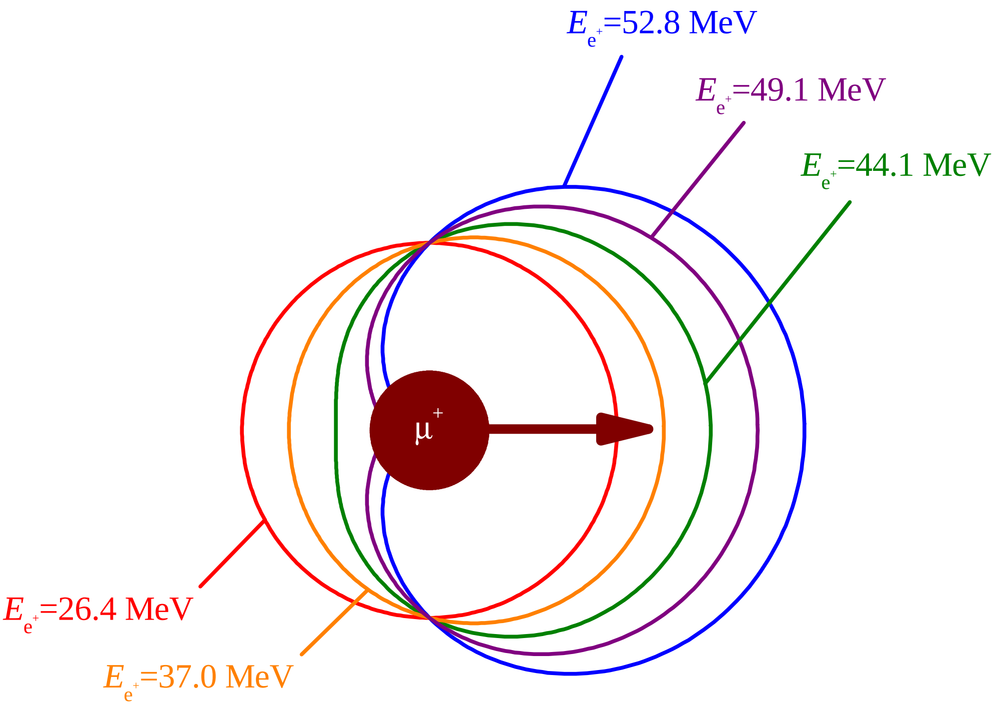

Figure 4.3: Angular probability distribution of the decay positron for different energies in the range 26.4 MeV$\leq E_{e^+} \leq$ 52.8 MeV according to Eq. 4.1.

This has to be considered in μSR experiments, because the positron detectors are not energy selective.

Due to this anisotropic muon decay, it is possible to extract the muon-spin polarization $\vec{P}(t)$ from the muon decay histogram by measuring the time difference $t = t_\mathrm{e} - t_\mathrm{s}$ between the implantation time t_s and the decay time t_e of the μ^+, detected via the decay positron:

$$N(t) = N_0\, \mathrm{e}^{-t/\tau_\mu} \left[1 + A\, \vec{P}(t) \cdot \vec{n}\right] + N_\mathrm{Bkg}, \tag{4.3}$$

with the positron count rate $N(t)$, N_0 gives the scale of the counted positrons, the direction of observation $\vec{n}$, and N_Bkg is a time-independent background of uncorrelated events. The observable decay asymmetry A is in the range $0.2 - 0.3$. It is generally smaller than the theoretical value of $1/3$ since for instance the solid angle covered by the detectors (to record the decay positrons) is finite and the muons are not completely 100 % spin polarized. The muon spin polarization is reduced to $90 - 95$ % because the muon beam is collected from a finite solid angle and it consists not only of surface muons but also of muons created from low-momentum pions in flight, so-called "cloud muons". The term $A\,\vec{P}(t)\cdot\vec{n}$ includes the physical information like the value of the local magnetic field, the local magnetic field distribution, or possible fluctuations present at the muon stopping site in the investigated material. The μSR spectra are devided in three different classes:

- Zero field (ZF): no magnetic field is applied to the sample
- Transverse field (TF): the initial muon spin direction is perpendicular to the applied magnetic field
- Longitudinal field (LF): the initial muon spin direction is parallel to the applied magnetic field

4.3 Low-energy μSR

The commonly used surface muons have a kinetic energy of 4.12 MeV when implanted into the sample. Therefore they stop in condensed matter on a length scale of a couple of 100 μm. To investigate thin-film and multi-layer systems or to do depth dependent studies muons with tunable energies in the range of keV are required. The low-energy μ^+ beamline LEM at PSI, depicted in Fig. 4.4, realizes this by moderating the surface muons with the help of a few hundred nm thick condensed layer of solid rare gases and/or nitrogen deposited on a 125 μm thick Ag foil, creating epithermal muons with a mean energies of about 15 eV [69]. The moderation efficiency is in the order of $10^{-4} - 10^{-5}$, dependent on the gas used and the momentum of the surface muon [70]. The muons keep their spin polarization during moderation [71]. After moderation the μ^+ are reaccelerated with static electric fields to typically 15 keV. The final energy is reached by applying a voltage at the sample plate and can be varied in the range $0.5 - 30$ keV. By passing through the carbon foil of the start detector the muons lose on average about $0.5 - 1.0$ keV of their kinetic energy, leading to an uncertainty in the energy of about 400 eV.

The whole muon beam transport system is placed within ultra high vacuum (UHV) chambers to minimize losses and to prevent the moderator from degrading. An electrostatic mirror separates the low-energy muons from the surface muons by deflecting the slow ones by 90 degrees. To realize different alignments between the initial muon spin direction and the applied magnetic field a spin rotator is mounted, which combines electrical and magnetic fields so that the muon spin is rotated while the deflection of the muon beam is corrected [72]. The start detector for the time-differential μSR experiments is a thin grid

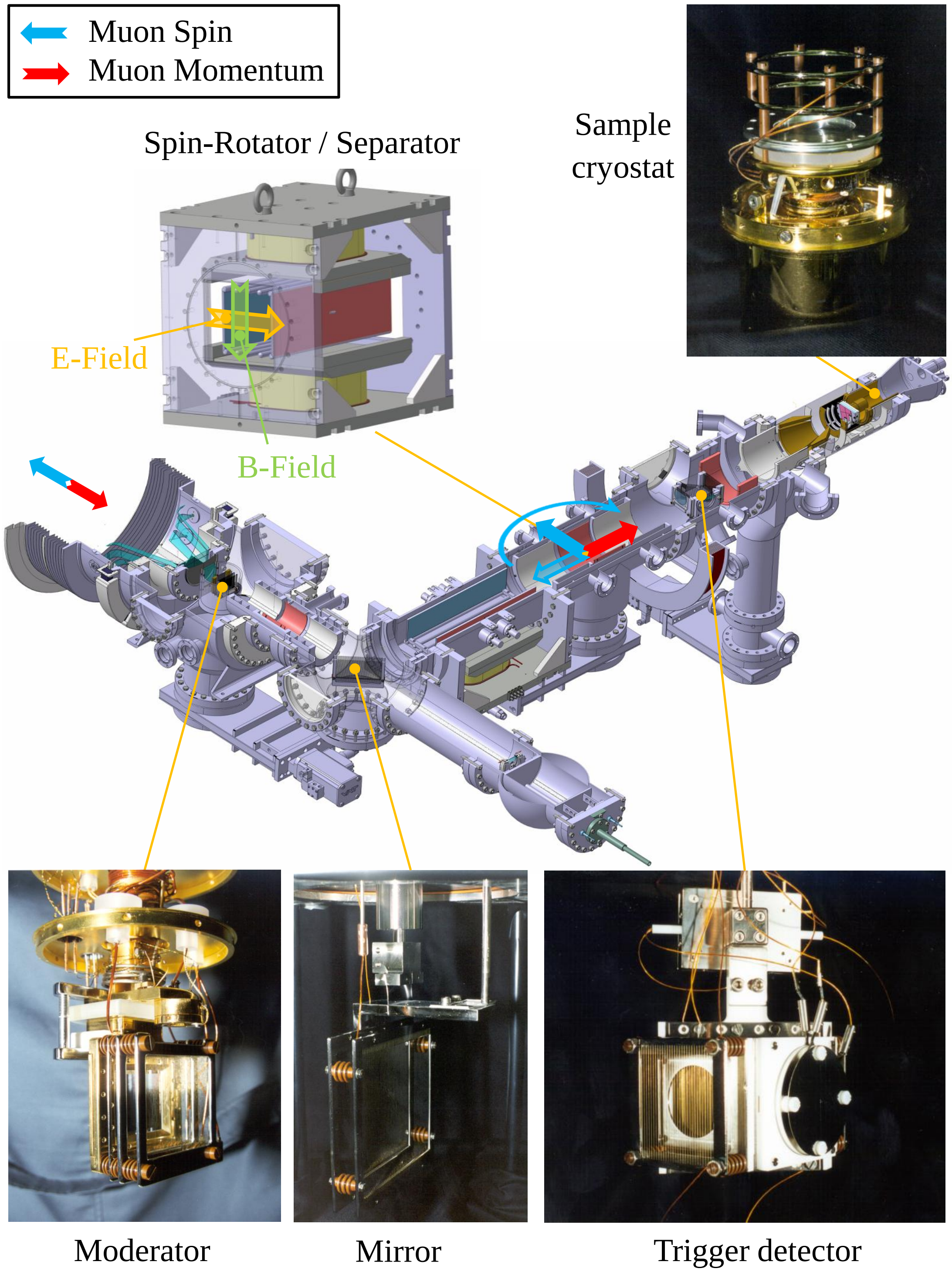

Figure 4.4: Three dimensional model of the low-energy muon beamline at PSI. The muon spin direction is indicated with the red arrow, the muon momentum with a blue one.

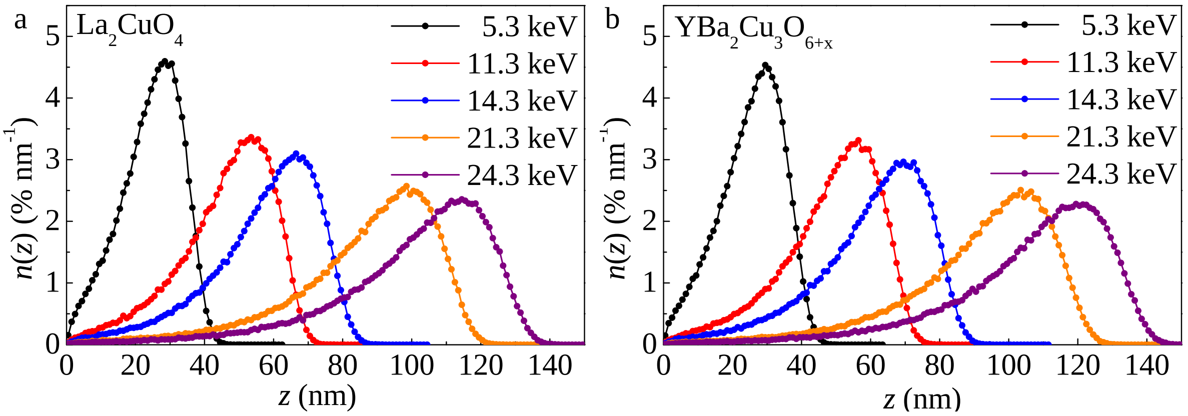

Figure 4.5: Normalized stopping profiles $n(z)$ of positively charged muons implanted in LCO (a) and in YBCO (b) for different implantation energies (stated in the figure) as simulated with TRIM.SP [73].

with a thin carbon foil, called the trigger detector (see Fig. 4.4). When the muons collide with the carbon atoms free electrons are generated. Detecting them by a channel plate releases the start signal, in contrast to conventional μSR where a thin scintillator acts as start detector.

Decay positrons are detected by BC-400 scintillator segments surrounding the sample region outside the UHV chamber. The sample is mounted electrically isolated on a cold finger cryostat to vary the temperature in the range $4 - 320\,\mathrm{K}$.

The stopping distribution of muons with a defined implantation energy in condensed matter is calculated with the Monte Carlo code TRIM.SP [73]. The reliability of these calculations was investigated in metal-insulator bilayer systems and superconducting films [74, 75]. The normalized muon stopping profiles of YBCO and LCO are presented in Fig. 4.5. Depending on the material and the implantation energy the mean penetration depth varies between a few and a few hundred nanometers.

Applications of the LE-μSR are for instance the most direct determination of the London penetration depth of superconductors in the Meissner state, the study of proximity effects of different orders in multi-layer systems or the investigation of muonium formation in semiconductors. More details on the beamline and possible applications are given in Refs. [69, 75–81].

4.4 Theoretical description of the asymmetry spectra

In the following the theoretical functions, used to describe the measured muon depolarization functions $AP(t)$ for ZF and weak TF experiments, are explained for magnetic as well as superconducting samples. More general details on the μSR analysis can be found in Refs. [67, 68, 82].

4.4.1 Zero-field μSR spectra for different magnetic phases in cuprates

First we will have a look at the description of ZF spectra. At the low-doped side of cuprate systems different magnetic states may be present. At high temperatures the systems are paramagnetic and the electronic magnetic moments can be considered independent of each other. They fluctuate fast on μSR time scale. In the paramagnetic case only nuclear magnetic moments (e.g. of La or Cu) influence the μSR spectra and can be assumed static on the muon time scale. The electronic magnetic moments usually fluctuate fast in this magnetic state and hence are not observed in ZF on the μSR time scale. In the case of a three dimensional random Gaussian distribution of the nuclear moments a Gaussian Kubo-Toyabe function [83] describes $AP(t)$:

$$A\,P^{\mathrm{PM}}\,(t) = A\;\left[\frac{1}{3}+\frac{2}{3}\left(1-\sigma^2 t^2\right)\,\mathrm{e}^{-\frac{1}{2}\sigma^2 t^2}\right], \tag{4.4}$$

with the decay asymmetry A and the depolarization rate σ, representing the width of a Gaussian field distribution around zero (Fig. 4.6a). At lower temperatures the cuprates enter the antiferromagnetic phase. In the transition range the fluctuations of the electronic magnetic moments slow down and lead to a strong depolarization of the muon-spin polarization function. An exponential function is suitable for this situation:

$$A\,P^{\mathrm{EXP}}\,(t) = A\,\mathrm{e}^{-\lambda t}, \tag{4.5}$$

with the corresponding depolarization rate λ (Fig. 4.6a). Also a combination of the introduced functions is possible in the transition range. In the antiferromagnetic state static antiparallel ordered electronic magnetic moments are present yielding a local magnetic field

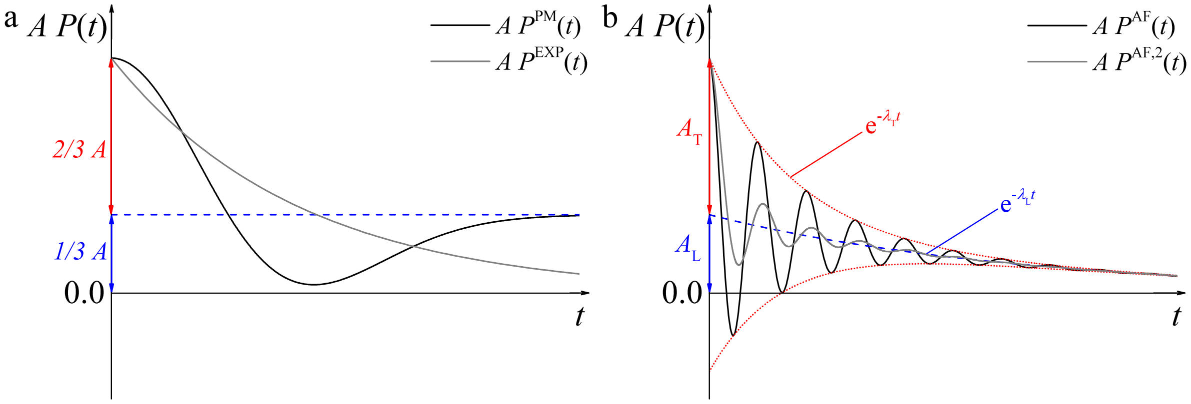

Figure 4.6: Asymmetry spectra $A\,P^{\mathrm{PM}}\,(t)$, $A\,P^{\mathrm{EXP}}\,(t)$, $A\,P^{\mathrm{AF}}\,(t)$, and $A\,P^{\mathrm{AF,2}}\,(t)$. The longitudinal contribution (blue dashed line) and the enfolding curve (red dotted line) are shown.

at the muon stopping site(Fig. 4.6b):

$$A\,P^{\mathrm{AF}}\,(t) = \sum_i A_{\mathrm{T_i}}\,\cos(\gamma_\mu\,B_{\mathrm{loc,i}}\,t + \phi)\,\mathrm{e}^{-\lambda_{\mathrm{T_i}}\,t} + A_{\mathrm{L}}\,\mathrm{e}^{-\lambda_{\mathrm{L}}\,t}. \tag{4.6}$$

Here, the decay asymmetry A splits into two fractions: A_{T} reflects the part of muons having their initial spin perpendicular aligned to the internal magnetic field, whereas A_{L} corresponds to the parallel alignment. The relative strength of A_{T} and A_{L} reflects the spacial arrangement of the magnetic moments. If the magnetic moments point equally in all three dimensions, $A_{\mathrm{T}} : A_{\mathrm{L}}$ is $\frac{2}{3} : \frac{1}{3}$. A ratio of $\frac{1}{2} : \frac{1}{2}$ is observed when only planar components of the magnetic moments are present at the muon stopping site. The width of the internal magnetic field distribution is reflected by the depolarization rate λ_{T}. If λ_{T} is much larger than $\gamma_\mu B_{\mathrm{loc}}$, the oscillations are overdamped, leading to the situation described for the transition range. The longitudinal depolarization rate λ_{L} is typically below $0.1\,\mu\mathrm{s}^{-1}$, if only nuclear dipole moments contribute to this part and no fluctuating magnetic fields are present. The detector phase ϕ is commonly the initial phase between the muon spin direction with respect to the positron detector. Therefore, ϕ is usually constant and temperature-independent. Should this not be the case it is an evidence that the magnetic structure deviates from a perfect antiferromagnetic order and the model has to be adapted. For instance in the case of an incommensurate magnetic structure, where the antiferromagnetic unit cell is not a multiple of the crystallographic unit cell, $AP(t)$ is better described by a Bessel function of the first kind $J_0(t)$ [67] (Fig. 4.6b):

$$A\,P^{\mathrm{AF},2}\,(t) = A_{\mathrm{T}}\,J_0\left(\gamma_\mu\,B_{\mathrm{loc}}\,t\right)\,\mathrm{e}^{-\lambda_{\mathrm{T}}t} \;+\; A_{\mathrm{L}}\,\mathrm{e}^{-\lambda_{\mathrm{L}}t}, \tag{4.7}$$

which takes an additional damping and a phase shift of $\Delta\phi = 45°$ at long times into account:

$$A\,P^{\mathrm{AF},2}\,(t) \overset{t\to\infty}{\longrightarrow} A_{\mathrm{T}}\,\sqrt{\frac{2}{\pi\,\gamma_\mu\,B_{\mathrm{loc}}\,t}}\,\cos\left(\gamma_\mu\,B_{\mathrm{loc}}\,t - \frac{\pi}{4}\right)\,\mathrm{e}^{-\lambda_{\mathrm{T}}t} + A_{\mathrm{L}}\,\mathrm{e}^{-\lambda_{\mathrm{L}}t}. \tag{4.8}$$

So far it was assumed that the muons are only implanted in the sample. In the experiment the beam spot exceeds the size of the sample yielding a background contribution of the sample plate. A silver covered sample plate causes a temperature-independent constant background signal due to its small depolarization rate, whereas a nickel covered sample plate gives a fast depolarizing contribution on short time scales ($t < 0.1\,\mu$s) in addition to the constant background [$A_{\mathrm{Bkg}}(t) = A_{\mathrm{Bkg}}$]. Thus, the choice of the sample plate has to be done thoughtfully. A nickel plate should be only used for ZF measurements if the first $0.1\,\mu$s can be excluded from the analysis.

In conclusion, ZF measurements provide direct evidence of local magnetic orders and give a scale of the internal magnetic field distribution. In our studies we used therefore ZF μSR experiments on one side to identify possible magnetic contributions in superconducting samples to be able to take their influence into account. On the other side, the magnetic phases of low-doped cuprates have been studied. The absolute value of the local magnetic fields are directly determined. By measuring the temperature dependence of these local magnetic fields it is possible to obtain the Néel temperature and the order parameter of the AF phase.

4.4.2 Weak transverse-field μSR in magnetic materials

When investigating magnetic samples, not only the average magnetic field and field distribution are of interest. The magnetic volume fraction is also important. To obtain this fraction a weak transverse field $B_{\mathrm{ext}} \ll B_{\mathrm{loc}}$ is applied to the sample. The internal magnetic fields present in the sample superimposes with the applied magnetic field, which leads to a strong damping of the depolarization function. Therefore we analyze only the paramagnetic part of the μSR asymmetry spectra described by

$$AP_{\mathrm{wTF}}(t) = A_{\mathrm{T}}\,\cos(\gamma_\mu B_{\mathrm{ext}}t + \phi)\,\mathrm{e}^{-\frac{1}{2}\sigma_{\mathrm{T}}^2 t^2} + A_{\mathrm{Bkg}}\,\cos(\gamma_\mu B_{\mathrm{ext}}t + \phi)\,\mathrm{e}^{-\lambda_{\mathrm{Bkg}}t} + A_{\mathrm{L}}\,\cos(\phi)\,\mathrm{e}^{-\lambda_{\mathrm{L}}t}. \tag{4.9}$$

In the paramagnetic state A_{T} is the full asymmetry corresponding to an absent magnetic volume fraction. If the sample is in an ordered magnetic state A_{T} is reduced to the nonmagnetic fraction. A temperature independent background contribution A_{Bkg} has to be taken into account in both situations. It depends again on the sample size compared to the muon spot size and the used background material. If the samples cover an area of $2 \times 2\,\mathrm{cm}^2$, about 85 % of the beam hits the sample, yielding a contribution of an Ag covered sample plate of $A_{\mathrm{Bkg}} = 0.17(3)\,A_{\mathrm{max}}$. Since the depolarisation of Ag is very small, it is not possible to separate the two precessing contributions from each other within the fit. The background contribution A_{Bkg} is acceptable. Thus, the term is neglected within the analysis. The presence of static magnetism is indicated by A_{L} since it corresponds to the part of non-precessing muon spins. The second moment of the magnetic field distribution present in the nonmagnetic parts is reflected by σ_{T}, whereas λ_{L} is generally small and therefore set to zero. The detector phase ϕ is purely geometric and a temperature independent constant.

4.4.3 Low-energy μSR investigation of the Meissner state

LE-μSR allows to measure the local magnetic field at different depths on a nanometer scale in condensed matter in the most direct manner. By applying a small external magnetic field $B_{\mathrm{ext}}/\mu_0 < H_{\mathrm{c_1}}$ to an superconductor at temperatures $T < T_{\mathrm{c}}$ the magnetic screening profile $B(z)$ can be determined. LE-μSR is therefore an unique and powerful technique to measure non-trivial $B(z)$ on a nanometer scale in a wide variety of superconducting single crystals [49], thin films [84], and heterostructures [85, 86], allowing also the observation of non-local effects [87–89]. The direction along which the magnetic screening profile is measured is the moving direction of the muon, labeled here as z direction. Lets assume that the initial muon spin points along the y direction. A muon spin precession in the local magnetic field within the superconductor is then realized by applying the external field transverse to the initial muon spin direction, in this scenario along x. The shielding current flows in the yz-plane, so the London penetration depth λ_{yz} is determined (see Fig. 4.7). Since cuprates grow preferentially c axis oriented the sample is mounted with z corresponds to the c axis, having the ab plane as surface. By measuring different alignments the intrinsic penetration depths λ_a, λ_b, and λ_c can be extracted. In the case of cuprates

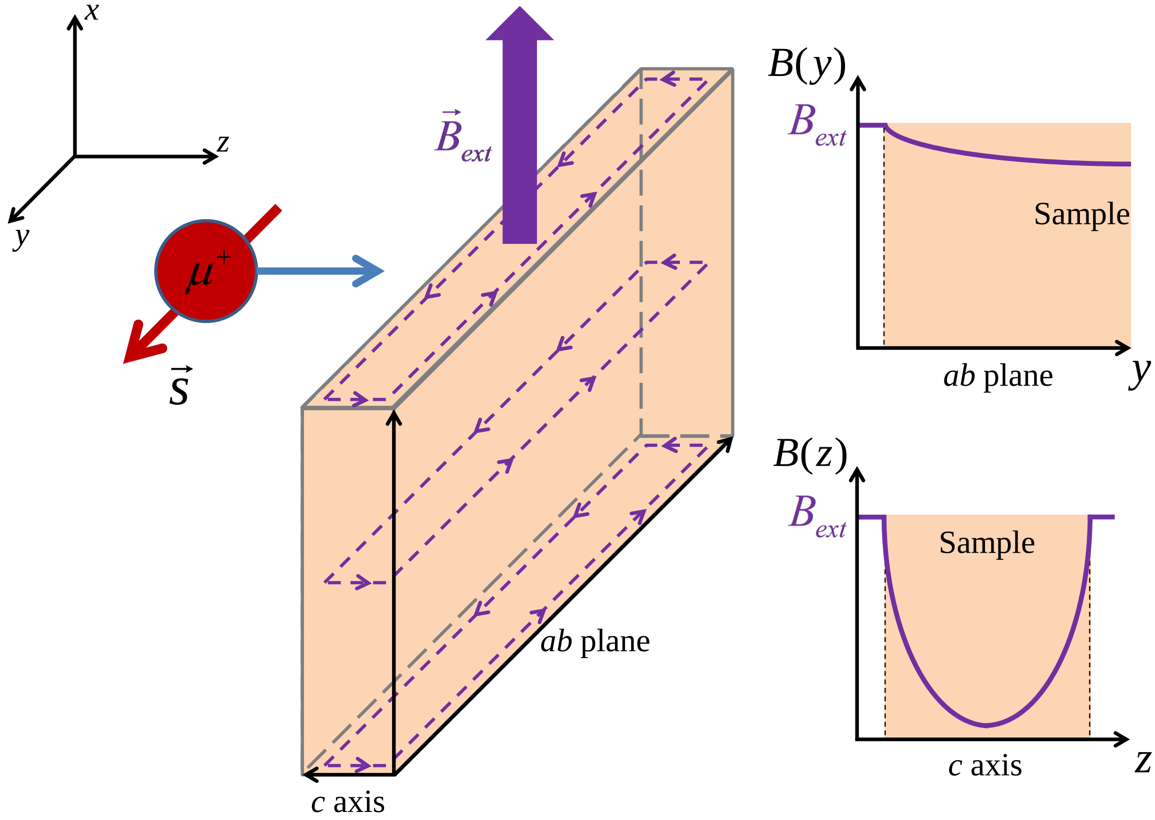

Figure 4.7: Schematic drawing of the experimental setup. The muons are implanted along the z direction (blue arrow) with the spin polarized along the y direction (red arrow). The external magnetic field (purple arrow) is applied along the x direction. The shielding currents are represented by the purple dashed line, $B(z)$ and $B(y)$ as solid purple lines.

the contributions of the shielding currents along the c-direction can be neglected since λ_a and λ_b are a factor 5-8 times smaller than λ_c.

The μSR asymmetry spectra in the Meissner state is described by

$$A\,P_{\text{Meissner}}(t) = A\,\mathrm{e}^{-\frac{1}{2}\sigma^2 t^2} \int n\,(z)\,\cos\left[\gamma_\mu B\,(z)\,t + \phi\right]\,\mathrm{d}z, \tag{4.10}$$

where σ is the depolarization rate, which is a measure of any inhomogeneous additional broadening, $n(z)$ is the normalized muon stopping profile for the corresponding implantation energy, and ϕ is the initial phase of the muon spin with respect to the positron detector.

For extreme type-II superconductors, where the coherence length is much smaller than the penetration depth, the screening of an applied magnetic field in the Meissner state ($H_{\mathrm{ext}} < H_{\mathrm{c_1}}$) is described by the London equation [41, 42]:

$$\frac{\mathrm{d}^2 B(z)}{\mathrm{d}z^2} = \frac{1}{\lambda_{\mathrm{L}}^2} B(z)\,. \tag{4.11}$$

Since the London penetration depth λ_{L} is an ideal theoretical limit, we determine within the μSR experiment the magnetic penetration depths λ_i, labeled according to the direction of the shielding currents. The experimental values λ_i are in contrast to the London penetration depth temperature dependent and anisotropic. For a semi-infinite sample the solution $B(z)$ is then:

$$B(z) = \begin{cases} B_{\mathrm{ext}} \cdot \mathrm{e}^{-\dfrac{z-z_0}{\lambda_i}} & , z \geq z_0 \\ B_{\mathrm{ext}} & , z < z_0 \end{cases}\,. \tag{4.12}$$

Here we take a dead layer z_0 into account. Within this layer no field screening is present, due to the sample roughness [90] or to the reduction of the order parameter close to the surface. For a thin film with a finite thickness d this profile changes to a cosh, since the magnetic field penetrates exponentially from both interfaces into the sample:

$$B(z) = \begin{cases} B_{\mathrm{ext}} \cdot \dfrac{\cosh\left(\dfrac{z - z_0 - d_{\mathrm{SC}}/2}{\lambda_i}\right)}{\cosh\left(\dfrac{d_{\mathrm{SC}}/2}{\lambda_i}\right)} & , z_0 \leq z \leq d_{\mathrm{SC}} + z_0 \\ B_{\mathrm{ext}} & , z < z_0, z > d_{\mathrm{SC}} + z_0 \end{cases}\,, \tag{4.13}$$

with the superconducting layer thickness $d_{\mathrm{SC}} = d - 2 \cdot z_0$. To illustrate the magnetic penetration profile the average magnetic field

$$\bar{B} = \int B(z)\, n(z)\, \mathrm{d}z \tag{4.14}$$

is plotted as a function of the mean implantation depth

$$\bar{z} = \int z\, n(z)\, \mathrm{d}z, \tag{4.15}$$

where $n(z)$ is the normalized stopping profile for a certain implantation energy.

Therefore, LE-μSR experiments provide the possibility to detect small changes in the magnetic penetration profiles. The magnetic screening profile is linked via the magnetic penetration depth λ to the superfluid density $n_\mathrm{s} \propto 1/\lambda^2$ [41, 42], as required to study the influence of illumination on the microscopic properties of superconductors.

5 Studies of Thin-Film $La_{2-x}Sr_xCuO_4$

$La_{2-x}Sr_xCuO_4$ (LSCO) is one of the most studied cuprate systems. Over the past years, investigations have been focused on thin-film systems and particularly multi-layers. Although the critical temperature strongly depends on the chosen substrate and therefore on the strain acting on the film [91–93], the influence of strain on the magnetic part of the phase diagram has not been investigated. The findings presented here allow to differentiate strain-induced effects in the thin films from photo-induced changes. Resistivity measurements showed, that illumination with visible light increases the number of charge carriers in LSCO [19]. Since the magnetic state of LSCO is very sensitive to changes in the charge carrier concentration, illumination may affect the antiferromagnetism. In this chapter the compound is introduced first, followed by a detailed investigation of the differences between bulk and thin-film LSCO in the magnetic regimes. Finally, the sensitivity of these magnetic orders to visible-light illumination, investigated by resistivity and LE-μSR measurements, are discussed.

5.1 The $La_{2-x}Sr_xCuO_4$ compound

$La_{2-x}Sr_xCuO_4$ was discovered in 1986 [94] shortly after the first copper oxide superconductor $Ba_{2-x}La_xCuO_4$ [2]. The parent compound La_2CuO_4 (LCO) crystallize in the K_2NiF_4 structure [36]. At high temperatures the tetragonal *I4/mmm* structure is formed. At $T_s = 520\,K$ LCO undergoes a structural phase transition to an orthorhombic *Bmab* structure, which is depicted in Fig. 5.1a. The structural transition temperature T_s decreases strongly when adding Sr to the system (see Fig. 5.2).

$La_{2-x}Sr_xCuO_4$ exhibits a rich magnetic phase diagram (see Fig. 5.2). Below the Néel temperature T_N, the copper electronic moments are aligned antiparallel along the a^* and b^* direction, respectively, within the CuO_2 planes. The resulting antiferromagnetic (AF) spin-structure is shown in Fig 5.1b. While the Néel temperature is about 300 K in the parent compound [31, 95, 97–100], T_N strongly decreases with Sr doping. At low temperatures the charge carriers introduced by doping localize around Sr impurities into a spin-glass-like state superimposed on the AF state, forming a “spin freezing” phase [98, 99]. The spin degree of freedom freeze. The corresponding transition temperature T_f increases linearly with doping: $T_f \simeq 815\,K{\cdot}x$ [98]. If the Sr content exceeds 0.02 the AF state is completely

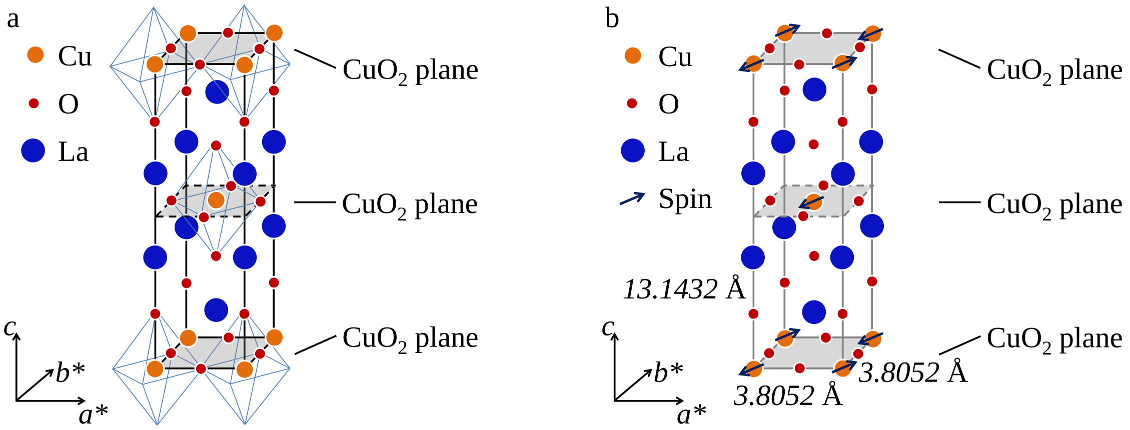

Figure 5.1: The crystallographic orthorhombic structure (a) and the spin structure [95] (b) of La_2CuO_4. The lattice parameters $a^* = b^* = \sqrt{a^2 + b^2}/2$ and c, with a,b,c as determined by Reehuis et al. [96], are given in the figure. The CuO_2 planes are marked in gray. The direction of the copper electronic moment is indicated by the blue arrow. The oxygen octahedrons surrounding the copper atoms are colored in light blue.

suppressed. In the doping range $0.02 \lesssim x \lesssim 0.06$ only short-range antiferromagnetic correlations are present at temperatures $T \leq T_\mathrm{g}$ and spontaneous zero-field precession is observed by μSR [98, 99]. This phase is referred as "cluster spin glass" (CSG) as mentioned before. The corresponding transition temperature T_g decreases with increasing Sr content, $T_\mathrm{g} \propto 1/x$ [98], reverse to T_f. At $x = 0.05$ superconductivity arises, leading to a coexistence of the CSG and the superconducting (SC) phase [31, 98]. The maximum in T_c is reached at $x \approx 0.15$ with 40 K. For higher Sr concentrations T_c decreases until it vanishes at $x \approx 0.28$ [101, 102]. Therefore, the SC phase is in general divided into the underdoped region ($0.05 \lesssim x \lesssim 0.15$), the optimally doping level ($x \approx 0.15$), and the overdoped region ($0.15 \lesssim x \lesssim 0.28$). At the strongly doped side of the phase diagram, $La_{2-x}Sr_xCuO_4$ exhibits the properties of a metallic Fermi-liquid. An additional feature of the $La_{2-x}Sr_xCuO_4$ phase diagram is the so called pseudogap phase, which is generic for the cuprates as discussed in Chapter 2.

5.2 Sample preparation and characterization of $La_{2-x}Sr_xCuO_4$

The LSCO family was heavily investigated ever since its discovery. In the present study we focused on thin-film samples, exhibiting significant deviations from the bulk electronic

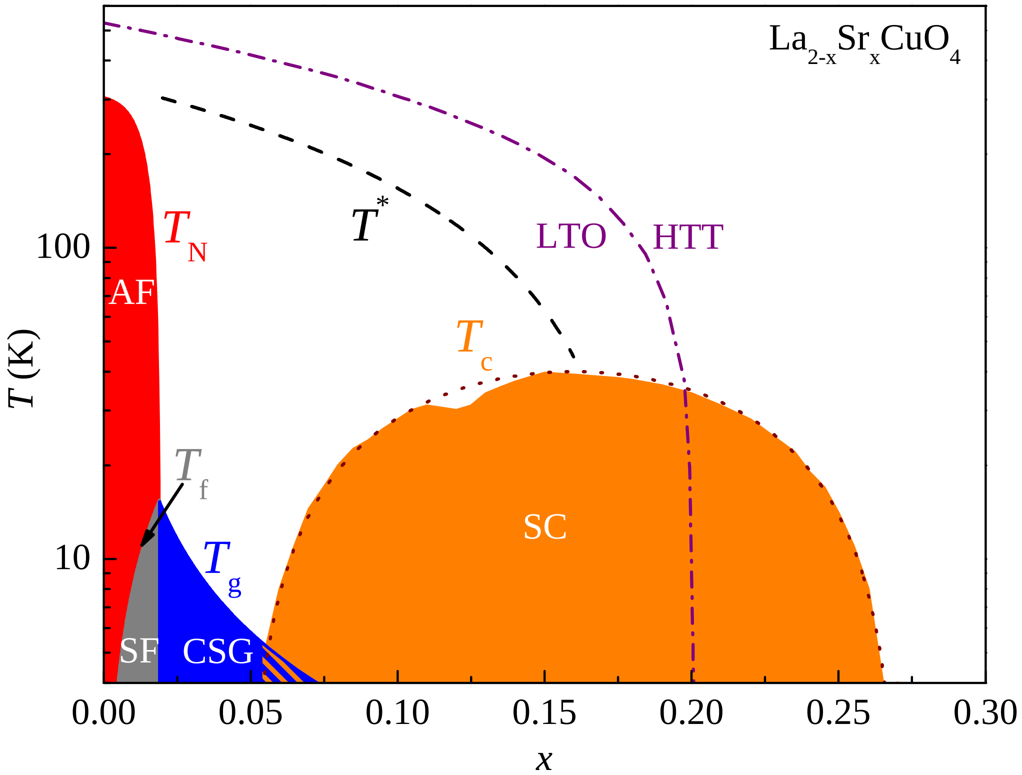

Figure 5.2: Schematic phase diagram of $La_{2-x}Sr_xCuO_4$: AF - antiferromagnetic phase with the Néel temperature T_N, SF - spin freezing phase with transition temperature T_f, CSG - cluster spin glass phase with the transition temperature T_g, SC - superconducting phase with the critical temperature T_c, and the pseudogap temperature T^* (black dashed line). The structural phase transition from high temperature tetragonal structure (HTT) to low temperature orthorhombic structure (LTO) is indicated by the purple dot-dashed line. The universal parabolic behavior of T_c, introduced in Chapter 2, is represented by the short-dashed line.

properties. The used thin-film samples were grown by molecular-beam epitaxy at the Brookhaven National Laboratory [103]. This method allows to grow thin films layer by layer. To obtain an excellent sample quality the growth rates are controlled by an atomic absorption spectroscopy system. As substrate (001) oriented single-crystalline $LaSrAlO_4$ (LSAO) of the size $10 \times 10 \times 1\,\mathrm{mm}^3$ was used. The samples are c-axis oriented (c axis is perpendicular to the surface) and exhibit a thickness of about 53 nm. Since we are interested in the magnetic part of the phase diagram the nominal Sr content x ranges from 0.00 to 0.06.

To characterize the samples we performed x-ray diffraction and resistivity measurements.

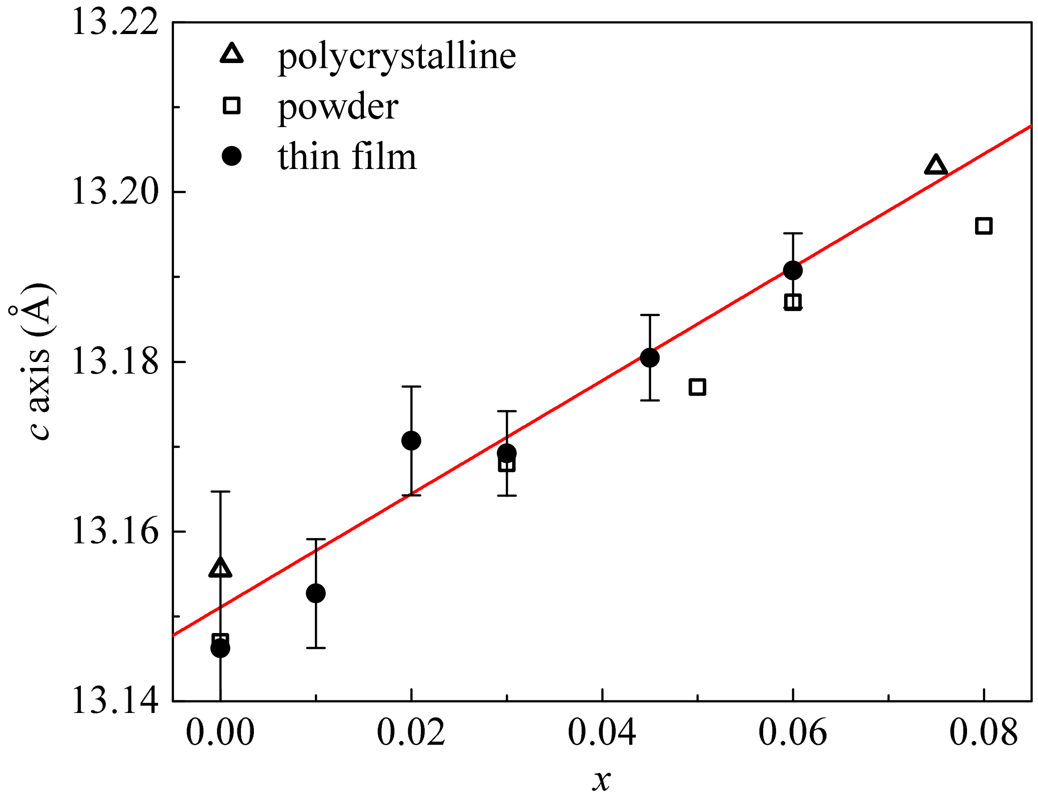

Figure 5.3: The c-axis lattice constant versus the doping level x of $La_{2-x}Sr_xCuO_4$ powder [104] (squares), polycrystals [105] (triangles) and thin films (circles).

Using the Bragg law, the crystallographic c axes were calculated from the Bragg-reflexion angles 2θ and its order n of the θ-2θ-spectra:

$$n \cdot \lambda = 2 \cdot d_{hkl} \cdot \sin(\theta)\,, \tag{5.1}$$

with a wavelength of $\lambda = 1.54056\,\text{Å}$ of the copper anode and a distance between the lattice planes of $d_{002} = c/2$. The reflexion angles of the SLAO substrate where used to identify the position of $\theta = 0$. The obtained c-axis lattice constants are linearly related to the Sr content x and agree with bulk values of powders [104] and polycrystals [105] as depicted in Fig. 5.3. Therefore all thin films are relaxed, meaning no significant strain originating from the mismatch between the lattice parameters of the sample and the substrate is present. This is expected for every sample with a thickness exceeding the critical thickness, identified to be about 20 unit cells (about 26 nm) [106].

The resistivity measurements were obtained in the four-point probe geometry using the

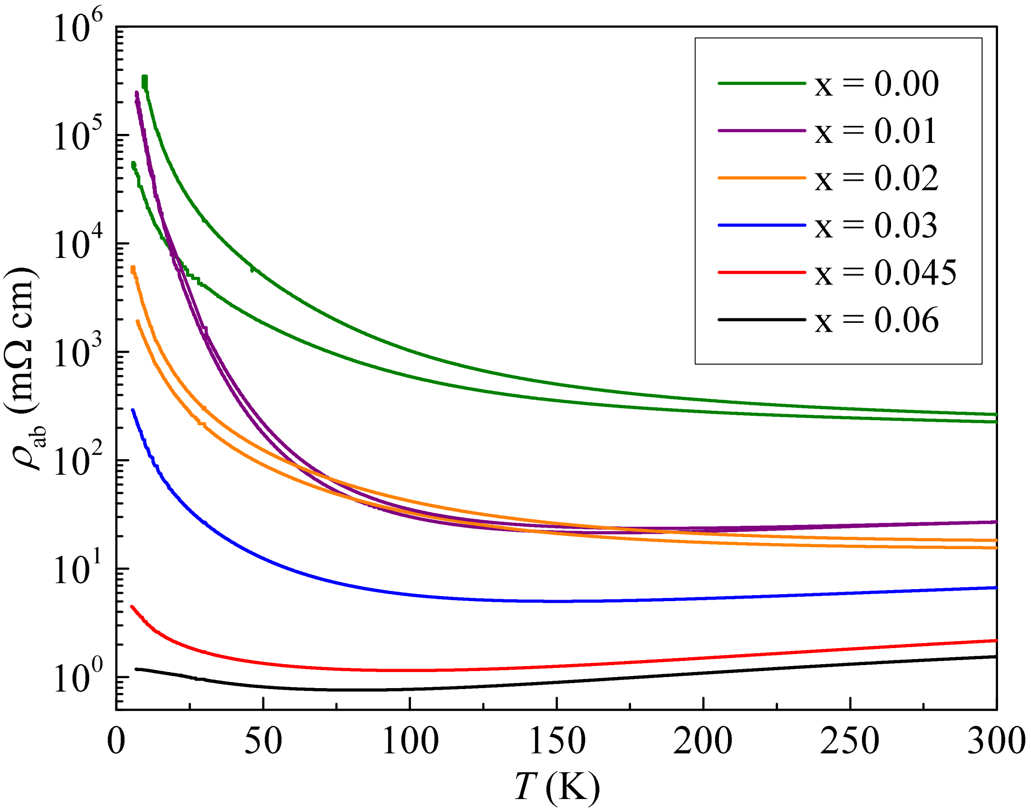

Figure 5.4: Resistivity ρ_{ab} versus temperature T of thin-film $La_{2-x}Sr_xCuO_4$ for different doping level x.

setup described in Chapter 3. To decrease the contact resistivity, 100 nm thick pads of Ag and Au were sputtered on the sample surface. From the resulting defined geometry the conversion factor from resistance to resistivity for the LSCO thin films was found to be 0.00616 mΩ cm/Ω, using the theoretical concept of mirror charges [107, 108]. The parent compound exhibits an insulating behavior, whereas samples with higher doping level show a semiconducting temperature dependence in resistivity, see Fig. 5.4. This behavior is in agreement with previous studies [109]. The temperature dependence of LSCO with $x = 0.02$ deviates from the literature. No minimum is observed in the temperature dependence of ρ_{ab}. The minimum of the resistivity curves is in general shifted to higher values. These differences compared to bulk samples may result from a different amount of disorder, which plays an important role in thin films. Transmission electron microscopy and electron energy loss spectroscopy revealed the presence of shear defects, stacking faults and misfit dislocations [110]. The formation of the misfit dislocations is associated with the relaxation of the thin-film lattice parameters during growth (when the critical thickness is reached). Resistivity measurements of two LSCO samples with $x = 0.00$ show also a slightly different behavior compared to each other. Besides disorder, also a slightly different oxygen content could be the origin of this derivation. To conclude the LSCO samples are of excellent quality having properties close to bulk, but they exhibit still a non-negligible amount of disorder.

5.3 Magnetic phase diagram of thin-film $La_{2-x}Sr_xCuO_4$

To investigate photo-induced effects on LSCO we used thin-film samples, since they exhibit a large surface. The light also penetrates only about 100 nm into the material, and it is easier to make contacts for resistivity measurements. To be able to distinguish between intrinsic and photo-induced effects the magnetic states of LSCO thin films grown on single-crystal $LaSrAlO_4$ substrates with $0.00 \leq x \leq 0.06$ were studied in detail by low-energy muon-spin rotation. The phase diagram of the thin films shows the same features as the one of bulk $La_{2-x}Sr_xCuO_4$, but the transition temperatures between distinct magnetic states are shifted. The Néel temperature T_N is decreased. No hole spin freezing is observed for LSCO with $x = 0.01$ down to 5 K. By contrast, the transition temperature to the cluster spin-glass state T_g is enhanced. Oxygen off-stoichiometry, strain-induced changes of the lattice parameters, or higher-order magnetic coupling constants are unlikely to explain the observed differences. Misfit dislocations through strain release is the most probable explanation. On the other side, the thin-film and bulk samples exhibit similar magnitude, temperature, and doping dependence of the staggered magnetization. The border between the AF and the CSG phase ($x \simeq 0.02$) is identical. Thus, the determined magnetic phase diagram provides a solid basis for future studies of multilayer and superlattice LSCO thin films.

Details on this work are published in:

E. Stilp, A. Suter, T. Prokscha, E. Morenzoni, H. Keller, B. M. Wojek, H. Luetkens, A. Gozar, G. Logvenov, and I. Božović, *Magnetic phase diagram of low-doped $La_{2-x}Sr_xCuO_4$ thin films studied by low-energy muon-spin rotation*, Phys. Rev. B **88**, 064419 (2013).

URL: http://journals.aps.org/prb/abstract/10.1103/PhysRevB.88.064419

DOI: 10.1103/PhysRevB.88.064419

PACS: 76.75.+i, 74.72.-h, 75.70.-i

PHYSICAL REVIEW B **88**, 064419 (2013)

Magnetic phase diagram of low-doped $La_{2-x}Sr_xCuO_4$ thin films studied by low-energy muon-spin rotation

E. Stilp,[1,2] A. Suter,[1] T. Prokscha,[1] E. Morenzoni,[1] H. Keller,[2] B. M. Wojek,[1,2,*] H. Luetkens,[1]
A. Gozar,[3] G. Logvenov,[3,†] and I. Božović[3]
[1]*Laboratory for Muon Spin Spectroscopy, Paul Scherrer Institut, CH-5232 Villigen PSI, Switzerland*
[2]*Physik-Institut der Universität Zürich, Winterthurerstrasse 190, CH-8057 Zürich, Switzerland*
[3]*Brookhaven National Laboratory, Upton, New York 11973-5000, USA*

(Received 14 June 2013; revised manuscript received 29 July 2013; published 23 August 2013)

The magnetic phase diagram of $La_{2-x}Sr_xCuO_4$ thin films grown on single-crystal $LaSrAlO_4$ substrates has been determined by low-energy muon-spin rotation. The diagram shows the same features as the one of bulk $La_{2-x}Sr_xCuO_4$, but the transition temperatures between distinct magnetic states are significantly different. In the antiferromagnetic phase the Néel temperature T_N is strongly reduced, and no hole spin freezing is observed at low temperatures. In the disordered magnetic phase ($x \gtrsim 0.02$) the transition temperature to the cluster spin-glass state T_g is enhanced. Possible reasons for the pronounced differences between the magnetic phase diagrams of thin-film and bulk samples are discussed.

DOI: 10.1103/PhysRevB.88.064419 PACS number(s): 76.75.+i, 74.72.−h, 75.70.−i

I. INTRODUCTION

The bulk magnetic phase diagram of the cuprates, especially $La_{2-x}Sr_xCuO_4$ (LSCO), has been extensively studied in the past two decades.[1–4] At lowest Sr contents ($x \lesssim 0.02$) bulk LSCO is an antiferromagnetic (AF) charge-transfer insulator. Long-range three-dimensional (3D) AF order appears below the Néel temperature $T_N \simeq 300$ K in the parent compound La_2CuO_4 (LCO).[2,5–8] It results from the ordering of spin-1/2 Cu^{2+} moments due to superexchange with the in-plane exchange coupling constant $J/k_B \simeq 1500$ K. LCO is considered as a model system of a spin-1/2 quasi-two-dimensional (2D) Heisenberg antiferromagnet on a square lattice. The in-plane magnetic properties are well described by the so-called renormalized classical regime as derived by Chakravarty *et al.*[9] and experimentally verified.[10,11] The 3D order is established predominantly by the weak out-of-plane exchange coupling $J' \simeq 10^{-5} J$.[10] At a nominal Sr content of $x \simeq 0.02$ the Néel temperature decreases to zero as shown in the schematic phase diagram in Fig. 1. Within the AF state, charge localization of the doped holes is observed below the freezing temperature T_f ["spin freezing" (SF)] which depends linearly on the doping level, as $T_f = 815\ \mathrm{K}\cdot x$ (Ref. 6).

For nominal Sr contents $x \gtrsim 0.02$ short-range AF correlations within the CuO_2 planes persist. A complicated interplay between the doped holes in the CuO_2 planes and the remaining AF correlations leads to a yet not well understood electronic state with a pseudogap in the excitation spectrum.[12] In this doping region, below the freezing temperature T_g spontaneous zero-field precession is observed in muon-spin rotation (μSR) studies.[6,7] This is often referred to as the "cluster spin-glass" (CSG) phase. The "glass" transition temperature T_g decreases as $1/x$ (Ref. 6) and is also detected within the superconducting phase that starts at $x \simeq 0.05$.

Thin films open the door to new physical properties and phenomena, since electronic or magnetic properties of thin-film structures can be very different from those of the single constituents as found in bulk samples. Phenomena driven by various couplings and dimensional effects may appear. For instance, the proximity between different orders can be studied in multilayer systems and superlattices. In different cuprate heterostructures a giant proximity effect has been found,[13–15] where low doped cuprates sandwiched between superconducting layers, can transmit supercurrent or exhibit a Meissner effect over surprisingly large distances at temperatures where these layers are intrinsically in the normal state. It is usually assumed that the magnetic layers in thin-film systems behave as in the bulk material. Yet, this was never systematically studied. As a local magnetic probe of thin films low-energy muon-spin rotation (LE-μSR) is well suited to address this question.[16] Previous studies by this technique of canonical spin glasses,[17] metal-insulator LSCO superlattices,[18] and nickel-oxide superlattices[19] showed that dimensional effects might strongly influence the magnetic ground state and its excitations. In addition, the mismatch between the lattice constants of the thin-film material and of the substrate leads to biaxial positive or negative strain in the film. For example, LSCO grown on single-crystal $LaSrAlO_4$ (LSAO) substrates are under compressive strain, whereas on single-crystal $SrTiO_3$ (STO) substrates they are under tensile strain. Epitaxial strain leads to significant changes in the lattice constants of the films (contraction or expansion), which in turn affects the superconducting transition temperature[20–24] as well as the electronic band structure.[25] Since both the substrates and the cuprates are essentially ionic crystals, apart from the above "geometric" effect ("Poisson strain"),[23] there is an additional effect due to unscreened, long-range Coulomb interactions ("Madelung strain"),[26] which manifests itself as a significant change in the unit cell volume. Finally, in a preliminary study by Suter *et al.*[27] changes were also observed in T_N of LCO, depending on the choice of substrate. Therefore, the question arises how epitaxial strain, potential strain release, and the substrate, in general, affect the magnetic properties of LSCO thin films.

Here we present a study on the magnetic phase diagram of LSCO thin films in the low-doping regime (thickness $\simeq 53$ nm, $0.00 \leqslant x \leqslant 0.06$) grown on LSAO. In Sec. II the

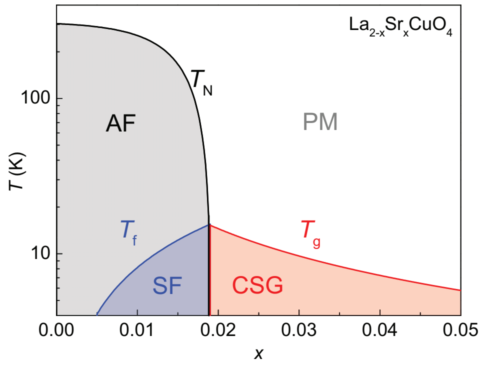

FIG. 1. (Color online) Schematic magnetic phase diagram of bulk LSCO. The Néel temperature T_N, the spin freezing temperature of doped holes T_f, and the glass transition temperature T_g are shown in dependence of the Sr content x.

experimental details are given. Sections III A and III B present the LE-μSR results of the AF and CSG phases, respectively. This technique allows stopping muons in matter at different depths in the nanometer range,[28] and is therefore well suited to investigate magnetic thin-film samples on a microscopic scale. In Sec. III C the differences in the magnetic phase diagrams as obtained for bulk and thin-film samples are discussed, followed by the summary and conclusions in Sec. IV.

II. EXPERIMENTAL DETAILS

The $La_{2-x}Sr_xCuO_4$ films studied here were synthesized using molecular-beam epitaxy (MBE) at the Brookhaven National Laboratory. We used single-crystal LSAO substrates, $10 \times 10 \times 1$ mm^3 in size and polished with the surface perpendicular to the [001] crystal axis. The typical film thickness was 53 nm. Further information about the growing process has been published elsewhere.[29] Here, we have investigated thin films with $x = 0.00$, 0.01, 0.02, 0.03, 0.045, and 0.06. The doping level was controlled during the deposition by using well-calibrated MBE sources; the rates were monitored and controlled in real time using a custom-built 16-channel atomic absorption spectroscopy system.[29] The film growth and quality was monitored in real time using reflection high-energy electron diffraction, and checked subsequently by atomic force microscopy as well as by resistivity, susceptibility, and x-ray diffraction measurements. The c-axis lattice parameters of the samples were extracted from θ-2θ scans (Fig. 2). They show a linear behavior as a function of the nominal Sr content x, and agree well with the bulk data of polycrystalline samples[30] and powder samples.[31] A comparison of the room-temperature resistivity for LSCO single crystals[32] and the investigated thin films as a function of x is depicted in Fig. 3. The resistivity at 300 K shows the expected decrease with increasing Sr content x. The thin-film resistivity data are comparable to the single-crystal data.

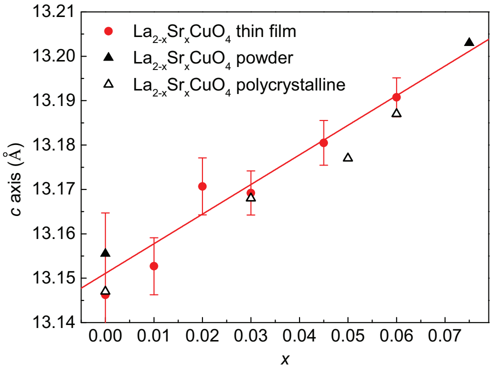

FIG. 2. (Color online) The crystallographic c-axis lattice constant as a function of the nominal Sr content x in 53-nm-thick LSCO films deposited on single-crystal LSAO substrates, as determined by x-ray diffraction (red circles) and in LSCO bulk samples [black open (Ref. 30) and filled (Ref. 31) triangles]. The red solid line is a linear fit to the thin-film data.

To study the magnetic phase diagram of thin-film LSCO, LE-μSR experiments were performed at the μE4 beam line at the Paul Scherrer Institute (PSI, Switzerland).[16] In a μSR experiment positively charged muons μ^+ with ~100% spin polarization are implanted in the sample where they thermalize within a few picoseconds without noticeable loss of polarization. Because of interactions of the μ^+ spins with internal local magnetic fields B_{loc} the magnetic moments of the μ^+ precess with the Larmor frequency $\omega_L = \gamma_\mu B_{\text{loc}}$ ($\gamma_\mu = 2\pi \times 135.54$ MHz/T) in the sample until they decay with a mean lifetime of $\tau_\mu = 2.197$ μs into neutrinos ($\bar{\nu}_\mu, \nu_e$) and positrons (e^+):

$$\mu^+ \rightarrow e^+ + \bar{\nu}_\mu + \nu_e.$$

The emission probability for the positron along the muon-spin direction is enhanced due to the parity-violating muon decay. Measuring the time difference $t = t_e - t_s$ between the implantation time t_s of the μ^+ and its decay time t_e, detected via the decay positron (for $\sim 5 \times 10^6 \mu^+$), allows one to determine the temporal evolution of the muon-spin polarization $P(t)$

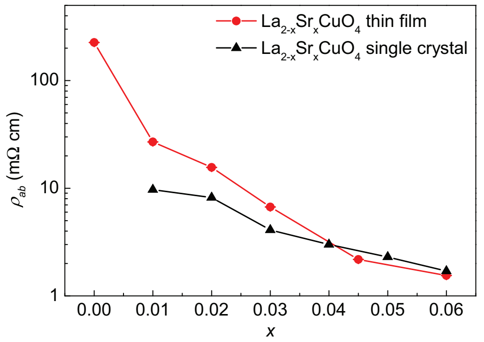

FIG. 3. (Color online) Resistivity ρ_{ab} at $T = 300$ K versus the nominal Sr content x of MBE-grown LSCO thin films (red circles) and LSCO single crystals (black triangles, from Ref. 32). The lines are guides to the eye.

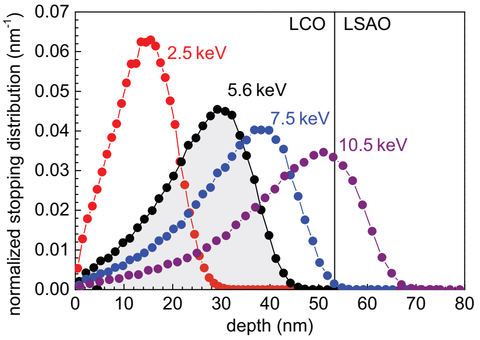

FIG. 4. (Color online) The normalized stopping distribution of muons with different implantation energies (numbers given in the figure) of a 53-nm-thick LCO film deposited on a single-crystal LSAO substrate calculated using TRIM.SP (Ref. 35). The lines are guides to the eye.

(time ensemble average) via the positron count rate $N(t)$:

$$N(t) = N_0\,\mathrm{e}^{-t/\tau_\mu}[1 + AP(t)] + N_{\mathrm{bkg}}, \qquad (1)$$

were N_0 gives the scale of the counted positrons, N_{bkg} is a time-independent background of uncorrelated events, and A is the observable decay asymmetry. The latter is a function of the positron energy and the solid angle of the positron detectors. In our experimental setup $A \simeq 0.25 = A_{\mathrm{max}}$. The exponential function describes the radioactive muon decay. From the measured $P(t)$ one can extract the local magnetic fields, field distributions, and field fluctuations present in the sample.[33] In bulk μSR experiments μ^+ with an energy of $\sim$4.1 MeV are used, which originate from the positively charged pion decay at rest at the surface of the muon production target ("surface muons"). In this case the mean stopping depth in condensed matter is of the order of $\sim 100\ \mu$m. To investigate thin films LE-μSR makes use of epithermal muons (~ 15 eV). They are created by moderating surface muons.[28,34] After reacceleration, the final muon implantation energy is controlled by applying a voltage to the sample. By tuning the energy between 1 keV and 30 keV, mean depths between a few and a few hundred nanometers can be chosen. The normalized stopping distribution of μ^+ in a LCO film deposited on a LSAO substrate for different implantation energies is depicted in Fig. 4.

For each Sr content, we used a mosaic of four thin-film samples, each with lateral dimensions of 1×1 cm^2, glued onto a silver-coated aluminum plate with silver paint. To reach temperatures in the range 3 K to 300 K a cold-finger cryostat was used. The experiments were performed in ultrahigh vacuum at a pressure of about 10^{-9} mbar. The data presented here were all obtained with a muon implantation energy $E_{\mathrm{impl}} = 5.6$ keV. For this energy Monte Carlo simulations performed using TRIM.SP[35] yield a mean implantation depth of about 30 nm, which is optimal for these films (Fig. 4). In order to check the homogeneity of the films across their thickness μSR time spectra $N(t)$ for different values of E_{impl} were measured showing no differences. LE-μSR measurements were performed in zero magnetic field (ZF) to determine the internal magnetic fields at the muon stopping site, which are related to the staggered magnetization, as well as in weak transverse magnetic fields (wTF) in the range of 2.8 mT to 9.8 mT to obtain the magnetic transition temperatures T_{N}, T_{f}, T_{g}, and the magnetic volume fractions f.

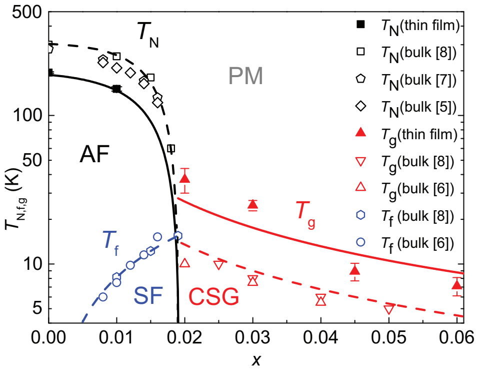

FIG. 5. (Color online) The magnetic phase diagram of LSCO for thin films (solid lines) and bulk samples (dashed lines). The Néel temperature T_{N}, the freezing temperature T_{f}, and the glass transition temperature T_{g} are shown as a function of the nominal Sr content x. The black lines are guides to the eye. The blue and red lines follow the relations $T_{\mathrm{f}} \propto x$ and $T_{\mathrm{g}} \propto 1/x$, respectively.

III. RESULTS AND DISCUSSION

A. Antiferromagnetic regime

We first investigated thin-film samples with $x = 0.00$ and $x = 0.01$ in the AF regime of the phase diagram. From temperature scans in a weak magnetic field the Néel temperatures were determined to be $T_{\mathrm{N}}^{x=0.00} = 195(3)$ K and $T_{\mathrm{N}}^{x=0.01} = 151(5)$ K (Fig. 5). These values are much lower compared to bulk values, as will be discussed later in detail.

In the paramagnetic (PM) state ($T \gg T_{\mathrm{N}}$) the asymmetry time spectra in ZF, $A\,P_{\mathrm{ZF}}^{\mathrm{PM}}(t)$, are well described by a Gaussian Kubo-Toyabe function [Fig. 6(a)], corresponding to a 3D Gaussian field distribution of dense randomly oriented static magnetic moments:

$$AP_{\mathrm{ZF}}^{\mathrm{PM}}(t) = A\left[\tfrac{1}{3} + \tfrac{2}{3}(1 - \sigma^2 t^2)\,\mathrm{e}^{-(1/2)\sigma^2 t^2}\right], \qquad (2)$$

where A is the decay asymmetry and σ is the depolarization rate. This is expected since only the nuclear moments of La and Cu contribute to $AP_{\mathrm{ZF}}^{\mathrm{PM}}(t)$. The PM fluctuation rate of the electronic Cu moments is too high to have an observable influence on the ZF spectra. The nuclear moments, however, are static on μSR time scales. In all ZF fits a temperature-independent constant background asymmetry $A_{\mathrm{bkg}} = 0.17(3)A_{\mathrm{max}}$ was taken into account, which originates from the muons stopping in the silver coating of the sample plate. Only about 80 % to 85 % of the muons stop in the sample. Close to the magnetic transition ($T \gtrsim T_{\mathrm{N}}$) the time spectrum $AP(t)$ changes first to a combination of a Gaussian Kubo-Toyabe function with an exponential decay [Fig. 6(e)] and then to a superposition of exponential decay functions [Figs. 6(b) and 6(f)]. At these temperatures the electronic fluctuations slow down, giving rise

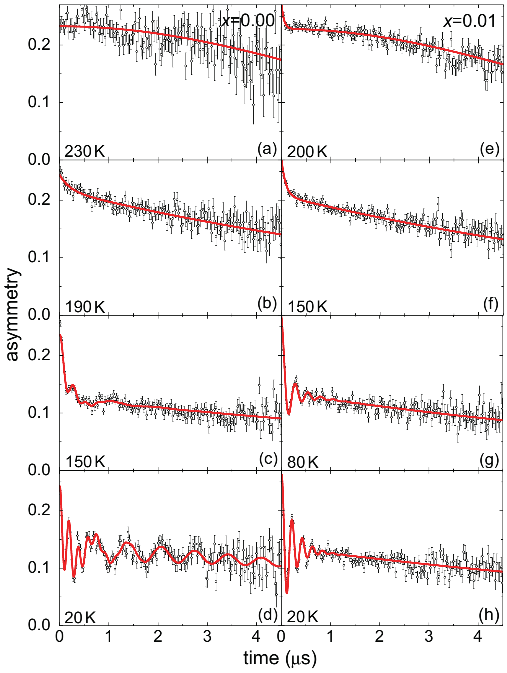

FIG. 6. (Color online) The ZF asymmetry time spectra of LSCO thin films with $x = 0.00$ (left panels) and $x = 0.01$ (right panels) at different temperatures for $E_{\rm impl} = 5.6$ keV. The solid red lines are fits to the data done with MUSRFIT (Ref. 36). See text for more details.

to a stronger depolarization of the muons. This behavior is also observed in the PM phase of bulk samples.[7]

In the AF phase, for $T \ll T_{\rm N}$, the ordered magnetic moments generate a local magnetic field $B_{\rm loc}$ at the stopping site of the muon, which is related to the sublattice magnetization of the Cu^{2+} electronic moments. By using first-principles cluster calculations[37] the muon stopping site has been located at (0.119, 0.119, 0.2128) in the orthorhombic unit cell, 1.0 Å off the apical oxygen, as in an oxygen-hydrogen bond (circles in Fig. 7). The ZF asymmetry spectra $AP^{\rm AF}_{\rm ZF}(t)$ can then be described by

$$AP^{\rm AF}_{\rm ZF}(t) = \sum_i A_{{\rm T},i}\cos(\gamma_\mu B_{{\rm loc},i}\, t + \phi)\,{\rm e}^{-\lambda_{{\rm T},i} t} + A_{\rm L}\,{\rm e}^{-\lambda_{\rm L} t}, \tag{3}$$

where $A_{\rm T}$ and $A_{\rm L}$ reflect the fraction of the muons having their spin initially transverse and longitudinal to the internal field direction, respectively. The relaxation rate $\lambda_{\rm T}$ is proportional to the width of the internal field distribution sensed by the muon. In the presence of disorder $\lambda_{\rm T}$ can be larger than $\gamma_\mu B_{\rm loc}$, resulting in an overdamped asymmetry spectrum without oscillations. In the presence of fluctuating magnetic fields the longitudinal part of the muon-spin polarization is relaxing as well with the corresponding rate $\lambda_{\rm L}$ ($\lambda_{\rm L} < 0.1\ \mu{\rm s}^{-1}$ likely due to nuclear dipole depolarization only). The phase ϕ is, in general, a temperature-independent constant.

In the AF phase for $T \lesssim T_{\rm N}$, the strongly damped oscillations in $AP^{\rm AF}_{\rm ZF}(t)$ can be better described by a Bessel function of the first kind, $J_0(t)$, which at larger times is equivalent to a cosine with a phase shift of $\Delta\phi = 45^\circ$ and an additional damping of $\sqrt{2/(\pi\gamma_\mu B_{\rm loc} t)}$ [see Figs. 6(c) and 6(g)]. When using the pure cosine function the phase ϕ strongly increases with increasing temperature, from less than 10° at 5 K to more than 40° at higher temperatures. In this case the Bessel function provides a better description of the measured $AP^{\rm AF}_{\rm ZF}(t)$:

$$\begin{aligned} AP^{\rm AF,2}_{\rm ZF}(t) =&\ A_{\rm T}\,{\rm e}^{-\lambda_{\rm T} t}\, J_0(\gamma_\mu\, B_{\rm loc}\, t) + A_{\rm L}\,{\rm e}^{-\lambda_{\rm L} t} \\ \approx&\ A_{\rm T}\,{\rm e}^{-\lambda_{\rm T} t}\sqrt{\frac{2}{\pi\,\gamma_\mu\, B_{\rm loc}\, t}}\,\cos\left(\gamma_\mu\, B_{\rm loc}\, t - \frac{\pi}{4}\right) \\ &+ A_{\rm L}\,{\rm e}^{-\lambda_{\rm L} t}. \end{aligned} \tag{4}$$

This behavior may arise from incommensurate magnetism,[33] where the period of the magnetic structure is not an integer multiple of the lattice constant, or from the presence of nanometer scale AF domains. Both cases lead to an asymmetric magnetic field distribution, which is better described by a Bessel function. In neutron diffraction studies on bulk material incommensurate magnetism was only observed for $x > 0.05$ and $T < 7$ K.[39] For $T \ll T_{\rm N}$, $AP^{\rm AF}_{\rm ZF}(t)$ is well described by a cosine function as in bulk samples, see Figs. 6(d) and 6(h).

In the AF state, the relative strength of the parameters $A_{\rm T}$ and $A_{\rm L}$ [see Eq. (3)] reflects the local magnetic field distribution which is determined by the spatial arrangement of the Cu electronic magnetic moments. If the field at the muon stopping site is isotropic, corresponding to an electronic moment vector pointing with equal probability in all three directions, then the ratio $A_{\rm T} : A_{\rm L}$ is $\frac{2}{3} : \frac{1}{3}$. If the spins are aligned within the CuO_2 planes, corresponding to a field at the stopping site with only planar components, the ratio $A_{\rm T} : A_{\rm L}$ is $\frac{1}{2} : \frac{1}{2}$. Both LSCO samples ($x = 0.00$ and $x = 0.01$) show at the lowest temperature a ratio close to $\frac{1}{2} : \frac{1}{2}$. This result is in agreement with neutron data which revealed that the Cu electronic magnetic moments are preferentially aligned in the CuO_2 planes.[40]

As evidenced by the beating in the asymmetry spectrum two frequencies, corresponding to two local fields, are observed in LCO thin films [Fig. 6(d)]. Extrapolating the temperature dependence of the measured fields to $T = 0$ K by a power law yields $B_{\rm loc,1}(0\ {\rm K}) = 40.9(4)$ mT and $B_{\rm loc,2}(0\,{\rm K}) = 11.2(1)$ mT. For LCO bulk samples only one local magnetic field $B_{\rm loc}(0\,{\rm K}) \cong 43$ mT has been reported,[7] although there are hints of a similar lower second field from unpublished data of high quality single crystals. A possible explanation for the appearance of an additional local magnetic field is a mixture of different alignments of the Cu electronic magnetic moments within the CuO_2 planes. From powder neutron diffraction experiments on LCO the spin structure shown in Fig. 7(a) was determined.[40] The electronic spins of different CuO_2 planes (black and green) are aligned parallel or antiparallel to each other in the orthorhombic unit cell. By taking only dipole magnetic fields arising from the Cu electronic magnetic moments into account [$m_{\rm Cu} = 0.645\,\mu_{\rm B}$ (Ref. 41)], this arrangement leads to the magnetic field distribution in the plane of the muon stopping site shown in Fig. 7(e). Since the muon stops close to the apical oxygen, the same magnetic field value is present at crystallographically equivalent muon

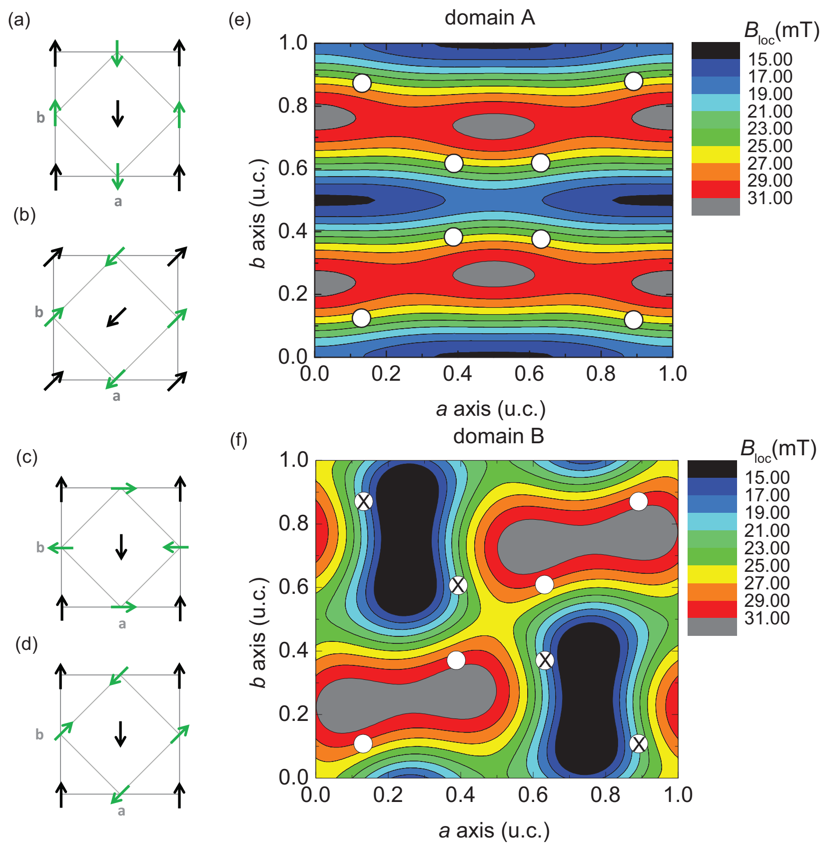

FIG. 7. (Color online) (a)–(d) show different arrangements of the Cu electronic magnetic moments as viewed along the c axis of the orthorhombic unit cell of LSCO ($a = 5.3568$ Å, $b = 5.4058$ Å, $c = 13.1432$ Å) (Ref. 38). Configuration (a) leads to one local magnetic field B_{loc} at the muon stopping site ("domain A"), whereas configurations (b)–(d) exhibit two B_{loc} ("domain B"). The black and green arrows in (a)–(d) correspond to moments in adjacent CuO_2 layers ($z = 0$ and $z = c/2$, respectively). (e) and (f) show the resulting magnetic field maps for the spin arrangements (a) and (b) for the plane $z = 0.2128\,c$ based on dipole field distribution calculations. The circles mark the muon stopping sites within the unit cell where $B_{\mathrm{loc},1}$ (open circles) or $B_{\mathrm{loc},2}$ (circles with crosses) is present.

stopping sites [marked with circles in Fig. 7(e)]. Therefore, only *one* B_{loc} is observable in this "domain A." A similar AF ordering but with rotated Cu spins within the CuO_2 planes [see, for example, Figs. 7(b)–7(d)] generates two different magnetic field values at crystallographically equivalent muon stopping sites indicated by "domain B" [see Fig. 7(f)]. The calculated field values differ from the local magnetic fields determined by LE-μSR. This deviation is not surprising, because transferred hyperfine fields as well as higher-order corrections, e.g., due to the Dzyaloshinskii-Moriya (DM) interactions, which could change the field values by a factor of two, are neglected here. To determine the magnetic field values precisely full density functional theory calculations have to be performed. The asymmetry $A_{\mathrm{T},1} = 0.074$ (related to $B_{\mathrm{loc},1}$) is more than two times larger compared to $A_{\mathrm{T},2} = 0.030$ (related to $B_{\mathrm{loc},2}$). Since the ZF oscillation amplitudes A_i are proportional to the magnetic volume fractions of the domains in the sample a mixture of two spin arrangements has to be present. While $B_{\mathrm{loc},1}$ is present in both domains but $B_{\mathrm{loc},2}$ only in domain B, the asymmetry ratio corresponds to a volume ratio domain A to domain B of 42% : 58% for the two spin arrangements.

Different Cu spin arrangements could originate from structural changes. In general, the c axis of thin-film samples grown on a LSAO substrate is larger compared to the bulk value. These changes in the crystal structure have a strong influence on the anisotropic parts of the spin Hamiltonian,[42] and hence on the spin configuration. This is consistent with observations for LCO crystallizing in the metastable tetragonal Nd_2CuO_4 structure with a c-axis lattice parameter of 12.52 nm only.[43] Bulk μSR (Ref. 43) revealed a lower internal magnetic field of $B_{\mathrm{loc}}(0\text{ K}) = 11$ mT and a different spin arrangement is expected compared to LCO in the orthorhombic phase. In our study no changes are observed in the c-axis lattice parameter compared to bulk values. So the existence of a mixture of tetragonal and orthorhombic phases seems unlikely. It is more likely that magnetic domains with different spin arrangements

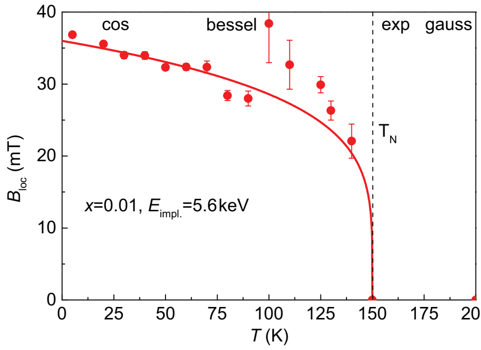

FIG. 8. (Color online) The temperature dependence of the local magnetic field B_{loc} at the muon stopping site for the LSCO film with $x = 0.01$ for $E_{\mathrm{impl}} = 5.6$ keV. The red solid line is a fit to the data using $B_{\mathrm{loc}}(T) = B_{\mathrm{loc}}(0\ \mathrm{K})(1 - T/T_{\mathrm{N}})^{0.21}$.

are present. This would also explain that in some bulk samples a second field is observed, where no tetragonal structure exists and T_{N} is higher compared to thin films. A change in the Cu spin arrangement could be caused by dislocations or defects, which could arise in thin films from the lattice mismatch between LSCO and LSAO.

For the nominal Sr content $x = 0.01$ the generic behavior of $AP_{\mathrm{ZF}}(t)$ as a function of T is similar as for $x = 0.00$, but only one B_{loc} is present just like in bulk samples [Fig. 6(h)]. In bulk samples with $x = 0.01$ spin freezing of the doped holes is observed below $T_{\mathrm{f}} = 8$ K (Fig. 5). As determined by ZF μSR measurements, this freezing below T_{f} manifests itself as a drastic increase of the slope $\mathrm{d}B_{\mathrm{loc}}/\mathrm{d}T$ (see Ref. 7). In the present study no increase is observed down to 5 K (Fig. 8). Thus the shape of $B_{\mathrm{loc}}(T)$ and the fact that $B_{\mathrm{loc}}^{x=0.01}(0\ \mathrm{K}) = 36.0(5)$ mT is below $B_{\mathrm{loc}}^{x=0.00}(0\ \mathrm{K}) = 40.9(4)$ mT indicate a strong suppression of hole spin freezing in LSCO thin-film samples.

The Néel temperatures as well as the magnetic volume fractions were determined from temperature scans in a weak magnetic field $\mathbf{B}_{\mathrm{ext}}$ applied perpendicular to the initial muon spin polarization and to the film surface. The asymmetry time spectra $AP_{\mathrm{wTF}}(t)$ in a wTF are described by

$$AP_{\mathrm{wTF}}(t) = A_{\mathrm{T}}^{\mathrm{TF}} \cos(\gamma_\mu B_{\mathrm{ext}} t + \phi)\, \mathrm{e}^{-(1/2)\sigma_{\mathrm{T}}^2 t^2} + A_{\mathrm{L}}^{\mathrm{TF}} \cos(\phi)\, \mathrm{e}^{-\lambda_{\mathrm{L}} t}. \tag{5}$$

Equation (5) represents the paramagnetic part of the muon-spin polarization. The superposition of the antiferromagnetic and the applied fields leads to a strong damping of the full polarization with a rate $\gtrsim 50\ \mu\mathrm{s}^{-1}$ which has been neglected in the fit. $A_{\mathrm{T}}^{\mathrm{TF}}$ and $A_{\mathrm{L}}^{\mathrm{TF}}$ are the transverse and longitudinal oscillation amplitudes. Above T_{N}, $A_{\mathrm{T}}^{\mathrm{TF}}$ is the full asymmetry, since only $\mathbf{B}_{\mathrm{ext}}$ is present. Below T_{N}, the superposition of the small external and the internal magnetic fields leads to a strong dephasing of the signal, so $A_{\mathrm{T}}^{\mathrm{TF}}$ decreases to a level corresponding to the nonmagnetic fraction plus the background level. $A_{\mathrm{L}}^{\mathrm{TF}}$ represents the part of nonprecessing muon spins. A decrease in $A_{\mathrm{T}}^{\mathrm{TF}}$ with a simultaneous increase in $A_{\mathrm{L}}^{\mathrm{TF}}$ demonstrates static magnetism. σ_{T} is the depolarization rate of the precessing muon fraction and reflects the field width observed by the muons in the nonmagnetic parts of the sample. At the lowest temperature it is dominated by the nuclear magnetic moments of La and Cu. The depolarization rate is $\lambda_{\mathrm{L}} \simeq 0$ for all measurements, and ϕ is the temperature-independent detector phase.

TABLE I. Values of the transition temperatures $T_{\mathrm{N,g}}$ and the corresponding magnetic volume fractions f for various nominal Sr contents x of LSCO thin films obtained from wTF μSR data.

x	$T_{\mathrm{N,g}}$ (K)	f (%)
0.00	195(3)	90(3)
0.01	151(5)	89(3)
0.02	37(7)	93(3)
0.03	25(2)	80(3)
0.045	9(2)	93(3)
0.06	7(1)	93(3)

The magnetic volume fraction f is given by

$$f = \frac{A_{\mathrm{T_{max}}}^{\mathrm{TF}} - A_{\mathrm{T_{min}}}^{\mathrm{TF}}}{A_{\mathrm{T_{max}}}^{\mathrm{TF}} - A_{\mathrm{bkg}}}, \tag{6}$$

taking into account a constant background asymmetry of $A_{\mathrm{bkg}} = 0.17(3) A_{\mathrm{T_{max}}}^{\mathrm{TF}}$ as in ZF measurements. The determined volume fractions are listed in Table I. The magnetic transition temperatures $T_{\mathrm{N,g}}$ were defined as the temperature for which

$$A_{\mathrm{T}}^{\mathrm{TF}}(T_{\mathrm{N,f,g}}) = \tfrac{1}{2}\left(A_{\mathrm{T_{max}}}^{\mathrm{TF}} + A_{\mathrm{T_{min}}}^{\mathrm{TF}}\right), \tag{7}$$

yielding $T_{\mathrm{N}}^{x=0.00} = 195(3)$ K (see Fig. 9) and $T_{\mathrm{N}}^{x=0.01} = 151(5)$ K. Both values are well below the respective bulk values of $T_{\mathrm{N}}^{x=0.00} \simeq 300$ K and $T_{\mathrm{N}}^{x=0.01} \simeq 250$ K (see Fig. 5). The relation between the normalized internal magnetic field $B_{\mathrm{loc}}(T)/B_{\mathrm{loc}}(0\ \mathrm{K})$ and the normalized temperature T/T_{N} can be analyzed using[7]

$$\frac{B_{\mathrm{loc}}(T)}{B_{\mathrm{loc}}(0\ \mathrm{K})} = \left[1 - \frac{T}{T_{\mathrm{N}}}\right]^{\beta}. \tag{8}$$

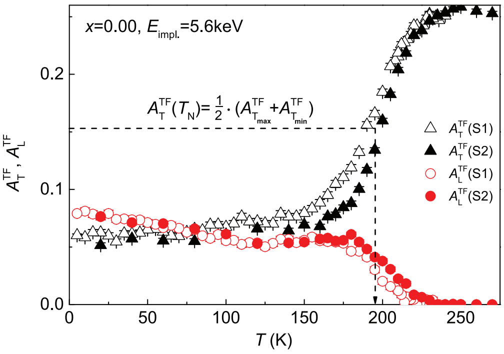

FIG. 9. (Color online) The transverse ($A_{\mathrm{T}}^{\mathrm{TF}}$) and longitudinal ($A_{\mathrm{L}}^{\mathrm{TF}}$) asymmetry as a function of T determined in an external magnetic field of $B_{\mathrm{ext}} = 2.9$ mT for $E_{\mathrm{impl}} = 5.6$ keV for two sets of LSCO thin-film samples (S1,S2) with $x = 0.00$. The dashed arrow shows how T_{N} was determined.

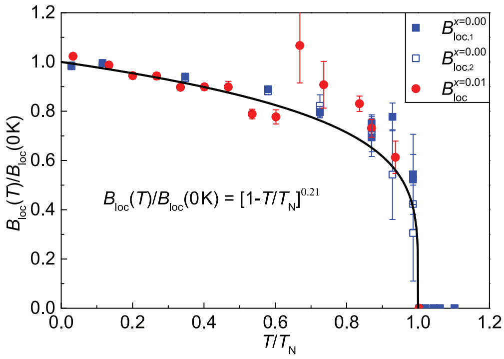

FIG. 10. (Color online) The normalized internal magnetic field $B_{\mathrm{loc}}(T)/B_{\mathrm{loc}}(0\text{ K})$ as a function of the normalized temperature T/T_N for LSCO thin films ($x = 0.00$ and $x = 0.01$). The solid black line corresponds to the power law given in Eq. (8) with $\beta = 0.21$ and $B_{\mathrm{loc},1}^{x=0.00}(0\text{ K}) = 41$ mT, $B_{\mathrm{loc},2}^{x=0.00}(0\text{ K}) = 11$ mT, and $B_{\mathrm{loc}}^{x=0.01}(0\text{ K}) = 36$ mT.

The obtained exponent β is similar for both Sr contents x as well as for $B_{\mathrm{loc},1}$ and $B_{\mathrm{loc},2}$, suggesting a common underlying ordering mechanism. The thin-film data are well described with $\beta = 0.21$ found in the bulk[7] (Fig. 10). Furthermore, the doping dependence of the normalized staggered magnetization $M^+(x,0\text{ K})/M^+(0,0\text{ K}) \propto B_{\mathrm{loc}}(x,0\text{ K})/B_{\mathrm{loc}}(0,0\text{ K})$ in the thin-film samples of the present work are in agreement with nuclear quadrupole resonance (NQR) and μSR results obtained for bulk samples[7] (Fig. 11). The staggered magnetization follows the empirical relation given in Ref. 7:

$$M^+(x,0\text{ K})/M^+(0,0\text{ K}) = \left[1 - \frac{x}{x_c}\right]^n, \qquad (9)$$

with a critical doping of $x_c = 0.0203$ and an exponent $n = 0.236$ (Fig. 11).

In summary, whereas in the AF phase of LSCO the generalized behavior of $B(T)/B(0\text{ K})$ as a function of x and T/T_N is similar in thin films and bulk samples (Figs. 10 and 11), T_N is strongly suppressed, and T_f is not observed down to 5 K in thin films. The local magnetic fields at the muon stopping site are instead very similar in bulk and thin films, indicating an equal magnitude of ordered electronic moments.

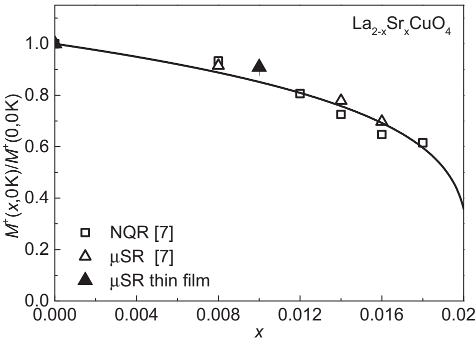

FIG. 11. The normalized staggered magnetization $M^+(x,0\text{ K})/M^+(0,0\text{ K})$ as a function of the nominal Sr content x of LSCO thin films (solid triangles) and LSCO bulk samples as inferred from NQR and μSR experiments (open symbols) given in Ref. 7. The black line is a fit to the bulk data using Eq. (9).

B. Disordered magnetic phase for $x \gtrsim 0.02$

In LSCO films with $x = 0.02$ and $x = 0.03$ the ZF asymmetry time spectra show an oscillation at the lowest temperatures [Figs. 12(c) and 12(e)], while the temperature dependence of B_{loc} given by Eq. (8) is changed drastically. The best fit to $B_{\mathrm{loc}}(T)$ for $x = 0.02$ yields $\beta = 0.04(2)$. Since $\beta \simeq 0.2$ is characteristic for the AF phase, samples with $x \gtrsim 0.02$ have to be instead in the peculiar low-temperature magnetic phase (Fig. 5), leading to ZF μSR precession too. This phase is termed in the literature as spin-glass or CSG phase.[4,6,8] Although somewhat misleading, we adopt this terminology for consistency with the literature. In the CSG phase dynamical spin and charge stripes have been found in some cuprate systems.[44,45] Microsegregation of mobile holes leads to hole-poor AF areas separated by hole-rich nonmagnetic domain walls. The presence of charge or spin density waves within the CSG phase is another proposed state.[46] At low temperatures the dynamics of the CSG state slow down and oscillations are observed in the ZF asymmetry time spectra in bulk samples.[8] For LSCO thin-film samples oscillations are observed at low temperatures too [Figs. 12(c) and 12(e)]. At 3 K the Bessel function [Eq. (4)] describes the obtained μSR data for $x = 0.02$ and $x = 0.03$ very well. This suggests the presence of incommensurate magnetism in the CSG phase as observed by neutron diffraction in bulk samples.[39]

For $x = 0.045$ and $x = 0.06$ the whole temperature scale is shifted down since $T_g \propto 1/x$. Therefore no ZF oscillations were observed down to 3 K [Figs. 12(h) and 12(k)]. The asymmetry time spectra at 3 K ($x = 0.045$) and 4.6 K ($x = 0.06$) show instead a strong double-exponential behavior (sum of two exponential functions) with considerably enhanced depolarization rates, as present at 20 K for $x = 0.02$ and $x = 0.03$. For $T \gtrsim T_g$ all asymmetry time spectra for $x \geqslant 0.02$ show an exponential decay [Figs. 12(g) and 12(j)], while for $T \gg T_g$ they are described by a Gaussian Kubo-Toyabe function [Figs. 12(a), 12(f), and 12(i)]. Therefore, the LSCO μSR spectra for all investigated samples show the same behavior, namely, a slowing down of electronic fluctuations in the PM phase.

From wTF μSR measurements the glass transition temperature T_g and the magnetic volume fraction f were determined for different x with the method described in the previous section [Eqs. (6) and (7)]. The corresponding values are listed in Table I. The present values of T_g are all significantly larger than those determined by bulk μSR[7,8] (see Fig. 5). This difference could not be ascribed to the method for determining T_g. If we define T_g in the same way as in Refs. 7 and 8 we obtain consistent values.

C. Discussion

What is the origin of the differences between the thin-film and the bulk phase diagrams? There are various potential

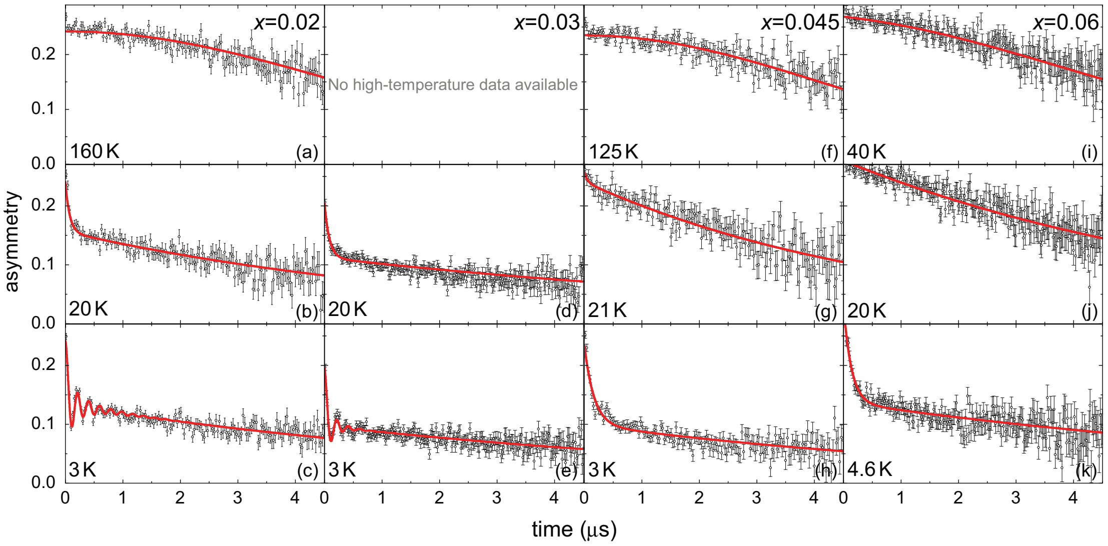

FIG. 12. (Color online) The ZF asymmetry time spectra of LSCO thin films with $x = 0.02$, 0.03, 0.045, and 0.06 at different temperatures as indicated for $E_{\text{impl}} = 5.6$ keV. The solid red lines are fits to the data done with MUSRFIT (Ref. 36). See text for more details.

mechanisms and parameters which may modify the phase diagram, such as oxygen off-stoichiometry, strain, geometric frustration, or defects.

Oxygen off-stoichiometry would indeed lead to an increase of doped holes in the CuO_2 planes and hence to a $x_{\text{eff}} > x$. This in turn would yield a lower T_N (Ref. 47) as found in this study (Fig. 5). However, at the same time T_f should increase, while T_g should decrease. This is the exact opposite to our observation. The case $x_{\text{eff}} > x$ is also unlikely, since B_{loc} is the same in bulk material and thin films (Figs. 11 and 13). Furthermore, the border between the AF and the CSG phase ($x \simeq 0.02$) is not shifted (Fig. 5). Additional interstitial oxygen in the films would expand the c-axis lattice parameter,[26] different to our observations: $c^{x=0.00} = 13.15(2)$ Å $= c^{\text{bulk}}$ (Fig. 2). In order to double-check the possible effects of the variations in oxygen stoichiometry, we postannealed two sets of LCO films in high vacuum, using two *different* procedures (temperature and time). Both sets show the same T_N and the same temperature dependence of the staggered magnetization. Therefore, oxygen off-stoichiometry is quite small and cannot be the dominant source of the differences between the bulk and the thin-film samples.

For undoped cuprates T_N is related to the interplane coupling constant J' and the 2D in-plane correlation length ξ_{2D} by

$$k_B T_N \simeq J'(m^+)^2 \left[\frac{\xi_{2D}(J,T_N,y)}{\alpha}\right]^2, \tag{10}$$

where α is the distance between the copper moments and m^+ is the reduced magnetic moment.[9,48,49] J' might be sensitive to strain, whereas ξ_{2D} is influenced by the in-plane coupling constant J (Ref. 50) and the amount of disorder y (Ref. 51). A reduction of J' and/or ξ_{2D} would lead to the observed decrease in T_N.

In the following possible strain effects will be discussed, assuming the absence of any disorder ($y = 0$). In this case ξ_{2D} is given by

$$\frac{\xi_{2D}(J,T_N,0)}{\alpha} = 0.567 \frac{J}{2\pi\rho_s} e^{2\pi\rho_s/k_B T_N} \left[1 - \frac{k_B T_N}{4\pi\rho_s}\right], \tag{11}$$

with a spin stiffness $2\pi\rho_s = 0.94J$ for LCO.[48,50]

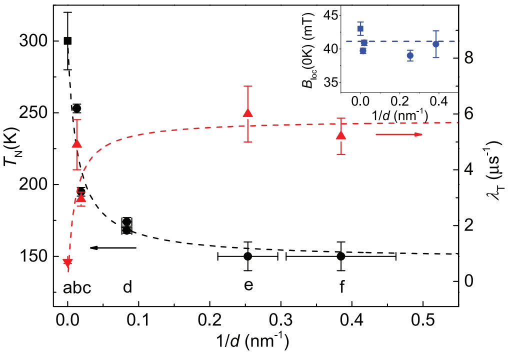

FIG. 13. (Color online) The Néel temperature T_N, the ZF depolarization rate λ_T, and the internal magnetic field $B_{\text{loc}}(0\text{ K})$ (inset) as a function of the inverse sample thickness $1/d$ for different LCO samples. The bulk thickness is set to infinity. The black, red, and blue dashed lines are guides to the eye. (a) LCO bulk material (Refs. 2 and 5–8); (b) LCO/STO thin film (unpublished); (c) present data; (d) LCO/STO and LCO/LSAO thin films (Ref. 27); (e) LCO/LSCO superlattices (Ref. 18); and (f) LCO/$LaAlO_3$ superlattices (unpublished).

Poisson strain is likely to modify J as well as J', because the lattice parameters are changed keeping the unit cell volume constant. When compared to its bulk value, the c axis is, in general, enlarged for LSCO grown on LSAO due to compressive strain of the substrate[52] (as long as the sample thickness is below the critical value of about 20 unit cells[26]), reducing J'. At the same time LCO grown on LSAO should exhibit a higher J because of the changed in-plane lattice constants [$J \propto 1/\alpha^{6.4}$ (Ref. 50)]. To reach the observed T_N, a $J'_{\text{film}} \approx 10^{-2} J'_{\text{bulk}}$ is required. Since the c-axis lattice constants of the films are very close to the bulk values, such a strong reduction of J' is unlikely. Thus, Poisson strain is not the main reason for the drastic T_N reduction.

In strain released LCO thin films the a and b lattice parameters differ from their bulk values[26] through Madelung strain, leading to a smaller unit cell volume as also obtained by applying hydrostatic pressure. Raman-scattering studies on AF single-crystal LCO[50] showed that pressure leads to an enhancement of J and therefore to an increase of T_N. Therefore, J and T_N should be also increased in LCO thin films. This is the opposite to our observations. A reduction of the Néel temperature through Madelung strain is therefore unlikely.

Geometrical frustration within a system may also influence the transition temperatures. A low asymmetry between the in-plane lattice constants $r = 1 - a/b$ could lead to a reduced J'. A tetragonal system ($r = 0$) consists of perfectly geometrically frustrated Cu electronic moments, since the CuO_2 layers within one unit cell are shifted by half a unit cell against each other [Fig. 7(a)]. A more orthorhombic system ($r \neq 0$) is less frustrated and exhibits a larger J'. In LCO thin films a lower in-plane lattice constants asymmetry is observed compared to bulk values:[26] $r_{\text{film}} = 0.001 < r_{\text{bulk}} = 0.01$. Thin films are hence more frustrated, which leads to a reduction of J', resulting in a lower T_N. But if geometrical frustration would be the main source of the reduced Néel temperature a similar system with $r = 0$ should have an even lower T_N because of a lower J'. $Sr_2CuCl_2O_2$ (SCCO) is such a system. It exhibits almost the same in-plane coupling constant ($J_{\text{SCCO}}/k_B = 1450\ \text{K} \approx J_{\text{LCO}}/k_B$), but at the same time a reduced Cu electronic magnetic moment [SCCO, $m_{\text{Cu}} = 0.31\mu_B$ (Ref. 53); LCO, $m_{\text{Cu}} = 0.645\mu_B$ (Ref. 41)]. Although SCCO is perfectly frustrated and $J'_{\text{SCCO}} \simeq 10^{-6} J < J'_{\text{LCO}} \simeq 10^{-5} J$ it shows a $T_N = 256$ K,[53] which is well above that observed for LCO thin films ($T_N = 195$ K, $d = 53$ nm). Even though geometrical frustration will lead to a reduction of T_N, the observed reduction is too substantial to originate from this source only.

What might influence the magnetic ground state as well are higher-order terms which are present in addition to the dominant superexchange, such as next-nearest-neighbor exchange. It has been shown that especially the DM interaction is very sensitive to the crystal symmetry,[42] which could naturally explain the spin re-orientation discussed in Sec. III A. However, it is unlikely that these higher-order corrections will have a substantial effect on T_N, T_f, or T_g as observed in this study.

Epitaxial thin films differ from the bulk samples by the presence of strain-induced defects, such as stacking faults and misfit dislocations. The latter have been observed in high-resolution cross-section transmission electron microscopy measurements in LCO films.[54] Typically, the defect density in stress released thin films is much higher compared to bulk samples. Depending on the nature of the defect, it can lead to charge trapping or pinning of collective modes such as charge stripes, charge density waves, or spin density waves (weak collective pinning in the case of point defects, or strong pinning in the case of dislocations), likely to be present at higher doping ($x \gtrsim 0.02$). This could indeed give rise to an increase of T_g as discussed by Shengelaya *et al.* (Ref. 55). This picture is also supported theoretically as discussed in Refs. 51 and 56 where the influence of short-length-quantum and long-range disorder on the spin-1/2 quasi-2D Heisenberg antiferromagnet on a square lattice (QHAF) is discussed. In Ref. 51 disorder by dilution is studied leading to an explicit expression for the reduction of T_N as a function of dilution, which was experimentally verified by Carretta *et al.* (Ref. 57). This dilution is likely to introduce also magnetic frustration which has been clarified by new experimental results by Carretta *et al.* (Ref. 58) and theoretically by Liu and Chernyshev (Ref. 59). Whereas disorder and/or frustration by dilution are directly applicable to Zn and Mg doping in LSCO, it is probably not the case for thin films for which misfit dislocations are the most likely source of disorder. Murthy[56] showed that a QHAF is much more sensitive to random fields than to moderate random in-plane couplings. Hence, misfit dislocations due to strain and strain release would have a much stronger influence on T_N as suggested in Ref. 51. Unfortunately, no quantitative expression for the reduction of T_N has been derived in Ref. 56. The measured ZF depolarization rates λ_T [Eq. (3)] support this interpretation. In Fig. 13 the Néel temperature T_N, the ZF depolarization rate λ_T, as well as the local magnetic field $B_{\text{loc}}(0\ \text{K})$ (inset) of LCO and LCO superlattices are plotted as a function of the inverse thickness $1/d$. While $B_{\text{loc}}(0\ \text{K})$ stays constant, T_N decreases with decreasing thickness d systematically. At the same time λ_T increases with decreasing d. The ZF depolarization rate λ_T is a measure of the magnetic disorder, which is related to the before-mentioned random fields.[56] According to theory[51,56] disorder leads to a reduction of T_N in agreement with Fig. 13. So disorder seems to be a probable mechanism which could explain consistently the differences in T_N and T_g of bulk and thin-film magnetic phase diagrams.

Extended LE-μSR studies of thin films with different thicknesses on the same substrate and thin films with the same thickness on different substrates, would be necessary to test the presented interpretations.

IV. SUMMARY AND CONCLUSIONS

In this study we determined the magnetic phase diagram of LSCO thin films (thickness 53 nm) in the doping range $0 \leqslant x \leqslant 0.06$. The absolute scales of the transition temperatures differ substantially between the bulk and thin-film samples. The Néel temperatures T_N are strongly reduced in the thin films and in the AF region no spin freezing is observed down to 5 K. The CSG transition temperatures T_g lie well above the corresponding bulk values. Oxygen off-stoichiometry and strain-induced changes of the lattice parameters or higher-order magnetic coupling constants are unlikely to explain the observed differences. Misfit dislocations through strain release might well be at the heart of the discovered effects. Overall, the thin-film and bulk samples exhibit similar magnitude, temperature, and doping dependence of the staggered magnetization and the same border between the AF and the CSG phase ($x \simeq 0.02$). The determined magnetic phase diagram provides a solid basis for future studies of multilayer and superlattice LSCO thin films.

ACKNOWLEDGMENTS

We gratefully acknowledge Hans-Peter Weber for his excellent technical support. This work was partly supported by the Swiss National Science Foundation. Research at Brookhaven was supported by the US Department of Energy, Basic Energy Sciences, Materials Sciences and Engineering Division.

---

[*] Present address: KTH Royal Institute of Technology, ICT Materials Physics, Electrum 229, 164 40 Kista, Sweden.

[†] Present address: Max Planck Institute for Solid State Research, Heisenbergstrasse 1, D-70569 Stuttgart, Germany.

[1] E. Dagotto, Rev. Mod. Phys. **66**, 763 (1994).

[2] M. A. Kastner, R. J. Birgeneau, G. Shirane, and Y. Endoh, Rev. Mod. Phys. **70**, 897 (1998).

[3] H. Sato, A. Tsukada, M. Naito, and A. Matsuda, Phys. Rev. B **61**, 12447 (2000).

[4] A. Rigamonti, P. Carretta, and N. Papinutto, Lect. Notes Phys. **684**, 351 (2006).

[5] J. H. Cho, F. C. Chou, and D. C. Johnston, Phys. Rev. Lett. **70**, 222 (1993).

[6] F. C. Chou, F. Borsa, J. H. Cho, D. C. Johnston, A. Lascialfari, D. R. Torgeson, and J. Ziolo, Phys. Rev. Lett. **71**, 2323 (1993).

[7] F. Borsa, P. Carretta, J. H. Cho, F. C. Chou, Q. Hu, D. C. Johnston, A. Lascialfari, D. R. Torgeson, R. J. Gooding, N. M. Salem, and K. J. E. Vos, Phys. Rev. B **52**, 7334 (1995).

[8] Ch. Niedermayer, C. Bernhard, T. Blasius, A. Golnik, A. Moodenbaugh, and J. I. Budnick, Phys. Rev. Lett. **80**, 3843 (1998).

[9] S. Chakravarty, B. I. Halperin, and D. R. Nelson, Phys. Rev. Lett. **60**, 1057 (1988); Phys. Rev. B **39**, 2344 (1989).

[10] B. Keimer, N. Belk, R. J. Birgeneau, A. Cassanho, C. Y. Chen, M. Greven, M. A. Kastner, A. Aharony, Y. Endoh, R. W. Erwin, and G. Shirane, Phys. Rev. B **46**, 14034 (1992).

[11] M. Matsumura, H. Yasuoka, Y. Ueda, H. Yamagata, and Y. Itoh, J. Phys. Soc. Jpn. **63**, 4331 (1994).

[12] D. M. Ginsberg, *Physical Properties of High Temperature Superconductors* (World Scientific, Singapore, 1989–1996).

[13] I. Božović, G. Logvenov, M. A. J. Verhoeven, P. Caputo, E. Goldobin, and M. R. Beasley, Phys. Rev. Lett. **93**, 157002 (2004).

[14] E. Morenzoni, B. M. Wojek, A. Suter, T. Prokscha, G. Logvenov, and I. Božović, Nat. Commun. **2**, 272 (2011).

[15] B. M. Wojek, E. Morenzoni, D. G. Eshchenko, A. Suter, T. Prokscha, H. Keller, E. Koller, Ø. Fischer, V. K. Malik, C. Bernhard, and M. Döbeli, Phys. Rev. B **85**, 024505 (2012).

[16] T. Prokscha, E. Morenzoni, K. Deiters, F. Foroughi, D. George, R. Kobler, A. Suter, and V. Vrankovic, Nucl. Instrum. Methods Phys. Res., Sect. A **595**, 317 (2008).

[17] E. Morenzoni, H. Luetkens, T. Prokscha, A. Suter, S. Vongtragool, F. Galli, M. B. S. Hesselberth, N. Garifianov, and R. Khasanov, Phys. Rev. Lett. **100**, 147205 (2008).

[18] A. Suter, E. Morenzoni, T. Prokscha, B. M. Wojek, H. Luetkens, G. Nieuwenhuys, A. Gozar, G. Logvenov, and I. Božović, Phys. Rev. Lett. **106**, 237003 (2011).

[19] A. V. Boris, Y. Matiks, E. Benckiser, A. Frano, P. Popovich, V. Hinkov, P. Wochner, M. Castro-Colin, E. Detemple, V. K. Malik, C. Bernhard, T. Prokscha, A. Suter, Z. Salman, E. Morenzoni, G. Cristiani, H.-U. Habermeier, and B. Keimer, Science **332**, 937 (2011).

[20] H. Sato and M. Naito, Physica C **274**, 221 (1997).

[21] J.-P. Locquet, J. Perret, J. Fompeyrine, E. Mächler, J. W. Seo, and G. Van Tendeloo, Nature (London) **394**, 453 (1998).

[22] W. Si, H.-C. Li, and X. X. Xi, Appl. Phys. Lett. **74**, 2839 (1999).

[23] I. Božović, G. Logvenov, I. Belca, B. Narimbetov, and I. Sveklo, Phys. Rev. Lett. **89**, 107001 (2002).

[24] W. Si and X. X. Xi, Appl. Phys. Lett. **78**, 240 (2001).

[25] M. Abrecht, D. Ariosa, D. Clotta, S. Mitrovic, M. Onellion, X. X. Xi, G. Margaritondo, and D. Pavuna, Phys. Rev. Lett. **91**, 057002 (2003).

[26] V. Y. Butko, G. Logvenov, N. Božović, Z. Radović, and I. Božović, Adv. Mater. **21**, 3644 (2009).

[27] A. Suter, J.-P. Locquet, E. Morenzoni, T. Prokscha, D. G. Eshchenko, N. Garifianov, R. Khasanov, H. Luetkens, and J. W. Seo, J. Magn. Magn. Mater. **272–276**, 110 (2004).

[28] E. Morenzoni, T. Prokscha, A. Suter, H. Luetkens, and R. Khasanov, J. Phys.: Condens. Matter **16**, S4583 (2004).

[29] I. Božović, IEEE Trans. Appl. Supercond. **11**, 2686 (2001).

[30] D. Lampakis, D. Palles, E. Liarokapis, C. Panagopoulos, J. R. Cooper, H. Ehrenberg, and T. Hartmann, Phys. Rev. B **62**, 8811 (2000).

[31] P. G. Radaelli, D. G. Hinks, A. W. Mitchell, B. A. Hunter, J. L. Wagner, B. Dabrowski, K. G. Vandervoort, H. K. Viswanathan, and J. D. Jorgensen, Phys. Rev. B **49**, 4163 (1994).

[32] Y. Ando, S. Komiya, K. Segawa, S. Ono, and Y. Kurita, Phys. Rev. Lett. **93**, 267001 (2004).

[33] A. Yaouanc and P. Dalmas de Réotier, *Muon Spin Rotation, Relaxation, and Resonance: Applications to Condensed Matter* (Oxford University Press, Oxford, 2011); V. P. Smilga and Yu. M. Belousov, *The Muon Method in Science* (Nova Science Publishers, Commack, 1994).

[34] D. R. Harshman, A. P. Mills, Jr., J. L. Beveridge, K. R. Kendall, G. D. Morris, M. Senba, J. B. Warren, A. S. Rupaal, and J. H. Turner, Phys. Rev. B **36**, 8850 (1987).

[35] W. Eckstein, *Computer Simulation of Ion-Solid Interactions* (Springer, Berlin, 1991).

[36] A. Suter and B. M. Wojek, Phys. Procedia **30**, 69 (2012).

[37] H. U. Suter, E. P. Stoll, and P. F. Meier, Physica B **326**, 329 (2003).

[38] M. Reehuis, C. Ulrich, K. Prokeš, A. Gozar, G. Blumberg, S. Komiya, Y. Ando, P. Pattison, and B. Keimer, Phys. Rev. B **73**, 144513 (2006).

[39] K. Yamada, C. H. Lee, K. Kurahashi, J. Wada, S. Wakimoto, S. Ueki, H. Kimura, Y. Endoh, S. Hosoya, G. Shirane, R. J. Birgeneau, M. Greven, M. A. Kastner, and Y. J. Kim, Phys. Rev. B **57**, 6165 (1998).

[40] D. Vaknin, S. K. Sinha, D. E. Moncton, D. C. Johnston, J. M. Newsam, C. R. Safinya, and H. E. King, Jr., Phys. Rev. Lett. **58**, 2802 (1987).

[41] R. Pozzi, M. Mali, D. Brinkmann, and A. Erb, Phys. Rev. B **60**, 9650 (1999).

[42] D. Coffey, T. M. Rice, and F. C. Zhang, Phys. Rev. B **44**, 10112 (1991).
[43] R. Hord, H. Luetkens, G. Pascua, A. Buckow, K. Hofmann, Y. Krockenberger, J. Kurian, H. Maeter, H.-H. Klauss, V. Pomjakushin, A. Suter, B. Albert, and L. Alff, Phys. Rev. B **82**, 180508 (2010).
[44] J. M. Tranquada, B. J. Sternlieb, J. D. Axe, Y. Nakamura, and S. Uchida, Nature (London) **375**, 561 (1995).
[45] A. Bianconi, N. L. Saini, A. Lanzara, M. Missori, T. Rossetti, H. Oyanagi, H. Yamaguchi, K. Oka, and T. Ito, Phys. Rev. Lett. **76**, 3412 (1996).
[46] D. H. Torchinsky, F. Mahmood, A. T. Bollinger, I. Božović, and N. Gedik, Nat. Mater. **12**, 387 (2013).
[47] B. O. Wells, Y. S. Lee, M. A. Kastner, R. J. Christianson, R. J. Birgeneau, K. Yamada, Y. Endoh, and G. Shirane, Science **277**, 1067 (1997).
[48] P. Hasenfratz and F. Niedermeyer, Phys. Lett. B **268**, 231 (1991).
[49] S. Chakravarty and R. Orbach, Phys. Rev. Lett. **64**, 224 (1990).
[50] M. C. Aronson, S. B. Dierker, B. S. Dennis, S.-W. Cheong, and Z. Fisk, Phys. Rev. B **44**, 4657 (1991).
[51] Y.-C. Chen and A. H. Castro Neto, Phys. Rev. B **61**, R3772 (2000).
[52] A. Tsukada, T. Greibe, and M. Naito, Phys. Rev. B **66**, 184515 (2002).
[53] M. Greven, R. J. Birgeneau, Y. Endoh, M. A. Kastner, B. Keimer, M. Matsuda, G. Shirane, and T. R. Thurston, Phys. Rev. Lett. **72**, 1096 (1994).
[54] J. He, R. F. Klie, G. Logvenov, I. Božović, and Y. Zhu, J. Appl. Phys. **101**, 073906 (2007).
[55] A. Shengelaya, Guo-meng Zhao, C. M. Aegerter, K. Conder, I. M. Savić, and H. Keller, Phys. Rev. Lett. **83**, 5142 (1999).
[56] G. Murthy, Phys. Rev. B **38**, 5162 (1988).
[57] P. Carretta, A. Rigamonti, and R. Sala, Phys. Rev. B **55**, 3734 (1997).
[58] P. Carretta, G. Prando, S. Sanna, R. De Renzi, C. Decorse, and P. Berthet, Phys. Rev. B **83**, 180411(R) (2011).
[59] S. Liu and A. L. Chernyshev, Phys. Rev. B **87**, 064415 (2013).

5.4 Photo-induced effects on the magnetic state

The influence of light on the electrical properties of LCO where first studied by Thio et al. [19] in 1990. The illumination of LCO single crystals with pulsed and continuous light leads to transient photoconductivity. The determined recombination time exceeds 10 s at room temperature. The photoconductance per square normalized to the photon flux is increased by about four orders of magnitude above a photon energy of 2 eV. Therefore, this energy was identified as the threshold for charged excitations.

The intent of the present study was to characterize the temperature and intensity dependence more precisely, and to have a closer look on the relaxation behavior with the help of additional resistance measurements. Furthermore, the study was extended to Sr doped samples to investigate the interplay between intrinsically doped and photo-doped charge carriers. The influence of illumination on the magnetic state was studied by LE-μSR in addition to clarify if the photo-excited charge carriers have a similar effect as the Sr doping, meaning reducing the Néel temperature.

5.4.1 Resistance measurements

To study the photo-induced effect on the parent compound LCO, three different samples were investigated. First measurements where performed with a 76 nm thick thin film grown by pulsed laser deposition (PLD) on $SrTiO_3$ (STO) at the University of Fribourg. The results were compared to two samples of the LCO set grown on LSAO by MBE in Brookhaven, having a thickness of 53 nm.

The photo-induced changes in resistivity R were determined at different temperatures. First, the samples were kept at a defined temperature for half an hour, to reach equilibrium and to obtain the dark conductivity $\sigma_{\mathrm{dark}} = 1/(c \cdot R_0)$ with the conversion factor c [107, 108]. Afterwards the Bluepoint LED was switched on for a defined time. From the change in resistivity the corresponding photoconductivity is calculated:

$$\sigma_{\mathrm{photo}} = \sigma_{\mathrm{light\ on}} - \sigma_{\mathrm{dark}} = \frac{1}{\rho_{ab,\mathrm{on}}} - \frac{1}{\rho_{ab,0}} = \frac{R_0 - R_{\mathrm{on}}}{c \cdot R_0 \cdot R_{\mathrm{on}}}. \tag{5.2}$$

After switching off the light the resistivity was tracked for an hour to study the relaxation before stabilizing the next temperature. A typical characteristic of the influence of illumination on the resistance R for LCO grown on STO is shown in Fig. 5.5.

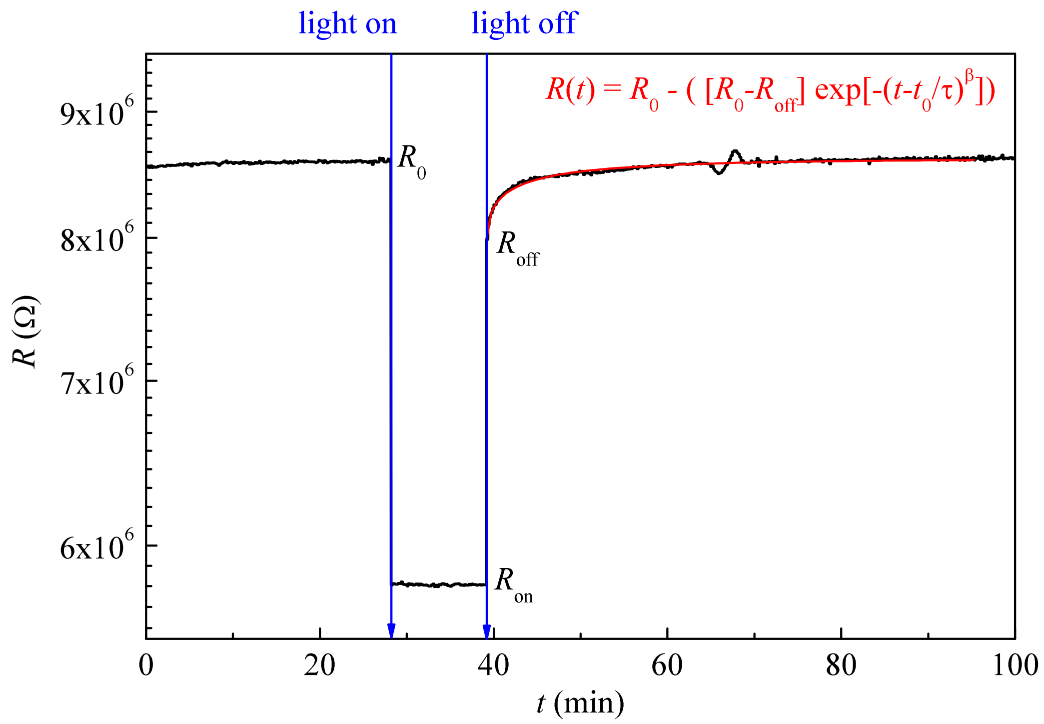

Figure 5.5: Resistance R versus time t of LCO grown on STO at 100 K. The blue arrows indicate at which time the light was switched on and off, respectively. The relaxation after switching the light off was fitted with a stretched exponential function (red line, formula given in the figure) with fixed t_0, R_0, R_{off} and $\beta = 0.5$. The relaxation time was determined to be $\tau = 198\,\mathrm{s}$.

When the light is switched on the resistance drops within one second from R_0 to R_{on}. During illumination it stays basically constant, indicating that an equilibrium between the creation of electron-hole pairs and their recombination is reached. If the creation of electron-hole pairs slightly dominates the resistance further decreases. This small reduction in R_{on} is taken into account when determining the error of the photoconductivity σ_{photo}. Due to small temperature variations R_0 also exhibits experimental uncertainty.

After switching off the light a large fraction of the electron-hole pairs recombine instantly, meaning within our time resolution of 1 s. The remaining fraction $R_0 - R_{\mathrm{off}}$ slowly relaxes back on timescales of several hundreds of seconds. The relaxation to the initial value R_0 could be described by a stretched exponential function:

$$R(t) = R_0 - \left([R_0 - R_{\mathrm{off}}] \exp \left[- \left(\frac{t - t_0}{\tau} \right)^{\beta} \right] \right), \tag{5.3}$$

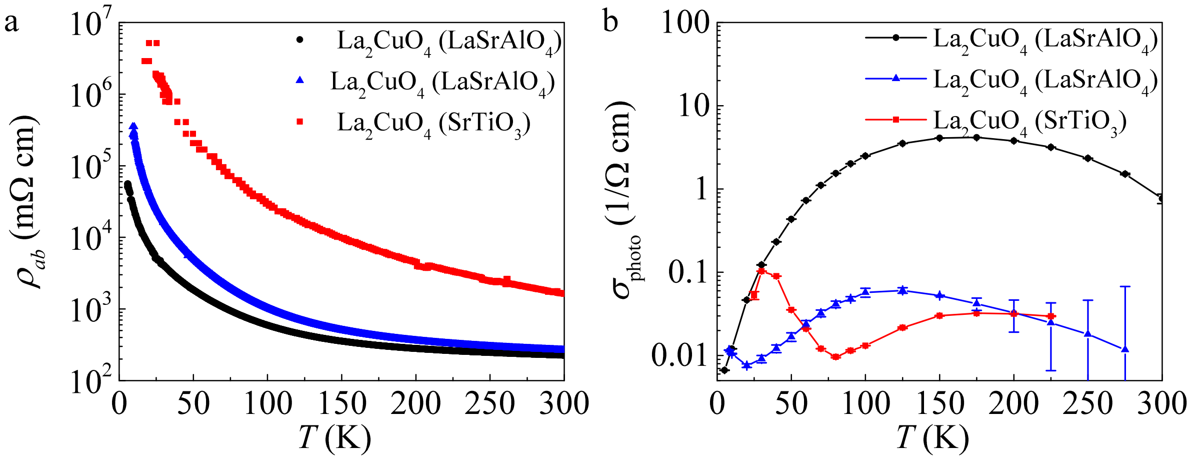

Figure 5.6: Resistivity ρ_{ab} (a) and the photoconductivity σ_{photo} (b) versus temperature T for a PLD grown thin film with STO as substrate (red squares) and for two MBE grown thin films with LSAO as substrate (black circles and blue triangles).

where the light was switched off at t_0 and τ gives the time scale of the relaxation. The exponent β describes how strong the relaxation deviates from an exponential behavior. The fits at different temperatures revealed exponents in the range $0.2 - 0.8$ and relaxation times in the range $10 - 420$ s without any systematic trend. If β is fixed to 0.5, τ still does not show a systematic trend as function of temperature, but it did vary only between $100 - 400$ s.

The calculated photoconductivity σ_{photo} varies strongly between the different LCO samples, as shown in Fig. 5.6b. Fig. 5.6a presents the temperature dependence of the in-plane resistivity ρ_{ab}. Since the PLD film is thicker compared to the MBE grown ones, the conversion factor from resistance to resistivity is $c(\text{PLD}) = 0.004296\,\text{m}\Omega\,\text{cm}/\Omega$, only slightly different to $c(\text{MBE}) = 0.00616\,\text{m}\Omega\,\text{cm}/\Omega$. The higher resistivity for this sample could be due to a higher defect density present in PLD grown films, as indicated by a higher ZF depolarization rate found by μSR measurements, as discussed in the previous section. A strong variation in σ_{photo} between different LCO samples was also observed by Thio *et al.* [19]. The photoconductivity depends on the quantum efficiency η, the average mobility μ, the average lifetime of the photocarriers τ and the incident photon flux F:

$$\sigma_{\text{photo}} \propto \eta\,\mu\,\tau\,F. \tag{5.4}$$

The intensity of the bluepoint LED was kept constant, so that F is identical for all investigated samples at all temperatures. The maximum in σ_{photo} could result from the temperature dependence of the charge carrier mobility, which exhibits a maximum at about 140 K [111]. Furthermore, τ shortens with increasing temperature. At higher temperatures the electrons are less trapped due to temperature fluctuations, leading to an increase of the recombination rate. When the electron-hole pairs exist for shorter times, the resulting equilibrium state exhibits a much lower photoconductivity. So a reduced τ additionally decreases σ_{photo} at $T > 100\,\text{K}$. The quantum efficiency depends mainly on the photon energy, which was kept constant within this study [19].

For LCO grown on STO, the shape of the photoconductivity as function of temperature is substantially distinct from that one of LCO on LSAO. The photoconductivity exhibits a minimum at about 80 K and a maximum at about 30 K. The difference to the other LCO samples could result from additional excited charge carriers from the substrate. The STO substrate shows an anomalous photoconductivity [112, 113]. The resistivity under light illumination strongly drops below 100 K and show anomalies below 60 K. Since the light penetration depth is expected to be of the order of 100 nm, a strong influence of the substrate for LCO grown on STO is probable.

In the case of LCO grown on LSAO, the photoconductivity increases up to $100 - 170\,\text{K}$. At higher temperatures it decreases with temperature. This observation agrees with the measurements of Thio *et al.* [19] on single crystals, who observed a maximum in σ_{photo} at about 100 K. Therefore, we exclude a contribution of the LSAO substrate although photo-induced voltages have been observed in LSAO single crystals [114].

A bolometric effect, caused by the high intensity of the light source, could be excluded too. In the case of a heating of the sample the photoconductivity would follow the temperature dependence of the conductivity. This is not the case for the samples of the present study. In previous energy-dependent measurements bolometric heating was only observed for low photon energies in agreement with our results.

The strong differences in the photoconductivity of different LCO thin films may arise from slightly different oxygen contents between the investigated samples or could be due to oxygen atoms occupying interstitial sites, reducing conductivity and σ_{photo}. Since the oxygen concentration seems to have a strong influence on the electrical properties reproducibility of the results is difficult.

Still the data show some conclusive findings. The illumination time has no significant influence on the value of the photo-induced changes in resistance, as presented in Fig. 5.7. The temperature dependences of the change in resistivity for illumination times of 1 min, 10 min and 60 min agree within experimental uncertainty. Also the fraction of resistance,

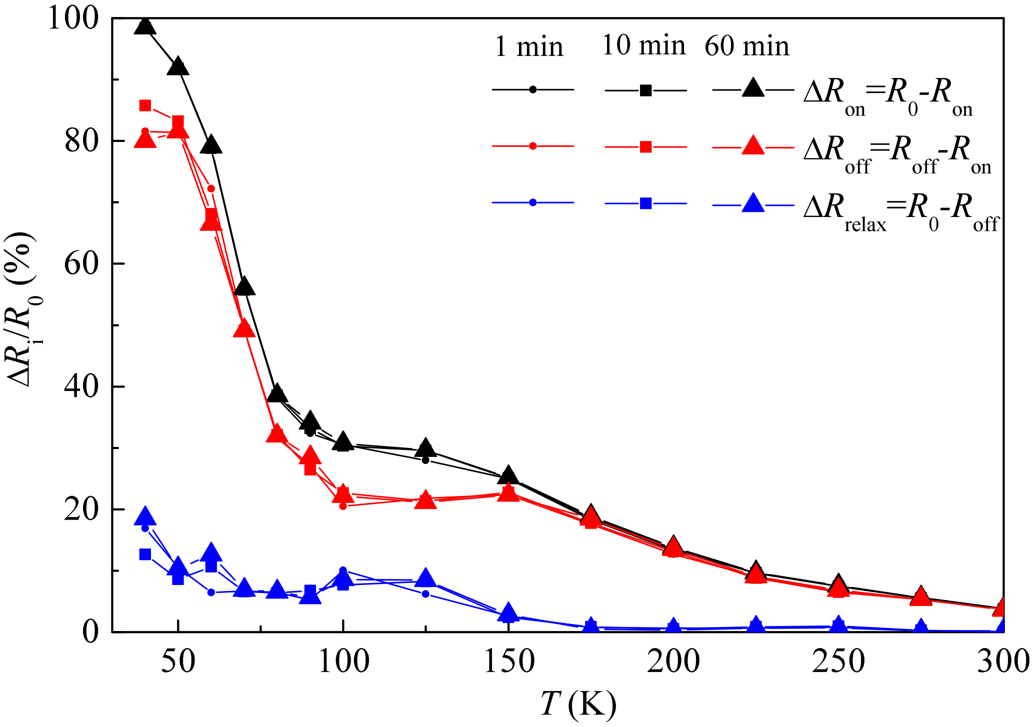

Figure 5.7: Resistivity change when switching the light on ΔR_{on}, when switching the light off ΔR_{off} and during the relaxation after illumination ΔR_{relax} versus temperature T for LCO grown on STO.

which is immediately recovered after switching of the light, does not change with longer light exposure.

If holes are doped into the system (by adding Sr) the normalized photo-induced conductivity decreases at all temperatures, as shown in Fig. 5.8a. It is calculated as:

$$\frac{\sigma_{\text{photo}}}{\sigma_{\text{dark}}} = \frac{\sigma_{\text{light on}} - \sigma_{\text{dark}}}{\sigma_{\text{dark}}} = \frac{\frac{1}{\rho_{ab,\text{on}}} - \frac{1}{\rho_{ab,0}}}{\frac{1}{\rho_{ab,0}}} = \frac{R_0 - R_{\text{on}}}{R_{\text{on}}}. \tag{5.5}$$

As more Sr is introduced to the system the photo-induced effect gets weaker in relation to the initial conductivity. The trend of the temperature dependence itself does not change by adding Sr. The largest changes in the normalized photoconductivity are observed at the lowest temperatures.

The absolute change of the photoconductivity σ_{photo} instead shows an opposite behavior. At $T < 50\,\text{K}$ $(1/T > 0.02\,\text{K}^{-1})$, σ_{photo} is higher for samples with a higher nominal Sr content x. Since the mobility in LSCO increases with x [115] this is expected, but not to

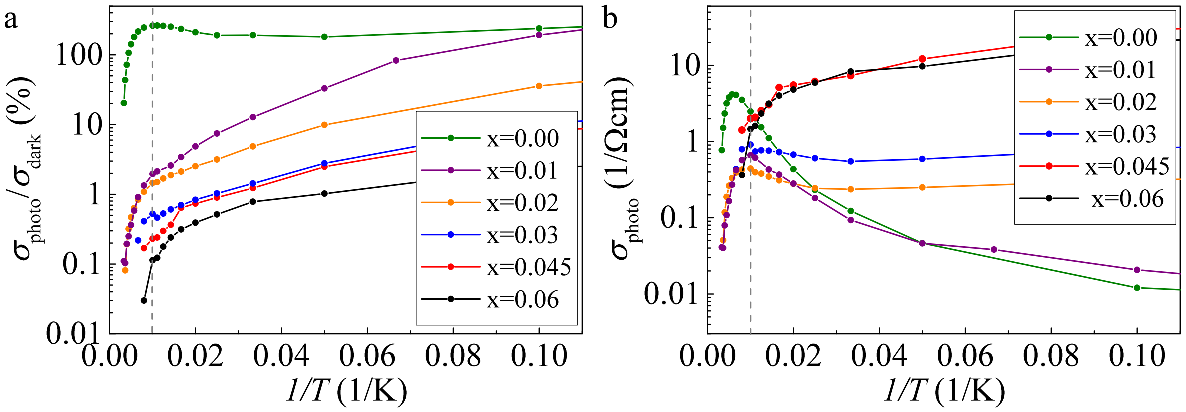

Figure 5.8: The normalized photoconductivity $\sigma_{\text{photo}}/\sigma_{\text{dark}}$ (a) and the photoconductivity σ_{photo} (b) versus the inverse temperature $1/T$ for LSCO thin-film samples with different nominal Sr contents x. The solid lines are guides to the eye and the dashed lines assign $T = 100\,\text{K}$.

that extent. The lifetime of the charge carriers seems not to be decreased by the presence of additional charge carriers. Surprisingly, the photoconductivity is of the same order for all samples at about 100 K. A maximum in $\sigma_{\text{photo}}(T)$, as observed in LCO around 100 K, is only present for $0.00 \leq x \leq 0.03$. The temperature of $\sigma_{\text{photo}_{\text{max}}}$ does not coincide with the minimum in resistivity. At higher temperatures the photoconductivity strongly decreases for all doping levels. This agrees with the interpretation, that the electrons could not be trapped very well above 100 K, leading to a much faster recombination time for all LSCO samples at higher temperatures. As obvious from Fig. 5.8, a simple thermal activation model ($\sigma_{\text{photo}} \propto \tau \propto \mathrm{e}^{E_\Delta/k_\mathrm{B}T}$ [19]) cannot describe the data.

The presented measurements were all performed with an intensity of $200\,\text{mW/cm}^2$. A reduction of the intensity allowed us to study the intensity dependence. The mathematical description of the intensity dependence of σ_{photo} is difficult, because the determined upper limit of the photoconductivity is arbitrary. If we look instead on the change in resistivity systematic trends are identified. In Fig. 5.9 the intensity scans for different doping levels x at different temperatures T are presented. The obtained change in resistivity as function of the intensity is phenomenologically well described by a stretched exponential function:

$$\frac{R_0 - R_{\text{on}}}{R_0} = 1 - \exp\left[-\left(\frac{I}{I_{\text{sat}}}\right)^{\alpha}\right],$$

where I_{sat} gives a scale at which intensity 63 % of the maximum possible change in R is reached ($[R_0 - R_{\text{on}}]/R_0 = 1 - 1/e$). The exponent α had to be added since the change in

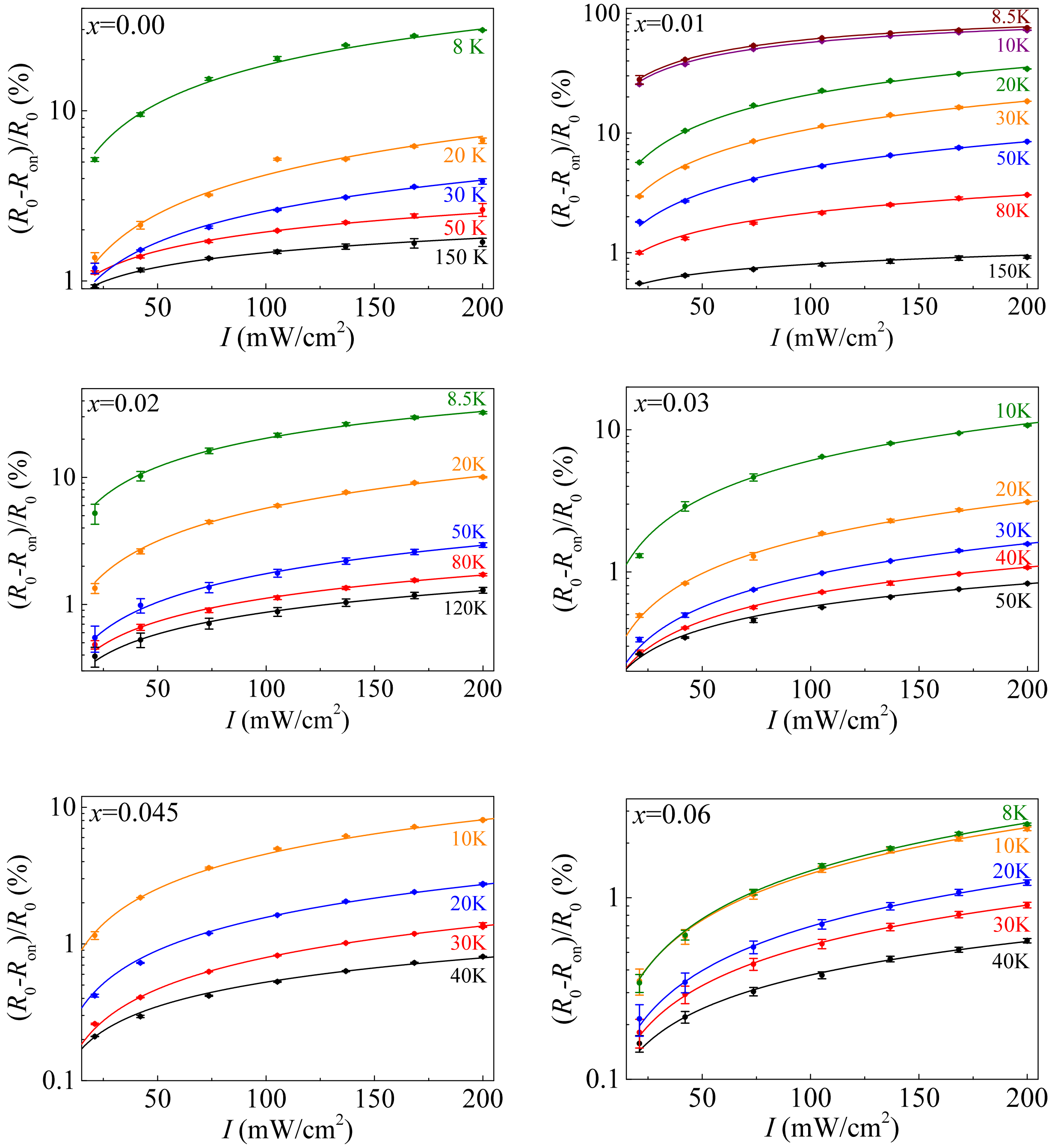

Figure 5.9: Change in resistance $\Delta R_{\mathrm{on}}/R = (R - R_{\mathrm{on}})/R$ as function of intensity I for different temperatures T at different doping levels x of $\mathrm{La}_{2-x}\mathrm{Sr}_x\mathrm{CuO}_4$. The lines are fits to the data using $\Delta R_{\mathrm{on}}/R = 100\%(1 - \exp(I/I_{\mathrm{sat}})^{\alpha})$.

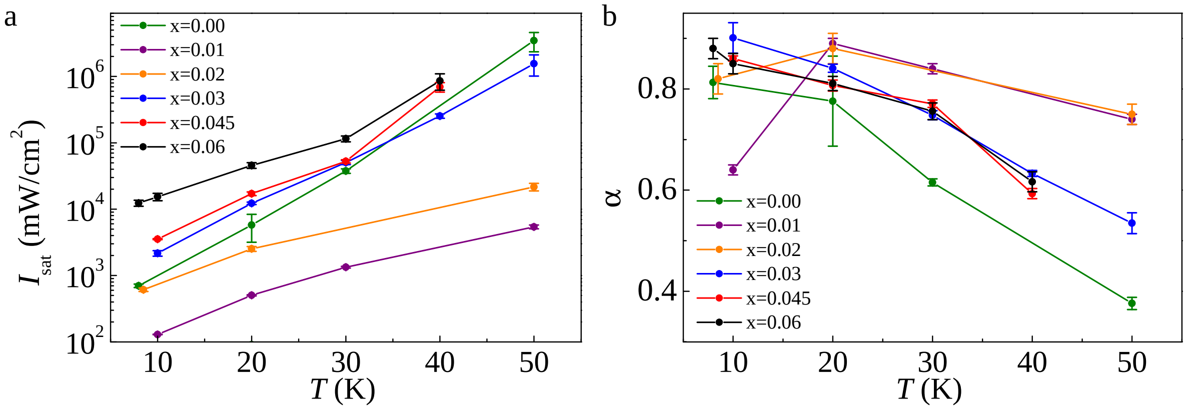

Figure 5.10: Saturation intensity I_{sat} (a) and fitting parameter α (b) versus temperature T for different doping level x of $La_{2-x}Sr_xCuO_4$.

R strongly deviates from an exponential growth.

At all doping levels the parameter I_{sat} depends on temperature, as depicted in Fig. 5.10a. This is in agreement with the previous results. At higher temperatures more photons are necessary to obtain the same change in resistivity in the equilibrium state, since the recombination times of the created electron-hole pairs are shorter. The exponent α varies between 0.3 and 0.9 in all investigated samples. It decreases systematically with increasing temperature, but does not show a trend as function of the Sr content x (see Fig. 5.10b).

The photo-induced conductivity of LSCO reveals a delicate interplay between recombination mechanisms and charge carrier mobility. The role of the quantum efficiency is still an open issue. Especially in the LCO samples the dynamics of the oxygen and the small changes in its content have a strong influence on the resulting photoconductivity, whereas the influence is less pronounced in the doped compound.

5.4.2 μSR results

The LE-μSR measurements were performed at 20 K in ZF with a muon implantation energy of $E_{\text{impl}} = 5.6$ keV on the thin-film sample set with a Sr content of $x = 0.01$. Since a change in resistivity was only observed during light illumination, the μSR spectra were taken during a longer illumination period to see if changes appear. As presented in Fig. 5.11, a local magnetic field of $B_{\text{loc}}(20\,\text{K}) = 36.3(4)$ mT was observed before illumination, in agreement with previous measurements [99]. When the light is switched on, additional charge carriers are created. If the photo-doped charge carriers act in the same way as Sr doping does, a lower magnetic field value is expected from the empirical law of the staggered magnetization M^+ observed by Borsa et al. [99]:

$$\frac{B_{\mathrm{loc}}(x, 0\,\mathrm{K})}{B_{\mathrm{loc}}(0, 0\,\mathrm{K})} = \frac{M^+(x, 0\,\mathrm{K})}{M^+(0, 0\,\mathrm{K})} = \left[1 - \frac{x}{x_{\mathrm{c}}}\right]^n, \tag{5.6}$$

here $x_{\mathrm{c}} = 0.0203$ is the critical doping level and the exponent n was determined to be 0.236. The LE-μSR spectra taken at 5.5 h of illumination shows instead a local magnetic field of $B_{\mathrm{loc}}(20\,\mathrm{K}) = 37.4(5)\,\mathrm{mT}$, not significantly higher than the dark value. Also no illumination time dependence of B_{loc} was observed, as depicted in Fig. 5.12c, in agreement with the resistivity measurements. Using Equation 4.6 for fitting the ZF spectra, no significant changes are observed in the transverse and longitudinal asymmetry $A_{\mathrm{T/L}}$ and in the corresponding depolarization rates $\lambda_{\mathrm{T/L}}$, as shown in Fig. 5.12a+b. Thus, the created electron-hole pairs do not effect the local magnetic field, the planar Cu electronic spin configuration and the magnetic field distribution.

This could be due to the short recombination times, requiring much higher illumination intensities to implant enough additional charge carriers. Assuming small changes in the

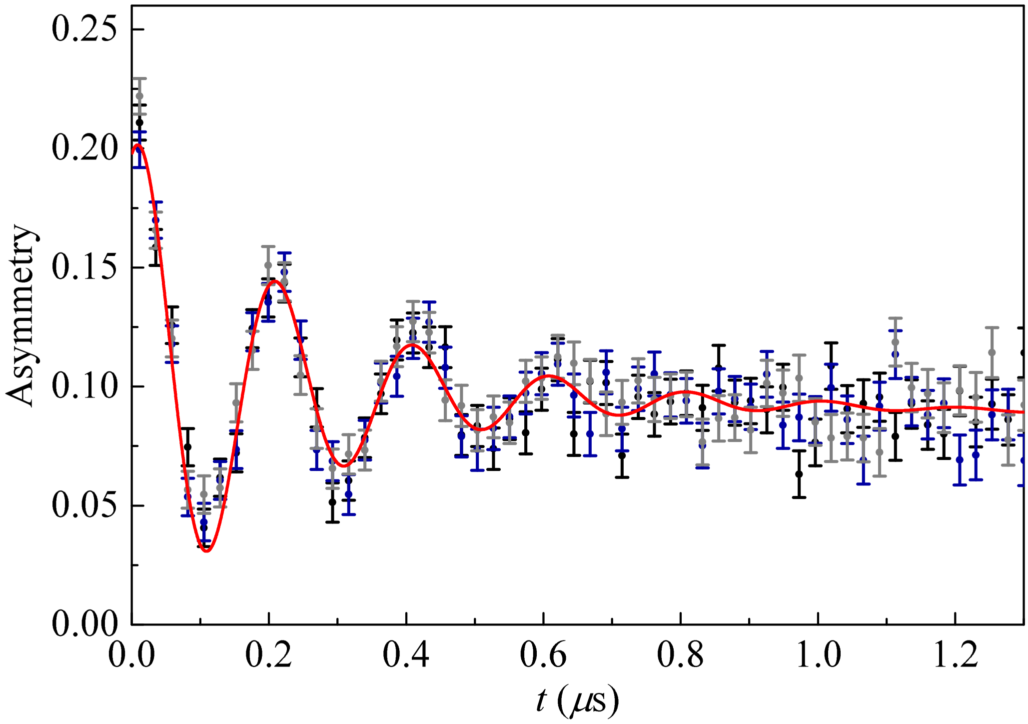

Figure 5.11: LE-μSR asymmetry time spectra for LSCO with $x = 0.01$ before (black) and under illumination (blue and gray) at 20 K in ZF with $E_{\mathrm{impl}} = 5.6\,\mathrm{keV}$. The solid lines are fits to the data obtained with the MUSRFIT program [116].

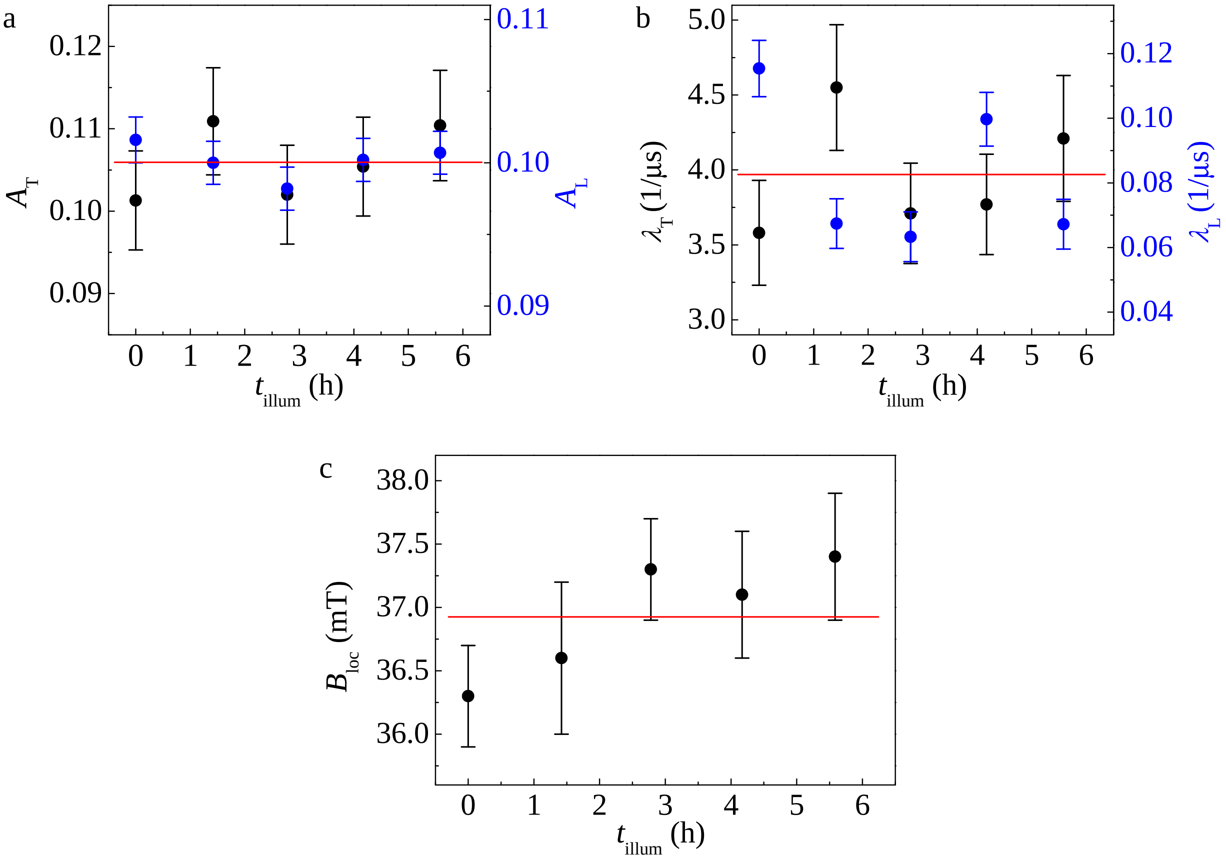

Figure 5.12: Transverse/longitudinal asymmetry $A_{\mathrm{T/L}}$ (a), transverse/longitudinal depolarization rate $\lambda_{\mathrm{T/L}}$ (b) and the local magnetic field B_{loc} (c) present at the muon stopping site as function of the illumination time t_{illum} for $\mathrm{La}_{2-x}\mathrm{Sr}_x\mathrm{CuO}_4$ with $x = 0.01$ determined in zero magnetic field using Eq. 4.6.

doping level x, Eq. 5.6 yields

$$\frac{\Delta B}{\Delta x} \approx \frac{\partial B}{\partial x} = -B_{\mathrm{loc}}(0, 0\,\mathrm{K}) \cdot \left[1 - \frac{x}{x_{\mathrm{c}}}\right]^{n-1} \cdot \frac{n}{x_{\mathrm{c}}}. \tag{5.7}$$

The determined average depolarization rate of $\lambda_{\mathrm{T}} \simeq 4\,\mu\mathrm{s}^{-1}$ (Fig. 5.12b) corresponds to a magnetic field width of about 4.7 mT. To resolve a change in the local magnetic field it has to be shifted by more than $\Delta B = 2.4\,\mathrm{mT}$. According to this field shift the change in the doping x is

$$\Delta x = \frac{\Delta B}{B_{\mathrm{loc}}(0, 0\,\mathrm{K})} \cdot \left[1 - \frac{x}{x_{\mathrm{c}}}\right]^{1-n} \cdot \frac{x_{\mathrm{c}}}{n} = 3 \cdot 10^{-3}, \tag{5.8}$$

using $B_{\mathrm{loc}}(0, 0\,\mathrm{K}) = 40.9\,\mathrm{mT}$ and $x = 0.01$.

To induce 0.003 holes per Cu-atom within the unit cell (about 10^{18} holes/cm^3 at 20 K) in our sample volume of $V = 1\,\mathrm{cm}^2 \cdot 53\,\mathrm{nm} = 3 \cdot 10^{16}$ unit cells, about 10^{14} charge carriers have to be created by illumination. From the change in resistivity only a $\Delta x = 0.0006$ (about 10^{13} holes) is obtained, although we used an intensity of 80 mW/cm^2 (corresponding to 10^{17} implanted photons per second per cm^2). This leads to the conclusion that we need about 10^4 photons to create one contributing charge carrier and that the rest of the created charge carries recombine within 1 s. So we need a much higher intensity to resolve a change in the magnetic field. Therefore, we are far away from the necessary conditions.

In conclusion, the magnetic state of LSCO can not be tuned by photo-induced charge carriers. The created dynamic electron-hole pairs do not introduce magnetic disorder as observed with the LE-μSR experiments.

6 Low-energy μSR Studies of $YBa_2Cu_3O_{6+x}$

$YBa_2Cu_3O_{6+x}$ (YBCO) is until today, together with $Bi_2Sr_2CaCu_2O_{8+x}$, the most promising high temperature superconductor with respect to applications, e.g. as power cable. The properties of YBCO strongly depend on the oxygen content and, more specifically, on the oxygen order. Due to changes in the oxygen order, the superconducting properties of YBCO could be improved in thin films by adding Au nanoparticles or generally in YBCO by illumination. Photo persistent conductivity in YBCO was observed first in 1990 [21, 117], but little is known about the length scale on which the electrical properties change. In this chapter the YBCO compound is introduced, followed by a description of the preparation of YBCO thin films as well as of single crystals. LE-μSR experiments are presented, investigating the microscopic changes in YBCO due to Au nanoparticles and visible light illumination.

6.1 The $YBa_2Cu_3O_{6+x}$ compound

$YBa_2Cu_3O_{6+x}$ is one of the cuprates which exhibits (with $T_{\mathrm{c,max}} \approx 94\,\mathrm{K}$) a critical temperature above the boiling temperature of nitrogen (77 K). The YBCO system is driven from an antiferromagnetic insulator to a superconductor by varying the oxygen content x as depicted in Fig. 6.1. In the range $0.3 \leq x \leq 0.4$ YBCO is in the cluster spin glass state at low temperatures, common for cuprate systems (see Chapter 2). Zero-field μSR [118] and neutron scattering studies [119] revealed a static incommensurate magnetic order with the propagation vector along the a-axis. This inhomogeneous magnetic order appears close to the metal-insulator transition and survives within the superconducting region [118]. The dependence of the critical temperature T_{c} on the number of doped holes p is described very well by the universal parabolic function given in Chapter 2 (see dashed purple line in Fig. 6.1). At a doping around $p = 1/8$ the observed T_{c} is below this parabolic relation. This flat region with $0.6 \leq x \leq 0.67$ is referred to as the "60 K plateau". Its origin is still controversial. One possible explanation of this deviation is the formation of charge stripes [120], which compete with superconductivity. The charge stripes result from an unidirectional microscopic segregation of doped holes, leading to a modulation of the charge density along one lattice direction [121]. Another proposed interpretation connects

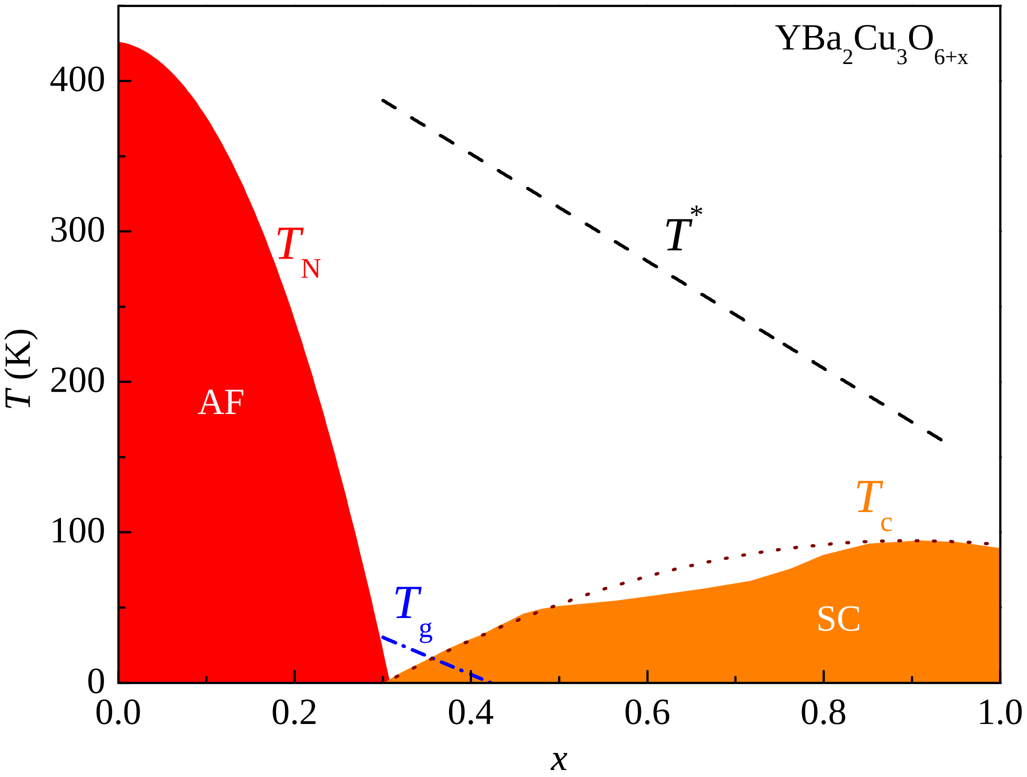

Figure 6.1: Schematic phase diagram of $YBa_2Cu_3O_{6+x}$ as function of the nominal oxygen content $6 + x$: AF - antiferromagnetic phase (red) with the Néel temperature T_N, spin freezing transition temperature T_CSG (blue dash-dotted line), SC - superconducting phase with the critical temperature T_c, and the pseudogap temperature T^* (black dashed line).

the reordering of the oxygen in the CuO_x layers with this anomaly in T_c, which will be discussed later in detail. It assumes a constant valence state of the Cu ions and therefore a constant hole concentration within the 60-K plateau [120].

As other cuprates YBCO exhibit a pseudogap in the excitation spectrum, discussed in detail in Chapter 2. This crossover is indicated with the dashed line.

The YBCO structure, shown in Fig. 6.2, differs compared to most of the other cuprates. Besides two CuO_2 planes the unit cell consists of CuO_x layers with a variable oxygen content x. At low x the oxygen atoms in the CuO_x layers are isolated, so that their p orbitals are full [123]. Thus, mainly O^{-2} states are present in the CuO_x layers. Therefore, YBCO exhibits a disordered tetragonal crystal structure and it is insulating for $x < 0.3$. At an oxygen content of $x \approx 0.3$ Cu-O chains form along the crystallographic b axis, leading to an orthorhombic structure. Due to the transformation of O^{-2} states into O^{-1} states

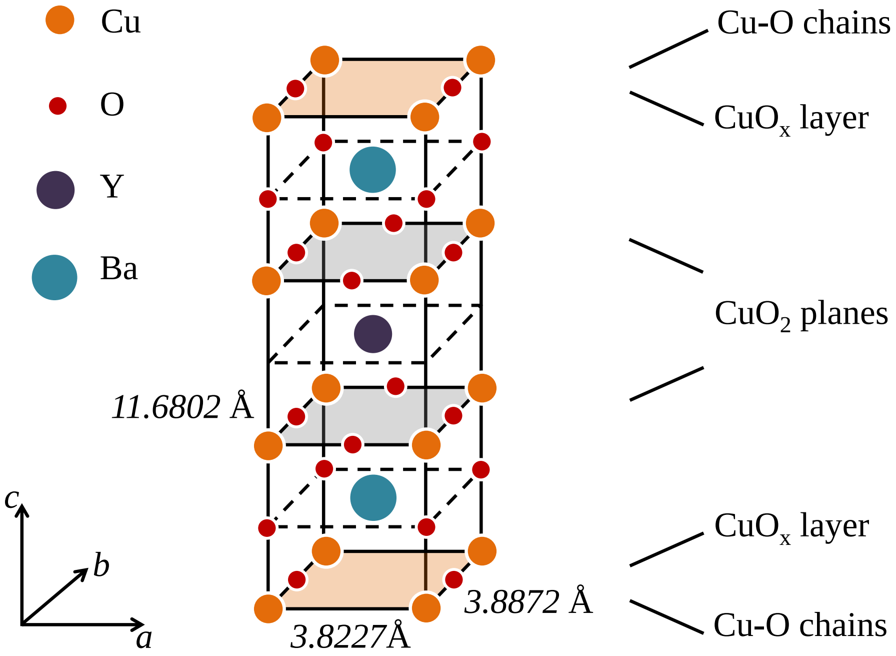

Figure 6.2: Crystal structure of $YBa_2Cu_3O_{6+x}$. The lattice parameters of orthorhombic optimally doped YBCO [122] are given in the figure. CuO_2 planes are marked in gray whereas the CuO_x layers, where the Cu-O chains form, are colored in orange.

the p-orbitals are only partially filled. Therefore, localized holes are formed in the CuO_x layers. If the Cu-O chains exceed a critical length l_{cr} electrons from the CuO_2 planes are transferred to the Cu-O chains, hence doping the CuO_2 planes with mobile holes. The system turns metallic. The number of transferred holes is proportional to the average chain length, meaning the number of oxygen atoms within the Cu-O chain. A longer average chain length leads to a higher conductivity and to higher T_{c} [124]. Consequently, the oxygen ordering also influences the relation $p(x)$. Above $x = 0.3$ the relation is close to linear, as indicated with the red dashed line in Fig. 6.3, but it is not unique. For well ordered chains p is higher for the same x value. In the tetragonal phase the values of p are strongly reduced due to the absence of Cu-O chains.

Within the orthorhombic structure different sequences of empty Cu and full Cu-O chains appear depending on the oxygen content x and the temperature as observed by electron microscopy techniques (see Fig. 6.3). The superstructures are labeled according to the periodicity along the a axis as ortho-I, ortho-II, ortho-III, ortho-V and ortho-VIII. In the

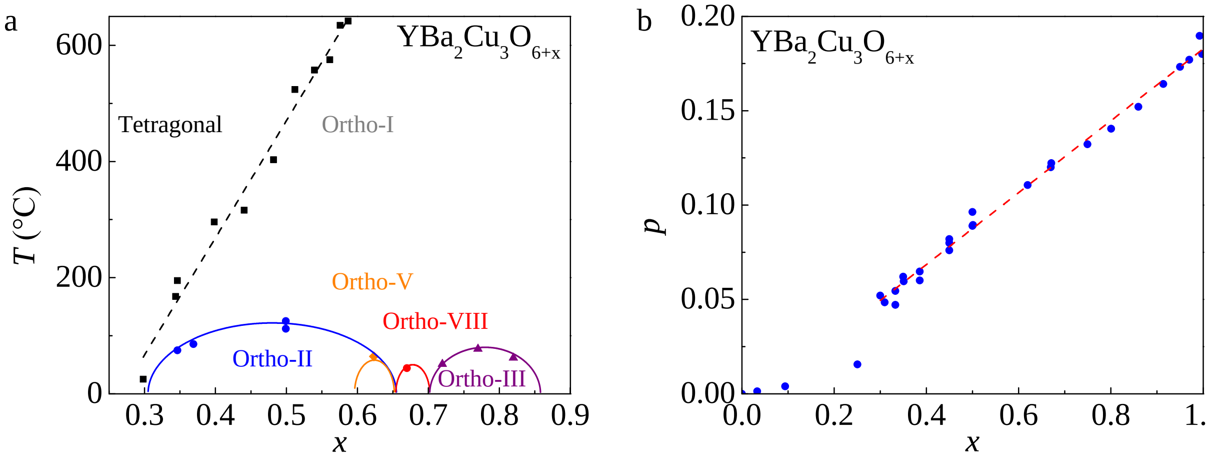

Figure 6.3: Structural phase diagram (a) and the hole concentration p within the CuO_2 planes (b) as function of oxygen content x of $YBa_2Cu_3O_{6+x}$ (from Refs. [125, 126]). The lines are guides to the eye.

ortho-I structure only filled Cu-O chains are present, empty and full chains alternate in the stable ortho-II phase, while the sequences of ortho-III, ortho-V, and ortho-VIII are more complicated. All the superstructures exhibit short-range order due to the formation of twin domains [125]. Only the ortho-I, orhto-II as well as the tetragonal phase are equilibrium states.

From the complicated structure of YBCO, it is concluded that the detailed superconducting properties are very sensitive to crystal defects, especially to the oxygen ordering. Slow oxygen-ordering kinetics at room temperatures have to be taken into account when investigating the YBCO system.

6.2 Sample preparation and characterization of $YBa_2Cu_3O_{6+x}$

The $YBa_2Cu_3O_{6+x}$ thin films were deposited on single crystal $1 \times 1\,\mathrm{cm}^2$ (001) $SrTiO_3$ (STO) substrates by on-axis pulsed laser deposition from a stoichiometric target using a KrF excimer laser ($\lambda = 248\,\mathrm{nm}$). They were prepared at the Institute for Metallic Materials (IFW Dresden) and for the Au nanoparticle study at the Friedrich-Schiller University in Jena (detailed description of this samples in the next section). A detailed description of the PLD technique and the growth of oxygen-deficient YBCO thin films is given in Refs. [127–129]. To grow YBCO layers with a thickness of 400(20) nm and 490(60) nm, 3000 and 4800

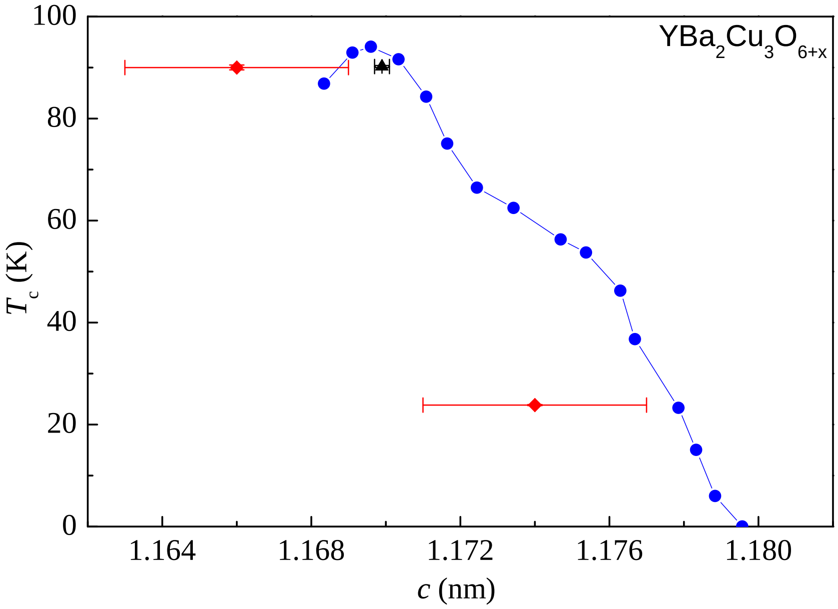

Figure 6.4: Critical temperature T_c as function of the c-axis lattice constant for YBCO crystals (blue dots, from Ref. [126]), and YBCO thin-film samples (red diamonds - IFW Dresden, black triangle - Jena). The YBCO thin-film samples with $T_\mathrm{c} \approx 90\,\mathrm{K}$ are optimally doped.

laser pulses with a laser repetition rate of 5 Hz were used under an oxygen partial pressure of 0.3 mbar. After deposition at 800 °C, the samples were cooled to 780 °C, where the chamber was flooded with 400 mbar oxygen to achieve fully oxidized films with a $T_\mathrm{c} = 90.0(5)\,\mathrm{K}$. The sample thicknesses were determined by counting the YBCO layers at chemical etched edges, ranging from the surface to the substrate, using atomic force microscopy. To check the homogeneity of the samples the thickness was measured at several points. To determine the oxygen content we used the experimentally obtained relation between T_c and x given in Ref. [126] (orange in Fig. 6.1).

The reduction of the oxygen content was realized by a post-annealing process in a tubular furnace [130]. In particular, the samples were annealed at a defined time and temperature in a flowing O_2/N_2 gas mixture. The process was concluded with a rapid cooling step to temperatures below 100 °C in order to freeze in the oxygen concentration of the thin films. Annealing of the 400 nm thick samples at 450 °C for 40 min in 2860 ppm O_2 atmosphere reduced the T_c of the YBCO sample to 66.7(8) K (corresponding to $x = 0.67$). The 490 nm thick films with $T_\mathrm{c} = 21(2)\,\mathrm{K}$ ($x = 0.42$) were annealed for 70 min at 500 °C in a 215 ppm O_2 atmosphere. In order to determine T_c, resistivity measurements were performed with a four-point measurement on a cold finger cryostat in ultra high vacuum under the same

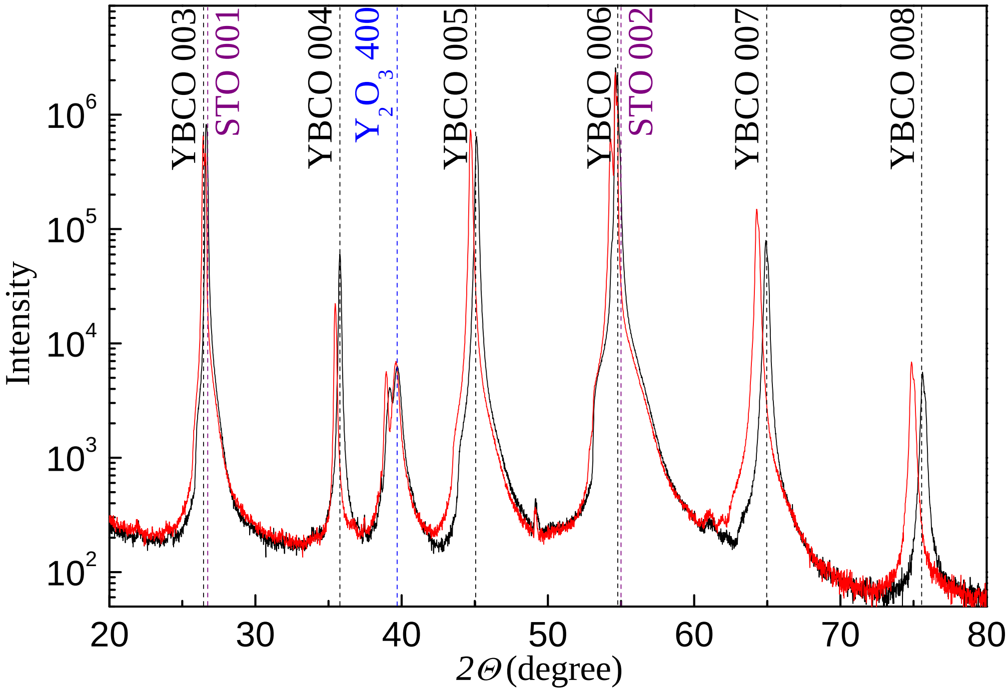

Figure 6.5: $\Theta - 2\Theta$ XRD pattern obtained from the underdoped YBCO sample YZ4 before (black, optimal doping) and after oxygen annealing (red, $x = 0.42$): YBCO reflections (black dashed lines), STO reflections (purple dashed lines), and Y_2O_3 reflections (blue dashed line) are marked.

conditions used for the μSR experiments (details are given in Section 6.4).

Purely c-axis oriented growth of YBCO was verified by $\Theta - 2\Theta$ measurements at the IFW Dresden using a Bruker D8 Advance X-ray powder diffractometer with a Co anode. The determined c-axis lattice constants are lower compared to the bulk values before and after temperature annealing as shown in Fig. 6.4. This seems not to be common for thin-film YBCO samples grown on STO, since the tendency is reversed in the YBCO samples prepared at the Friedrich-Schiller University in Jena. The $\Theta - 2\Theta$ spectra revealed the presence of a Y_2O_3 phase within all samples (see Fig. 6.5). The result agrees with the Rutherford backscattering spectrometry (RBS) measurements performed at ETH Zürich. If the RBS spectra are normalized to the Ba and Cu peaks, the YBCO samples have an excess of Y and O, eg. sample YZ6 with $x = 6.42$ has the following stoichiometric composition:

- Y: $1 + 0.30(5)$
- Ba: $2 - 0.01(8)$
- Cu: $3 + 0.01(12)$
- O: $6.42 + 1.7(8)$

Within the first $100 - 150\,\mathrm{nm}$ from the surface, a reduction of the Ba content and an increase of the Y content could be identified towards the vacuum interface.

The investigated YBCO ortho-VIII single crystals were grown at the University of British Columbia by the self-flux technique described in detail in Ref. [131]. For the growth, $BaZrO_3$ ceramic crucibles were fabricated. After the self-flux growth the YBCO crystals were annealed in flowing oxygen for six days at 648 °C, to set the oxygen content to $x = 0.67$. Afterwards the crystals were sealed in a quartz tube and annealed at 570 °C for four days to homogenize the oxygen. During detwinning, the sample is heated to $180 - 250\,^\circ\mathrm{C}$ and squeezed with a pressure of about 100 MPa along one of the a/b axes under flowing nitrogen gas, causing the twin domains to reorient so that the a-axis (which has a shorter lattice constant) is along the direction of the pressure. For the formation of the oxygen vacancy ordered superstructure ortho-VIII, the YBCO single crystals were low temperature annealed at $40 - 42\,^\circ\mathrm{C}$ for five days. The final YBCO ortho-VIII single crystals had an estimated critical temperature of $T_\mathrm{c} \simeq 66.5(5)\,\mathrm{K}$. One year later a $T_\mathrm{c} = 67.8(5)\,\mathrm{K}$ was determined with a *Quantum Design* MPMS SQUID magnetometer. The increase of T_c of about 1 K with time is natural in these crystals and is even expected, as the chain oxygens slowly become better ordered even at room temperature and some of the interstitial oxygen impurities enter the Cu-O chains. For the present μSR experiments a set of 13 crystals with the same annealing history were used.

6.3 Influence of Au nanoparticles in superconducting $\mathrm{YBa_2Cu_3O_{6+x}}$

The quality of thin-film samples is usually strongly influenced on the amount of disorder as discussed for the LSCO thin films before. Adding of Au nanoparticles showed improved superconducting properties in YBCO thin films. The transition temperature T_c and the critical current density j_c are increased. While the higher j_c can be explained by a stronger pinning of the flux vortices at the Au nanoparticles, the enhanced T_c is still an open issue. To investigate the microscopic changes due to the Au nanoparticles, LE-μSR measurements have been performed in the Meissner state of optimally doped $\mathrm{YBa_2Cu_3O_{7-\delta}}$ thin films. To monitor the distribution of the Au nanoparticles within the thin film Rutherford backscattering spectrometry (RBS) experiments, carried out at the ETH Zürich, were performed. The average magnetic penetration depth λ_{ab} was found to decrease in the films containing Au nanoparticles, but its temperature dependence stays the same. In summary, we have shown by using LE-μSR that the increase of T_c in thin-film YBCO containing Au nanoparticles is accompanied by an increase of the superfluid density $n_\mathrm{s} \propto 1/\lambda_\mathrm{L}^2$. This could be originated by a lowering of the defect density due to a nucleation of defects at the Au nanoparticles. The diffusion of Au into the Cu-O chains may also contribute to the observed changes of T_c and n_s. When Cu is exchanged by Au within the Cu-O chains of YBCO single crystals, T_c is enhanced. The results indicate that Au nanoparticles have a similar effect in thin-film YBCO.

Details on this work are published in:

E. Stilp, A. Suter, T. Prokscha, Z. Salman, E. Morenzoni, H. Keller, C. Katzer, F. Schmidl, and M. Döbeli, *Modifications of the Meissner screening profile in* $YBa_2Cu_3O_{7-\delta}$ *thin films by gold nanoparticles*, Phys. Rev. B **89**, 020510(R) (2014).

URL: http://journals.aps.org/prb/abstract/10.1103/PhysRevB.89.020510

DOI: 10.1103/PhysRevB.89.020510

PACS: 74.78.-w, 74.62.Dh, 76.75.+i, 82.80.Yc

RAPID COMMUNICATIONS

PHYSICAL REVIEW B **89**, 020510(R) (2014)

Modifications of the Meissner screening profile in $YBa_2Cu_3O_{7-\delta}$ thin films by gold nanoparticles

E. Stilp,[1,2] A. Suter,[1] T. Prokscha,[1] Z. Salman,[1] E. Morenzoni,[1] H. Keller,[2] C. Katzer,[3] F. Schmidl,[3] and M. Döbeli[4]

[1]*Laboratory for Muon Spin Spectroscopy, Paul Scherrer Institut, CH-5232 Villigen PSI, Switzerland*
[2]*Physik-Institut der Universität Zürich, Winterthurerstrasse 190, CH-8057 Zürich, Switzerland*
[3]*Institut für Festkörperphysik, Friedrich-Schiller-Universität, Helmholtzweg 5, D-07743 Jena, Germany*
[4]*Laboratory of Ion Beam Physics, ETH-Zürich, Schafmattstrasse 20, CH-8093 Zürich, Switzerland*

(Received 29 November 2013; revised manuscript received 8 January 2014; published 28 January 2014)

Adding Au nanoparticles to $YBa_2Cu_3O_{7-\delta}$ thin films leads to an increase of the superconducting transition temperature T_c and the critical current density j_c. While the higher j_c can be understood in terms of a stronger pinning of the flux vortices at the Au nanoparticles, the enhanced T_c is still puzzling. In the present study, we determined the microscopic magnetic penetration profiles and the corresponding London penetration depths λ_L in the Meissner state of optimally doped $YBa_2Cu_3O_{7-\delta}$ thin films with and without Au nanoparticles by low-energy muon spin rotation. By Rutherford backscattering spectrometry, we show that the Au nanoparitcles are distributed over the whole thickness of the thin-film samples. The superfluid density $n_s \propto 1/\lambda_L^2$ was found to increase in the films containing Au nanoparticles. We attribute this increase of n_s to a reduction of the defect density possibly due to defect condensation at the Au nanoparticles.

DOI: 10.1103/PhysRevB.89.020510 PACS number(s): 74.78.−w, 74.62.Dh, 76.75.+i, 82.80.Yc

The influence of disorder on cuprate systems is still an open issue. It is known that disorder directly affects the superconducting properties of these systems, but the underlying mechanisms are not fully clarified [1]. In $YBa_2Cu_3O_{7-\delta}$ (YBCO), for instance, the charge carrier transfer from the Cu-O chains to the CuO_2 planes is crucial for the appearance of superconductivity. This charge transfer depends strongly on the oxygen order and on the oxygen mobility within the Cu-O chains [2]. Substitution of chain Cu by other metal ions leads generally to a suppression of the superconducting transition temperature T_c [3]. Surprisingly, this does not apply to Au. Superconducting quantum interference device (SQUID) and neutron diffraction measurements performed by Cieplak *et al.* [4,5] show that it is possible to incorporate 10 at.% Au into the structure of polycrystalline YBCO, where Au exclusively replaces the chain Cu(1) atoms. This leads to an increase of T_c of about 1.5 K and to an increase of the *c*-axis lattice constant. The Cu-O bond length between Cu(1) and the oxygen in the Cu-O chains as well as between Cu(1) and the bridging oxygen are enlarged. Previous studies revealed also a lower normal state resistance and a minor influence on the normal state magnetization and on the upper critical field [6].

Recently, it has been demonstrated that Au nanoparticles, incorporated in YBCO thin films, lead to an increase of T_c and the critical current density j_c (from 4×10^7 A/cm^2 to 6×10^7 A/cm^2 at 10 K) [7,8]. Since YBCO is superconducting above the boiling temperature of nitrogen this is of special interest for applications. A stronger flux pinning of the vortices at the Au nanoparticles causes a higher j_c, which is crucial in order to improve superconducting magnetic field sensors [8,9] as used in dc-SQUID gradiometers.

Until now, little is known about the effect of the inclusion of Au nanoparticles on the microscopic superconducting parameters, such as the superfluid density n_s. In the present study, we investigated two sets of YBCO thin films with different Au contents by means of low-energy muon spin rotation (LE-μSR) experiments and Rutherford backscattering spectrometry (RBS). The amount and the distribution of the Au nanoparticles were determined as well as the microscopic changes of the Meissner screening profile and the London penetration depth λ_L. This is of special interest, since λ_L is related to the superfluid density n_s:

$$\lambda_L^2 \propto \frac{m^*}{n_s}, \qquad (1)$$

where m^* is the effective mass of the supercarriers.

The optimally doped YBCO thin films studied in this work were prepared by pulsed-laser-deposition (PLD) using a KrF excimer laser ($\lambda = 248$ nm, $\tau = 25$ ns) at the Friedrich-Schiller-Universität in Jena. Single-crystal $SrTiO_3$ $10 \times 10 \times 1$ mm^3 in size and polished with the surface perpendicular to the [001] crystal axis was used as substrate. In order to realize clustered Au nanoparticles, an initial gold seed layer of 1.8-nm thickness was sputtered on the substrates by dc-magnetron sputtering ($I = 10$ mA, $U = 215$ V, growth rate: 4 nm/min, $p_{Ar} = 5$ mbar). Subsequently, the Au coated substrates were heated to 780°C to achieve a dewetting of the Au seed layer. The resulting nanoparticles were overgrown by YBCO in an *in situ* process. The YBCO deposition was realized by a PLD process in an oxygen atmosphere (repetition rate: 5 Hz, laser fluence: 2.2 J/cm^2, growth rate: 20 nm/min, $p_{O_2} = 0.5$ mbar). In order to obtain the orthorhombic phase, the resulting YBCO thin films were cooled down to room temperature at a rate of 50 K/min in pure oxygen ($p_{O_2} = 800$ mbar). The resulting optimally doped YBCO thin films have a typical thickness of 120–200 nm and are *c*-axis oriented. With the Au seed layer thickness used the typical Au particle size is in the range 10–40 nm [8]. The area distribution of the Au nanoparticles is quite homogeneous, whereas the concentration within the depth profile varies, as later discussed. More details on the growth and the properties of the used samples can be found in Refs. [7] and [8]. The mean distance between the Au nanoparticles is about 50 nm. The samples are therefore still in the clean limit, since the correlation length is of the order of 2 nm.

Here, we studied two sample sets with ($YBCO_{Au}$) and without (YBCO) Au nanoparticles. As expected, slightly higher T_c values were observed by resistivity measurements

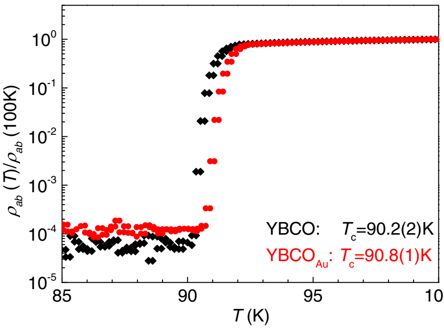

FIG. 1. (Color online) In-plane resistivity ρ_{ab} normalized at 100 K vs temperature T of PLD-grown optimally doped YBCO thin-film samples: YBCO (black diamonds) and YBCO$_{\mathrm{Au}}$ (red circles). The listed values of the superconducting transition temperatures T_{c} are defined by $\rho_{ab}(T_{\mathrm{c}})/\rho_{ab}(100\ \mathrm{K}) \leqslant 2.5 \times 10^{-4}$. They are averaged over five measurement cycles (heating and cooling).

for the YBCO$_{\mathrm{Au}}$ compared to the pristine YBCO thin-film samples (see Fig. 1). In order to monitor precisely the amount as well as the distribution of Au as a function of depth in the thin-film samples, RBS measurements were performed at ETH Zürich. For RBS, a ^{4}He beam with an energy of 2–5 MeV and a silicon PIN diode detector at a scattering angle of 168° were used [10]. The elemental composition was determined by using the RUMP software [11]. In the YBCO samples no Au peak is present in the RBS spectra as expected. The stoichiometry of optimally doped YBCO was confirmed within experimental uncertainty. The Au concentrations as function of depth were determined in the YBCO$_{\mathrm{Au}}$ samples as depicted in Fig. 2. In these samples the Au nanoparticles are distributed over the whole superconducting region. On average there are about $4(1) \times 10^{15}$ Au atoms/cm^2 in this region. The so-called dead layer close to the substrate interface d_{DL} contains less nanoparticles and exhibits no macroscopic Meissner screening. This is consistent with the lower T_{c} generally observed in this region in these thin-film samples [12].

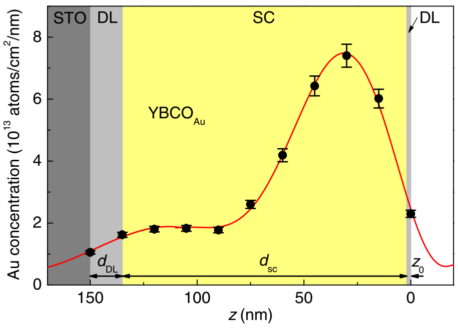

FIG. 2. (Color online) Gold concentration vs depth z along the crystallographic c axis for a YBCO$_{\mathrm{Au}}$ thin-film sample determined by RBS. The different regions are labeled: STO is the substrate region (dark gray), DL is the dead layer at the substrate (d_{DL}) and the vacuum (z_0) interface (light gray), SC is the superconducting region with thickness d_{sc} (yellow). The red line is a guide to the eye.

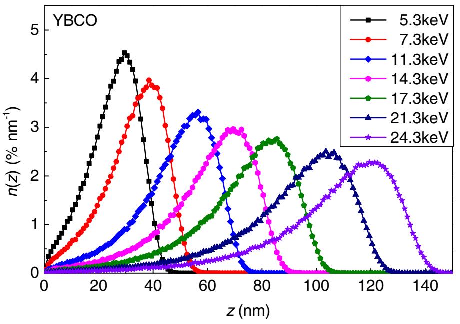

FIG. 3. (Color online) The normalized stopping distribution of positively charged muons $n(z)$ for different implantation energies (see inset) of a 150-nm-thick YBCO film simulated with TRIM.SP [15]. The lines are guides to the eye.

In order to determine the Meissner screening profile $B(z)$ and the temperature dependence of the magnetic penetration depth λ_{L} in a straightforward way, LE-μSR experiments were performed at the μE4 beamline at the Paul Scherrer Institut (PSI, Switzerland) [13,14]. A mosaic of four samples from one set was glued with silver paint on a nickel coated aluminum plate. The low-energy muons (μ^+) are produced at a rate of about $10^4\ \mathrm{s}^{-1}$ using a solid Ar/N$_2$ moderator. After reacceleration, the final energy of the muons is adjusted by a bias voltage at the sample. By tuning the energy between 5 and 25 keV the mean stopping depth of the muons can be varied in a range of 25–106 nm in YBCO (see Fig. 3).

In condensed matter, muons act as local magnetic probes. Measuring the time difference $t = t_{\mathrm{e}} - t_{\mathrm{s}}$ between the implantation time t_{s} and the decay time t_{e} of the μ^+, detected via the decay positron, allows one to determine the temporal evolution of the muon-spin polarization $P(t)$ [16]. This is possible due to the parity violation of the weak decay, which results in a positron emission preferentially along the μ^+ spin direction at the time of decay. The positron count rate $N(t)$ is given by

$$N(t) = N_0\, \mathrm{e}^{-t/\tau_\mu}[1 + AP(t)] + N_{\mathrm{Bkg}}, \qquad (2)$$

with a mean μ^+ lifetime of $\tau_\mu = 2.197\ \mu$s, where N_0 gives the scale of the counted positrons, N_{Bkg} is a time-independent background of uncorrelated events, and A is the observable decay asymmetry.

The experiments were performed in the Meissner state. After zero field cooling to 5 K, a magnetic field $B_{\mathrm{ext}} = 8\ \mathrm{mT} < \mu_0 H_{c_1}$ is applied parallel to the thin-film surfaces and perpendicular to the initial muon spin. In this case, the muon-spin polarization $P(t)$ is given by

$$P(t) = e^{-\sigma^2 t^2/2} \int n(z) \cos[\gamma_\mu B(z) t + \phi] dz, \qquad (3)$$

with the initial phase ϕ, the muon gyromagnetic ratio $\gamma_\mu = 2\pi \times 135.5$ MHz/T, and the depolarization rate σ,

TABLE I. Summary of the parameters determined for the investigated optimally doped YBCO thin-film samples with ($\mathrm{YBCO_{Au}}$) and without Au nanoparticles (YBCO). The superconducting transition temperatures T_c were obtained from resistivity measurements. The average film thicknesses $\overline{d}$ were extracted from RBS measurements. From a global fit of the LE-μSR data, the superconducting thicknesses d_{sc}, the dead layer thicknesses to the vacuum interface z_0, and the London penetrations depths $\lambda_{ab}(10\ \mathrm{K})$ were determined. $\lambda_{ab}(0\ \mathrm{K})$ and the superconducting gap Δ_0 were extracted from a linear fit in the range 5–35 K of $\lambda_{ab}(T)$ measured with LE-μSR. For comparison single crystal values [20] are also presented.

Sample	T_c (K)	$\overline{d}$ (nm)	d_{sc} (nm)	z_0 (nm)	$\lambda_{ab}(10\ \mathrm{K})$ (nm)	$\lambda_{ab}(0\ \mathrm{K})$ (nm)	Δ_0 (meV)
YBCO film	90.2(2)	150(8)	119(1)	0(2)	161(1)	158(1)	22(2)
$\mathrm{YBCO_{Au}}$ film	90.8(1)	152(8)	133(1)	1(2)	154(1)	150(1)	24(2)
YBCO bulk [20]	94.1(1)			10.3(5)		115(4)	20(4)

which is a measure of any inhomogeneous local magnetic field distribution at the μ^+ site. The muon stopping distributions $n(z)$ for different energies are simulated using the Monte Carlo code TRIM.SP [15] (see Fig. 3). The applicability of the TRIM.SP code for low-energy muons stopping in matter is demonstrated in Ref. [17]. Since the thin films have twinned a and b axes, the average magnetic penetration depth λ_{ab} is determined with the present experimental setup. To analyze the data, the London model profile for thin films was used, resulting from an exponential decay of B_{ext} from both interfaces:

$$B(z) = \begin{cases} B_{\mathrm{ext}} \dfrac{\cosh[(z - z_0 - d_{sc}/2)/\lambda_{ab}]}{\cosh(d_{sc}/2\lambda_{ab})}, & z \geqslant z_0, \\ B_{\mathrm{ext}}, & z < z_0, \end{cases} \qquad (4)$$

where d_{sc} is the thickness of the superconducting region, z is the depth along the c axis, and z_0 is the effective dead layer at the vacuum interface (see Fig. 2). This dead layer may be due to the roughness of the surface [18] or to a reduction of the order parameter close to the surface.

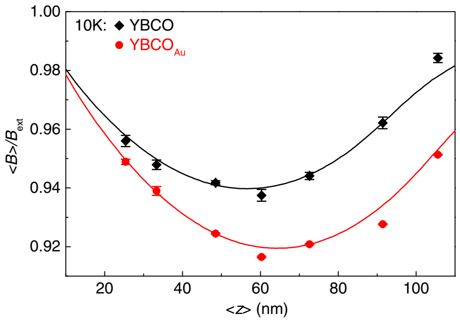

FIG. 4. (Color online) The average local magnetic field normalized to the applied field $\langle B\rangle/B_{\mathrm{ext}}$ vs the mean muon implantation depth $\langle z\rangle$ measured in an applied magnetic field $B_{\mathrm{ext}} = 8$ mT parallel to the film surface at 10 K for thin-film YBCO and $\mathrm{YBCO_{Au}}$. The solid lines represent the results of the global fits obtained with musrfit [19], where seven μSR spectra with different energies were analyzed simultaneously. The used parameter values are listed in Table I. The data points are determined from single energy fits using $\langle B\rangle = \int n(z)B(z)\mathrm{d}z$, where $n(z)$ is the muon implantation profile of the corresponding energy (see Fig. 3).

By the simultaneous analysis of the μSR spectra measured at seven different implantation energies at 10 K, the Meissner screening profiles of the two sample sets YBCO and $\mathrm{YBCO_{Au}}$ were determined (see Fig. 4). The resulting values of the parameters are listed in Table I. The thickness of the superconducting layer d_{sc} is substantially smaller than the average film thickness $\overline{d}$ in both sample sets. This confirms the presence of a dead layer at the substrate interface d_{DL} of about 31 nm for YBCO and about 18 nm for $\mathrm{YBCO_{Au}}$. The interface layer (d_{DL}) exhibits only weak superconductivity as mentioned before. No macroscopic Meissner screening is observed in this region. This could be explained by the presence of grain boundaries due to mechanical strain [12], leading also to the reduction of T_c in thin films compared to single-crystal YBCO. Note that d_{DL} is smaller for the $\mathrm{YBCO_{Au}}$ samples, indicating that the Au nanoparticles may relax the mechanical strain. The dead layers to the vacuum interface are surprisingly small in both sets ($z_0 \approx 1$ nm) compared to single-crystal YBCO ($z_0 \simeq 10$ nm) [20] and other YBCO thin-film measurements ($z_0 \simeq 8$ nm) [21].

$\mathrm{YBCO_{Au}}$ screens the magnetic field better, and therefore exhibits a smaller λ_{ab} than our pristine YBCO (Fig. 4). The temperature dependence of λ_{ab} of thin-film YBCO and $\mathrm{YBCO_{Au}}$ is presented in Fig. 5. These values of λ_{ab} were extracted from μSR spectra measured at the energy corresponding to the minimal average local magnetic field $\langle B\rangle_{\mathrm{min}}$ at 10 K. Both sample sets show a linear increase in λ_{ab} up to 35 K, which is characteristic for a d-wave pairing [22]:

$$\lambda_{ab}(T) = \lambda_{ab}(0\ \mathrm{K})[1 + \ln(2)\, k_B T/\Delta_0]. \qquad (5)$$

The slopes for YBCO and $\mathrm{YBCO_{Au}}$ are very similar (≈0.4 nm/K), so the superconducting gaps Δ_0 are the same within experimental uncertainty (see Table I). The value of $\lambda_{ab}(0\ \mathrm{K})$ for $\mathrm{YBCO_{Au}}$ is smaller compared to YBCO, but still larger than that one of single-crystal YBCO. If the amount of Au nanoparticles is higher (Au seed layer of 3 nm instead of 1.8 nm) the same effects on T_c and λ_{ab} where observed. The nominal changes are smaller, since most of the Au nanoparticles remained at the interface to the substrate.

A possible explanation for the reduced magnetic penetration depth in $\mathrm{YBCO_{Au}}$ is the diffusion of Au from the nanoparticles into the Cu-O chains (likely during the YBCO deposition), since Au has a relatively high mobility at higher temperatures. A replacement of Cu(1) by Au in the Cu-O chains leads to an increase of the oxygen mobility [23]. An enhanced oxygen mobility favors longer Cu-O chain segments leading to in increase of the charge carrier transfer from the

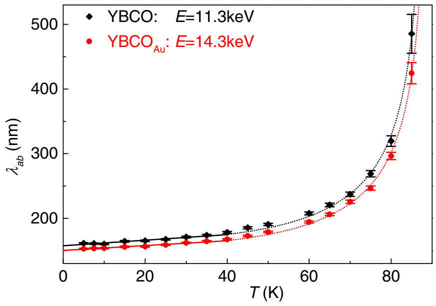

FIG. 5. (Color online) The London penetration depth λ_{ab} vs temperature T for thin-film YBCO and $YBCO_{Au}$. λ_{ab} was determined from $\langle B\rangle/B_{ext}$ (Gaussian fit to the μSR spectra with musrfit [19]) by using the parameters from the global fit determined at 10 K. The applied magnetic field was $B_{ext} = 8$ mT. The implantation energies E given in the figure were selected according to the minimum in $\langle B\rangle/B_{ext}$. The corresponding solid lines are linear fits to the data in the range 5–35 K by means of Eq. (5). The parameter values are listed in Table I. The dotted lines are fits to the power law $\lambda_{ab}(T) = \lambda_{ab}(0)[1-(T/T_c)^n]^{-1/2}$ with $n \simeq 2.7$.

Cu-O chains to the CuO_2 planes [2]. Since more charge carriers can contribute to superconductivity, n_s increases while λ_{ab} decreases. In this case the c-axis lattice constant should be slightly increased [4]. This, however, was not observed in the investigated samples.

Another possibility is that the presence of Au nanoparticles in the superconducting region of YBCO lowers the defect density and leads therefore to the observed reduction of λ_{ab} in $YBCO_{Au}$. A reduced defect density could originate from a condensation of defects at the Au nanoparticles, so that the CuO_2 planes and the structure are less disturbed. To evaluate the defect density we take the c-axis lattice constant as an indication. In $YBCO_{Au}$, we observe a slightly smaller c-axis lattice constant [$c_{YBCO_{Au}} = 1.1688(2)$ nm $< c_{YBCO} = 1.1699(2)$ nm]. YBCO single crystals have an even smaller c-axis lattice constant [$c_{bulk} = 1.167(1)$ nm] [24]. A lower defect density is generally expected in single-crystal YBCO compared to thin-film YBCO, which is consistent with the trend of the c-axis lattice constants. From this point of view, $YBCO_{Au}$ has a lower defect density than our pristine YBCO, but a higher one compared to single-crystal YBCO. Since single-crystal YBCO has also a smaller λ_{ab} and a higher T_c compared to our YBCO and $YBCO_{Au}$ samples, a reduced defect density is a possible reason for the slightly different values of T_c and $\lambda_{ab}(0)$ in $YBCO_{Au}$ compared to pure YBCO films.

In summary, we have shown by using LE-μSR that the increase of T_c in thin-film YBCO containing Au nanoparticles is accompanied by a reduction of the average magnetic penetration depth λ_{ab}. We attribute this reduction to a lowered defect density. The diffusion of Au into the Cu-O chains may also contribute to the observed changes of T_c and n_s. In previous studies on YBCO, Cu was exchanged by Au within the Cu-O chains to obtain an enhanced T_c. Our results indicate that the presence of Au nanoparticles has a similar effect in thin-film YBCO.

We acknowledge Hans-Peter Weber for his excellent technical support. This work was partly supported by the Swiss National Science Foundation and the Landesgraduiertenföderung Thüringen.

[1] H. Alloul, J. Bobroff, M. Gabay, and P. J. Hirschfeld, Rev. Mod. Phys. **81**, 45 (2009).
[2] A. A. Aligia and J. Garces, Phys. Rev. B **49**, 524 (1994).
[3] L. Shlyk, G. Krabbes, G. Fuchs, G. Stöver, S. Gruss, and K. Nenkov, Physica C **377**, 437 (2002).
[4] M. Z. Cieplak, G. Xiao, C. L. Chien, J. K. Stalick, and J. J. Rhyne, Appl. Phys. Lett. **57**, 934 (1990).
[5] M. Z. Cieplak, G. Xiao, C. L. Chien, A. Bakhshai, D. Artymowicz, W. Bryden, J. K. Stalick, and J. J. Rhyne, Phys. Rev. B **42**, 6200 (1990).
[6] U. Welp, S. Fleshler, W. K. Kwok, J. Downey, G. W. Crabtree, H. Claus, A. Erb, and G. Müller-Vogt, Phys. Rev. B **47**, 12369 (1993).
[7] C. Katzer, M. Westerhausen, I. Uschmann, F. Schmidl, U. Hübner, and P. Seidel, Supercond. Sci. Technol. **26**, 125008 (2013).
[8] C. Katzer, M. Schmidt, P. Michalowski, D. Kuhwald, F. Schmidl, V. Grosse, S. Treiber, C. Stahl, J. Albrecht, U. Hübner, A. Undisz, M. Rettenmayr, G. Schütz, and P. Seidel, Europhys. Lett. **95**, 68005 (2011).
[9] C. Katzer, C. Stahl, P. Michalowski, S. Treiber, F. Schmidl, P. Seidel, J. Albrecht, and G. Schütz, New J. Phys. **15**, 113029 (2013).
[10] M. Döbeli, J. Phys.: Condens. Matter **20**, 264010 (2008).
[11] L. R. Doolittle, Nucl. Instrum. Methods Phys. Res. B **15**, 227 (1986).
[12] H. Schneidewind, F. Schmidl, S. Linzen, and P. Seidel, Physica C **250**, 191 (1995).
[13] E. Morenzoni, T. Prokscha, A. Suter, H. Luetkens, and R. Khasanov, J. Phys.: Condens. Matter **16**, S4583 (2004).
[14] T. Prokscha, E. Morenzoni, K. Deiters, F. Foroughi, D. George, R. Kobler, A. Suter, and V. Vrankovic, Nucl. Instrum. Methods Phys. Res., Sect. A **595**, 317 (2008).
[15] W. Eckstein, *Computer Simulation of Ion-Solid Interactions* (Springer, Berlin, 1991).
[16] A. Yaouanc and P. Dalmas de Reotier, *Muon Spin Rotation, Relaxation, and Resonance: Applications to Condensed Matter* (Oxford University Press, Oxford, 2011); V. P. Smilga and Yu. M. Belousov, *The Muon Method in Science* (Nova Science Publishers, New York, 1994).
[17] E. Morenzoni, H. Glückler, T. Prokscha, R. Khasanov, H. Luetkens, M. Birke, E. M. Forgan, Ch. Niedermayer, and M. Pleines, Nucl. Instr. Meth. B **192**, 254 (2002).
[18] M. Lindstrom, B. Wetton, and R. Kiefl, J. Eng. Math. (2013), doi:10.1007/s10665-013-9640-y.
[19] A. Suter and B. M. Wojek, Physics Procedia **30**, 69 (2012).

[20] R. F. Kiefl, M. D. Hossain, B. M. Wojek, S. R. Dunsiger, G. D. Morris, T. Prokscha, Z. Salman, J. Baglo, D. A. Bonn, R. Liang, W. N. Hardy, A. Suter, and E. Morenzoni, Phys. Rev. B **81**, 180502(R) (2010).
[21] T. J. Jackson, T. M. Riseman, E. M. Forgan, H. Glückler, T. Prokscha, E. Morenzoni, M. Pleines, Ch. Niedermayer, G. Schatz, H. Luetkens, and J. Litterst, Phys. Rev. Lett. **84**, 4958 (2000).
[22] C. P. Poole, Jr., H. A. Farach, R. J. Creswick, and R. Prozorov, *Superconductivity* (Academic Press, London, 2007).
[23] H. Claus, S. Yang, H. K. Viswanathan, G. W. Crabtree, J. W. Downey, and B. W. Veal, Physica C **213**, 185 (1993).
[24] P. Benzi, E. Bottizzo, and N. Rizzi, J. Cryst. Growth **269**, 625 (2004).

6.3.1 Remarks on the paper

We investigated besides YBCO (without Au nanoparticles) and YBCO(Au) (with Au nanoparticles) a third set of samples with a thicker Au seed layer (3 nm instead of 1.8 nm), labeled YBCO(Au2). The results were not published since the film thicknesses d within this sample set vary a lot (Tab. 6.1). The μSR results have a large systematic error, because we can not include this strong variation in thickness in our analysis. An average superconducting thickness had to be assumed to analyze the LE-μSR spectra.

By means of resistivity measurements a critical temperature $T_\mathrm{c} = 90.4(1)$ K was obtained for the YBCO sample SO65. This is higher compared to the investigated pristine YBCO thin film ($T_\mathrm{c} = 90.2(2)$ K), but lower compared to the sample with less Au nanoparticles ($T_\mathrm{c} = 90.8(1)$ K), as shown in Fig. 6.6. This may be understood taking the Rutherford backscattering spectrometry results for this sample into account. Most of the Au nanoparticles are located within the dead layer at the interface to the substrate, as depicted in

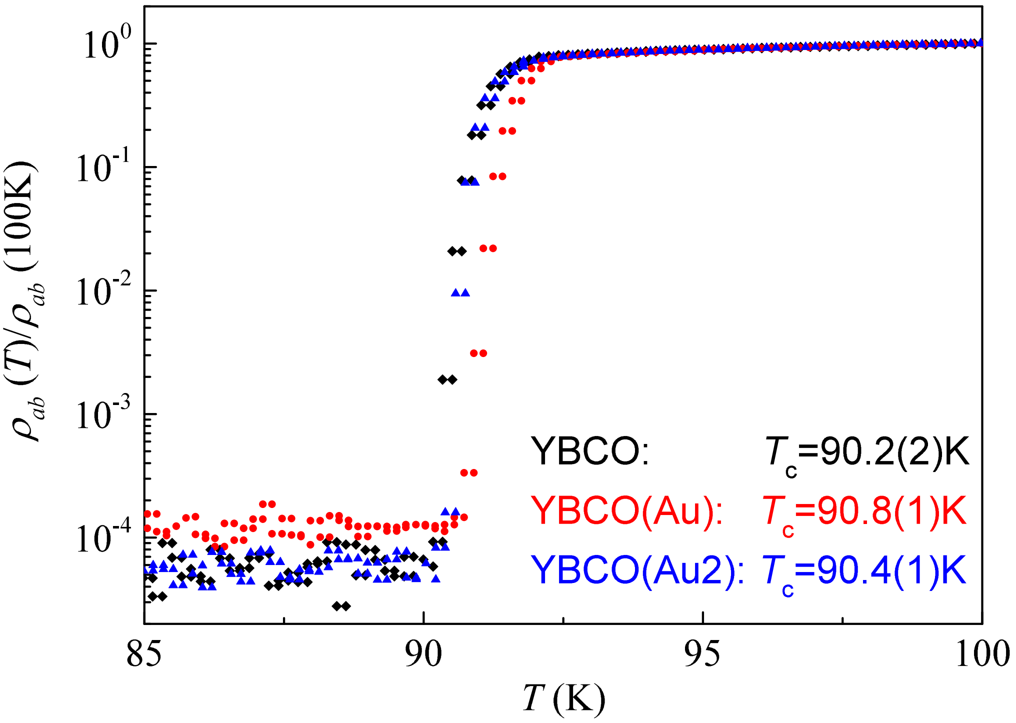

Figure 6.6: In-plane resistivity ρ_{ab} normalized at 100 K vs temperature T for a thin-film sample from set YBCO (black diamonds), YBCO(Au) (red circles) and YBCO(Au2) (blue triangles). The listed T_c are determined by $\rho_{ab}(T_\mathrm{c})/\rho_{ab}(100\,\mathrm{K}) \leq 2.5 \cdot 10^{-4}$ averaged over five cooling-heating cycles.

Table 6.1: Overview of the thickness d and the Au concentration c_{Au} of the thin-film sample set YBCO(Au2).

Sample	d (nm)	c_{Au} (atoms/cm^2)
SO65	175	$6.8 \cdot 10^{15}$
SO66	167	$5.3 \cdot 10^{15}$
SO68	118	$5.9 \cdot 10^{15}$
SO72	120	$6.5 \cdot 10^{15}$
Ø	145(26)	$6.1(5) \cdot 10^{15}$

Fig. 6.7. Thus, the amount of nanoparticles placed within the superconducting region (SC) is smaller compared to the total amount present in the sample and also compared to the sample of set YBCO(Au). But this Au distribution is not present in all samples of the YBCO(Au2) set. The Au particle distributions of the samples SO66 and SO68 have a peak close to the vacuum interface, whereas the one of sample SO72 looks similar to that of sample SO65. This leads to an additional variation of the superconducting properties between the YBCO(Au2) samples, making a μSR analysis even more challenging.

To exclude magnetic contributions, which would influence measurements in the Meissner

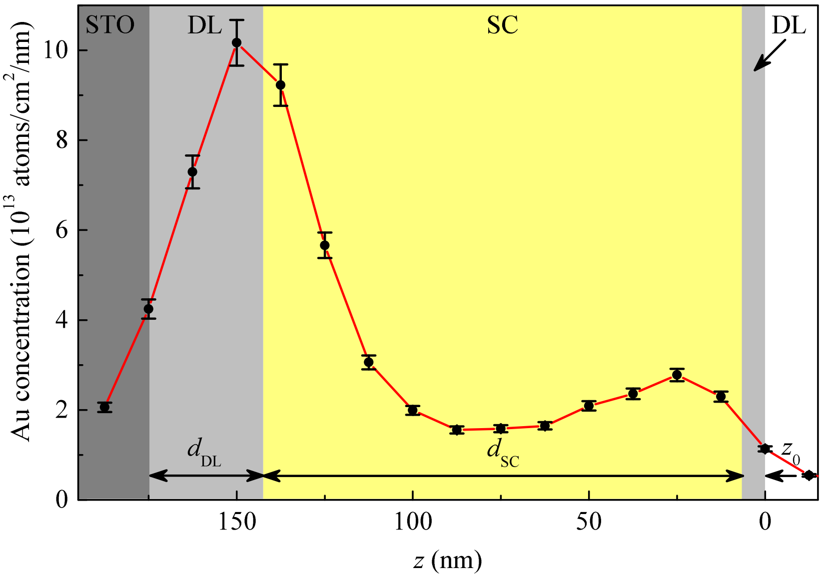

Figure 6.7: Gold concentration versus depth z along the crystallographic c axis for the YBCO thin-film sample SO65 from set YBCO(Au2). The labeled and colored regions are: substrate region (STO,dark gray), the dead layer (DL, light gray) to the substrate interface and to the vacuum interface, and the superconducting region (SC, yellow). The red line is a guide to the eye.

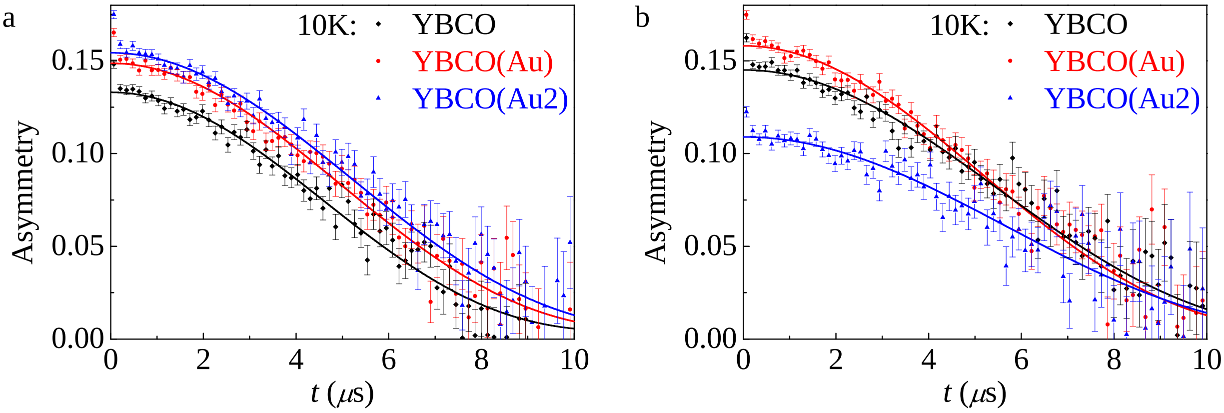

Figure 6.8: LE-μSR spectra in zero magnetic field of the thin-film sample sets YBCO (black diamonds), YBCO(Au) (red circles) and YBCO(Au2) (blue triangles) with implantation energies of 5.3 keV (a) and $22-24$ keV (b). The solid lines are the results of fits with the Gaussian Kubo-Toyabe function [83].

state, zero field measurements at two different energies have been performed in addition to the TF energy scans. All three sample sets show only a contribution of nuclear magnetic moments, since the spectra could be well described with a Gaussian Kubo-Toyabe function (Section 4.4.1) as depicted in Fig. 6.8. The asymmetry between the samples varies, because the three sample sets where not glued at the exactly same position, which directly influences the asymmetry. The depolarization rates of the three sets are in the order of $0.13-0.16\,\mu\mathrm{s}^{-1}$. No difference between sample sets with and without Au nanoparticles is observed.

The LE-μSR data were analyzed assuming the London model profile [given in Eq. (4.13)] with the superconducting thickness d_{SC} and a dead layer z_0 (see Chapter 4). The simultaneous fit of seven spectra taken at different implantation energies converged, although the thicknesses and Au distributions of the samples vary substantially (Tab. 6.1). The determined penetration profile is shown in Fig. 6.9. The applied magnetic field is shielded more strongly in YBCO(Au2) compared to the other investigated sample sets. The dead layer of $z_0 = 8\,\mathrm{nm}$ is larger compared to YBCO and YBCO(Au) thin-film sample sets, which could simply result from the strong variation in thickness. The measured average magnetic penetration depth $\lambda_{ab}(10\mathrm{K}) = 150\,\mathrm{K}$ is smaller compared to the value of YBCO(Au) at 10 K. Therefore, it seems likely that the amount of Au nanoparticles has a direct influence on how much the defect density is reduced. In order to substantiate this conclusion a systematic study on the influence of the Au seed layer thickness needs to be carried out. Also the influences of the substrate quality and the size of the nanoparticles have to taken into account to obtain a conclusive picture. Another open issue is under which growth

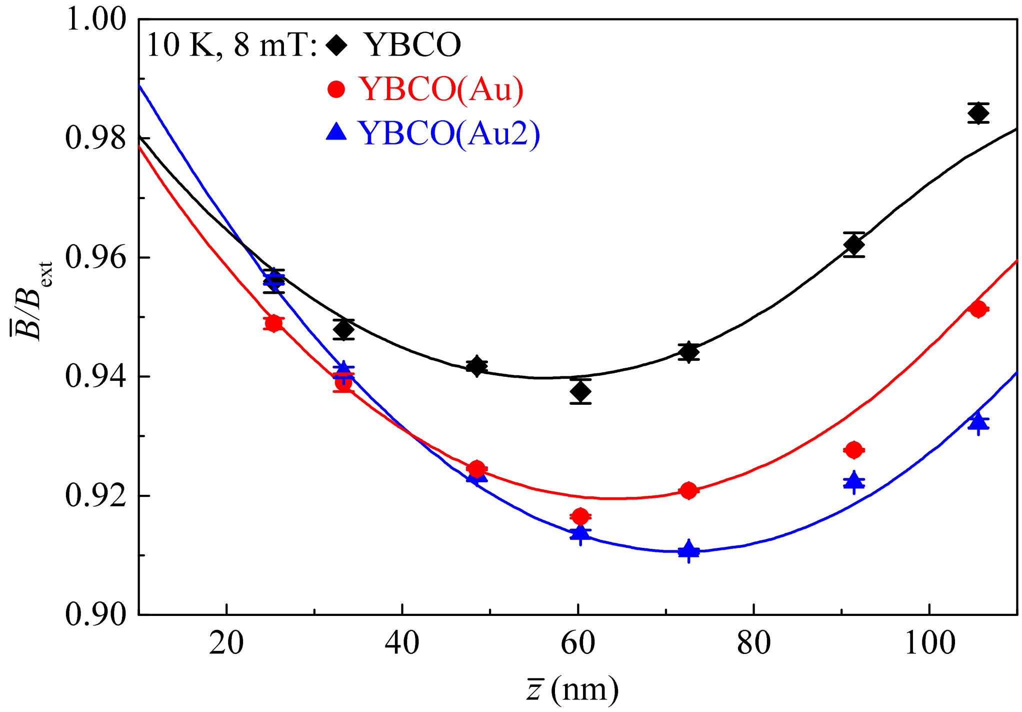

Figure 6.9: The average local magnetic field normalized to the applied magnetic field $\bar{B}/B_{\rm ext}$ versus the mean muon implantation depth $\bar{z}$ in an applied magnetic field of $B_{\rm ext} = 8\,{\rm mT}$ parallel to the thin-film surface measured at 10 K of the thin-film sets YBCO (black diamonds), YBCO(Au) (red circles) and YBCO(Au2) (blue triangles). The solid lines are the result of a global fit, whereas the data points are obtained from single fits.

conditions the Au particles remain close to the substrate, accumulate close to the vacuum interface, or distribute homogeneously. To clarify these open questions systematic RBS and resistivity measurements are adequate, since the knowledge of T_c and the amount and distribution of the Au nanoparticles is sufficient.

Assuming d-wave pairing for the low-temperature behavior of the average magnetic penetration depth,

$$\lambda_{ab}(T) = \lambda_{ab}(0{\rm K}) \cdot [1 + \ln(2) \cdot k_{\rm B}T/\Delta_0]\,, \qquad (6.1)$$

one obtains $\lambda_{ab}(0{\rm K}) = 147(1)\,{\rm nm}$ and $\Delta_0 = 24(3)\,{\rm meV}$ for the YBCO(Au2) sample set (Fig. 6.10). The average magnetic penetration depth at $T = 0$ is below the value of YBCO(Au) with less Au concentration and below the pristine YBCO thin films, but still higher compared to bulk samples, as expected from the global fit at 10 K. The superconducting gap instead is of the same order of magnitude in all investigated YBCO sample

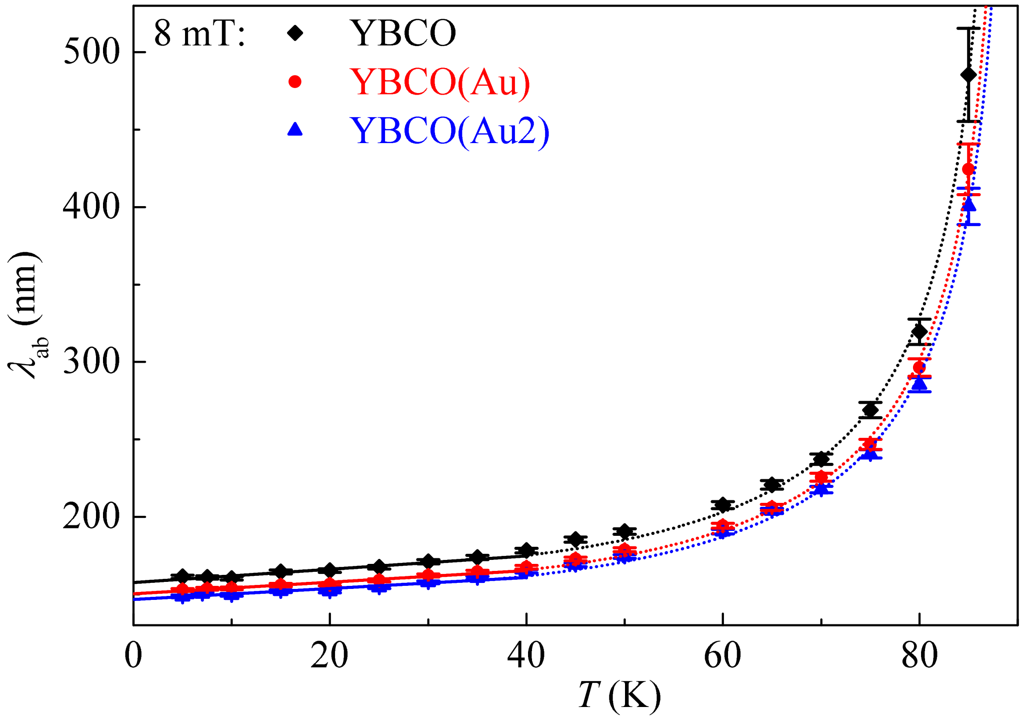

Figure 6.10: The average magnetic penetration depth λ_{ab} versus temperature T for the thin-film sets YBCO (black diamonds), YBCO(Au) (red circles) and YBCO(Au2) (blue triangles) in an applied magnetic field of $B_{\mathrm{ext}} = 8\,\mathrm{mT}$. The solid lines are fits to Eq. (6.1) and the dotted lines are fits to Eq. (6.2).

sets. At higher temperatures the data are well described by a power law:

$$\lambda_{ab}(T) = \lambda_{ab}(0\mathrm{K})[1 - (T/T_{\mathrm{c}})^n]^{-1/2}. \tag{6.2}$$

This model reveals a higher critical temperature for YBCO(Au2) compared to YBCO(Au), in contrast to the resistivity measurement of sample SO65, leading to the conclusion that the YBCO(Au2) set exhibits variations in T_{c} of the order of the difference between the YBCO(Au) and the YBCO(Au2) sample sets ($\Delta T_{\mathrm{c}} \approx 1\,\mathrm{K}$). The exponent n is for all three sets about 2.7(1). The values of $\lambda_{ab}(0\mathrm{K})$ are not relevant since the model is only useful for higher temperatures. These findings agree with the previous results: The fundamental properties, like the size of the superconducting gap and the temperature dependence of λ_{ab}, stays the same when adding Au nanoparticles to YBCO thin films. The reduction of disorder leads instead to a reduced average magnetic penetration depth, to a higher T_{c} and an increased j_{c} (Section 6.3).

6.4 Photo-induced effects in superconducting $YBa_2Cu_3O_{6+x}$

The interaction with light weakens the superconducting ground state in classical superconductors [23]. Remarkably, studies on $YBa_2Cu_3O_{6+x}$ with reduced oxygen content ($x < 1$) show a persistent increase in the electrical conductivity after continuous illumination with visible light in thin films [21, 117] as well as in single crystals [132]. The critical temperature T_c is shifted to higher values for a broad range of oxygen concentrations ($0.4 \leq x \leq 0.9$) up to $\Delta T_\mathrm{c,max} = 15\,\mathrm{K}$ [133]. The magnitude of the shift strongly depends on the oxygen content x, the temperature at which the illumination is performed, and the photon dose [133]. YBCO samples with $x < 0.4$, which are close to the metal-insulator transition, even become superconducting under illumination [123]. The photo-induced effects are only present for photon energies higher than 1.6 eV. The changes in resistivity and T_c persist until the temperature is raised beyond 270 K. Accordingly, in the literature the effect is referred to as photo-persistent conductivity (PPC). Above 270 K the resistivity relaxes back on time scales of hours to days, depending on the temperature [123]. This time scale is similar to that required for YBCO samples to stabilize their properties at room temperature after deoxygenation of the sample at high temperatures [134]. The PPC is fully reversible and reproducible. If infrared (IR) light is used for illumination an increase in conductivity is observed as well, but with a much smaller magnitude [135]. But if IR illumination is performed after illumination with visible light, the PPC is reduced by about $2 - 10\%$ even at low temperatures.

Different origins have been proposed to explain the PPC, which can be generally divided into two main lines: (a) Photo-induced charge transfer and (b) photo-assisted oxygen ordering. The underlying mechanisms can only be understood by taking into account the anisotropic structure of YBCO, or more precisely the properties of the Cu-O chains. As mentioned before, the ordering of oxygen in the CuO_x layers plays a major role for conductivity as well as for superconductivity in YBCO. A longer average chain length leads to a higher charge carrier density in the CuO_2 planes and to a higher T_c [124] on the underdoped side of the phase diagram.

The scenario discussed above is crucial for an understanding of the proposed PPC mechanisms. In the case of photo-induced charge transfer, the absorbed photons create electron-hole pairs. The electrons are trapped at defects such as oxygen vacancies, preventing recombination. The holes are transfered to the CuO_2 planes where they contribute to the conductivity and at low temperatures to the superconductivity. Thus, mechanism (a) explains the increase in conductivity and the shift in T_c. However, it does not provide a natural explanation for the effects of IR light exposure [135]. The IR quenching which frees trapped electrons recovers only a small percentage of the photo-induced conductivity, leading to the conclusions that the electrons are not optically accessible or possibly another mechanism has to be taken into account.

The photo-assisted oxygen ordering mechanism (b) assumes that the photons initiate a reordering of oxygen in the CuO_x layers, so that longer Cu-O chain fragments are formed. This leads to an enhanced charge carrier transfer to the CuO_2 planes where superconductivity takes place. The proposed mechanism agrees with the observation that the time dependence of the resistivity relaxation is similar for photo-induced changes and for oxygen reordering after annealing. However, mechanism (b) alone fails to explain the IR experiments and why the oxygen atoms move under illumination.

Therefore, a combination of both mechanisms was proposed [135]. In the combined model the trapped electrons at the oxygen vacancies act as local perturbations that modify the local electric field distribution. The induced dipole moments cause the movement of the oxygen in the CuO_x layers, resulting in a lengthening of the chain fragments. A simplified cellular automata model [136] agrees well with this interpretation. It confirms that local perturbations can affect the average chain length. Experimental [137] as well as theoretical [138] investigations have also shown that electrical fields influence the oxygen ordering and change T_c. The combined mechanism accounts for the infrared quenching, predicts the correct time dependence of the photo-excitation process, and gives the correct scale of the changes in resistivity produced by illumination.

Even though extensive structural studies were able to correlate the chain ordering to the charge transfer, leading to changes of the resistivity and T_c, little is known how illumination affects the superconducting state on the microscopic level. In our study we focused on a detailed investigation of the magnetic screening profile $B(z)$ in the Meissner state, utilizing LE-μSR. Two sets of YBCO thin films ($x = 0.42, 0.67$) with twinned crystallographic a and b axes, labeled $YBCO_{6.42}$ and $YBCO_{6.67}$ from here on, were investigated along with a detwinned single-crystal mosaic, exhibiting the ortho-VIII structure ($x = 0.67$).

Before studying the effects due to illumination we further characterized the sample sets by zero field LE-μSR experiments. The ortho-VIII single crystal set shows the expected signature of nuclear magnetic moments, described with the Gaussian Kubo-Toyabe function (Section 4.4.1), independent from temperature and implantation energy (Fig. 6.11a).

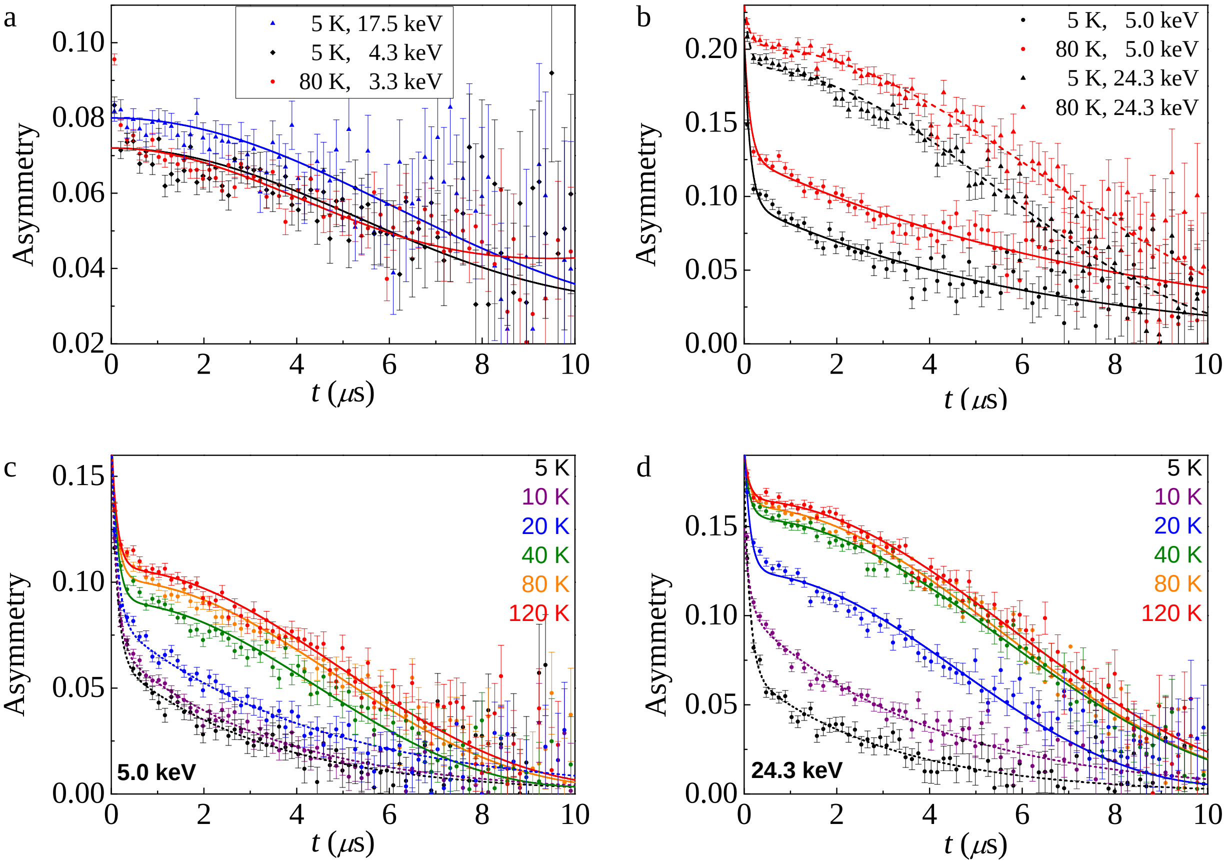

Figure 6.11: LE-μSR spectra in zero magnetic field for the YBCO ortho-VIII single crystal mosaic (a), the thin-film sample set $YBCO_{6.67}$ (b) and $YBCO_{6.42}$ (c & d). The selected temperatures and implantation energies are stated in the figures. The solid lines are the results of fits with the Gaussian Kubo-Toyabe function [83], whereas the dashed lines are fits to an exponential decay. The contribution of the Ni background at early times is taken into account by adding a second exponentially decaying term.

In the thin-film set $YBCO_{6.67}$ the expected line shape of the nuclear magnetic moments is only present at high implantation energies (Fig. 6.11b). By sampling the region close to the surface an exponential damping is observed, which indicates the presence of magnetic contributions at all investigated temperatures. In the strongly underdoped $YBCO_{6.42}$ sample set magnetic contributions appear below 20 K independent of the investigated sample region, as observed in ZF spectra at several temperatures (Fig. 6.11a & d). Since besides this, the critical temperature is about also 20 K and the expected penetration depth is very large, magnetic screening profiles could only be determined at 5 and 10 K. The measurements at 5 K are strongly influenced by the magnetic contributions as depicted in Fig. 6.12.

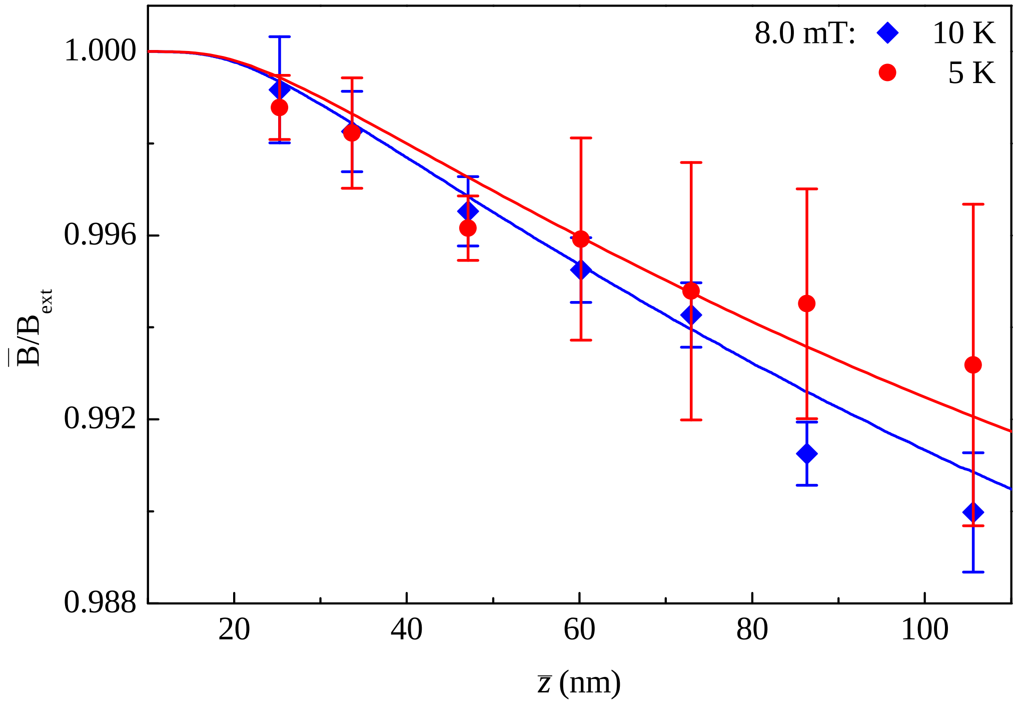

Figure 6.12: The average local magnetic field normalized to the applied field $\bar{B}/B_{\mathrm{ext}}$ versus the mean muon implantation depth $\bar{z}$ in an applied magnetic field of $B_{\mathrm{ext}} = 8\,\mathrm{mT}$ parallel to the thin-film surface measured at 10 K (blue) and 5 K (red) of the thin-film set $\mathrm{YBCO}_{6.42}$. The solid lines are the results of global fits whereas the data points are obtained from single fits.

The screening of the applied magnetic field could hardly fitted to the London model and is even weaker than at 10 K, probably because of pair-breaking due to the magnetism. These problems do not appear at 10 K. This gives us the possibility to study the photo-induced effects also in the underdoped samples, but only at 10 K.

To compare the results of the photo-induced effects to previous studies, resistivity measurements have been performed with the four probe technique in addition to the μSR experiments under comparable conditions. The average transition temperature $T_{\mathrm{c}} = 66.7(8)\,\mathrm{K}$ of $\mathrm{YBCO}_{6.67}$ agrees with the LE-μSR measurements. The temperature dependence of the average magnetic penetration depth revealed a $T_{\mathrm{c}} = 64.3(2)\,\mathrm{K}$, by using a power law [Eq. (6.2)] to fit the temperature data above 30 K (see Fig. 6.13). Below 30 K the data were fitted with the d-wave approach [Eq. (6.1)], yielding a superconducting gap of $\Delta_0 = 12(1)\,\mathrm{meV}$ and $\lambda_{ab}(0\mathrm{K}) = 265(3)\,\mathrm{nm}$. Compared to optimally doped single crystals with $\Delta_0 = 20(4)\,\mathrm{meV}$ [49], the estimated superconducting gap is smaller. As expected for

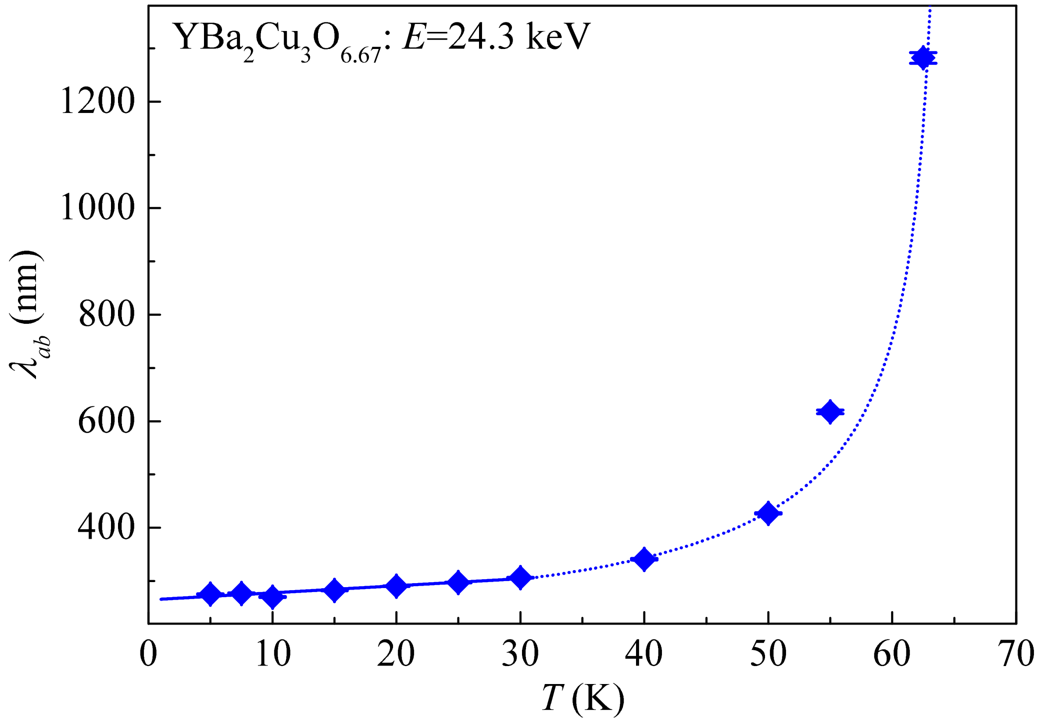

Figure 6.13: The average magnetic penetration depth λ_{ab} versus temperature T for the YBCO thin-film set $YBaCuO_{6.67}$ in an applied magnetic field of $B_{\mathrm{ext}} = 9.5\,\mathrm{mT}$. The solid line is a fit to Eq. (6.1) and the dotted line is a fit to Eq. (6.2).

underdoped thin films $\lambda_{ab}(0\mathrm{K})$ is well above the bulk value of optimally doped YBCO with 115(4) nm [49], generally related to the reduced oxygen content and amplified by a higher amount of disorder present in the thin films. Disorder could result e.g. from defects, misfit dislocation, or less ordered CuO_x layers. Maybe the twinning of the a and b axes also influences the absolute value of the average magnetic penetration depth λ_{ab}. Due to the magnetic contributions and the low T_{c} the temperature dependence of λ_{ab} could not be determined for $YBCO_{6.42}$.

The changes in resistivity due to light exposure have been measured after illuminating single samples of the thin-film sets with about $7 \cdot 10^{22}$ photons/cm^2. The YBCO thin films show shifts of $\Delta T_{\mathrm{c}} = 6.4(6)\,\mathrm{K}$ ($x = 0.42$) and $\Delta T_{\mathrm{c}} = 0.9(1)\,\mathrm{K}$ ($x = 0.67$), see Fig. 6.14, in agreement with previous results [133]. After warming up the thin-film YBCO samples to room temperature for 24 h the initial state is recovered in both sets.

The magnetic screening profiles $\bar{B}(\bar{z})$ determined by LE-μSR, as outlined in Section 4.4.3, exhibit for the initial state of YBCO an exponential decay for the single crystals and a cosh behavior in the thin films as depicted in Fig. 6.15. After illumination all magnetic

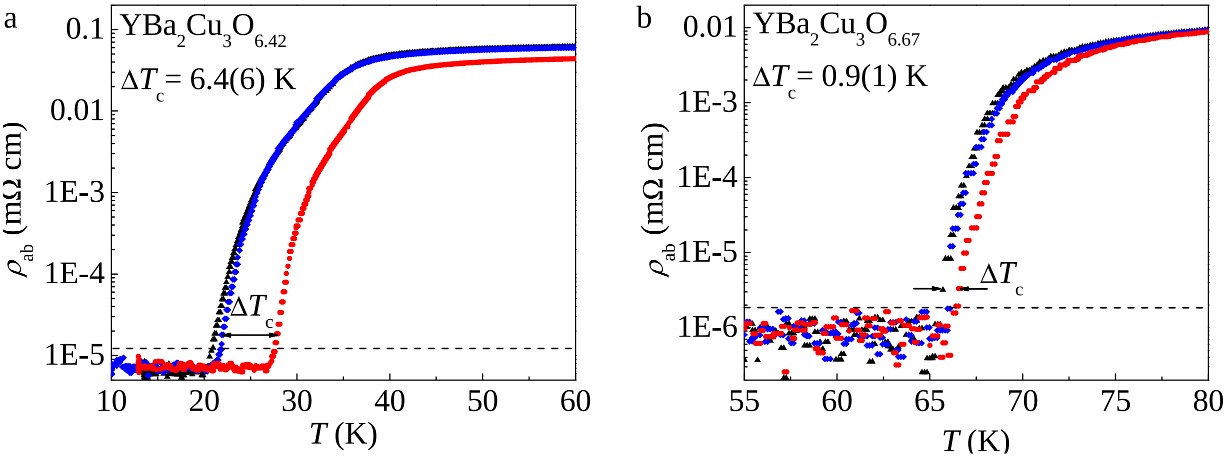

Figure 6.14: Resistivity ρ_{ab} versus temperature T of the thin film sets $YBaCuO_{6.42}$ (a) and $YBaCuO_{6.67}$ (b) for the initial state (blue diamonds, before illumination), the illuminated state (red circles, after illumination at 270 K), and the recovered state (black triangles, sample kept above room temperature for about one day). The critical temperature T_c was determined as the temperature where ρ_{ab} exceeds twice the RMS of the noise when heating the samples (horizontal dashed line). The arrows indicate the shifts in the transition temperatures ΔT_c due to visible-light illumination.

screening profiles are shifted to lower values and exhibit a pronounced change in shape. After the thermal reset the original Meissner screening profile is recovered. Thus, the PPC is fully reversible in all samples. The temperatures and times for illumination and recovery of the samples during the LE-μSR experiments are given in Table 6.2.

The superfluid density n_s is enhanced in all samples investigated after illumination, since the magnetic field is more strongly screened (see Fig. 6.15). To analyze the screening profiles after illumination in detail one has to think about how n_s is influenced to find a proper fitting model. Two different scenarios for the PPC change of n_s as function of the depth z can be envisaged:

(i) The additional charge carriers are mobile along the lattice c direction, hence they are distributed homogeneously over the whole sample. The superfluid density is raised, but is still constant as a function of depth z. Thus only the absolute value of the magnetic penetration depth is changed. Since the additional superfluid density is spatially averaged over the volume in scenario (i), the PPC changes of n_s would be much less pronounced in single crystals compared to thin films. However, this does not account for our results, since a change in $\bar{B}(\bar{z})$ is observed in the YBCO ortho-VIII single crystals (see Fig. 6.15d).

(ii) The PPC charge carriers are pinned to the layer where they are created. Here, the

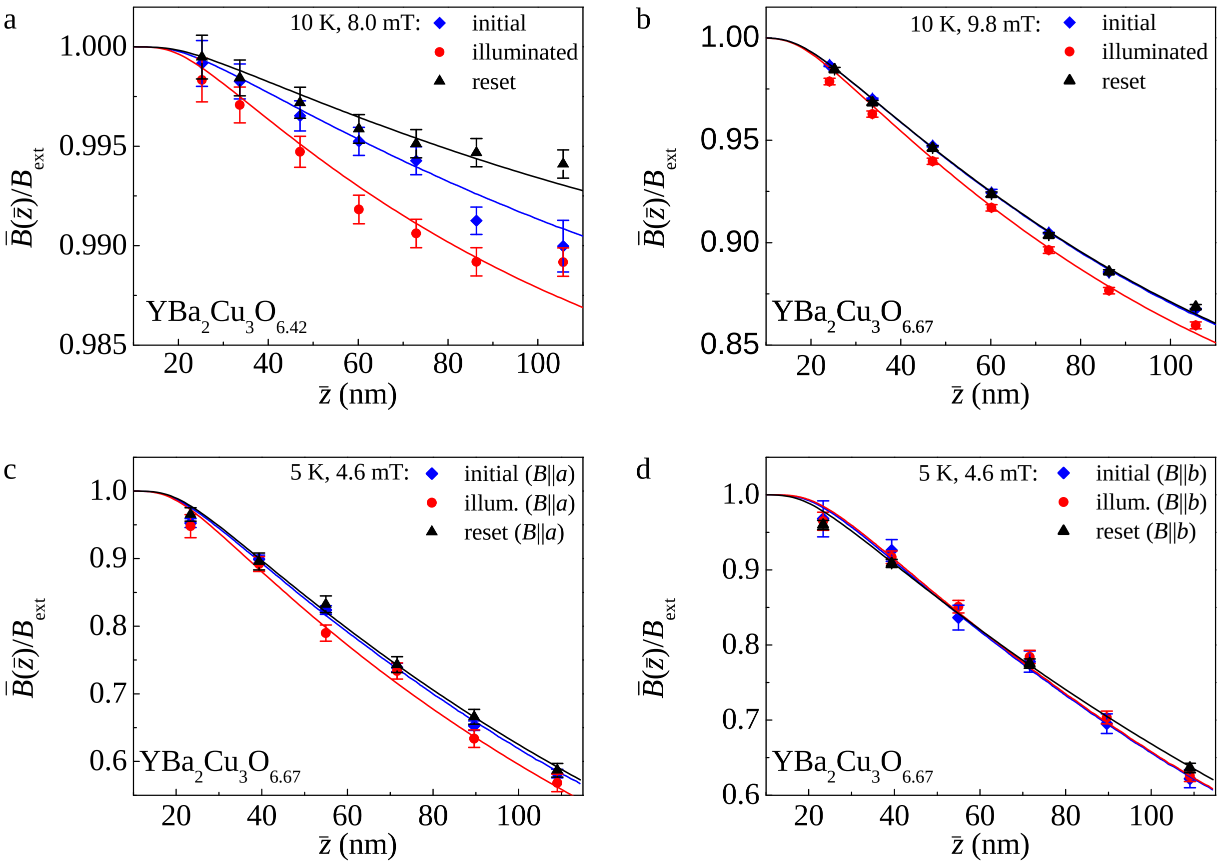

Figure 6.15: The magnetic penetration profile $\bar{B}(\bar{z})$ along the crystallographic c axis normalized to the applied magnetic field B_{ext} of the thin-film sets $\mathrm{YBaCuO_{6.42}}$ (a) and $\mathrm{YBaCuO_{6.67}}$ (b), and of detwinned YBCO ortho-VIII single crystal mosaic for B_{ext} applied parallel to the crystallographic a axis (c) and for B_{ext} parallel to the b axis (d). The presented field profiles correspond to the initial state (blue diamonds, before illumination), to the illuminated state (red circles, after illumination) and to the recovered state (black triangles, after heating up to room temperature for about 24 h).

changes in the superfluid density would be proportional to the light penetration profile: n_{s} increases mainly close to the vacuum interface, since the light penetrates into the sample according to an exponential decay. A depth-dependent superfluid density leads in turn to a modification of the Meissner screening field profile $B(z)$. Our results agree with the second scenario. At small depths z the applied magnetic field is more strongly shielded compared to the initial state. At higher z values the $B(z)$ curves are almost parallel. We

Table 6.2: Summary of the parameters used for the illumination and the recovery of the various YBCO samples during the LE-μSR experiments. The critical temperatures T_c were obtained from resistivity measurements for the thin films and with a *Quantum Design* MPMS SQUID magnetometer for the single crystals one year after the last annealing to set the oxygen content. The given values are averaged over the used samples. The uncertainty on $\overline{T_\mathrm{c}}$ corresponds to the variation between the samples. The illumination temperature T_illum, illumination time t_illum, and the corresponding photon dose d_ph are listed. The given temperatures T_reset and times t_reset have been used for the recovery.

Sample		$\overline{T_\mathrm{c}}$	T_illum	t_illum	d_ph	T_reset	t_reset
$\mathrm{YBCO_{6.42}}$	thin film	21(2) K	270 K	76 h	$4.4 \cdot 10^{22}$ photons/cm^2	315 K	24 h
$\mathrm{YBCO_{6.67}}$	thin film	66.7(8) K	270 K	72 h	$4.2 \cdot 10^{22}$ photons/cm^2	315 K	16 h
$\mathrm{YBCO_{6.67}}$	ortho-VIII	67.8(5) K					
	for λ_a		270 K	80 h	$4.6 \cdot 10^{22}$ photons/cm^2	315 K	24 h
	for λ_b		270 K	82 h	$4.8 \cdot 10^{22}$ photons/cm^2	310 K	24 h

therefore describe the magnetic penetration profiles of the illuminated samples by:

$$\frac{\mathrm{d}^2 B\,(z)}{\mathrm{d}z^2} = \left(\frac{1}{\lambda_\mathrm{L}^2} + \frac{1}{\lambda_\mathrm{P}^2} e^{-z/\zeta}\right) B(z), \tag{6.3}$$

where $1/\lambda_\mathrm{L}^2$ is proportional to the initial superfluid density before illumination $n_\mathrm{s,0}$, $1/\lambda_\mathrm{P}^2$ corresponds to the photo-induced superfluid density at the vacuum interface $n_\mathrm{s,illum}$, and ζ is the characteristic length over which the changes of n_s take place. The estimated values of ζ obtained from the LE-μSR data are of the order of the optical light penetration depth. Taking ellipsometry measurements of our thin film samples into account, performed at the University of Fribourg, we find an average light penetration depth of $\zeta = 60(10)\,\mathrm{nm}$ (Fig. 6.16), consistent with previous studies [139, 140]. Hence, we used this value for the detailed analysis of $n_\mathrm{s}(z)$. More details on the ellipsometry measurements are stated in the Appendix.

Eq. (6.3) can be solved analytically for the boundary conditions $B(z_0) = B(d_\mathrm{SC}+z_0) = B_\mathrm{ext}$. The solution for thin films and for $z_0 \leq z \leq d_\mathrm{SC} + z_0$ is

$$\begin{aligned}\frac{B\,(z)}{B_\mathrm{ext}} = \frac{1}{N} \{ & I_{\nu_-}\left(\nu_\mathrm{p} \exp\left[-\left(z - z_0\right)/\left(2\zeta\right)\right]\right) \left[I_{\nu_+}(\nu_\mathrm{p}) - I_{\nu_+}(\nu_\mathrm{p}\beta)\right] \\ & - I_{\nu_+}\left(\nu_\mathrm{p} \exp\left[-\left(z - z_0\right)/\left(2\zeta\right)\right]\right) \left[I_{\nu_-}\left(\nu_\mathrm{p}\right) - I_{\nu_-}\left(\nu_\mathrm{p}\beta\right)\right] \},\end{aligned}$$

Table 6.3: The magnetic penetration depth λ_{L} and the dead layer to the vacuum interface z_0 determined with a global fit of the LE-μSR spectra for YBCO in the initial state. The photo-induced magnetic penetration depth λ_{P} was extracted from LE-μSR spectra of the illuminated state.

Sample		z_0	λ_{L}	λ_{P}
$YBCO_{6.42}$ thin film		23(2) nm	1255(10) nm	732(20) nm
$YBCO_{6.67}$ thin film		19.9(3) nm	269(1) nm	396(5) nm
$YBCO_{6.67}$ ortho-VIII	$B\|\|b$-axis	24.4(9) nm	177(5) nm	-
	$B\|\|a$-axis	22.5(7) nm	158(2) nm	187(12) nm

with

$$\begin{aligned} N &= I_{\nu_-}\left(\nu_{\mathrm{p}}\beta\right) I_{\nu_+}\left(\nu_{\mathrm{p}}\right) - I_{\nu_-}\left(\nu_{\mathrm{p}}\right) I_{\nu_+}\left(\nu_{\mathrm{p}}\beta\right), \\ \nu_{\pm} &= \pm\frac{2\zeta}{\lambda_{\mathrm{L}}}, \\ \nu_{\mathrm{p}} &= \frac{2\zeta}{\lambda_{\mathrm{P}}}, \\ \beta &= \exp\left[-d_{\mathrm{sc}}/\left(2\zeta\right)\right], \end{aligned}$$

where $I_\nu(x)$ is the modified Bessel function of the first kind [141], which can be written as

$$I_\nu(x) = (x/2)^\nu \sum_{k=0}^{\infty} \frac{(x/2)^{2k}}{k!\ \Gamma\left(\nu + k + 1\right)}.$$

For the single crystal, where a semi-infinite thickness is assumed ($d_{\mathrm{SC}} \to \infty$), the solution for $z > z_0$ is:

$$\frac{B\left(z\right)}{B_{\mathrm{ext}}} = \frac{I_{\nu_+}\left(\nu_{\mathrm{p}}\sqrt{\exp\left[-\left(z - z_0\right)/\zeta\right]}\right)}{I_{\nu_+}\left(\nu_{\mathrm{p}}\right)},$$

with

$$\begin{aligned} \nu_+ &= \frac{2\zeta}{\lambda_{\mathrm{L}}} \\ \nu_{\mathrm{p}} &= \frac{2\zeta}{\lambda_{\mathrm{P}}}. \end{aligned}$$

Taking this phenomenological model into account, the spectra for illuminated YBCO were

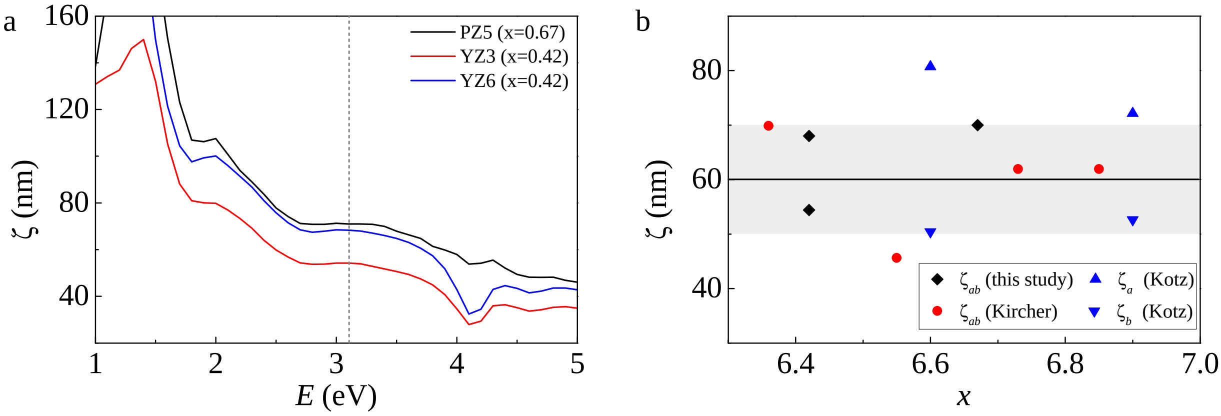

Figure 6.16: The determined penetration depth ζ versus the photon energy E for three YBCO thin-film samples (a). The vertical gray dashed line corresponds to the energy $E = 3.1\,\mathrm{eV}$ used for illumination in the LE-μSR experiments. b: Overview of the penetration depth ζ for $E = 3.1\,\mathrm{eV}$ as function of doping x for YBCO samples of the present study and of the Refs. [139, 140]. The indices i of ζ_i refer to the respective dielectric function ϵ_i. The black line and the gray area correspond to the average light penetration depth and its error, respectively.

analyzed. The determined quantities are stated in Table 6.3. Parameters known from the initial state and the ellipsometry measurements (z_0, λ_L, and ζ) were fixed. In Fig. 6.17 the theoretical curves assuming the London model (blue), according to the fitting results of the YBCO measurements before illumination, are plotted in combination with the theoretical curves of the illuminated state. Since $\zeta \simeq 60\,\mathrm{nm}$ is short compared to λ_L the difference between the illuminated penetration profile the initial magnetic penetration profile is a parallel shift for larger z-values in the case of the single crystal (Fig. 6.17c). For the thin films the parallel shift to lower $B(z)$ values due to illumination is observed in a broad region around the center. Only at small z-values are the magnetic penetration profiles not parallel, and the magnetic field is screened more strongly. The penetration profile in the thin films is asymmetric after illumination and the minimum is shifted to lower z-values (Fig. 6.17a+b). Within the theoretical curves these findings agree with our observations from the LE-μSR studies. The adapted model describes our LE-μSR data very well, as presented in Fig. 6.15.

The substantial changes of n_s due to illumination are more pronounced for strongly underdoped samples. The measured change of the superfluid density at the vacuum interface $n_\mathrm{s,illum}/n_\mathrm{s,0} = 1 + (\lambda_\mathrm{L}/\lambda_\mathrm{P})^2$ is much larger for $x = 0.42$ [$n_\mathrm{s,illum}/n_\mathrm{s,0} = 3.9(2)$] than for $x = 0.67$ [$n_\mathrm{s,illum}/n_\mathrm{s,0} = 1.45(3)$ and $n_\mathrm{s,illum}/n_\mathrm{s,0}$(ortho-VIII)$= 1.7(1)$]. Comparing the magnetic penetration depth of optimally doped YBCO $\lambda_\mathrm{L,optimal}$ to the minimal penetration

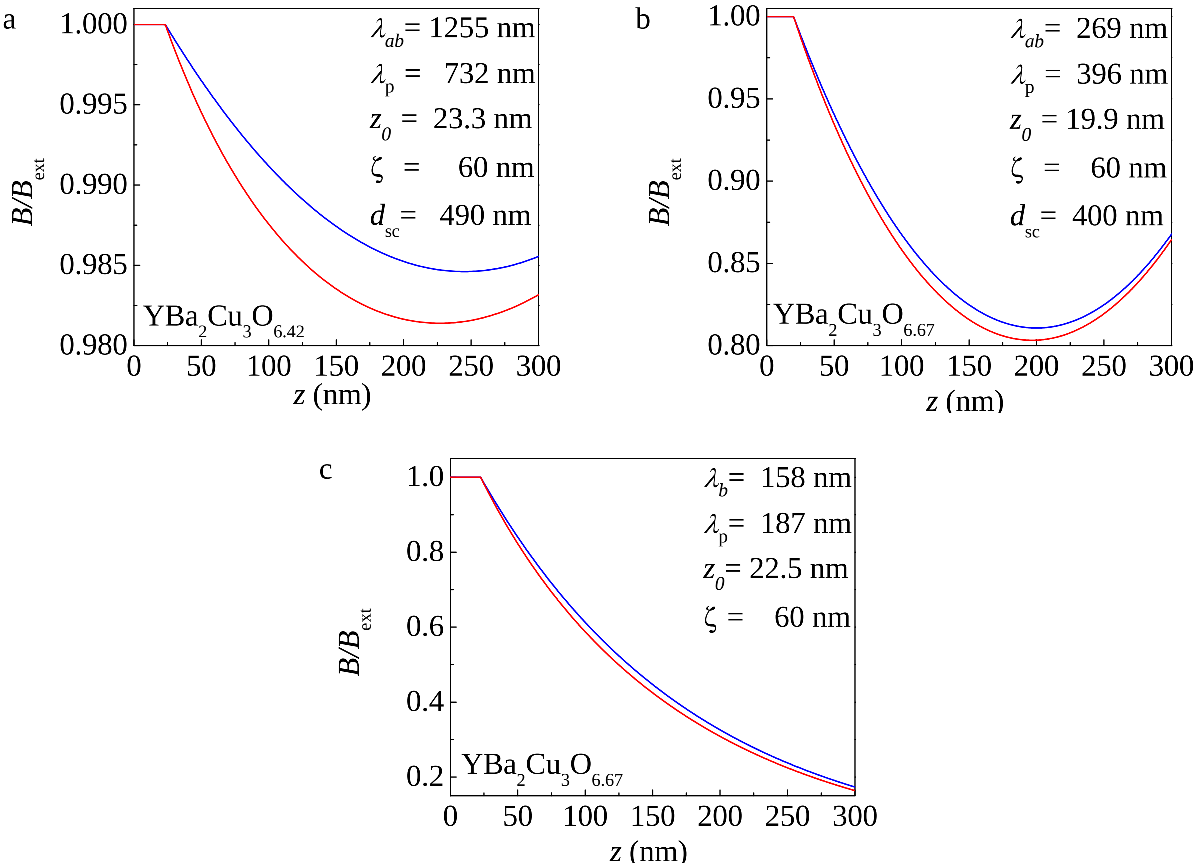

Figure 6.17: Calculated magnetic penetration profile $B(z)$ along the crystallographic c axis normalized to an applied magnetic field B_{ext} using the parameters obtained from thin-film set $\text{YBaCuO}_{6.42}$ (a), thin-film set $\text{YBaCuO}_{6.67}$ (b), and detwinned YBCO ortho-VIII single crystal mosaic (c). The presented magnetic field profiles correspond to the initial state (blue) and to the illuminated state (red).

depth present after illumination in our samples at $z = z_0$

$$\lambda_{\text{min}} = \frac{1}{\sqrt{\frac{1}{\lambda_{\text{L}}^2} + \frac{1}{\lambda_{\text{P}}^2}}}, \tag{6.4}$$

listed in Table 6.4, leads to the conclusion, that optimal doping is not yet reached in any part of the different samples. The ortho-VIII single crystal set is much closer to optimal doping at the surface compared to the YBCO thin-film set of the same doping. This is expected, since the single crystals are better ordered compared to the thin films, which is in agreement with the lower magnetic penetration depth before illumination. The value of the strongly underdoped thin-film set with $x = 0.42$ is far from optimal doping (see Tab. 6.4).

Table 6.4: Magnetic penetration depth $\lambda_{\mathrm{L,optimal}}$ of optimally doped YBCO [49] and the minimal reached penetration depth after illumination of our sample sets λ_{min}. In the case of the thin films the corresponding values of the average penetration depths are stated (λ_{ab}), while for the single crystal λ_b values are presented.

Sample	λ_{min}	$\lambda_{\mathrm{L,optimal}}$
$\mathrm{YBCO_{6.42}}$ thin films (10 K)	632(13) nm	
$\mathrm{YBCO_{6.67}}$ thin films (10 K)	223(1) nm	
$\mathrm{YBCO_{6.97}}$ thin films (20 K)		146(3) nm
$\mathrm{YBCO_{6.67}}$ ortho-VIII (10 K)	121(3) nm	
$\mathrm{YBCO_{6.97}}$ single crystals (8 K)		112(4) nm

This is not surprising, because much more charge carriers have to be introduced to reach optimal doping in the strongly underdoped case. Thus, the reached superfluid density is still below that of the other sample sets, although the total amount of additionally created charge carriers is much larger.

Studies of single crystals can be used to determine the role of disorder on the influence of the photo-induced changes. The investigated YBCO ortho-VIII single crystals consist of alternating Cu-O chains which are completely empty or full, forming a superstructure in the CuO_x layers [125]. Therefore, the amount of disorder is greatly reduced compared to our thin-film samples with equal doping level ($x = 0.67$). Moreover, the single crystals are detwinned which allows us to investigate the anisotropy of the photo-induced effect. Assuming pinned charge carriers along the crystallographic c axis [scenario (ii)], photo-persistent effects comparable to those in the thin films are expected. In the ortho-VIII single crystal mosaic, the superfluid density at the vacuum interface is indeed increased [$n_{\mathrm{s,illum}}/n_{\mathrm{s,0}}$(ortho-VIII)$= 1.7(1)$] if the magnetic field is applied along the crystallographic a axis (shielding currents flow along the Cu-O chains). The slightly larger effect in the single crystal compared to the thin films could result from the 15 % higher photon dose due to the longer illumination time. The observation agrees with our thin-film results, implying that the Cu-O chains are also lengthened in less disordered single crystals due to illumination. When the magnetic field is applied parallel to the crystallographic b axis no effect on $B(z)$ is observed. Within the experimental uncertainty the change of the superfluid density at the vacuum interface $n_{\mathrm{s,illum}}/n_{\mathrm{s,0}}$ has to be smaller than 1.06 for $B_{\mathrm{ext}}||b$-axis.

The anisotropic PPC behavior can be related to the in-plane anisotropy present in YBCO. The in-plane magnetic penetration depths at 10 K were found to be $\lambda_a = 177(5)$ nm ($B_{\mathrm{ext}}||b$) and $\lambda_b = 158(2)$ nm ($B_{\mathrm{ext}}||a$). The anisotropy between λ_a and λ_b is well known from opti-

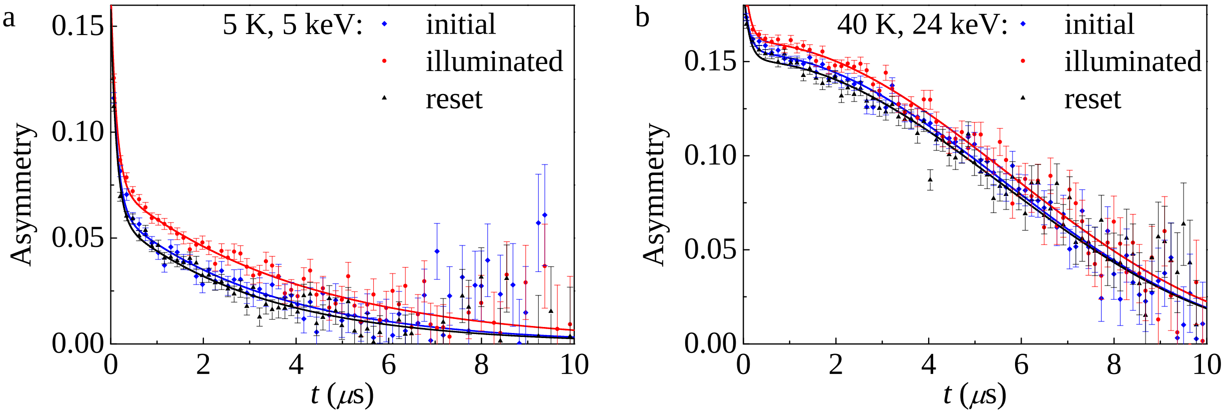

Figure 6.18: LE-μSR spectra in zero magnetic field for the thin-film sample set $YBCO_{6.42}$ measured with implantation energies of 5.0 keV (a) and 24.3 keV (b). The solid lines in (b) are the results of fits with the Gaussian Kubo-Toyabe function [83], whereas the solid lines in (a) are fits to an exponential decay. The contribution of the Ni background at early times is taken into account by adding a second exponentially decaying term.

mally doped YBCO [49, 142]. The ratio $\lambda_a/\lambda_b = 1.12(3)$ of the ortho-VIII single crystals is only slightly smaller compared to the values of optimally doped YBCO determined by various methods (λ_a/λ_b = 1.16–1.6, LE-μSR at 8 K: $\lambda_a/\lambda_b = 1.19$) [49], although it strongly depends on the doping level and the amount of oxygen disorder. The large in-plane anisotropy is discussed in the context of multiband effects [143]. This picture suggests a contribution of the Cu-O chains to the superfluid screening current along the chain direction, leading to a lower λ_b. Since the illumination of YBCO rearranges the Cu-O chains, the additional charge carriers may modify the contribution of the Cu-O chains to the superfluid density. Therefore, the photo-persistent effect would be clearly observed when the shielding currents flow along the chains ($B||a$-axis), but would be virtually absent for $B||b$-axis, consistent with our experiments (see Fig. 6.15c & d).

The light exposure does not only effect the superconducting state of YBCO, but also the magnetic properties as observed by ZF LE-μSR measurements. A weakening of the magnetic contributions was observed in the $YBCO_{6.42}$ set as depicted in Fig. 6.18. This could be due to a lower magnetic volume fraction or a change in the depolarization rate. To clarify the origin LF-μSR measurements would be required. A change in the asymmetry spectra is observed at all investigated temperatures ($5-40$ K) and also at high implantation energies, corresponding to a depth of about 100 nm. While the superconducting state is strengthened close to the vacuum interface, the magnetic contributions are suppressed over a broad region, indicating a competition between magnetism and superconductivity.

The presented LE-μSR data show a significant change in the magnetic penetration profile in the Meissner state of underdoped YBCO caused by an accumulated superfluid density n_s close to the surface. The persistent photo-induced changes of $n_s(z)$ appear only on a length scale comparable to the light penetration depth ζ. The illumination stimulates a self-organization of the Cu-O chains in YBCO and hence reduces disorder. This suggests that the reduced disorder leads to a non-trivial modification of the local band structure, probably due to hybridization of CuO_2 planes and chain layers, which in turn strengthens the superconducting ground state. Our results show the tremendous impact of nano-scale disorder on the superconducting ground state of cuprate superconductors.

This work is published in:

E. Stilp, A. Suter, T. Prokscha, Z. Salman, E. Morenzoni, H. Keller, P. Pahlke, R. Hühne, C. Bernhard, Ruixing Liang, W. N. Hardy, D. A. Bonn, J. C. Baglo, and R. F. Kiefl, *Controlling the near-surface superfluid density in underdoped* $YBa_2Cu_3O_{6+x}$ *by photo-illumination*, Sci. Rep. **4**, 6250 (2014).

URL: http://www.nature.com/srep/index.html

DOI: 10.1038/srep06250

SCIENTIFIC REPORTS

OPEN

SUBJECT AREAS:

SUPERCONDUCTING PROPERTIES AND MATERIALS

SURFACES, INTERFACES AND THIN FILMS

Received
15 May 2014

Accepted
13 August 2014

Published
1 September 2014

Correspondence and requests for materials should be addressed to E.S. (evelyn.stilp@psi.ch)

Controlling the near-surface superfluid density in underdoped $YBa_2Cu_3O_{6+x}$ by photo-illumination

E. Stilp[1,2], A. Suter[1], T. Prokscha[1], Z. Salman[1], E. Morenzoni[1], H. Keller[2], P. Pahlke[3,4], R. Hühne[4], C. Bernhard[5], Ruixing Liang[6,7], W. N. Hardy[6,7], D. A. Bonn[6,7], J. C. Baglo[6] & R. F. Kiefl[6]

[1]Laboratory for Muon Spin Spectroscopy, Paul Scherrer Institut, CH-5232 Villigen PSI, Switzerland, [2]Physik-Institut der Universität Zürich, Winterthurerstrasse 190, CH-8057 Zürich, Switzerland, [3]Institut für Festkörperphysik, Technische Universität Dresden, D-01062 Dresden, Germany, [4]Institute for Metallic Materials, IFW Dresden, D-01069 Dresden, Germany, [5]Department of Physics, University of Fribourg, CH-1700 Fribourg, Switzerland, [6]Department of Physics and Astronomy, University of British Columbia, Vancouver, British Columbia, Canada V6T 1Z1, [7]Canadian Institute for Advanced Research, Toronto, Ontario, Canada M5G 1Z8.

The interaction with light weakens the superconducting ground state in classical superconductors. The situation in cuprate superconductors is more complicated: illumination increases the charge carrier density, a photo-induced effect that persists below room temperature. Furthermore, systematic investigations in underdoped $YBa_2Cu_3O_{6+x}$ (YBCO) have shown an enhanced critical temperature T_c. Until now, studies of photo-persistent conductivity (PPC) have been limited to investigations of structural and transport properties, as well as the onset of superconductivity. Here we show how changes in the magnetic screening profile of YBCO in the Meissner state due to PPC can be determined on a nanometer scale utilizing low-energy muons. The data obtained reveal a strongly increased superfluid density within the first few tens of nanometers from the sample surface. Our findings suggest a non-trivial modification of the near-surface band structure and give direct evidence that the superfluid density of YBCO can be controlled by light illumination.

Tuning the superfluid density of cuprate systems without introducing additional disorder into the structure is challenging. Illumination with photons is one tool to realize this. Photo-persistent conductivity caused by visible light is widely known in semiconductors such as doping-modulated superlattices of hydrogenated amorphous silicon (a-Si:H)[1] or in low doped n-type Ge[2]. In these systems the recombination is inhibited by the spatial separation of electrons and holes, leading to long recombination lifetimes. In conventional superconductors, short-time illumination with photons having energies larger than the Cooper pair binding energy causes transient pair breaking, leading to the creation of quasiparticles[3]. In this case, illumination reduces the energy gap and therefore weakens superconductivity. In contrast, in cuprates it has been demonstrated that mid-infrared femtosecond pulses induce transient superconductivity[4].

Remarkably, studies on $YBa_2Cu_3O_{6+x}$ with reduced oxygen content ($x < 1$) show a persistent increase in the electrical conductivity after continuous illumination with visible light, in thin films[5,6] as well as in single crystals[7]. The critical temperature T_c is shifted to higher values for a broad range of oxygen concentrations ($0.4 \leq x \leq 0.9$) up to $\Delta T_{c,\max} = 15$ K[8]. The magnitude of the shift strongly depends on the oxygen content x, the temperature at which the illumination is performed, and the photon dose[8]. YBCO samples with $x < 0.4$, which are close to the metal-insulator transition, even become superconducting under illumination[9]. The photo-induced effects are only present for photon energies higher than 1.6 eV. The changes in resistivity and T_c persist until the temperature is raised beyond 270 K. Accordingly, in the literature the effect is referred to as photo-persistent conductivity. Above 270 K the resistivity relaxes back on time scales of hours to days, depending on the temperature[9]. This time scale is similar to that required for YBCO samples to stabilize their properties at room temperature after deoxygenation of the sample at high temperatures[10]. The PPC is fully reversible and reproducible. If infrared (IR) light is used for illumination an increase in conductivity is observed as well, but with a much smaller magnitude[11]. But if IR illumination is performed after illumination with visible light, the PPC is reduced by about 2 – 10% even at low temperatures.

Different origins have been proposed to explain the PPC, which can be generally divided into two main lines: (a) Photo-induced charge transfer and (b) photo-assisted oxygen ordering. The underlying mechanisms can only be understood by taking into account the anisotropic structure of YBCO. In contrast to most other cuprate systems, YBCO consists of CuO_2 planes separated by CuO_x layers which form Cu-O chains along the crystallographic b axis at higher doping levels x (Fig. 1). At low x the oxygen atoms in these CuO_x layers are isolated from each other[9]. Longer Cu-O chains form at higher x, leading to the formation of localized holes in the CuO_x layers. This results in a charge transfer of electrons from the CuO_2 planes to the Cu-O chains increasing the number of mobile holes in the CuO_2 planes. Therefore, the ordering of oxygen in the CuO_x layers plays a major role for conductivity as well as for superconductivity in YBCO. A longer average chain length leads to a higher charge carrier density in the CuO_2 planes and to a higher T_c[12] on the underdoped side of the phase diagram.

The scenario discussed above is crucial to an understanding of the proposed PPC mechanisms. In the case of photo-induced charge transfer, the absorbed photons create electron-hole pairs. The electrons are trapped at defects such as oxygen vacancies, preventing recombination. The holes are transfered to the CuO_2 planes where they contribute to the conductivity and, at low temperatures to the superconductivity. Thus mechanism (a) explains the increase in conductivity and the shift in T_c. However, it does not provide a natural explanation for the effects of IR light[11]. The photo-assisted oxygen ordering mechanism (b) assumes that the photons initiate a reordering of oxygen in the CuO_x layers, so that longer Cu-O chain fragments are present. This leads to an enhanced charge carrier transfer to the CuO_2 planes where superconductivity takes place. The proposed mechanism agrees with the observation that the time dependence of the resistivity relaxation is similar for photo-induced changes and for oxygen reordering after annealing. However, mechanism (b) alone fails to explain the IR experiments and why the oxygen atoms move under illumination. Therefore, a combination of both mechanisms was proposed[11].

In the combined model the trapped electrons at the oxygen vacancies act as local perturbations that modify the local electric field distribution. The induced dipole moments cause the movement of the oxygen in the CuO_x layers, resulting in a lengthening of the chain fragments. A simplified theoretical model[13] agrees with this interpretation. It confirms that local perturbations can affect the average chain length. Experimental[14] as well as theoretical[15] investigations have also shown that electrical fields influence the oxygen ordering and change T_c. The combined mechanism accounts for the infrared quenching, predicts the correct time dependence of the photo-excitation process, and gives the correct scale of the changes in resistivity produced by illumination.

Even though extensive structural studies were able to correlate the chain ordering to the charge transfer, leading to changes of the resistivity and T_c, little is known how illumination affects the superconducting state on the microscopic level. In our study we focused on a detailed investigation of the magnetic screening profile $B(z)$ in the Meissner state, utilizing low-energy muon spin rotation (LE-μSR)[16,17].

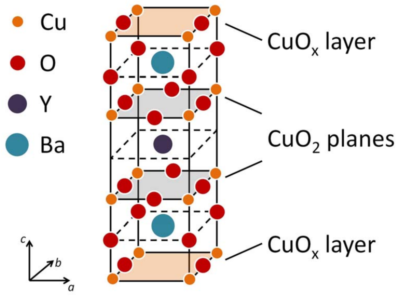

Figure 1 | **The crystal structure of $YBa_2Cu_3O_{6+x}$.**

Results & Discussion

LE-μSR is an unique and powerful technique to measure non-trivial $B(z)$ on a nanometer scale in a wide variety of superconducting single crystals[18], thin films[19,20], and heterostructures[21,22], allowing also the observation of non-local effects[23–25]. Positively charged muons are slowed down and implanted into the samples at different mean implantation depths $\bar{z}$ (Figs. 2 and 3). The Larmor frequency of the muons, $\omega_L(z)$, directly related to the local magnetic field B at the muon stopping site ($\omega_L = \gamma_\mu B$ with the muon gyromagnetic moment $\gamma_\mu = 2\pi \cdot 135.5$ MHz/T), is measured via the decay positron. For a semi-infinite sample, the London equation

$$\frac{d^2B(z)}{dz^2} = \frac{1}{\lambda_L^2} B(z), \tag{1}$$

yields a magnetic penetration profile $B(z) = B_{ext} \cdot \exp(-z/\lambda_L)$, for the boundary condition $B(z=0) = B_{ext}$. Therefore, measuring $B(z)$ allows one to determine the magnetic penetration depth λ_L and thereby the superfluid density $n_s \propto 1/\lambda_L^2$ [26]. The process cycle and the conditions of the LE-μSR measurements are presented schematically in Fig. 3. The in-situ illumination setup is described in detail in the supplementary section S1.

Two sets of YBCO thin films ($x = 0.42, 0.67$) with twinned crystallographic a and b axes were investigated along with a detwinned single-crystal mosaic ($x = 0.67$). The YBCO thin film sets show shifts of $\Delta T_c = 6.4(6)$ K ($x = 0.42$) and $\Delta T_c = 0.9(1)$ K ($x = 0.67$) after illumination with about $7 \cdot 10^{22}$ photons/cm^2, in agreement with previous results[8] (see Fig. 4). The magnetic screening profiles $\bar{B}(\bar{z})$ determined by LE-μSR show for the initial state (before illumination) an exponential decay for the single crystals and a cosh behaviour in the thin films (resulting from the exponential penetration of the magnetic field from both interfaces) as depicted in Fig. 2. After illumination, all magnetic screening profiles are shifted to lower values and exhibit a pronounced change in shape. The corresponding superfluid density n_s is enhanced in all sample sets investigated.

Two different scenarios for the PPC change of n_s as function of the depth z can be envisaged: (i) The additional charge carries are mobile along the lattice c direction, hence they are distributed homogeneously over the whole sample. The superfluid density is raised, but is still constant as a function of depth z. Thus only the absolute value of λ_L is changed. Since the additional superfluid density is spatially averaged over the volume in scenario (i), the PPC changes of n_s would be much less pronounced or more likely to be absent in single crystals compared to thin films. However, this does not account for our results, since a change in $\bar{B}(\bar{z})$ is observed in the YBCO ortho-VIII single crystals (see Fig. 2c). (ii) The PPC charge carriers are pinned to the layer where they are created. Here, the changes in the superfluid density would be proportional to the light penetration profile: n_s increases mainly close to the vacuum interface, since the light penetrates exponentially into the sample. A depth-dependent superfluid density leads in turn to a modification of the Meissner screening field profile $B(z)$. Our results agree with the second scenario. At small depths z the applied magnetic field is more strongly shielded compared to the initial state. At higher z values the $B(z)$ curves are almost parallel. We therefore describe the penetration profiles of the illuminated samples by:

$$\frac{d^2B(z)}{dz^2} = \left(\frac{1}{\lambda_L^2} + \frac{1}{\lambda_P^2} e^{-z/\zeta}\right) B(z), \tag{2}$$

where $1/\lambda_L^2$ is proportional to the initial superfluid density before illumination $n_{s,0}$, $1/\lambda_P^2$ corresponds to the photo-induced superfluid density at the vacuum interface $n_{s,illum}$, and ζ is the characteristic

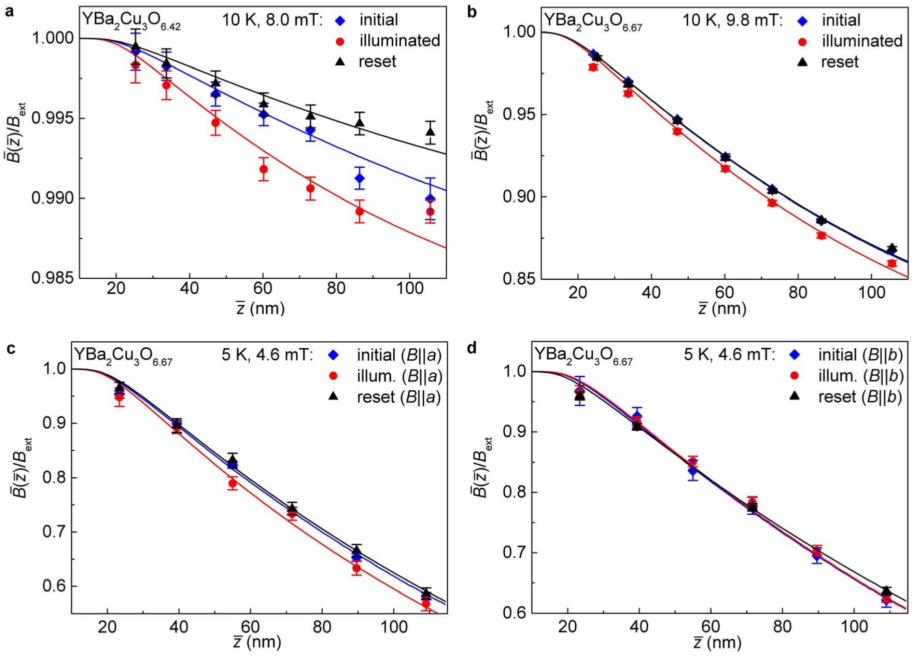

Figure 2 | Modifications of the magnetic screening profile due to illumination. The magnetic penetration profile $\bar{B}(\bar{z})$ along the crystallographic *c* axis normalized to the applied magnetic field B_{ext} of thin-film $YBa_2Cu_3O_{6.42}$ (**a**), thin-film $YBa_2Cu_3O_{6.67}$ (**b**), and detwinned $YBa_2Cu_3O_{6.67}$ single crystals in the ortho-VIII phase for B_{ext} applied parallel to the crystallographic *a* axis (**c**) and for B_{ext} parallel to the *b* axis (**d**). The applied magnetic field B_{ext} and the temperature are given in each figure. The presented field profiles correspond to the initial state (blue diamonds, before illumination), to the illuminated state (red circles, after illumination) and the recovered state (black triangles, after heating up to room temperature for about one day). The pronounced changes of the $\bar{B}(\bar{z})$ profiles (in magnitude and shape) due to visible light illumination are caused by a substantial increase of the superfluid density on the nanometer length scale to the vacuum interface.

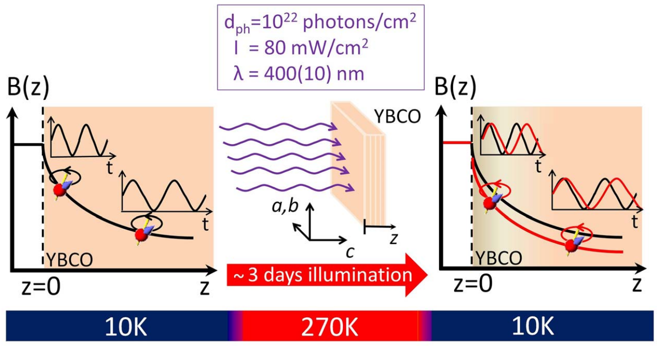

Figure 3 | Schematic diagram of the experimental μSR process cycle. Left panel: After zero field cooling (ZFC) the sample an external magnetic field $B_{ext}/\mu_0 < H_{c_1}$ was applied within the *ab*-plane. The interface to the vacuum is labeled with $z = 0$. The screened magnetic field values *B* at different depths *z* along the crystallographic *c* axis were determined via the Larmor frequency of the implanted positively charged muons (red circles) $\omega_L = \gamma_\mu B$ at 10 K for the YBCO thin films and at 5 K for the YBCO ortho-VIII single crystals. The muon spin precesses at ω_L around the local magnetic field *B* present in the sample. The Larmor frequency ω_L is extracted from the muon-spin polarization function $P(t)$ measured via the decay positron. Center panel: The LE-μSR measurements were followed by the in-situ photo illumination of the samples for ~ 3 days ($4-5 \cdot 10^{22}$ photons/cm^2) at 270 K with a high-intensity LED source. Right panel: Afterwards the samples were ZFC to 10 K/5 K, repeating the measurement of the screened magnetic field profile as described above. To return the YBCO system to its initial state it was kept above room temperature for about one day. The resistance measurements have been performed under comparable conditions (see supplementary section S1).

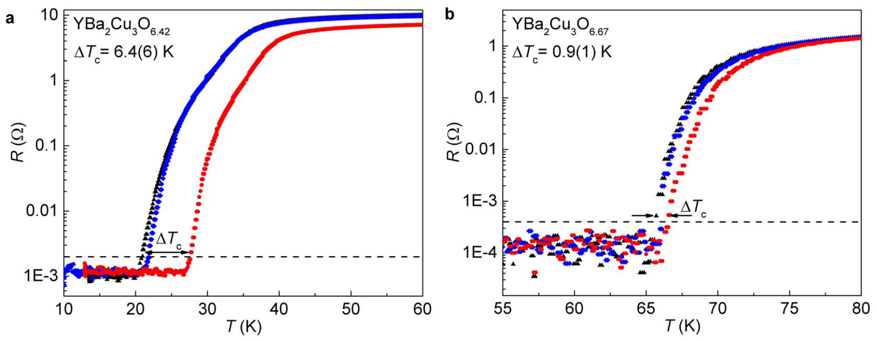

Figure 4 | Shifts in the critical temperature ΔT_c from resistance measurements. Resistance R versus temperature T of $YBa_2Cu_3O_{6.42}$ (**a**) and $YBa_2Cu_3O_{6.67}$ (**b**) thin films for the initial state (blue diamonds, before illumination), the illuminated state (red circles, after illumination at 270 K), and the recovered state (black triangles, sample kept above room temperature for about one day). The critical temperature T_c was determined as the temperature where R exceeds twice the RMS of the noise (dashed line) during heating of the samples. The shifts of the resistivity curves to lower values, after illumination at 270 K, reflect an increased charge carrier density at all temperatures $T < 270$ K. The arrows indicate the shifts in the transition temperatures ΔT_c due to visible-light illumination.

length over which the changes of n_s take place. The solution of this phenomenological model, used for fitting, is described in detail in the supplementary section S3. The estimated values of ζ obtained from the μSR data are of the order of the optical light penetration depth. Taking ellipsometry measurements of our thin film samples in the pristine state into account we find an average light penetration depth of $\zeta = 60(10)$ nm, consistent with previous studies on single crystals[27,28], as presented in the supplementary section S2. Hence, we used this value for the detailed analysis of $n_s(z)$.

The substantial changes of n_s due to illumination are more pronounced for strongly underdoped samples as observed in the thin film sets: The measured change of the superfluid density at the vacuum interface $n_{s,illum}/n_{s,0} = 1+(\lambda_L/\lambda_P)^2$ is much larger for $x = 0.42$ [$n_{s,illum}/n_{s,0} = 3.9(2)$] than for $x = 0.67$ [$n_{s,illum}/n_{s,0} = 1.45(3)$]. In all sample sets investigated the PPC is fully reversible. After the thermal reset, the original Meissner screening profile is recovered as depicted in Fig. 2.

Studies of single crystals were used to determine the role of disorder on the influence of the photo-induced changes. The investigated YBCO ortho-VIII single crystals consist of alternating Cu-O chains which are completely empty or full, forming a superstructure in the CuO_x layers[29]. Therefore, the amount of disorder is greatly reduced compared to our thin-film sample sets with equal doping level ($x = 0.67$). Moreover, the single crystals are detwinned which allows us to investigate the anisotropy of the photo-induced effect. Assuming pinned charge carriers along the c axis [scenario (ii)], photo-persistent effects comparable to those in the thin-film sets are expected. In the ortho-VIII single crystal mosaic, the superfluid density at the vacuum interface is increased [$n_{s,illum}/n_{s,0}$(ortho-VIII)= 1.7(1)] if the magnetic field is applied along the a axis (shielding currents flow along the Cu-O chains). The observation agrees with our thin-film results, implying that the Cu-O chains are also lengthened in less disordered single crystals due to illumination or showing that the order is not as perfect in the near-surface region compared to the bulk. The slightly larger effect in the single crystal mosaic compared to the thin-film set of equal doping could result from the 15% higher photon dose due to the longer illumination time (see supplementary table S1). When the magnetic field is applied parallel to the b axis no effect on $B(z)$ is observed. Within the experimental uncertainty the change of the superfluid density at the vacuum interface $n_{s,illum}/n_{s,0}$ has to be smaller than 1.06 for $B_{ext}||b$-axis.

The anisotropic PPC behaviour can be related to the in-plane anisotropy present in YBCO. The in-plane London penetration depths were determined as described in Refs. 18, 19 and found to be $\lambda_a = 177(5)$ nm ($B_{ext}||b$) and $\lambda_b = 158(2)$ nm ($B_{ext}||a$). The anisotropy between λ_a and λ_b is well known from optimally doped YBCO[18,30]. The ratio $\lambda_a/\lambda_b = 1.12(3)$ of the ortho-VIII single crystal set is only slightly smaller compared to the values of optimally doped YBCO determined by various methods (μSR: $\lambda_a/\lambda_b = 1.16–1.19$)[18], although it strongly depends on the doping level and the amount of oxygen disorder. The large in-plane anisotropy is discussed in the context of multiband effects[31]. This proximity model takes into account a contribution of the Cu-O chains to the superfluid density by assuming a hybridization of plane and chain wave functions within a three-band tight-binding Hamiltonian. Disorder within the Cu-O chains localizes a small fraction of the chain electron states, yielding a higher λ_b, but has no effect on λ_a[31]. Since the illumination of YBCO rearranges the Cu-O chains the amount of disorder within the Cu-O chains is reduced, thus diminishing the fraction of localized chain electrons. According to the proximity model, the additional superfluid density only affects λ_b, consistent with our experimental data (see Fig. 2c-d).

The presented LE-μSR data show a significant change in the magnetic penetration profile in the Meissner state of underdoped YBCO caused by an accumulated superfluid density n_s close to the surface. The persistent photo-induced changes of $n_s(z)$ appear only on a length scale comparable to the light penetration depth. The illumination stimulates a self-organization of the Cu-O chains in YBCO and hence reduces disorder. This may suggest that the reduced disorder leads to a non-trivial modification of the local band structure, probably due to hybridization of CuO_2 planes and chain layers, which in turn strengthens the superconducting ground state. Our results show the tremendous impact of nano-scale disorder on the superconducting ground state of cuprate superconductors.

Methods

Sample preparation and characterization. The $YBa_2Cu_3O_{6+x}$ (YBCO) thin films were deposited on single crystal 1×1 cm^2 (001) $SrTiO_3$ substrates by on-axis pulsed laser deposition from a stoichiometric target using a KrF excimer laser ($\lambda = 248$ nm). To grow YBCO layers with a thickness of 400(20) nm and 490(60) nm, 3000 and 4800 laser pulses with a laser repetition rate of 5 Hz were used under an oxygen partial pressure of 0.3 mbar. After deposition at 800°C, the samples were cooled to 780°C, where the chamber was flooded with 400 mbar oxygen to achieve fully oxidized films with a $T_c = 90.0(5)$ K. More details on the PLD growth are described in Refs. 32, 33. The layer thicknesses were determined by measuring the height of a chemical etched edge, ranging from the surface to the substrate, using atomic force microscopy. To check the homogeneity of the samples the thickness was measured at several points.

The reduction of the oxygen content was realized by a post-annealing process in a tubular furnace, described in detail in Ref. 34. In particular, the samples were annealed

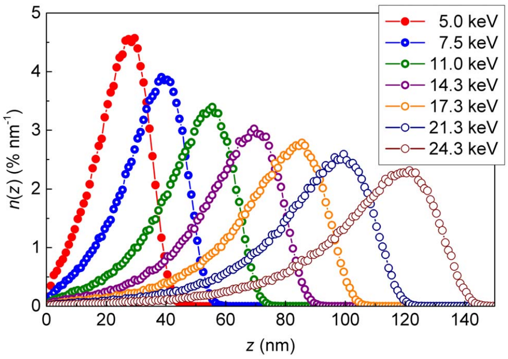

Figure 5 | Muon stopping profiles in YBCO. The normalized stopping distribution $n(z)$ for positively charged muons at different implantation energies for YBCO was simulated with TRIM.SP[38]. The lines are guides to the eye.

at a defined time and temperature in a flowing O_2/N_2 gas mixture. The process was concluded with a rapid cooling step to temperatures below 100°C in order to freeze in the oxygen concentration of the thin films. Annealing of the 400 nm thick samples at 450°C for 40 min in 2860 ppm O_2 atmosphere reduced the T_c of the YBCO to 66.7(8) K (corresponding to $x = 0.67$). The 490 nm thick films with $T_c = 21(2)$ K ($x = 0.42$) were annealed for 70 min at 500°C in a 215 ppm O_2 atmosphere. Purely c-axis oriented growth of YBCO was verified by $\Theta - 2\Theta$ measurements using a Bruker D8 Advance X-ray powder diffractometer with a Co anode. The resistivity measurements were performed with a four-point measurement on a cold finger cryostat in ultra high vacuum (about 10^{-8} mbar) under comparable conditions used for the μSR experiments.

The YBCO ortho-VIII single crystals were grown by the self-flux technique described in detail in Ref. 35. For the growth, $BaZrO_3$ ceramic crucibles were fabricated. After the self-flux growth the YBCO crystals were annealed in flowing oxygen for six days at 648°C, to set the oxygen content to $x = 0.67$. Afterwards the crystals were sealed in a quartz tube and annealed at 570°C for four days to homogenize the oxygen. During detwinning, the sample is heated to 180 – 250°C and squeezed with a pressure of about 100 MPa along one of the a/b axes under flowing nitrogen gas, causing the twin domains to reorient so that the a-axis (which has a shorter lattice constant) is along the direction of the pressure. For the formation of the oxygen vacancy ordered superstructure ortho-VIII, the YBCO single crystals were low temperature annealed at 40 – 42°C for five days. The final YBCO ortho-VIII single crystals had an estimated critical temperature of $T_c \simeq 66.5(5)$ K. One year later a $T_c = 67.8(5)$ K was determined with a Quantum Design MPMS SQUID magnetometer. The increase of T_c of about 1 K with time is natural in these crystals and is even expected, as the chain oxygen atoms slowly become better ordered even at room temperature and some of the interstitial oxygen impurities enter the Cu-O chains.

Low-energy muon spin rotation. The LE-μSR experiments were performed at the μE4 beamline at the Paul Scherrer Institut (PSI, Switzerland). For the thin-film measurements a mosaic of four 1×1 cm² large samples was glued with silver paint onto a nickel-coated aluminum plate. For the YBCO ortho-VIII measurements, a mosaic of 13 aligned single crystals, with an average size of about $2.1 \times 1.7 \times 0.2$ mm³, was used. The measurements have been performed in ultra high vacuum (about 10^{-9} mbar) on a cold finger cryostat.

The μSR technique uses positively charged muons (μ^+) as a local magnetic probe. To investigate the magnetic penetration depth profile $B(z)$, the muons are slowed down using a solid Ar/N_2 moderator, so that they stop on a nm scale in condensed matter. At the μE4 beamline the low energy muons are produced at a rate of about 10^4 s^{-1} [16] with ~ 100% spin polarization[36]. The muons are implanted into the sample where they thermalize within a few picoseconds without noticeable loss of polarization. There they decay after a mean μ^+ lifetime of $\tau_\mu = 2.197$ μs into a positron (e^+) and two neutrinos ($\bar{\nu}_\mu$, ν_e):

$$\mu^+ \rightarrow e^+ + \bar{\nu}_\mu + \nu_e.$$

The positrons are preferentially emitted along the μ^+ spin direction at the time of decay due to the parity violation in the weak decay. Therefore, the detection of the time difference $t = t_e - t_s$ between the implantation time t_s and the decay time t_e of the μ^+ allows one to determine the temporal evolution of the muon-spin polarization $P(t)$ using the expression[37]:

$$N(t) = N_0 \, e^{-t/\tau_\mu} [1 + AP(t)] + N_{\mathrm{Bkg}}, \tag{3}$$

where $N(t)$ is the number of decay positrons at time t. The scale of the counted positrons is given by N_0. A is the observable decay asymmetry and N_{Bkg} is a time-independent background of uncorrelated events. More details on the LE-μSR technique are given in Refs. 16, 17. The experiments were performed in the Meissner state. After zero field cooling to 5 K, a magnetic field $B_{\mathrm{ext}}/\mu_0 < H_{c1}$ was applied parallel to the surface of the sample. The muon-spin polarization function $P(t)$ is then given by

$$P(t) = e^{-\sigma^2 t^2/2} \int n(z) \cos[\gamma_\mu B(z) t + \phi] \, dz, \tag{4}$$

where ϕ is the initial angle of the muon spin direction relative to the positron detector. The gyromagnetic ratio of the muon is $\gamma_\mu = 2\pi \cdot 135.5$ MHz/T. The depolarization rate σ is a measure of any inhomogeneous local magnetic field distribution at the μ^+ stopping site. The muon stopping distributions $n(z)$ (see Fig. 5) were simulated for energies in the range 5 – 25 keV using the Monte Carlo code TRIM.SP[38]. The reliability of these simulations has been studied in various thin films[17,39]. The mean stopping depth $\bar{z} = \int n(z)\, z \, dz$ of the muons in YBCO is in the range 25 – 106 nm. The corresponding mean magnetic field is $\bar{B}(\bar{z}) = \int n(z)\, B(z)\, dz$. To analyse the data, the penetration profiles given in supplementary section S3 were used for $B(z)$. The penetration depths λ_L were determined from global fits with the μSR data analysis software package musrfit[40], where μSR spectra for different energies are analysed simultaneously.

See supplementary information for full details on the illumination conditions, the ellipsometry measurements, and the penetration profile model.

1. Kakalios, J. & Fritzsche, H. Persistent Photoconductivity in Doping-Modulated Amorphous Semiconductors. *Phys. Rev. Lett.* **53**, 1602 (1984).
2. Prokscha, T. *et al.* Photo-induced persistent inversion of germanium in a 200-nm-deep surface region. *Sci. Rep.* **3**, 2569 (2013).
3. Testardi, L. R. Destruction of Superconductivity by Laser Light. *Phys. Rev. B* **4**, 2189 (1971).
4. Fausti, D. *et al.* Light-induced Superconductivity in a Stripe-Ordered Cuprate. *Science* **331**, 189 (2011).
5. Kirilyuk, A. I., Kreines, N. M. & Kudinov, V. I. Frozen photoconductivity in YBaCuO films. *JETP Lett.* **52**, 49 (1990).
6. Kudinov, V. I., Kirilyuk, A. I. & Kreines, N. M. Photoinduced superconductivity in YBaCuO films. *Phys. Lett. A* **151**, 358 (1990).
7. Yu, G., Heeger, A. J., Stucky, G., Herron, N. & McCarron, E. M. Transient photoinduced conductivity in semiconducting single crystals of $YBa_2Cu_3O_{6.3}$: Search for photoinduced metallic state and for photoinduced superconductivity. *Solid State Commun.* **72**, 345-349 (1989).
8. Tanabe, K., Kubo, S., Hosseini Teherani, F., Asano, H. & Suzuki, M. Effects of Photoinduced Hole Doping on Normal-State and Superconducting Transport in Oxygen-Deficient $YBa_2Cu_3O_y$. *Phys. Rev. Lett.* **72**, 1537 (1994).
9. Kudinov, V. I. *et al.* Persistent photoconductivity in $YBa_2Cu_3O_{6+x}$ films as a method of photodoping toward metallic and superconducting phases. *Phys. Rev. B* **47**, 9017 (1993).
10. Veal, B. W. *et al.* Observation of temperature-dependent site disorder in $YBa_2Cu_3O_{7-\delta}$ below 150°C. *Phys. Rev. B* **42**, 6305 (1990).
11. Bubb, D. M. *et al.* Wavelength and photon dose dependence of infrared quenched persistent photoconductivity in $YBa_2Cu_3O_{6+x}$. *Phys. Rev. B* **60**, 6827 (1999).
12. Milić, M. M., Lazarov, N. Dj. & Cucić, D. A. Study on the photo-induced oxygen reordering in $YBa_2Cu_3O_{6+x}$. *Nucl. Inst. and Meth. in Phys. Res. B* **279**, 215-218 (2012).
13. Bubb, D. M. & Federici, J. F. Cellular automata model for persistent photoconductivity in YBCO. *J. Phys.: Condens. Matter* **12**, L261-L267 (2000).
14. Kula, W. & Sobolewski, R. Charging effect in partially oxygen-depleted superconducting Y-Ba-Cu-O thin films. *Phys. Rev. B* **49**, 6428(R) (1994).
15. Grigelionis, G., Tornau, E. E. & Rosengren, A. Effect of an electric field on oxygen ordering and superconducting temperature of $YBa_2Cu_3O_{6+x}$ thin films. *Phys. Rev. B* **53**, 425 (1996).
16. Prokscha, T. *et al.* The new μE4 beam at PSI: A hybrid-type large acceptance channel for the generation of a high intensity surface-muon beam. *Nucl. Instrum. Methods Phys. Res., Sect. A* **595**, 317 (2008).
17. Morenzoni, E., Prokscha, T., Suter, A., Luetkens, H. & Khasanov, R. Nano-scale thin film investigations with slow polarized muons. *J. Phys.: Condens. Matter* **16**, S4583 (2004).
18. Kiefl, R. F. *et al.* Direct measurement of the London penetration depth in $YBa_2Cu_3O_{6.92}$ using low-energy μSR. *Phys. Rev. B* **81**, 180502(R) (2010).
19. Jackson, T. J. *et al.* Depth-Resolved Profile of the Magnetic Field beneath the Surface of a Superconductor with a Few nm Resolution. *Phys. Rev. Lett.* **84**, 4958 (2000).
20. Stilp, E. *et al.* Modifications of the Meissner screening profile in $YBa_2Cu_3O_{7-\delta}$ thin films by gold nanoparticles. *Phys. Rev. B* **89**, 020510(R) (2014).
21. Morenzoni, E. *et al.* The Meissner effect in a strongly underdoped cuprate above its critical temperature. *Nat. Commun.* **2**, 272 (2011).
22. Wojek, B. M. *et al.* Magnetism, superconductivity, and coupling in cuprate heterostructures probed by low-energy muon-spin rotation. *Phys. Rev. B* **85**, 024505 (2012).

23. Suter, A. *et al.* Observation of nonexponential magnetic penetration profiles in the Meissner state: A manifestation of nonlocal effects in superconductors. *Phys. Rev. B* **72**, 024506 (2005).
24. Kozhevnikov, V. *et al.* Nonlocal effect and dimensions of Cooper pairs measured by low-energy muons and polarized neutrons in type-I superconductors. *Phys. Rev. B* **87**, 104508 (2013).
25. Romanenko, A. *et al.* Strong Meissner screening change in superconducting radio frequency cavities due to mild baking. *Appl. Phys. Lett.* **104**, 072601 (2014).
26. Sonier, Jeff, E., Brewer, Jess, H. & Kiefl, Robert, F. μSR studies of the vortex state in type-II superconductors. *Rev. Mod. Phys.* **72**, 769 (2000).
27. Kircher, J. *et al.* Anisotropy and oxygen-stoichiometry dependence of the dielectric tensor of $YBa_2Cu_3O_{7-\delta}$ ($0 \leq \delta \leq 1$). *Phys. Rev. B* **44**, 217 (1991).
28. Kotz, A. L. *et al.* Anisotropy of the optical dielectric function in the *ab* plane for $YBa_2Cu_3O_{7-\delta}$. *Phys. Rev. B* **45**, 2577(R) (1992).
29. Zimmermann, M. v. *et al* Oxygen-ordering superstructures in underdoped $YBa_2Cu_3O_{6+x}$ studied by hard x-ray diffraction. *Phys. Rev. B* **68**, 104515 (2003).
30. Basov, D. N. *et al.* In-Plane Anisotropy of the Penetration Depth in $YBa_2Cu_3O_{7-x}$ and $YBa_2Cu_4O_8$ Superconductors. *Phys. Rev. Lett.* **74**, 598 (1995).
31. Atkinson, W. A. Disorder and chain superconductivity in $YBa_2Cu_3O_{7-\delta}$. *Phys. Rev. B* **59**, 3377 (1999).
32. Hühne, R. *et al.* Preparation of coated conductor architectures on Ni composite tapes. *Supercond. Sci. Technol.* **20**, 709 (2007).
33. Kiessling, A. *et al.* Nanocolumns in $YBa_2Cu_3O_{7-x}/BaZrO_3$ quasi-multilayers: formation and influence on superconducting properties. *Supercond. Sci. Technol.* **24**, 055018 (2011).
34. Pahlke, P., Trommler, S., Holzapfel, B., Schultz, L. & Hühne, R. Dynamic variation of biaxal strain in optimally doped and underdoped YBa2Cu3O7- thin films. *J. Appl. Phys.* **113**, 123907 (2013).
35. Liang, R., Bonn, D. A. & Hardy, W. N. Growth of YBCO single crystals by the self-flux technique. *Philos. Mag.* **92**, 2563 (2012).
36. Morenzoni, E. *et al.* Generation of very slow polarized positive muons. *Phys. Rev. Lett.* **72**, 2793 (1994).
37. Yaouanc, A. & Dalmas de Reotier, P. *Muon Spin Rotation, Relaxation, and Resonance: Applications to Condensed Matter* (Oxford University Press, Oxford, 2011).
38. Eckstein, W. *Computer Simulation of Ion-Solid Interactions* (Springer, Berlin, 1991).
39. Morenzoni, E. *et al.* Implantation studies of keV positive muons in thin metallic layers. *Nucl. Instr. Meth. B* **192**, 254 (2002).
40. Suter, A. & Wojek, B. M. Musrfit: A Free Platform-Independent Framework for μSR Data Analysis. *Phys. Procedia* **30**, 69 (2012).

Acknowledgments

We gratefully acknowledge H.-P. Weber for his technical support. We are indebted to M. Döbeli for the RBS measurements, Ch. Wang for the help to perform the ellipsometry measurements and A. Boris for helpful discussion of the ellipsometry data. The LE-μSR experiments were carried out at the μE4 beamline at SμS, Paul Scherrer Institut, Switzerland. This work was partly supported by the Swiss National Science Foundation.

Author contributions

E.S., A.S. and T.P. proposed the idea, performed the resistivity and μSR measurements, analysed the data and wrote the paper. Z.S. and R.F.K. were involved in the μSR measurements. P.P. and R.H. prepared and characterized the YBCO thin films. J.C.B., R.L., W.N.H. and D.A.B. prepared and characterized the YBCO ortho VIII single crystals. C.B. analysed the ellipsometry data. E.S., A.S., T.P., Z.S., E.M., H.K., P.P., R.H., C.B., C.B., R.L., W.N.H., D.A.B. and R.F.K. discussed the results and contributed to the manuscript.

Additional information

Supplementary information accompanies this paper at http://www.nature.com/scientificreports

Competing financial interests: The authors declare no competing financial interests.

How to cite this article: Stilp, E. *et al.* Controlling the near-surface superfluid density in underdoped $YBa_2Cu_3O_{6+x}$ by photo-illumination. *Sci. Rep.* **4**, 6250; DOI:10.1038/srep06250 (2014).

7 Conclusion

The investigated photo-induced effects on the microscopic properties of $La_{2-x}Sr_xCuO_4$ and $YBa_2Cu_3O_{6+x}$ studied by resistivity and LE-μSR experiments revealed a complex interplay between disorder and electronic properties in cuprate high temperature superconductors.

Thin-film LSCO exhibits a changed absolute scale of the magnetic transition temperatures compared to single crystals. At the same time, the value of the staggered magnetization, its temperature dependence, and the influence of doping stay the same. The critical temperature in LSCO thin films differs from the bulk system as well. Whereas the sign of the change in T_c strongly depends on the kind of stress present in the film (compressive or tensile strain), the changes on the magnetic phases depend only slightly on the substrate. The sign is not changed. Thus, it is concluded that disorder within the films has a tremendous influence on the absolute scale of the magnetic transition temperatures.

Illumination of LSCO with visible light leads to a transient photoconductivity, disappearing on time scales of several hundred seconds after switching off the light. Below 100 K, the temperature dependence of the photoconductivity reverses when Sr is added. At high temperatures the photoconductivity is about $1/\Omega$cm for all investigated Sr concentrations. The created electron-hole pairs neither promote nor disturb the magnetic state of LSCO as observed by LE-μSR experiments, likely because the number of generated charge carriers is too small to cause a measurable change.

The magnetic and superconducting properties of YBCO strongly depend on the oxygen ordering. The quality of thin-film samples can be improved by adding Au nanoparticles. The higher T_c and the lower London penetration depth could be due to a lower defect density or a diffusion of Au into the Cu-O chains. The influence of the substrate quality is still an open issue. In order to obtain a homogeneous distribution of the Au nanoparticles within the YBCO film, systematic RBS and resistivity studies on the process parameters have to be performed in the future.

The photo persistent state of YBCO has also an influence on its superconducting properties. The superfluid density is raised within the first few ten nanometer below the vacuum interface according to the light penetration depth, as observed in thin films as well as single crystals. Photo illumination with visible light leads to a reordering of the oxygen within the Cu-O chains. This study also confirms the strong influence of disorder on the microscopic properties of cuprates. Until now, we proved that illumination may affect the superfluid density when T_c strongly depends on the amount of doped holes. In future studies it would be interesting to investigate if the photo-induced charge carriers also influence the superfluid density of optimally doped YBCO and of YBCO within the 60 K-plateau. Microscopic studies on other cuprate systems could reveal whether the Cu-O chains are crucial for the appearance of photo-persistent changes in the microscopic properties, which is still an open issue.

More than 25 years after the discovery of cuprate high-temperature superconductors the microscopic coupling mechanism remains unrevealed. The presented studies demonstrate again the complexity of the cuprate systems in respect to the role of disorder and the delicate interplay between magnetism and superconductivity in these fascinating novel materials.

Appendix

Ellipsometry measurements

The optical response of the YBCO thin-film samples in the spectral range near the 3.1 eV photon energy of the photo-doping was determined with ellipsometry at the University of Fribourg. The measurements were performed with a commercial spectroscopic ellipsometer (Woollam VASE [144]) with a rotating analyzer that covers the near-infrared to ultraviolet photon energy range of $0.5 - 6\,\mathrm{eV}$.

Ellipsometry is an optical technique in which the complex dielectric function of a material is obtained from the change of the polarization state of the light. Typically one uses linearly polarized light at a grazing angle of incidence, and the information on the dielectric function is obtained from the analysis of the elliptically polarized reflected light. This elliptical polarization arises because the components with the polarization vector parallel (p) and perpendicular (s) to the plane of incidence experience a different attenuation and phase shift upon reflection at the ambient-sample interface. This effect is described by the Fresnel equations and is commonly expressed in terms of the ellipsometric angles Ψ and Δ, and the complex reflection coefficient $\tilde{\rho}$:

$$\tilde{\rho} = \frac{\tilde{r}_{\mathrm{p}}}{\tilde{r}_{\mathrm{s}}} = \tan\left(\Psi\right) \cdot e^{i\Delta},$$

where $\tilde{r}_{\mathrm{p}}$ and $\tilde{r}_{\mathrm{s}}$ are the reflection coefficients of the p- and s-component, respectively. For an optically isotropic material the complex dielectric function $\tilde{\epsilon}$ can be calculated from the relationship:

$$\tilde{\epsilon} = \epsilon_1 + i\,\epsilon_2 = \sin^2\left(\varphi\right) + \left(\frac{1-\tilde{\rho}}{1+\tilde{\rho}}\right)^2 \tan^2\left(\varphi\right)\ \sin^2\left(\varphi\right),$$

where φ is the angle of incidence of the light with respect to the surface normal ($\varphi = 0$ corresponds to the crystallographic *c*-axis).

In optically anisotropic materials, such as the cuprate high temperature superconductors, only the so-called pseudo-dielectric function $\langle\epsilon\rangle$ is obtained from the ellipsometry data. In many cases the ellipsometric response is still governed by the p-component and the pseudo-dielectric function is a good approximation to the component of the dielectric function parallel to the plane of incidence. The cuprates exhibit a fairly strong uniaxial anisotropy with a metal-like response along the direction of the $\mathrm{CuO_2}$ planes (*ab*-plane), in contrast

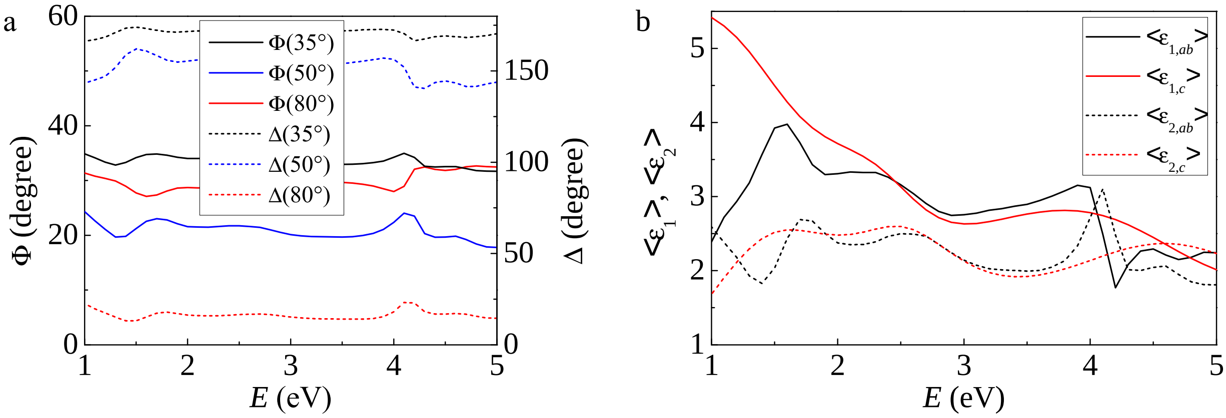

Figure 7.1: The measured ellipsometric angles Ψ and Δ (a) and the calculated components of the pseudo-dielectric function $\langle\epsilon_1\rangle$ and $\langle\epsilon_2\rangle$ (b) versus the photon energy E for sample YZ3 of the thin-film set YBCO$_{6.42}$.

to an almost insulator-like behavior in the perpendicular direction (along the c axis). For YBCO the optical anisotropy is fairly moderate in the optical and UV spectral range (of the interband transitions). A reasonable estimate of the dielectric function thus can be obtained from the as-measured pseudo-dielectric function. An accurate determination of the dielectric function still requires measurements at variable angles of incidence or on different surfaces for which the c axis is either parallel or perpendicular. The latter approach can be used for single crystals, while the former approach needs to be applied for epitaxial thin films for which the c axis is perpendicular to the surface. Therefore, we performed measurements at $\varphi = 35°, 50°$, and $80°$, depicted in the Fig. 7.1a. The data have been analyzed with an optical model that contains a layer of an uniaxial material with independent dielectric function for the in-plane (ab-) and the out-of-plane (c-) directions and a semi-infinite STO substrate. The dielectric function of the latter is already known from independent measurements on a bare substrate. It should be noted that in the relevant energy range of 1 to 5 eV, the penetration depth of the light is significantly shorter than the film thickness. Thus, the optical response is governed by the YBCO film. The ellipsometric angles Ψ and Δ measured at the three angles of incidence were fitted simultaneously in a wavelength-by-wavelength manner by optimizing $\langle\epsilon_{ab}\rangle$ and $\langle\epsilon_c\rangle$. Using this numerical procedure with the Woollam VASE software, the ab-plane and c-axis components of the dielectric function can be determined, as shown in Fig. 7.1b. The penetration depth of the light, ζ, at normal incidence (for our photo-doping geometry with $\varphi = 0°$) can be calculated as follows:

$$\zeta = \frac{\lambda}{4\pi}\left(\frac{2}{\sqrt{\langle\epsilon_{1,ab}\rangle^2 + \langle\epsilon_{2,ab}\rangle^2} - \langle\epsilon_{1,ab}\rangle}\right)^{1/2}.$$

The value around 3.1 eV (equal to $\lambda = 400\,\mathrm{nm}$) that is relevant for our photo-doping experiment is in the range of $\zeta = 50 - 70\,\mathrm{nm}$ at both doping levels and agrees reasonably well with the estimates for YBCO single crystals of about $\zeta = 46 - 81\,\mathrm{nm}$ obtained from the data in Refs. [139] and [140]. Therefore ζ was fixed to 60 nm in the μSR data analysis.

Bibliography

[1] H. Rogalla and P. H. Kes, *100 Years of Superconductivity*, Taylor & Francis, Boca Raton, 2011.

[2] J. G. Bednorz and K. A. Müller, *Possible high-T_c superconductivity in the Ba-La-Cu-O system*, Z. Phys. B - Condens. Matt. **64**, 189 (1986).

[3] A. Schilling, M. Cantoni, J. D. Guo, and H. R. Ott, *Superconductivity above 130 K in the Hg-Ba-Ca-Cu-O system*, Nature (London) **363**, 56 (1993).

[4] J. Bardeen, L. N. Cooper, and J. R. Schrieffer, *Microscopic Theory of Superconductivity*, Phys. Rev. **106**, 162 (1957).

[5] J. Bardeen, L. N. Cooper, and J. R. Schrieffer, *Theory of Superconductivity*, Phys. Rev. **108**, 1175 (1957).

[6] T. Dahm, V. Hinkov, S. V. Borisenko, A. A. Kordyuk, V. B. Zabolotnyy, J. Fink, B. Büchner, D. J. Scalapino, W. Hanke, and B. Keimer, *Strength of the spin-fluctuation-mediated pairing interaction in a high-temperature superconductor*, Nat. Phys. **5**, 217 (2009).

[7] P. W. Anderson, *The Resonating Valence Bond State in La_2CuO_4 and Superconductivity*, Science **235**, 1196 (1987).

[8] M. Vojta, Y. Zhang, and S. Sachdev, *Competing orders and quantum criticality in doped antiferromagnets*, Phys. Rev. B **62**, 6721 (2000).

[9] S. Sachdev, *Colloquium: Order and quantum phase transitions in the cuprate superconductors*, Rev. Mod. Phys. **75**, 913 (2003).

[10] J. P. Carbotte, *Properties of boson-exchange superconductors*, Rev. Mod. Phys. **62**, 1027 (1990).

[11] A. S. Alexandrov and N. F. Mott, *Bipolarons*, Rep. Prog. Phys. **57**, 1197 (1994).

[12] K. A. Müller, *On the superconductivity in hole doped cuprates*, J. Phys.: Condens. Matter **19**, 251002 (2007).

[13] C. W. Chu, P. H. Hor, R. L. Meng, L. Gao, Z. J. Huang, and Y. Q. Wang, *Evidence for superconductivity above* 40 *K in the La-Ba-Cu-O compound system*, Phys. Rev. Lett. **58**, 405 (1987).

[14] S. Yomo, C. Murayama, H. Takahashi, N. Mori, K. Kishio, K. Kitazawa, and K. Fueki, *High Pressure Study and the Critical Current of High* T_c *Superconductor* $(La_{0.9}Sr_{0.1})_2CuO_{4-y}$, Jpn. J. Appl. Phys. **26**, L603 (1987).

[15] M. J. Akhtar, C. R. A. Catlow, S. M. Clark, and W. M. Temmerman, *The pressure dependence of the crystal structure of* La_2CuO_4, J. Phys. C **21**, L917 (1988).

[16] J. Kakalios and H. Fritzsche, *Persistent Photoconductivity in Doping-Modulated Amorphous Semiconductors*, Phys. Rev. Lett. **53**, 1602 (1984).

[17] G. H. Döhler, H. Künzel, and K. Ploog, *Tunable absorption coefficient in GaAs doping superlattices*, Phys. Rev. B **25**, 2616 (1982).

[18] A. Gilabert, A. Hoffmann, M. Medici, and I. Schuller, *Photodoping Effects in High Critical Temperature Superconducting Films and Josephson Junctions*, J. Supercond. **13**, 0896 (2000).

[19] T. Thio, R. J. Birgeneau, A. Cassanho, and M. A. Kastner, *Determination of the energy gap for charged excitations in insulating* La_2CuO_4, Phys. Rev. B **42**, 10800 (1990).

[20] A. Hoffmann, I. K. Schuller, Z. F. Ren, J. Y. Lao, and J. H. Wang, *Persistent photoconductivity in overdoped high-*T_c *thin films*, Phys. Rev. B **56**, 13742 (1997).

[21] A. I. Kirilyuk, N. M. Kreines, and V. I. Kudinov, *Frozen photoconductivity in YBaCuO films*, JETP Letters **52**, 49 (1990).

[22] G. Nieva, E. Osquiguil, J. Guimpel, M. Maenhoudt, B. Wuyts, Y. Bruynseraede, M. B. Maple, and I. K. Schuller, *Photoinduced enhancement of superconductivity*, Appl. Phys. Lett. **60**, 2159 (1992).

[23] L. R. Testardi, *Destruction of Superconductivity by Laser Light*, Phys. Rev. B **4**, 2189 (1971).

[24] N. Plakida, *High-Temperature Cuprate Superconductors - Experiment, Theory, and Applications*, Springer-Verlag, Berlin Heidelberg, 2010.

[25] C. P. Poole Jr., H. A. Farach, and R. J. Creswick, *Superconductivity*, Academic Press, London, 2007.

[26] J. Zaanen, G. A. Sawatzky, and J. W. Allen, *Band gaps and electronic structure of transition-metal compounds*, Phys. Rev. Lett. **55**, 418 (1985).

[27] V. J. Emery and S. A. Kivelson, *Superconductivity in Bad Metals*, Phys. Rev. Lett. **74**, 3253 (1995).

[28] D. A. Bonn, *Are high-temperature superconductors exotic?*, Nat. Phys. **2**, 159 (2006).

[29] N. P. Armitage, P. Fournier, and R. L. Greene, *Progress and perspectives on electron-doped cuprates*, Rev. Mod. Phys. **82**, 2421 (2010).

[30] M. R. Presland, J. L. Tallon, R. G. Buckley, R. S. Liu, and N. E. Flower, *General trends in oxygen stoichiometry effects on* T_c *in Bi and Tl superconductors*, Physica C **176**, 95 (1991).

[31] C. Niedermayer, C. Bernhard, T. Blasius, A. Golnik, A. Moodenbaugh, and J. I. Budnick, *Common Phase Diagram for Antiferromagnetism in* $La_{2-x}Sr_xCuO_4$ *and* $Y_{1-x}Ca_xBa_2Cu_3O_6$ *as Seen by Muon Spin Rotation*, Phys. Rev. Lett. **80**, 3843 (1998).

[32] J. Rossat-Mignod, L. Regnault, C. Vettier, P. Burlet, J. Henry, and G. Lapertot, *Investigation of the spin dynamics in* $YBa_2Cu_3O_{6+x}$ *by inelastic neutron scattering*, Physica B: Cond. Matt. **169**, 58 (1991).

[33] H. Ding, T. Yokoya, J. C. Campuzano, T. Takahashi, M. Randeria, M. R. Norman, T. Mochiku, K. Kadowaki, and J. Giapintzakis, *Spectroscopic evidence for a pseudogap in the normal state of underdoped high-*T_c *superconductors*, Nature (London) **382**, 51 (1996).

[34] C. Renner, B. Revaz, J.-Y. Genoud, K. Kadowaki, and O. Fischer, *Pseudogap Precursor of the Superconducting Gap in Under- and Overdoped* $Bi_2Sr_2CaCu_2O_{8+\delta}$, Phys. Rev. Lett. **80**, 149 (1998).

[35] T. Timusk and B. Statt, *The pseudogap in high-temperature superconductors: an experimental survey*, Rep. Prog. Phys. **62**, 61 (1999).

[36] D. C. Johnston, *Normal state magnetism of the high* T_c *cuprate superconductors*, J. Magn. Magn. Mater. **100**, 218 (1991).

[37] W. W. Warren, R. E. Walstedt, G. F. Brennert, R. J. Cava, R. Tycko, R. F. Bell, and G. Dabbagh, *Cu spin dynamics and superconducting precursor effects in planes above* T_c *in* $YBa_2Cu_3O_{6.7}$, Phys. Rev. Lett. **62**, 1193 (1989).

[38] S. Chakravarty, R. B. Laughlin, D. K. Morr, and C. Nayak, *Hidden order in the cuprates*, Phys. Rev. B **63**, 094503 (2001).

[39] K. M. Kojima, Y. Krockenberger, I. Yamauchi, M. Miyazaki, M. Hiraishi, A. Koda, R. Kadono, R. Kumai, H. Yamamoto, A. Ikeda, and M. Naito, *Bulk superconductivity in undoped T'-*$La_{1.9}Y_{0.1}CuO_4$ *probed by muon spin rotation*, Phys. Rev. B **89**, 180508 (2014).

[40] W. Meissner and R. Ochsenfeld, *Ein neuer Effekt bei Eintritt der Supraleitfähigkeit*, Naturwissenschaften **21**, 787 (1933).

[41] F. London and H. London, *The Electromagnetic Equations of the Supraconductor*, Proc. R. Soc. Lond. A **149**, 71 (1935).

[42] F. London and H. London, *Supraleitung und Diamagnetismus*, Physica **2**, 341 (1935).

[43] M. Tinkham, *Introduction to superconductivity*, McGraw-Hill, New York, 1996.

[44] V. L. Ginzburg and L. D. Landau, *On the Theory of Superconductivity*, Zh. Eksp. Teor. Fiz. **20**, 1064 (1950).

[45] E. Dagotto, *Correlated electrons in high-temperature superconductors*, Rev. Mod. Phys. **66**, 763 (1994).

[46] A. A. Abrikosov, *On the Magnetic Properties of Superconductors of the Second Group*, Sov. Phys.–JETP **5**, 1174 (1957).

[47] C. C. Tsuei and J. R. Kirtley, *Pairing symmetry in cuprate superconductors*, Rev. Mod. Phys. **72**, 969 (2000).

[48] J. E. Sonier, R. F. Kiefl, J. H. Brewer, D. A. Bonn, J. F. Carolan, K. H. Chow, P. Dosanjh, W. N. Hardy, R. Liang, W. A. MacFarlane, P. Mendels, G. D. Morris, T. M. Riseman, and J. W. Schneider, *New muon-spin-rotation measurement of the temperature dependence of the magnetic penetration depth in* $YBa_2Cu_3O_{6.95}$, Phys. Rev. Lett. **72**, 744 (1994).

[49] R. F. Kiefl, M. D. Hossain, B. M. Wojek, S. R. Dunsiger, G. D. Morris, T. Prokscha, Z. Salman, J. Baglo, D. A. Bonn, R. Liang, W. N. Hardy, A. Suter, and E. Morenzoni, *Direct measurement of the London penetration depth in $YBa_2Cu_3O_{6.92}$ using low-energy μSR*, Phys. Rev. B **81**, 180502 (2010).

[50] R. Khasanov, A. Shengelaya, A. Maisuradze, F. L. Mattina, A. Bussmann-Holder, H. Keller, and K. A. Müller, *Experimental Evidence for Two Gaps in the High-Temperature $La_{1.83}Sr_{0.17}CuO_4$ Superconductor*, Phys. Rev. Lett. **98**, 057007 (2007).

[51] R. Khasanov, A. Shengelaya, J. Karpinski, A. Bussmann-Holder, H. Keller, and K. A. Müller, *s-Wave Symmetry Along the c-Axis and s+d In-plane Superconductivity in Bulk $YBa_2Cu_4O_8$*, J. Supercond. Novel Magn. **21**, 81 (2008).

[52] A. Bussmann-Holder, R. Khasanov, A. Shengelaya, A. Maisuradze, F. L. Mattina, H. Keller, and K. A. Müller, *Mixed order parameter symmetries in cuprate superconductors*, EPL **77**, 27002 (2007).

[53] A. Furrer, *Admixture of an s-Wave Component to the d-Wave Gap Symmetry in High-Temperature Superconductors*, J. Supercond. Nov. Magn. **21**, 1557 (2008).

[54] R. Stern, M. Mali, J. Roos, and D. Brinkmann, *Spin pseudogap and interplane coupling in $Y_2Ba_4Cu_7O_{15}$: A ^{63}Cu nuclear spin-spin relaxation study*, Phys. Rev. B **51**, 15478 (1995).

[55] Quantum Design Inc., *www.qdusa.com/products/ppms.html.*

[56] CryoVac GmbH & Co KG, *http://www.cryovac.de/frameset1.html.*

[57] TPT Wire Bonder GmbH & Co KG, *https://www.keithley.de/products/dcac/current-voltage.*

[58] Keithley Instruments Inc., *https://www.keithley.de/products/dcac/currentvoltage.*

[59] Dr. Hönle AG, *http://www.hoenle.de/uv-produkte/uv-geraete-bluepoint/bluepoint-led/.*

[60] Dr. Hönle AG, *http://www.hoenle.de/uv-produkte/uv-anlagen-messtechnik/uv-messgeraet/.*

[61] Rascom Computerdistribution GmbH, *http://www.noctua.at/main.php?show=productview&products_id=34&lng=en.*

[62] Thorlabs Inc., *http://www.thorlabs.us/thorcat/0600/FDS100-SpecSheet.pdf.*

[63] LI-COR Inc., *http://envsupport.licor.com/docs/LI-185B_Manual.pdf.*

[64] Thorlabs Inc., *http://www.thorlabs.com/thorproduct.cfm?partnumber=LA1353.*

[65] P. Truöl, *Myonen und Pionen in Teilchenphysik und Anwendungen - 30 Jahre experimentelle Forschung an der Schweizer Mesonenfabrik in Villigen*, Naturforschende Gesellschaft in Zürich, KOPRINT AG, Alpnach Dorf, 2007.

[66] F. Scheck, *Muon physics – Survey*, Zeitschrift für Physik C Particles and Fields **56**, S5 (1992).

[67] A. Yaouanc and P. Dalmas de Réotier, *Muon Spin Rotation, Relaxation, and Resonance: Applications to Condensed Matter*, Oxford University Press, Oxford, 2011.

[68] A. Schenck, *Muon Spin Rotation Spectroscopy: Principles and Applications in Solid State Physics*, Adam Hilger, Bristol, 1985.

[69] E. Morenzoni, E. Forgan, H. Glückler, T. Jackson, H. Luetkens, C. Niedermayer, T. Prokscha, T. Riseman, M. Birke, A. Hofer, J. Litterst, M. Pleines, and G. Schatz, *Muon Spin Rotation and Relaxation Experiments on Thin Films*, Hyperfine Interact. **133**, 179 (2001).

[70] E. Morenzoni, T. Prokscha, A. Hofer, B. Matthias, M. Meyberg, T. Wutzke, H. Glückler, M. Birke, J. Litterst, C. Neidermayer, and G. Schatz, *Characteristics of condensed gas moderators for the generation of very slow polarized muons*, J. Appl. Phys. **81**, 3340 (1997).

[71] E. Morenzoni, F. Kottmann, D. Maden, B. Matthias, M. Meyberg, T. Prokscha, T. Wutzke, and U. Zimmermann, *Generation of very slow polarized positive muons*, Phys. Rev. Lett. **72**, 2793 (1994).

[72] Z. Salman, T. Prokscha, P. Keller, E. Morenzoni, H. Saadaoui, K. Sedlak, T. Shiroka, S. Sidorov, A. Suter, V. Vrankovic, and H.-P. Weber, *Design and Simulation of a Spin Rotator for Longitudinal Field Measurements in the Low Energy Muons Spectrometer*, Phys. Procedia **30**, 55 (2012).

[73] W. Eckstein, *Computer Simulation of Ion-Solid Interactions*, Springer, Berlin, 1991.

[74] E. Morenzoni, H. Glückler, T. Prokscha, R. Khasanov, H. Luetkens, M. Birke, E. Forgan, C. Niedermayer, and M. Pleines, *Implantation studies of keV positive muons in thin metallic layers*, Nucl. Instr. Meth. B **192**, 254 (2002).

[75] E. Morenzoni, T. Prokscha, A. Suter, H. Luetkens, and R. Khasanov, *Nano-scale thin film investigations with slow polarized muons*, J. Phys.: Cond. Matt. **16**, S4583 (2004).

[76] E. Morenzoni, H. Glückler, T. Prokscha, H. Weber, E. Forgan, T. Jackson, H. Luetkens, C. Niedermayer, M. Pleines, M. Birke, A. Hofer, J. Litterst, T. Riseman, and G. Schatz, *Low-energy μSR at PSI: present and future*, Physica B: Cond. Matt. **289–290**, 653 (2000).

[77] T. Prokscha, E. Morenzoni, A. Suter, R. Khasanov, H. Luetkens, D. Eshchenko, N. Garifianov, E. Forgan, H. Keller, J. Litterst, C. Niedermayer, and G. Nieuwenhuys, *Thin Film, Near-Surface and Multi-Layer Investigations by Low-Energy μ^+SR*, Hyperfine Interact. **159**, 227 (2004).

[78] P. Bakule and E. Morenzoni, *Generation and applications of slow polarized muons*, Contemporary Physics **45**, 203 (2004).

[79] T. Prokscha, E. Morenzoni, K. Deiters, F. Foroughi, D. George, R. Kobler, A. Suter, and V. Vrankovic, *The new high-intensity surface muon beam μE4 for the generation of low-energy muons at PSI*, Physica B: Cond. Matt. **374–375**, 460 (2006).

[80] T. Prokscha, E. Morenzoni, K. Deiters, F. Foroughi, D. George, R. Kobler, A. Suter, and V. Vrankovic, *The new beam at PSI: A hybrid-type large acceptance channel for the generation of a high intensity surface-muon beam*, Nucl. Instrum. Methods Phys. Res., Sect. A **595**, 317 (2008).

[81] T. Prokscha, R. Scheuermann, U. Hartmann, A. Raselli, A. Suter, A. Amato, G. Nieuwenhuys, A. Dijksmann, F. Gärtner, U. Greuter, S. Mutter, N. Schlumpf, and E. Morenzoni, *A novel VME based μSR data acquisition system at PSI*, Physica B: Cond. Matt. **404**, 1007 (2009).

[82] V. P. Smilga and Y. M. Belousov, *The Muon Method in Science*, Nova Science Publishers, New York, 1994.

[83] R. Kubo and T. Toyabe, *A stochastic model for low field resonance and relaxation*, North Holland Publisher, Amsterdam, 1967, in *Magnetic Resonance and Relaxation, Proceedings of XIVth Colloque Ampre, Ljubljana.*

[84] T. J. Jackson, T. M. Riseman, E. M. Forgan, H. Glückler, T. Prokscha, E. Morenzoni, M. Pleines, C. Niedermayer, G. Schatz, H. Luetkens, and J. Litterst, *Depth-Resolved Profile of the Magnetic Field beneath the Surface of a Superconductor with a Few nm Resolution*, Phys. Rev. Lett. **84**, 4958 (2000).

[85] E. Morenzoni, B. M. Wojek, A. Suter, T. Prokscha, G. Logvenov, and I. Božovic, *The Meissner effect in a strongly underdoped cuprate above its critical temperature*, Nat. Commun. **2**, 272 (2011).

[86] B. M. Wojek, E. Morenzoni, D. G. Eshchenko, A. Suter, T. Prokscha, H. Keller, E. Koller, O. Fischer, V. K. Malik, C. Bernhard, and M. Döbeli, *Magnetism, superconductivity, and coupling in cuprate heterostructures probed by low-energy muon-spin rotation*, Phys. Rev. B **85**, 024505 (2012).

[87] A. Suter, E. Morenzoni, N. Garifianov, R. Khasanov, E. Kirk, H. Luetkens, T. Prokscha, and M. Horisberger, *Observation of nonexponential magnetic penetration profiles in the Meissner state: A manifestation of nonlocal effects in superconductors*, Phys. Rev. B **72**, 024506 (2005).

[88] V. Kozhevnikov, A. Suter, H. Fritzsche, V. Gladilin, A. Volodin, T. Moorkens, M. Trekels, J. Cuppens, B. M. Wojek, T. Prokscha, E. Morenzoni, G. J. Nieuwenhuys, M. J. Van Bael, K. Temst, C. Van Haesendonck, and J. O. Indekeu, *Nonlocal effect and dimensions of Cooper pairs measured by low-energy muons and polarized neutrons in type-I superconductors*, Phys. Rev. B **87**, 104508 (2013).

[89] A. Romanenko, A. Grassellino, F. Barkov, A. Suter, Z. Salman, and T. Prokscha, *Strong Meissner screening change in superconducting radio frequency cavities due to mild baking*, Appl. Phys. Lett. **104**, 072601 (2014).

[90] M. Lindstrom, B. Wetton, and R. Kiefl, *Mathematical modelling of the effect of surface roughness on magnetic field profiles in type II superconductors*, J. Eng. Math. **85**, 149 (2014).

[91] H. Sato and M. Naito, *Increase in the superconducting transition temperature by anisotropic strain effect in (001)* $La_{1.85}Sr_{0.15}CuO_4$ *thin films on* $LaSrAlO_4$ *substrates*, Physica C **274**, 221 (1997).

[92] J.-P. Locquet, J. Perret, J. Fompeyrine, E. Mächler, J. W. Seo, and G. Van Tendeloo, *Doubling the critical temperature of* $La_{1.9}Sr_{0.1}CuO_4$ *using epitaxial strain*, Nature (London) **394**, 453 (1998).

[93] I. Bozovic, G. Logvenov, I. Belca, B. Narimbetov, and I. Sveklo, *Epitaxial Strain and Superconductivity in* $La_{2-x}Sr_xCuO_4$ *Thin Films*, Phys. Rev. Lett. **89**, 107001 (2002).

[94] J. D. Jorgensen, H. B. Schüttler, D. G. Hinks, D. W. Capone II, K. Zhang, M. B. Brodsky, and D. J. Scalapino, *Lattice instability and high-*T_c *superconductivity in* $La_{2-x}Ba_xCuO_4$, Phys. Rev. Lett. **58**, 1024 (1987).

[95] G. Shirane, Y. Endoh, R. J. Birgeneau, M. A. Kastner, Y. Hidaka, M. Oda, M. Suzuki, and T. Murakami, *Two-dimensional antiferromagnetic quantum spin-fluid state in* La_2CuO_4, Phys. Rev. Lett. **59**, 1613 (1987).

[96] M. Reehuis, C. Ulrich, K. Prokeš, A. Gozar, G. Blumberg, S. Komiya, Y. Ando, P. Pattison, and B. Keimer, *Crystal structure and high-field magnetism of* La_2CuO_4, Phys. Rev. B **73**, 144513 (2006).

[97] J. H. Cho, F. C. Chou, and D. C. Johnston, *Phase Separation and Finite Size Scaling in* $La_{2-x}Sr_xCuO_{4+\delta}$ $[0 \leq (x, \delta) \leq 0.03]$, Phys. Rev. Lett. **70**, 222 (1993).

[98] F. C. Chou, F. Borsa, J. H. Cho, D. C. Johnston, A. Lascialfari, D. R. Torgeson, and J. Ziolo, *Magnetic phase diagram of lightly doped* $La_{2-x}Sr_xCuO_4$ *from* ^{139}La *nuclear quadrupole resonance*, Phys. Rev. Lett. **71**, 2323 (1993).

[99] F. Borsa, P. Carreta, J. H. Cho, F. C. Chou, Q. Hu, D. C. Johnston, A. Lascialfari, D. R. Torgeson, R. J. Gooding, N. M. Salem, and K. J. E. Vos, *Staggered magnetization in* $La_{2-x}Sr_xCuO_4$ *from* ^{139}La *NQR and* μ*SR: Effects of Sr doping in the range* $0 < x < 0.02$, Phys. Rev. B **52**, 7334 (1995).

[100] M. A. Kastner, R. J. Birgeneau, G. Shirane, and Y. Endoh, *Magnetic, transport, and optical properties of monolayer copper oxides*, Rev. Mod. Phys. **70**, 897 (1998).

[101] S. Uchida, H. Takagi, K. Kishio, K. Kitazawa, K. Fueki, and S. Tanaka, *Superconducting Properties of* $(La_{1-x}Sr_x)_2CuO_4$, Jpn. J. Appl. Phys. **26**, L443 (1987).

[102] R. J. Cava, R. B. van Dover, B. Batlogg, and E. A. Rietman, *Bulk superconductivity at 36 K in* $La_{1.8}Sr_{0.2}CuO_4$, Phys. Rev. Lett. **58**, 408 (1987).

[103] I. Bozovic, *Atomic-layer engineering of superconducting oxides: yesterday, today, tomorrow*, IEEE Trans. Appl. Supercond. **11**, 2686 (2001).

[104] P. G. Radaelli, D. G. Hinks, A. W. Mitchell, B. A. Hunter, J. L. Wagner, B. Dabrowski, K. G. Vandervoort, H. K. Viswanathan, and J. D. Jorgensen, *Structural and superconducting properties of* $La_{2-x}Sr_xCuO_4$ *as a function of Sr content*, Phys. Rev. B **49**, 4163 (1994).

[105] D. Lampakis, D. Palles, E. Liarokapis, C. Panagopoulos, J. R. Cooper, H. Ehrenberg, and T. Hartmann, *Phase transitions and Raman spectra correlations in* $La_{2-x}Sr_xCuO_4$ $(0.0 < x < 0.45)$, Phys. Rev. B **62**, 8811 (2000).

[106] V. Y. Butko, G. Logvenov, N. Bozovic, Z. Radovic, and I. Bozovic, *Madelung Strain in Cuprate Superconductors – A Route to Enhancement of the Critical Temperature*, Adv. Mater. **21**, 3644 (2009).

[107] B. M. Wojek, *PSI Memorandum: Four-point resistivity correction factors for thin films*, Villigen, 2009.

[108] A. Suter, *PSI Memorandum: Four-Point Resistivity Correction Factors for Thin Films: Addendum and Corrections*, Villigen, 2012.

[109] Y. Ando, S. Komiya, K. Segawa, S. Ono, and Y. Kurita, *Electronic Phase Diagram of High-*T_c *Cuprate Superconductors from a Mapping of the In-Plane Resistivity Curvature*, Phys. Rev. Lett. **93**, 267001 (2004).

[110] J. He, R. F. Klie, G. Logvenov, I. Bozovic, and Y. Zhu, *Microstructure and possible strain relaxation mechanisms of* $La_2CuO_{4+\delta}$ *thin films grown on* $LaSrAlO_4$ *and* $SrTiO_3$ *substrates*, J. Appl. Phys. **101**, 073906 (2007).

[111] N. W. Preyer, R. J. Birgeneau, C. Y. Chen, D. R. Gabbe, H. P. Jenssen, M. A. Kastner, P. J. Picone, and T. Thio, *Conductivity and Hall coefficient in* La_2CuO_{4+y} *near the insulator-metal transition*, Phys. Rev. B **39**, 11563 (1989).

[112] H. Katsu, H. Tanaka, and T. Kawai, *Anomalous Photoconductivity in* $SrTiO_3$, Jpn. J. Appl. Phys. **39**, 2657 (2000).

[113] H. Zhang, L. Yan, and H.-U. Habermeier, *Unusual ultraviolet photoconductivity in single crystalline* $SrTiO_3$, J. Phys.: Cond. Matt. **25**, 035802 (2013).

[114] L. Zhi-Qing, Z. Kun, Z. Hui, Z. Song-Qing, and Z. Qing-Li, *Ultraviolet laser-induced voltages in* $LaSrAlO_4$ *single crystal*, Chin. Phys. B **18**, 4521 (2009).

[115] Y. Ando, A. N. Lavrov, S. Komiya, K. Segawa, and X. F. Sun, *Mobility of the Doped Holes and the Antiferromagnetic Correlations in Underdoped High-*T_c *Cuprates*, Phys. Rev. Lett. **87**, 017001 (2001).

[116] A. Suter and B. Wojek, *Musrfit: A Free Platform-Independent Framework for* μ*SR Data Analysis*, Phys. Procedia **30**, 69 (2012).

[117] V. I. Kudinov, A. I. Kirilyuk, N. M. Kreines, R. Laiho, and E. Lähderanta, *Photoinduced superconductivity in YBaCuO films*, Phys. Lett. A **151**, 358 (1990).

[118] F. Coneri, S. Sanna, K. Zheng, J. Lord, and R. De Renzi, *Magnetic states of lightly hole-doped cuprates in the clean limit as seen via zero-field muon spin spectroscopy*, Phys. Rev. B **81**, 104507 (2010).

[119] D. Haug, V. Hinkov, Y. Sidis, P. Bourges, N. B. Christensen, A. Ivanov, T. Keller, C. T. Lin, and B. Keimer, *Neutron scattering study of the magnetic phase diagram of underdoped* $YBa_2Cu_3O_{6+x}$, New J. Phys. **12**, 105006 (2010).

[120] K. Segawa and Y. Ando, *Transport Anomalies and the Role of Pseudogap in the 60-K Phase of* $YBa_2Cu_3O_{7-\delta}$, Phys. Rev. Lett. **86**, 4907 (2001).

[121] A. J. Millis and M. R. Norman, *Antiphase stripe order as the origin of electron pockets observed in 1/8-hole-doped cuprates*, Phys. Rev. B **76**, 220503 (2007).

[122] J. D. Jorgensen, B. W. Veal, A. P. Paulikas, L. J. Nowicki, G. W. Crabtree, H. Claus, and W. K. Kwok, *Structural properties of oxygen-deficient* $YBa_2Cu_3O_{7-\delta}$, Phys. Rev. B **41**, 1863 (1990).

[123] V. I. Kudinov, I. L. Chaplygin, A. I. Kirilyuk, N. M. Kreines, R. Laiho, E. Lähderanta, and C. Ayache, *Persistent photoconductivity in* $YBa_2Cu_3O_{6+x}$ *films as a method of photodoping toward metallic and superconducting phases*, Phys. Rev. B **47**, 9017 (1993).

[124] M. M. Milic, N. D. Lazarov, and D. A. Cucic, *Study on the photo-induced oxygen reordering in* $YBa_2Cu_3O_{6+x}$, Nucl. Instr. Meth. Phys. Res. B **279**, 212 (2012).

[125] M. v. Zimmermann, J. R. Schneider, T. Frello, N. H. Andersen, J. Madsen, M. Käll, H. F. Poulsen, R. Liang, P. Dosanjh, and W. N. Hardy, *Oxygen-ordering superstructures in underdoped* $YBa_2Cu_3O_{6+x}$ *studied by hard x-ray diffraction*, Phys. Rev. B **68**, 104515 (2003).

[126] R. Liang, D. A. Bonn, and W. N. Hardy, *Evaluation of* CuO_2 *plane hole doping in* $YBa_2Cu_3O_{6+x}$ *single crystals*, Phys. Rev. B **73**, 180505 (2006).

[127] P. Pahlke, *Herstellung und Untersuchung von supraleitenden YBCO-Schichten auf piezoelektrischen Substraten*, Diploma thesis, Technische Universität Dresden, 2011.

[128] R. Hühne, V. S. Sarma, D. Okai, T. Thersleff, L. Schultz, and B. Holzapfel, *Preparation of coated conductor architectures on Ni composite tapes*, Supercond. Sci. Technol. **20**, 709 (2007).

[129] A. Kiessling, J. Hänisch, T. Thersleff, E. Reich, M. Weigand, R. Hühne, M. Sparing, B. Holzapfel, J. H. Durrell, and L. Schultz, *Nanocolumns in* $YBa_2Cu_3O_{7-x}/BaZrO_3$ *quasi-multilayers: formation and influence on superconducting properties*, Supercond. Sci. Technol. **24**, 055018 (2011).

[130] P. Pahlke, S. Trommler, B. Holzapfel, L. Schultz, and R. Hühne, *Dynamic variation of biaxial strain in optimally doped and underdoped* $YBa_2Cu_3O_{7-\delta}$ *thin films*, J. Appl. Phys. **113**, 123907 (2013).

[131] R. Liang, D. A. Bonn, and W. N. Hardy, *Growth of YBCO single crystals by the self-flux technique*, Philos. Mag. **92**, 2563 (2012).

[132] G. Yu, A. J. Heeger, G. Stucky, N. Herron, and E. M. McCarron, *Transient photoinduced conductivity in semiconducting single crystals of* $YBa_2Cu_3O_{6.3}$*: Search for photoinduced metallic state and for photoinduced superconductivity*, Solid State Comm. **72**, 345 (1989).

[133] K. Tanabe, S. Kubo, F. Hosseini Teherani, H. Asano, and M. Suzuki, *Effects of photoinduced hole doping on normal-state and superconducting transport in oxygen-deficient* $YBa_2Cu_3O_y$, Phys. Rev. Lett. **72**, 1537 (1994).

[134] B. W. Veal, A. P. Paulikas, H. You, H. Shi, Y. Fang, and J. W. Downey, *Observation of temperature-dependent site disorder in* $YBa_2Cu_3O_{7-\delta}$ *below* $150°C$, Phys. Rev. B **42**, 6305 (1990).

[135] D. M. Bubb, J. F. Federici, S. C. Tidrow, W. Wilber, J. Kim, and A. Piqué, *Wavelength and photon dose dependence of infrared quenched persistent photoconductivity in* $YBa_2Cu_3O_{6+x}$, Phys. Rev. B **60**, 6827 (1999).

[136] D. M. Bubb and J. F. Federici, *Cellular automata model for persistent photoconductivity in YBCO*, J. Phys.: Condens. Matter **12**, L261 (2000).

[137] W. Kula and R. Sobolewski, *Charging effect in partially oxygen-depleted superconducting Y-Ba-Cu-O thin films*, Phys. Rev. B **49**, 6428 (1994).

[138] G. Grigelionis, E. E. Tornau, and A. Rosengren, *Effect of an electric field on oxygen ordering and superconducting temperature of* $YBa_2Cu_3O_{6+x}$ *thin films*, Phys. Rev. B **53**, 425 (1996).

[139] J. Kircher, M. K. Kelly, S. Rashkeev, M. Alouani, D. Fuchs, and M. Cardona, *Anisotropy and oxygen-stoichiometry dependence of the dielectric tensor of* $YBa_2Cu_3O_{7-\delta}$ *(*$0 \leq \delta \leq 1$*)*, Phys. Rev. B **44**, 217 (1991).

[140] A. L. Kotz, M. V. Klein, W. C. Lee, J. Giapintzakis, D. M. Ginsberg, and B. W. Veal, *Anisotropy of the optical dielectric function in the ab plane for* $YBa_2Cu_3O_{7-\delta}$, Phys. Rev. B **45**, 2577 (1992).

[141] M. Abramowitz and I. A. Stegun, *Handbook of Mathematical Functions with Formulas, Graphs, and Mathematical Tables*, U.S. Government Printing Office, Washington, 1972.

[142] D. N. Basov, R. Liang, D. A. Bonn, W. N. Hardy, B. Dabrowski, M. Quijada, D. B. Tanner, J. P. Rice, D. M. Ginsberg, and T. Timusk, *In-Plane Anisotropy of the Penetration Depth in* $YBa_2Cu_3O_{7-x}$ *and* $YBa_2Cu_4O_8$ *Superconductors*, Phys. Rev. Lett. **74**, 598 (1995).

[143] W. A. Atkinson, *Disorder and chain superconductivity in* $YBa_2Cu_3O_{7-\delta}$, Phys. Rev. B **59**, 3377 (1999).

[144] J.A. Woollam Company, *http://www.jawoollam.com/vase_home.html.*

Acknowledgements

Die vorliegende Arbeit hätte ich nie ohne tatkräftige Unterstützung fertig stellen können. Hier möchte ich allen danken, die mich während der Promotion begleitet haben.

Als erstes möchte ich mich bei Hugo Keller bedanken. Du hast mir die Möglichkeit gegeben meinen PhD an der Uni Zürich zu absolvieren. Während der Promotion hast du mich stets gefördert, motiviert und mir einen differenzierten Blick auf die Forschung vermittelt. Die Gruppenmeetings und die Arbeit an den Publikationen haben meinen Horizont sehr erweitert. Danke für die tolle Zeit in deiner Gruppe.

Andreas Suter war mein direkter Betreuer. Du hast deinen Job erstklassig gemacht! Ich konnte alle meine Fragen und Ideen jeder Zeit mit dir diskutieren. Deine Unterstützung, sei es während der Strahlzeit oder bei dem Schreiben einer Publikation, hat mir sehr geholfen meine Promotion mit viel Begeisterung erfolgreich zu bewältigen. Dein Enthusiasmus springt einfach über. Danke für all die Geduld und Zeit, die du mir geschenkt hast.

Elvezio Morenzoni hat meine Promotion betreut. Dank dir konnte ich neben der Uni Zürich auch das PSI näher kennen lernen. Ich danke dir für deine fachliche Unterstützung und die Freiheiten, die du mir in meiner PhD Zeit gelassen hast. Diese haben mir sehr geholfen mich persönlich weiter zu entwickeln.

Thomas Prokscha, dem Gruppenleiter von LEM, möchte ich auch recht herzlich danken. Mit dir habe ich meine erste Strahlzeit absolviert. Du bist ein toller Gruppenleiter, der es versteht seine Mitarbeiter zu motivieren und allseitig zu unterstützen. Es hat mir sehr viel Spass gemacht ein Teil deiner Truppe zu sein.

Den Mitarbeitern der Gruppe Magnetismus und Supraleitung, insbesondere Markus Bendele, Saskia Bosma, Zurab Guguchia, Ludovic Howald, Alexander Maisuradze, Roman Puzniak, Josef Roos, Stefan Siegrist, Stephen Weyeneth und Bastian Wojek, möchte ich ebenfalls danken. Wir hatten tolle Diskussionen, viele gemütliche Abende und eine Menge Spass bei der Arbeit sowie in der Freizeit. Vielen lieben Dank euch allen!

Einen Dank auch an alle Mitarbeiter des Physik-Instituts der Uni Zürich. Ich hatte eine mega schöne Zeit bei euch!

Hans-Peter Weber danke ich für die exzellente technische Unterstützung. Ohne deine Hilfe wären meine Konstruktionen nur halb so gut.

Dem gesamten μSR-Team am PSI danke ich für die freundliche Aufnahme in ihren Kreis. Ihr habt mir stets geholfen und ich habe eure Gesellschaft sehr genossen.

Meinen Kollaboratoren Jordan Baglo, Christian Bernhard, Douglas Bonn, Ivan Božović, Max Döbeli, Adrian Gozar, Walter Hardy, Ruben Hühne, Christian Katzer, Robert Kiefl, Ruixing Liang, Gennady Logvenov, Patrick Pahlke and Frank Schmidl danke ich für die konstruktive und effiziente Zusammenarbeit. Unsere Projekte haben mir sehr viel Freude gemacht und ich habe viel gelernt.

Weiterhin möchte ich meinen Freunden und allen Mitgliedern der Sunday Board Games Group sowie den Starlight Diamonds und Jewels danken. Ihr habt dafür gesorgt das ich mich prima in Zürich eingelebt habe, meinen Lieblingssport das Synchroneiskunstlaufen wieder ausgeübt habe und immer jemand da war, wenn ich Probleme hatte. Danke euch allen, ich bin mega stolz euch zu kennen!

Abschliessend möchte ich meiner Familie und meinem Lebensgefährten Daniel danken. Meine Schwester Liane und meinen Grosseltern möchte ich sagen: Danke das ihr immer hinter mir steht, egal was kommt. Ihr, Mutti und Vati, habt mich seit meiner Kindheit unterstützt und seit mit mir durch alle Höhen und Tiefen gegangen, ohne mir je vorzuschreiben wie ich mein Leben leben soll. Ihr seit grossartig! Daniel, dich habe ich während meiner Promotion kennen und lieben gelernt. Du weist immer was in mir vorgeht und was mir gut tut. Wir haben so eine tolle Zeit zusammen. Du bist der Beste!

Diese Arbeit wurde finanziell unterstützt durch die Swiss National Science Foundation.

Curriculum Vitae

Personal data

Name	Stilp
Given names	Andrea Evelyn
Date of birth	October 27, 1986
Place of birth	Dresden, Germany
Nationality	German

Education

12/2010–11/2014	PhD studies of experimental physics, Physik-Institut der Universität Zürich and Labor für Myonenspinspektroskopie des Paul Scherrer Instituts, Switzerland
11/2010	Diploma in physics (equivalent to Master)
02/2009–06/2009	Foreign studies of physics, Loughborough University, United Kingdom
10/2005–11/2010	Diploma studies of physics, Technische Universität Dresden, Germany
07/2005	Abitur (university-entrance diploma)
08/1997–07/2005	Secondary school, Bertolt-Brecht-Gymnasium Dresden, Germany

Experience

02/2011–11/2014	Teaching assistant for physics, Physik-Institut der Universität Zürich, Switzerland
09/2006–11/2010	Student research assistant, Leibniz-Institut für Festkörper- und Werkstoffforschung Dresden, Germany
08/2008–10/2008	Industrial internship, Robert Bosch GmbH, Stuttgart, Germany
06/2002	Professional practical training, Institut für angewandte Photophysik der technischen Universität Dresden, Germany

Publications

- E. Stilp, A. Suter, T. Prokscha, Z. Salman, E. Morenzoni, H. Keller, P. Pahlke, R. Hühne, C. Bernhard, Ruixing Liang, W. N. Hardy, D. A. Bonn, J. C. Baglo, and R. F. Kiefl,

  Controlling the near-surface superfluid density in underdoped $YBa_2Cu_3O_{6+x}$ by photo-illumination,

  Sci. Rep. **4**, 6250 (2014).

- E. Stilp, A. Suter, T. Prokscha, E. Morenzoni, H. Keller, C. Katzer, F. Schmidl, and M. Döbeli,

  Modifications of the Meissner screening profile in $YBa_2Cu_3O_{7-\delta}$ thin films by gold nanoparticles,

  Phys. Rev. B **89**, 020510(R) (2014).

- T. Prokscha, K. H. Chow, E. Stilp, A. Suter, H. Luetkens, E. Morenzoni, G. J. Nieuwenhuys, Z. Salman, and R. Scheuermann,

  Photo-induced persistent inversion of germanium in a 200-nm-deep surface region,

  Sci. Rep. **3**, 2569 (2013).

- E. Stilp, A. Suter, T. Prokscha, E. Morenzoni, H. Keller, B. M. Wojek, H. Luetkens, A. Gozar, G. Logvenov, and I. Božović,

  Magnetic phase diagram of low-doped $La_{2-x}Sr_xCuO_4$ thin films studied by low-energy muon-spin rotation,

  Phys. Rev. B **88**, 064419 (2013).

- E. Stilp, J. Freudenberger, M. Seifert, A. K. Patra, S. Menzel, I. Moench, L. Schultz, and V. Neu,

  Probing the anisotropy constants of $SmCo_5$ and $PrCo_5$ by Hall resistance measurements in pulsed high magnetic fields up to 47T,

  J. Magn. Magn. Mater. **324**, 1711–1714 (2012).